Theses and Dissertations

May 2019

The Design and Optimization of Jet-in-Cross-Flow (JICF) for Engineering Applications: Thermal Uniformity in Gas-turbines and Cavitation Treatment in Hydro-turbines

Tarek Mahmoud Mohammed ElGammal

University of Wisconsin-Milwaukee

THE DESIGN AND OPTIMIZATION OF JET-IN-CROSS-FLOW (JICF) FOR

ENGINEERING APPLICATIONS: THERMAL UNIFORMITY IN GAS-

TURBINES AND CAVITATION TREATMENT IN HYDRO-TURBINES

by

Tarek ElGammal

A Dissertation Submitted in

Partial Fulfillment of the

Requirements for the Degree of

Doctor of Philosophy

in Engineering

at

The University of Wisconsin-Milwaukee

May 2019

ABSTRACT

THE DESIGN AND OPTIMIZATION OF JET-IN-CROSS-FLOW (JICF) FOR
ENGINEERING APPLICATIONS: THERMAL UNIFORMITY IN GAS-TURBINES AND
CAVITATION TREATMENT IN HYDRO-TURBINES

by

Tarek ElGammal

The University of Wisconsin-Milwaukee, 2019
Under the Supervision of Professor Ryoichi S. Amano

Jet-in-cross-flow (JICF) is a well-known term in thermal flows field. Ranging from the normal

phenomenon like the volcano ash and dust plumes to the designed film cooling and air fuel mixing

for combustion, JICF is always studied to understand its nature at different conditions. Realizing

the behavior of interacting flows and importance of many variables lead to the process of

reiterating the shapes and running conditions for better outcomes or minimizing the losses.

Summarizing the process under the name of optimization, two JICF applications are analyzed

based on the principles of thermodynamics and fluid mechanics, then some redesigns are proposed

to reach the optimal statuses for the goals sought. Correlations and recommendations are given

between the input variables and the outputs.

In the first application, annular thermal mixing chamber, the cold stream penetrates the axial

hot flow as circumferential inward jets. Thermal uniformity of the exit mixture is the target to

maximize, and accordingly, a streamlined body is firstly suggested to be placed at the center of the

chamber to divert the hot stream towards the cold one. Following the idea, the shape and

dimensions (length and maximum diameter) are tested experimentally with four 3-D printed bodies expressing different aspect, blockage, and profile ratios. Later, an Analysis LED Design stage (numerical then experimental) checked the effect of adding swirlers on the best streamlined shape. Swirlers shape, number, and height are examined for the relation with the uniformity and pressure drop. By defining a decision-making variable (usefulness efficiency), the two contradicting variables were consolidated into one, and the swirlers performance was easier to be quantified and the most efficient one was nominated. At the final stage, a numerical study searched the optimal design(s) using design of experiment and optimization (Global and Hybrid) algorithms. The study sought the optimality of the dimensional aspects (diameter, length, and position) of the swirling streamlined body based on minimizing the contradicting objectives. The results were represented by Pareto curve, correlation matrix, parallel axes, and response surface model. It was understood that the optimization can offer improvement of 68% and 15% to the uniformity number and the pressure drop respectively.

On the other hand, aeration treatment for cavitating flow in axial Kaplan turbine was considered for the second engineering application. Using CFD models of a 7.5-cm hydro-turbine, cavitation situation was simulated, then air is injected from the housing to redistribute around the blades of the rotor. The value of the vapor fraction is tracked over the blades and the hub areas throughout the time of turbine cycles. Comparison is achieved by evaluating an average value for the vapor fraction at each case. Air mass flowrate and ports distribution are found to be effective in reducing the cavitation phenomena. Proposed linear aeration distributor on the housing presented a promising technology for spreading the air over the blade chord in a better way than the circumferential distribution. The study allowed the understanding of the flow behavior (in

terms of air flow, liquid pressure, and cavitation formations) and turbine performance (i.e. mechanical power) at different air injection locations and turbine rotational speeds. A broader view of research investigated the functionality of linear aeration distributor on the hub with an air supply going through a hollow shaft. The invention of the hub air injection targets the marine industry (i.e. propellers) where the housing/shrouds do not exist, but it also can be a competitor to the housing air injection technology as well. For the two aeration approaches (housing and hub), the conducted numerical investigations were based on the vapor mitigation and power regain in the Kaplan turbine, meanwhile the experimentation looked for the vapor and motor power reduction for the propeller operation. A good agreement (qualitatively and quantitatively) was found between matching cases created for such purpose using tools for high-speed imaging, statistical analysis for turbulent flow, image processing and power measurements.

Finally, the dissertation sets some recommendations for the continuation of the researches on the two applications (thermal uniformity and aeration treatments) for better jets interaction with the cross flow by the consideration of the addition/orientation of guide vanes and the relocation of the jets on the turbine blades respectively.

TABLE OF CONTENTS

LIST OF FIGURES

LIST OF TABLES

NOMENCLATURE

2B3P	Two Blocks, 3 Ports
3-D	Three Dimensional
A	Area
ABS	Acrylonitrile Butadiene Styrene
AR	Aspect Ratio
BR	Blockage Ratio
C	Concentration
CAD	Computer-Aided Design
CAE	Computer-Aided Engineering
CC	Combustion Chamber
CFD	Computational Fluid Dynamics
CO	Carbon Monoxide
Cr	Chromium
C_P	Pressure Coefficient
C_{Pmin}	Minimum Pressure Coefficient
C_p	Specific Heat at Constant Pressure
D	Diffusion Coefficient
$\dfrac{D}{D}$	Total Derivative
d	Diameter

$\dfrac{d}{d}$	Derivative
E	Dispersion Coefficient
f	Mixture Fraction (Dimensionless Temperature Difference)
GT	Gas Turbine
$\vec{g}$	Gravitational acceleration
h	Jet depth into the cross flow
I	Identity matrix
ICE	Internal Combustion Engines
J	Diffusion Flux
JICF	Jet-in-Crossflow
k	Turbulence kinetic energy
L	Length
LE	Blade Leading Edge
LES	Large Eddy Simulation
l	Order of phase
M	Number of Design Variables
MHI	Mitsubishi Heavy Industries
N	Rotational Speed
N-S	Navier-Stokes
Ni	Nickel
NOx	Nitrogen Oxides

n	Total number of co-existed phases
P	Pressure
P	Mechanical Power
p	Position from the Chamber Center
PS	Blade Pressure Side
PR	Profile Ratio
Q	Flow rate
R	Radius
RBM	Rigid Body Motion
RANS	Reynolds Averaged Navier-Stokes
Re	Reynolds Number
S	Strain rate tensor
S	Swirl Number
SGS	Sub-Grid Scale
SR	Stationary Region
SS	Blade Suction Side
R	Radius
RR	Rotational Region
r	Arbitrary Radius
r	Momentum-flux ratio
T	Temperature

TE	Blade Trailing Edge
TIT	Turbine Inlet Temperature
TLV	Tip Leakage Vortex
t	Time
t	Rotational Domain thickness
$\tilde{t}$	Temporal cut-off value
$\vec{V}, V$	Velocity Vector and Magnitude
VOF	Volume of Fluid
VVF	Vapor Volume Fraction
WALE	Wall-Adapting Local Eddy Viscosity
x	Spatial Coordinate
x	Uniformity Number
$\tilde{x}$	Spatial cut-off value
y^+	Non-Dimensional Wall Distance
Z	Height from a Datum
z	Arbitrary Axial length

Greek and Symbols

α	Phase Volume Fraction
γ	Surface Tension
Δ	Difference
μ	Dynamic Viscosity

ν	Kinematic Viscosity
π	Pi (3.14159)
ρ	Density
σ	Cavitation number
τ	Turbulence Stress Tensor
φ	Source/ Sink
ϕ	Fluid or Flow property
$\forall$	Volume
$\dfrac{\partial}{\partial}$	Partial Differentiation Operator

Sub/Superscripts

Ann	Annulus
a	Air
avg	Averaged Value
b	bubble
c	Cell
cf	Crossflow
ex	At Exit Boundary
I	Cavitation Inception
i	Free Index
J	Jet

j	Dummy Index
L	Liquid Phase
min	Minimum
r	Radial Direction
res	Residual
s	Surrounding
T	Transpose
Turb	Turbulent
v	Vapor
w	Water
z	Axial Direction

ACKNOWLEDGMENTS

First of all, I would like to share my deep gratitude to Professor Ryoichi Amano who believed in my potential and gave me the opportunity to pursue my PhD at UWM. Alongside with the PhD, his research assignments were my ascending steps for knowledge and experience. Moreover, he nominated me to interview at Harley-Davidson while I was in the early stage of the program, which provided me a great chance to hone my skills and push me forward intellectually. Words will not be enough to express my appreciation to him.

I'd like to thank Professors Qu, Reisel, Lauko, and Cuzner for serving on my dissertation committee and for giving me guiding comments during the preliminary exam and the final dissertation. Their input to my research is valuable and contributes to a better version of my work.

In building my career, I cannot deny nor forget the great influence and guidance of Anthony Coffey, my supervisor in Harley-Davidson PDC, who is one of the most impressive people with whom I have ever interacted. He chose me to be the successor in H-D Co-op program with UWM and gave me the required trust needed at the beginning of the learning curve of the software, work progress, and H-D environment. The support I had from him pushed me to learn faster and serve as efficient as I can. No wonder! I felt as though I was at home with my family while working with him and the Harley Davidson CFD Team, as they gave me compassion and understanding. I am grateful and honored that I worked with him, Dr. Alka Gupta, Dr. Mojtaba Rajaee, and Rob Brummond.

My acknowledgment extends to my research mates and colleagues: Dr. Mohamed Ibrahim, Dr. Ammar, Dr. Yi-Hsin, Dr. Saman, Muhannad, Tomoki, Ahmad, Mandana, Hisham, Khafagi,

Osama, Alaa, Qandil, and Farah. I am grateful for every moment of support with mentoring, working together, and even having fruitful discussions or light talks. All of these moments helped me learn and left good impressions that shaped my personality throughout the research period and reflect on my work for a contemplative dissertation. I will also never forget the undergraduates who I was fortunate to work with: Nicholas, Caleb, Benjamin, Cody, and others. These gentlemen showed a great dedication to their missions in addition to their innovative minds in problem solving. I would always be delighted to recommend them for their future careers.

To all my close friends, I am grateful for every time you had me smiling and filling my soul with joy and faith. Every time of interaction, I was getting a chance to energize myself for work with full refreshment. The feeling of having you around was securing and comforting. I owe you a big part of my success. While the list of names could be long, I would like to mention at least three names: Sherif, Ahmed, and Rose.

Finally, I must honor my family, as they are the source where I came from and the reason for my existence and persistence to succeed. They have believed in me since my childhood and kept encouraging me for achievements during all the stages of my life. They have always envisioned more for me, and they nurtured me with the aptitude and resources to make the right decisions. They highly supported me for traveling for the PhD and made my life smooth with no trouble or pressure. They are the home that I belong to, regardless of the change or location and the passing of time.

With all the love I have in my heart and mind, I dedicate my work to them

To Mahmoud (Father), Sanaa (Mother), Mohammed (Brother), and Samar (Sister)

CHAPTER 1 - INTRODUCTION

1.1 Mixing Definition and Examples

Mixing is a process in which two or more substances with distinctive characteristics (density, temperature, viscosity…etc.) are set in one place to end as one homogeneous matter. In fluid mechanics, mixing between different fluids (static or in-motion) can be achieved in multiple ways (e.g. direct dissolution in a dominant fluid, osmosis, relative velocities between the components…. etc.), and the resulting blend has redistributed molecules of the primary components in the same intermolecular space. A daily example seen in normal life is pouring cold milk into hot coffee cup to have a desirable taste and temperature or turning on the hot and cold water tabs to have a comfortable temperature for showering with suitable mass flow rate[1]. Other naturally phenomena involve mixing are the confluence of rivers together or with sea water (different densities or mud/minerals concentration), and the entrance of clouds of ash and dense gases into the atmosphere from an active volcano (constituents and other physical properties are highly different) as seen in Figure 1-1, Figure 1-2, and Figure 1-3.

Figure 1-1: Meeting location of Rhone and Arve rivers in Geneva with slow mixing at the interface [2]

Figure 1-2: Space view of Zimbabwe river flowing into the Indian Ocean[3]

Figure 1-3: The Popocatepetl volcano, Mexico City 2013[4]

1.2 Mixing in Industry

In industrial field, mixing can be classified into reacting and non-reacting and, where the objective differs from the final product. Reacting mixture involves disassociation of compounds (if exist), chemical bonding between elements, and formation of compounds/elements were not initially present, while heat could be a factor in such reaction (either exothermic or endothermic). Combustion of air/fuel in Internal Combustion Engines (ICE) and Combustion Chambers (CC) of Gas Turbines (GT), Figure 1-4, is a very good example to this type of reacting mixing. The quality of a reaction is always related to the ratio between the reactant at the interaction location.
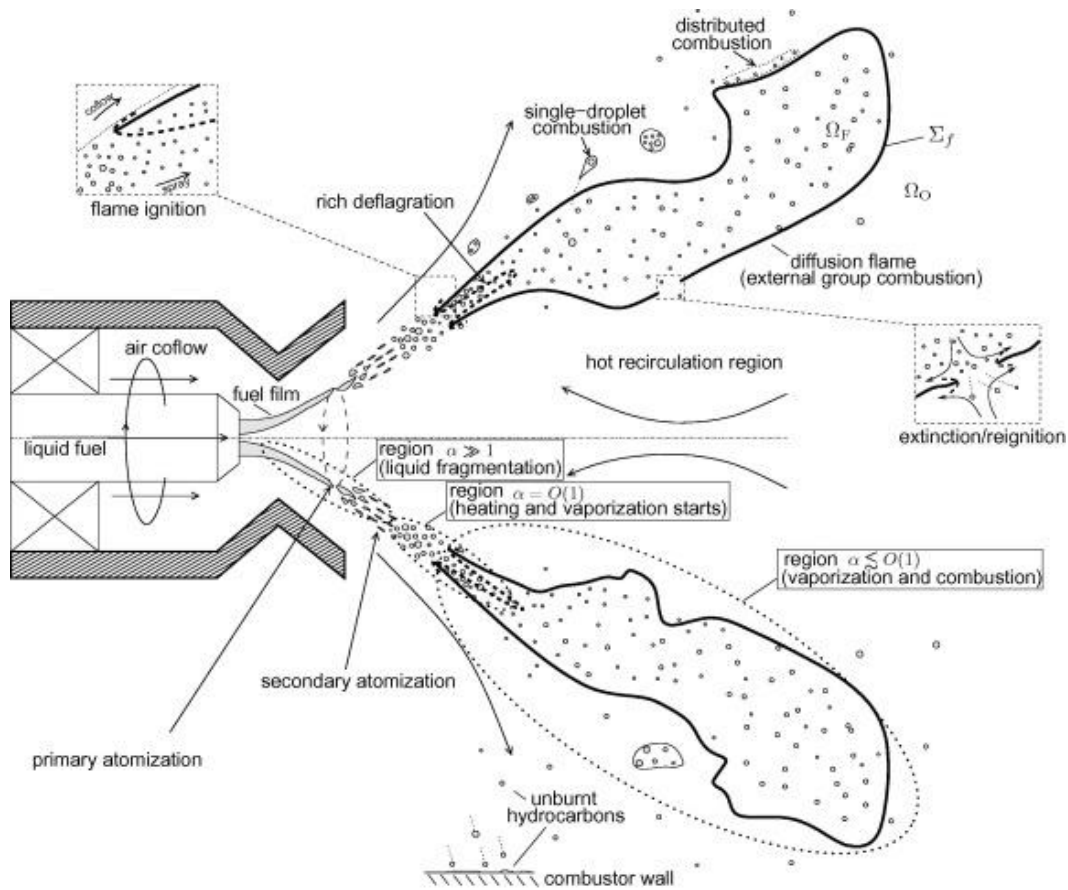
Figure 1-4: Interaction of fuel-spray with air forming a combustion process[5]

On the other side, the non-reacting mixing is developed when the components do not have the chemical affinity to interact, allowing their properties to shape outcome combination per their amounts (i.e. concentration) and the used blending technique. Air conditioning systems introduces water vapor to the dry air to increase relative humidity in a process called "humidification", and the resulted air is a multi-component gas with higher water vapor concentration. In the medical field, the anesthetic machine, diagramed in Figure 1-5, combines oxygen (O_2) and nitrous oxide (N_2O) gases, with the vaporized anesthetic agents to be supplied to the patient under surgery.

4
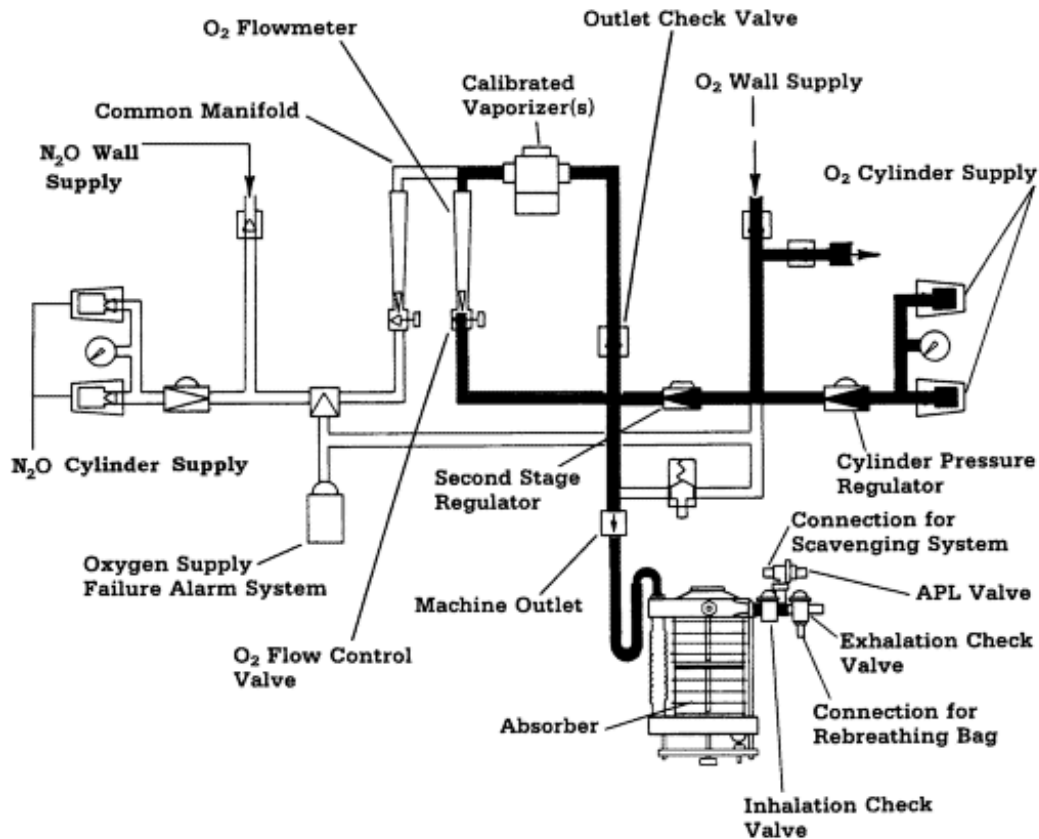
Figure 1-5: Schematic diagram of N_2O and O_2 gases flows in anesthetic machine[6]

1.3 Mixing Mechanisms

The three-primary mechanisms of transporting within a continuum are the advection, diffusion, and dispersion. Advection, which is different from the concept of convection[7], is the transference of the constituents from one point to another due to a uniform velocity (i.e. plug flow). In advection, different components acquire the same velocity magnitude and direction of the main fluid flow; however, mixing usually does not occur by convection solely since there is no external force to reposition the components with respect to the bulk of carrying fluid. Advection is dominant in open air or wide water streams with suspended particles.

Mixing is effectively induced by the other two mechanisms: diffusion and dispersion. Diffusion is a molecular-level irregular movement of a component from a high-concentration zone to an adjacent low-concentration one. Fick's law states that diffusion flux (J) is driven by the concentration gradient $(\frac{\partial C}{\partial x})$ with the regulation of the diffusion coefficient (D) as written in Eq. (1-1). It is worth mentioning that heat and flow momentum can be the diffused physical quantities because of the gradients of temperature and velocity components.

$$J = -D \, \frac{\partial C}{\partial x} \tag{1-1}$$

Dispersion is conceptually matching diffusion in redistributing the flow elements. Nevertheless, the dispersion scale is macro because of involving hydrodynamic parameters in the transport process (e.g. movement in non-uniform paths, source/sink, relative velocities between flow components, and velocity unequal profile). With a similar definition to Fick's law, dispersion coefficient (E) is significantly large compared to that of diffusion (D) since it is mathematically expressed with the characteristic flow velocity (V) and the macro length scale of resulted flow pattern (α_L). Equations (1-2) and (1-3) are briefly describing the governing relations of dispersion, while Figure 1-6 shows the difference between diffusion and dispersion of a solute in plug and parabolic profile flows. Dispersion is always faster than diffusion and accordingly wider in transference range at the end.

$$J = -E \, \frac{\partial C}{\partial x} \tag{1-2}$$

$$E = V \, \alpha_L \tag{1-3}$$
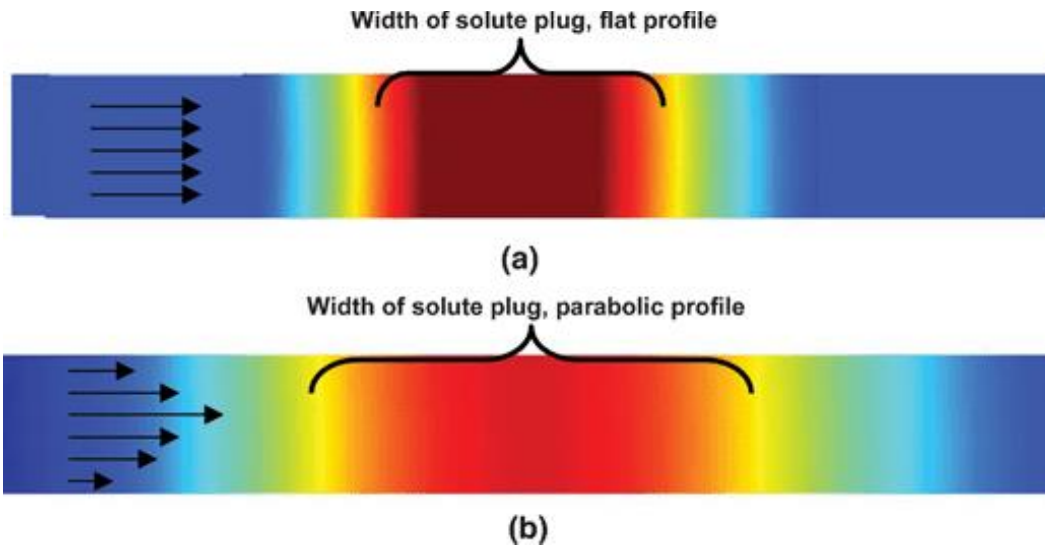
Figure 1-6: Cases of solute (a) diffusion within a plug flow, and (b) dispersion within a pressure-driven flow in a micro-channel[8]

1.4 Jet-in-crossflow (JICF)

Based on the previous classification, engineered systems usually adopt different techniques to maximize the benefit of dispersion for a mixing process. Jet-in-crossflow, aka transverse jet, is one of the approaches conducted to applications where two or more fluids are physically contact each other (i.e. dissimilar fluid masses flow into the same continuum). Considering two-fluids situation, JICF features orthogonal or at least angled flows such that the dispersive factors are primarily the existence of source and the relative direction between the velocities. An important aspect in JICF is the flows scale difference which appears in large area ratio between the main-stream (aka crossflow) and the jet (i.e. $A_{cf}/A_j \gg 1$). Scale variance makes the JIFC physical nature is unlike mixing pipes of same scale, and the mixing result is quite different. A simple sketch in Figure 1-7 represents the mixing process between two orthogonal streams of different characteristics.

7
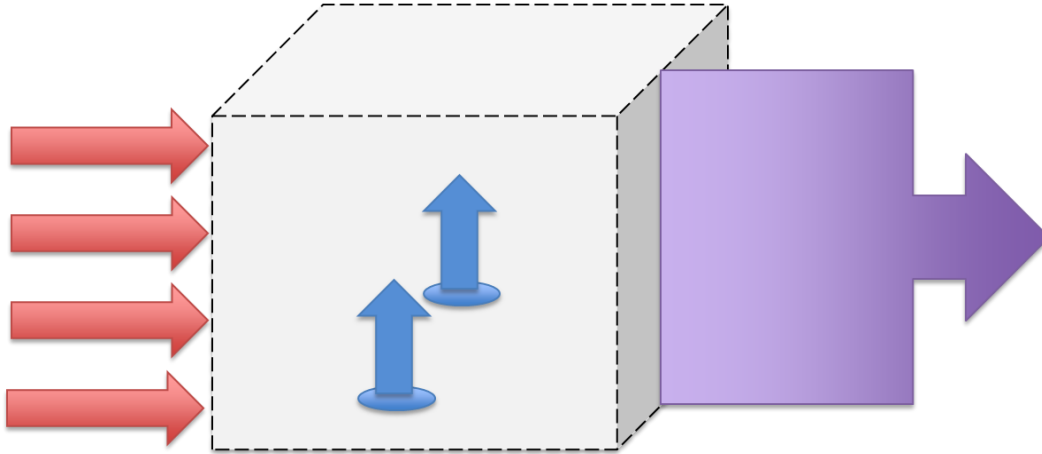
Figure 1-7: JICF sketch between perpendicular flows in a control volume, colors represent flows of different characteristics

1.5 JICF Applications

JICF is utilized in different applications to control two chief goals: the jet penetration height and width into the crossflow. The goals lead to achieving various purposes based on the main objective of the application. In GT, air-fuel pre-mixer shown in Figure 1-8 works on injecting gaseous fuel into circumferentially distributed air swirler slots to uniformly blend the components and reach proper equivalence ratios for low NOx and CO contents[9]. Wet scrubbers spray water through polluted air flow to impinge particulate matter and dissolve dense fumes into the droplets, resulting in purifying the unclean air. Horizontal and cyclone scrubber are direct examples of water jets in air crossflow as exhibited in Figure 1-9. Another application, emerging plume from a chimney, is designed with a rise in pressure and temperature to travel higher into the atmosphere and avoid dispersion of contaminants at the lower atmospheric air layers and clouds.
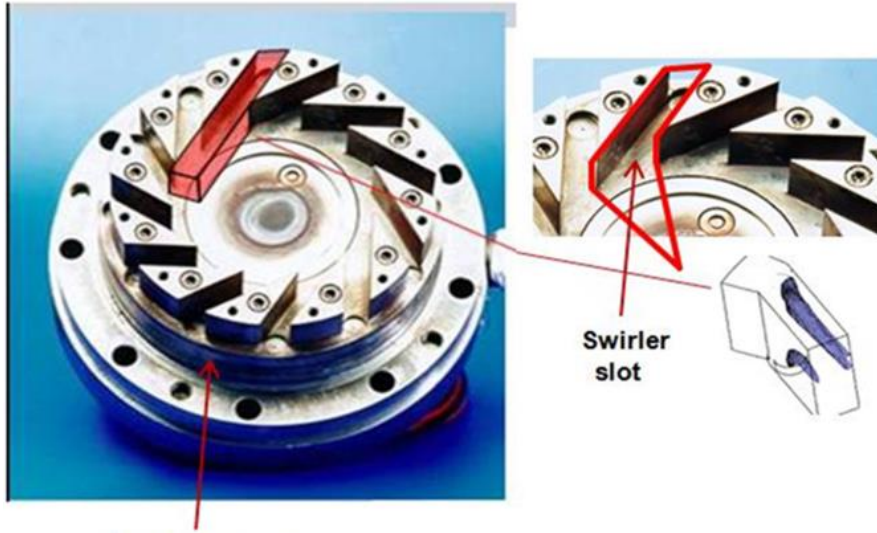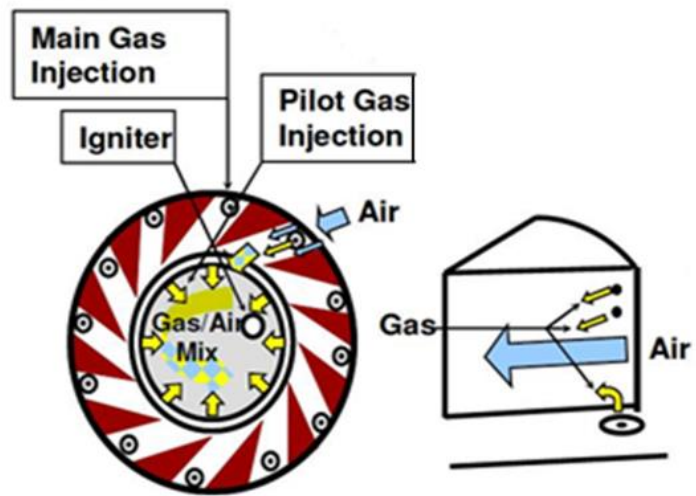
Figure 1-8: Radial swirler in a GT combustion system, gaseous fuel is injected as JICF with air stream through the rectangular slot[7]
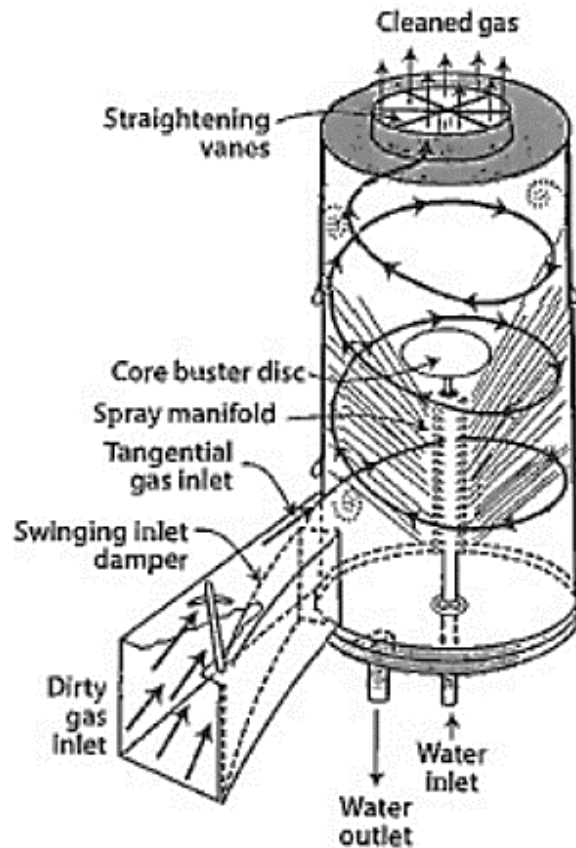
Figure 1-9: Cyclone wet scrubbers for air pollution control[10]

Sometimes, JICF can be used to form isolation layers for protection as targeted from the film-cooling of GT blades[11] to stand elevated temperatures of combustion gases (~ 1700 ºC)[11].

1.6 JICF Dissertation Topic

Adequate design of mixing jets results in a better mixture expressed in uniform profile of scalar physical quantities (e.g. concentration or temperature). In addition, a control of the associated pressure drop is a highly demanded requirement. The dissertation discusses the JICF technique in the view of two application of different purposes: 1) Thermal uniformity in combustion chamber dilution zone, and 2) Cavitation treatment in axial hydro turbine. Uniformity in temperature is experimentally and numerically tested with air/air modelling system, and the

10

comparison between geometrical modifications in the mixing zone is made in terms of temperature dimensionless numbers and pressure drop. Cavitation is sought to be minimized by radial injection of air towards the turbine rotor, and the work is conducted by numerical modeling and experimental investigation of cavitating flow around 7.5-cm Kaplan turbine. Cases results were expressed in values defining the vapor fraction and the produced power from rotor parts.

1.7 Dissertation Organization

Chapter 1 introduces the concept of mixing and the definition and importance of JICF and declares the objective of the dissertation.

Chapter 2 reviews the thermal mixing and cavitation physical phenomena, and states the previous work about the utilizing JICF for the benefit of both applications

Chapters 3 and 4 overview the experimental and numerical set up of the thermal mixing study. Explanation of the tools used, and procedures done is presented in the two chapters.

Chapter 5 and 6 discuss the investigations (experimental and CFD) for understanding the cavitation in turbine and the aeration treatment.

Chapter 7 provides all the results gotten and analysis discussion or both applications

Chapter 8 highlights the current conclusions and proposed recommendations for future work

CHAPTER 2 - LITERATURE REVIEW

2.1 JICF Characteristics:

Aforementioned applications seek to optimize the mixing process by understanding and controlling the attributes regarding the primary axial flow and more importantly the injected jet. Momentum-flux ratio, symbolled by 'r', is a crucial parameter which expresses the scale of the jet momentum to that of the cross flow as mathematically written in Eq. (2-1).

$$r = \sqrt{\frac{\rho V^2|_J}{\rho V^2|_{cf}}} \tag{2-1}$$

In which $\rho V^2|_J$ is the momentum of the jet, and $\rho V^2|_{cf}$ is the momentum of the cross flow (i.e. primary flow). Both momentums are based on the density and average velocities at the entrance to the mixing zone. In case of same fluids interaction and constant density assumption, the ratio is simplified to a velocity ratio between the two crossing flows [13]. Depending on the value of r and jet diameter d_J, the jet structure exhibits four major patterns showin in Figure 2-1: 'Horseshoe Vorticies' surrounding the jet exit hole with upstream start, 'Jet Shear Layer' shown as wrinkles around the out flowing jet, 'Wake Vorticies' formed as downstream eddies with ocasional columns connecting the system wall with the emerged jet , and 'Counter-Rotating Vortex Pair' (CVP) which is more clear by the full bend of the jet with cross flow direction and far from the original jet exit hole[14].
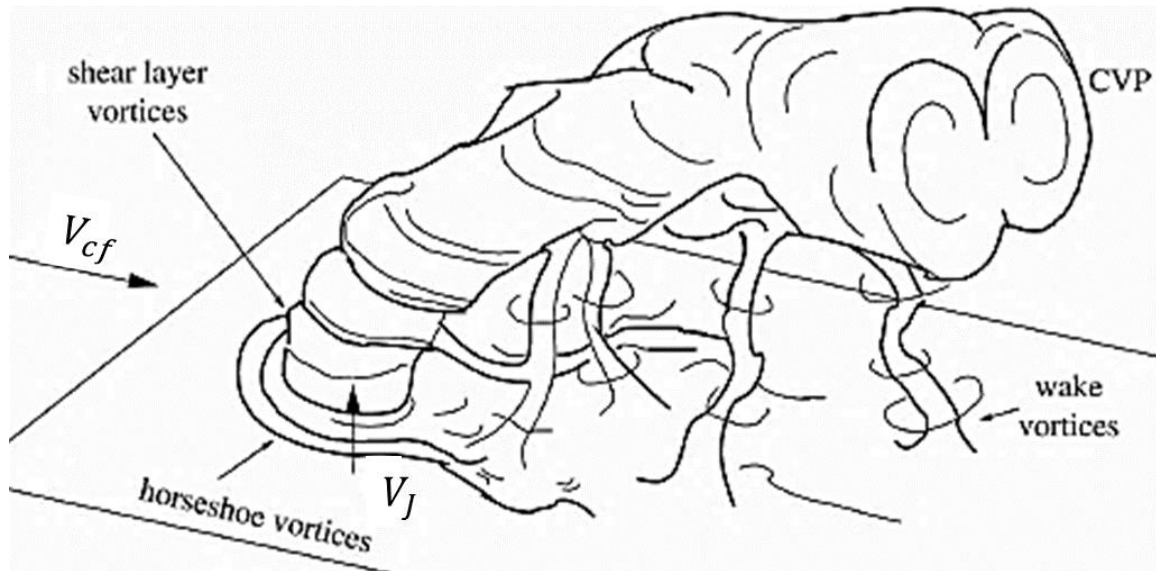
Figure 2-1: Jet structure when crossing a perpendicular flow[15]

Many of the work done by researchers were focused on high values of r (e.g. $r \geq 2$) to allow higher penetration and extended length of the jet into the crossflow and consequently more dispersion. Further analysis at high momentum ratios showed the weak diffusion relation between the the jet and the wake structure[16], emphasized on the crossflow and jet exit boundary layer as sources of vorticity in JICF[14]. Also the studies was able to predict the position of primary flow separation, jet far field of the CVP, and jet trajectory collapse in terms of (d_J), (rd_J), and $(r^2 d_J)$ respectively[14], [17],[18].

As for low momentum ratio flows ($r < 2$), like in the overboard discharge and film cooling of blades, the flow characteristics could be different. Gopalan *et al.* reported that the shear layer of the jet induces a semi-cylindrical vortical shell confining a slow reverse flow behind the jet, unlike the cases of ($r > 2$) which show wake structure similar to Von-Karman vortex sheet normal to the system wall due to the effect of crossflow around the jet circumference[19]. Also, the pressure fluctuations and advection speed are proportional with r at the low ratios. Further exploration by Terzis *et al.* on swirling low r jets reached to the fact that lower jet penetration corresponds to

13

higher swirling jets, and there is a critical swirl number (S) for the incoming jet at which the jet trajectory declines towards the wall shortly after injection. Moreover, jet swirl deforms the well-known CVP pattern from the symmetry to comma shaped vortex at hight values of S[20]. Updated experimental and numerical article presented by Gupta *et al.* focused on the low r circumferential jets for acheiveing thermal uniformity at the exit mixture temperature, and clarified a direct relation between high uniform mixture state and increased value of r. Up to 85% of equilibirium is attained at a certain value, and no more could be reached since the exergy destruction dominates the thermal dilution process. Based on a newly introduced Cooling Rate Number (CRN), the most diluted areas are the closet to the jet exit holes[21].

Other experimental and numerical trials tested jet shape (circular, elliptical, square, diamond, and triangular) with different orientations and aspect ratios, and some literature recommended non-circular geometries for raising mixing performance such as high aspect ratio elliptical and blunt square jet in subsonic flows[22], and equilateral triangle and diamond for supersonic condition[23]. Another experimental study recommended isosceles triangle jet as a non-circular jet in Re=15000 crossflow with hot tungsten wire measurements for the centerline mean flow and turbulence characteristics[24]. Huang *et al.* cared about studying the jet in a supersonic crossflow as one of the best configuration for fuel injection in scramjet. Reynolds Averaged Navier-Stokes (RANS) with k-ω SST turbulence model was adopted for the numerical simulations used Hydrogen and Nitrogen expressing low and high molecular weight injectants, and it was found that mixing is promoted by higher molecular weight at fixed jet-to-crossflow pressure ratio[23]. In 2015, Zhang *et al.* investigated experimentally by Particle Imaging Velocimetry (PIV) and numerically by Hybrid RANS/LES the same effect of molecular weight (Helium and Nitrogen) at constant jet-to-crossflow momentum ratio. The work witnessed the dominance of the velocity

gradient between the jet and the primary flow on breaking up the large-scale vortices into smaller leading to improved mixing with helium and higher penetration with Nitrogen[25].

2.2 Thermal Uniformity:

2.2.1 Gas turbine performance temperature

Nowadays applications like electric power generation and aircraft mechanical propulsion are relying on thermal energy extraction. Gas turbine (GT) is one of the commonly used systems for achieving this objective because of its merits of simple install, compact size, and better startup than steam turbine systems[26]. GT Technologies has been evolving for centuries; modified cycles, design variables, and components are being implemented to increase the output work and efficiency[27],[28]. One of the main control variables is the augmentation of turbine inlet temperature (TIT) so that GT can reach adequate levels of power production. Recently, and as graphed in Figure 2-2, Mitsubishi Heavy Industries, Ltd. (MHI) can reach TIT of 1600 and 1700 ⁰C by developing M501J series and M701F5 model which can exceed 61% thermal efficiency for the GT combined cycle[12],[29]. At the same time, because of these elevated temperatures, turbine blades are prone to thermal stresses causing oxidation and corrosion when interacting with the surrounding environment[30], and mechanical failure could happen in the short run. To reduce those detrimental effects, periodic and expensive blade safety managements are implemented such as blade cooling[11]and thermal barrier coatings[31].
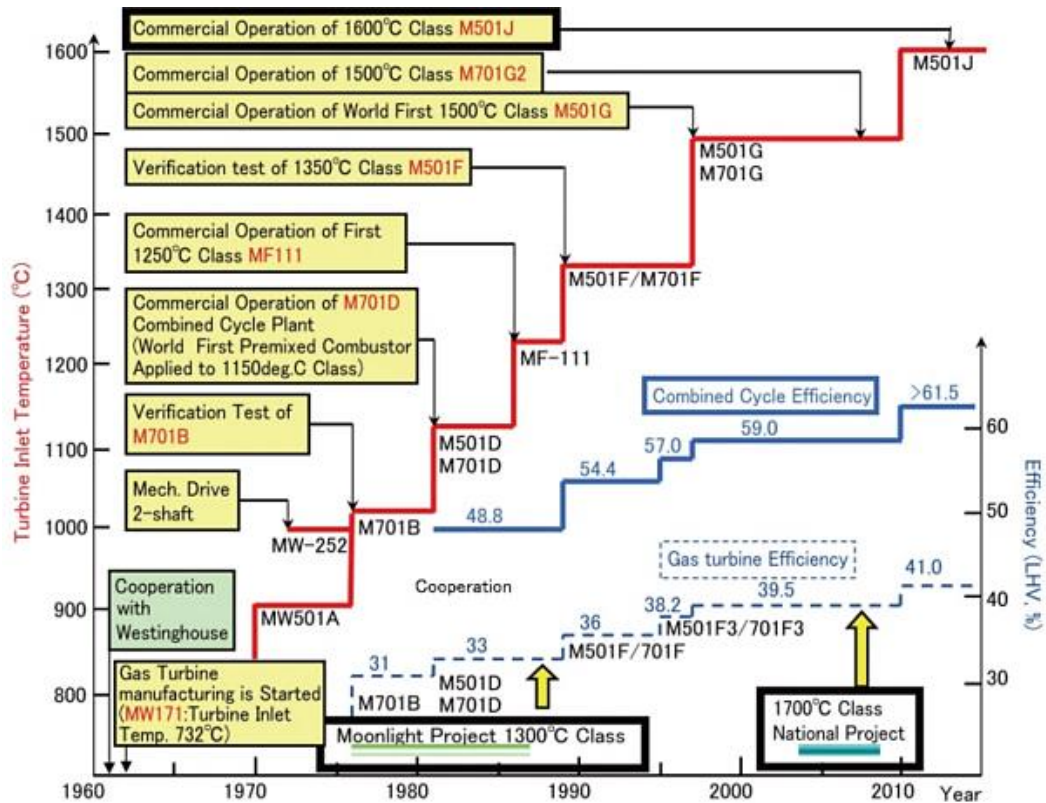
Figure 2-2: MHI gas turbines series timeline with corresponding TIT and combined efficiency[29]

2.2.2 Thermal side-effects on a turbine stage

Another form of harmful thermal effects in GT is the non-uniform pressure and temperature distributions over the flow cross section. Principally, temperature non-uniformity in the radial coordinate of combustion gases can cause uneven stress spots on the turbine blades and casing, leading to distortions and creep accelerating the tendency to failure. Many studies recorded, by numerical methods and real-life observances, the local strains and material damage in the metallic components (especially vanes and blades) and their corresponding temperature distribution[32]-[36]. Figure 2-3 illustrates the non-uniformity in the temperature distribution over the blades (real and numerical) even after considering internal cooling, while severe damage and fracture of gas turbine stage parts can be seen in Figure 2-4. Different types of microscopy and X-ray investigations used in the analysis of failed 40 MW GT after 1/5 expected lifetime only, and the

16

observations found the effect of high operation temperature on forming films high-order carbides at the base metal grain boundaries, resulting in the initiation of cracks that extend to large fractures at the end[37].
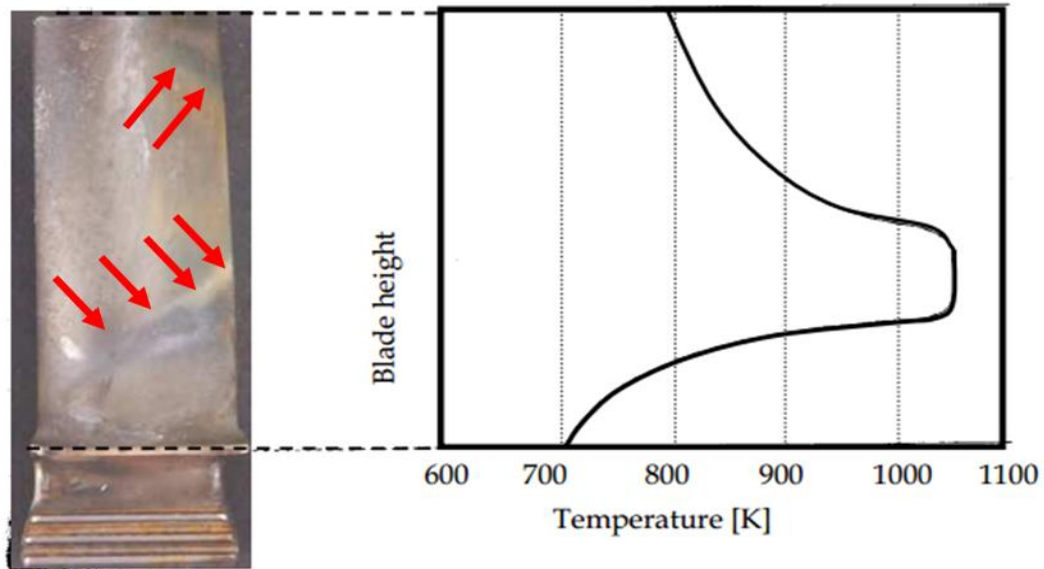
(a)
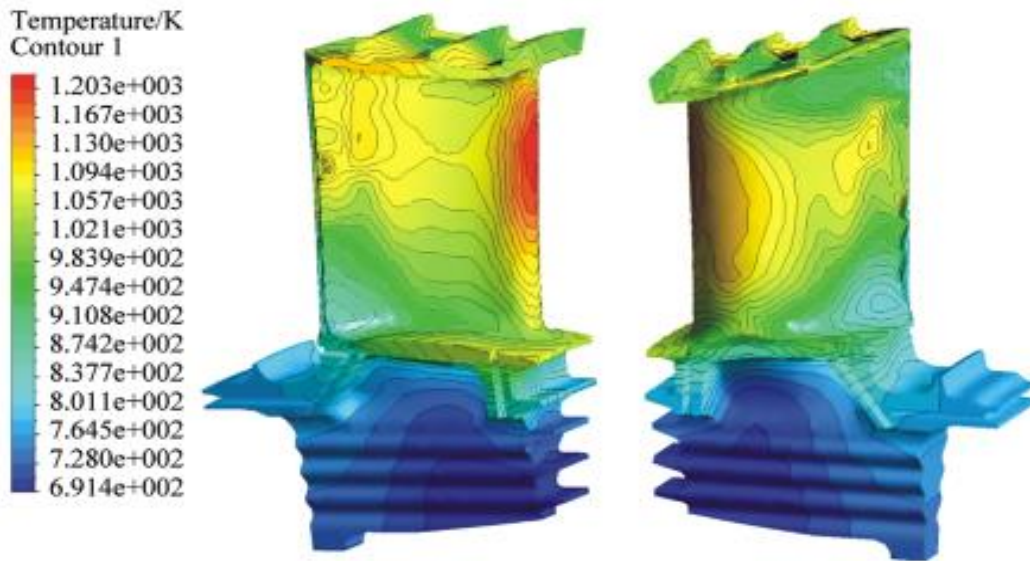
(b)

Figure 2-3: Temperature distribution along the blade height: (a) actual blade with color marks and plotted temperature variation[32], and (b) CFD thermal study of a turbine blade [36]
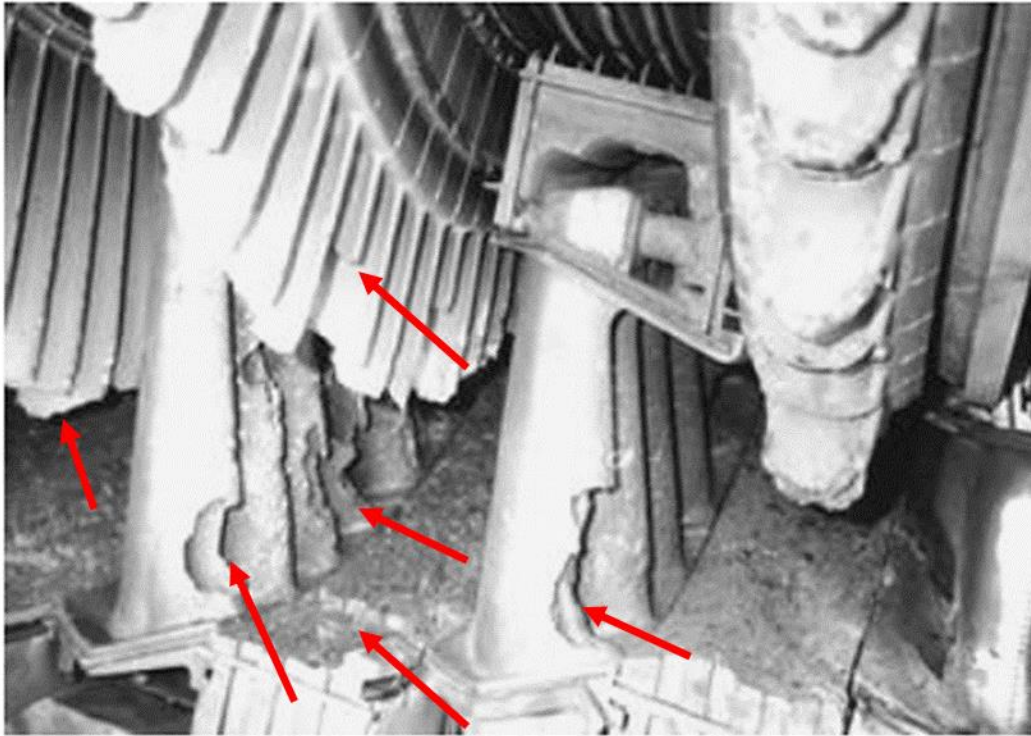
(a)

(b)

Figure 2-4: Gas turbine damage at: (a) Complete stage including vanes and casing, and (b) rotor blades[37]

2.2.3 **Hot streaks and combustor dilution**

The distortion of the inlet temperature profile is usually termed as "hot streak", and it is occurring radially and circumferentially from the combustion chamber exit as shown in Figure 2-5. Hot streak is a direct consequence to either the discrete combustion (e.g. cannular combustor[38] or multi-nozzle chamber[39]) or the imperfect atomization due to carbon residues on the injector[40].
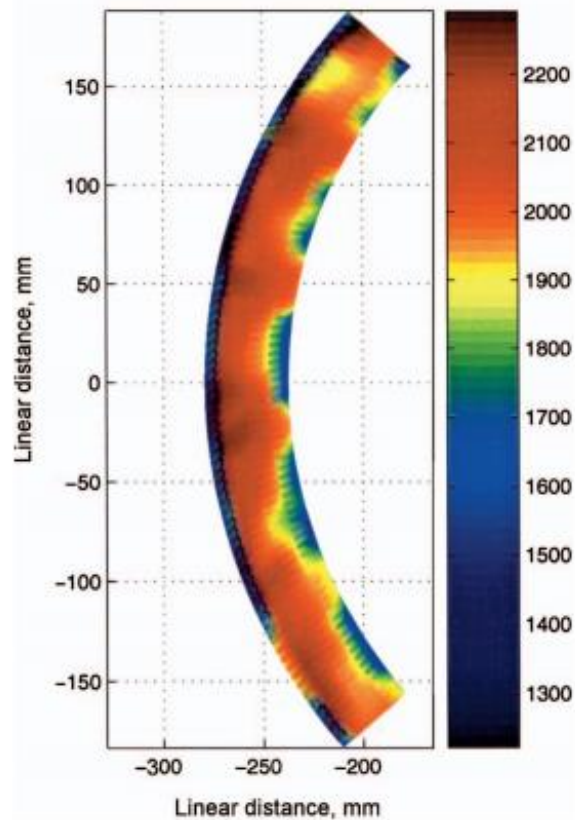
Figure 2-5: Radial and circumferential temperature variation at the inlet of the first stage turbine[41]

With the documented detrimental effects, solution is proposed to build the first turbine stage in way that partially avoid the path of the hot streaks of the flowing gases[39]. Additionally, another early-applied treatment is the mixing of hot main-stream with injected dilution air from the combustion chamber (aka. combustor) walls and downstream the supplementary combustion

19

airs (primary and intermediate/secondary) as depicted in Figure 2-6. The main purpose of dilution air is to 1) slightly cool the overall temperature of the combustion gases, and 2) control the temperature profile uniformity by managing the mixing jet variables. A secondary mission of dilution is cooling the liner (i.e. inner wall of combustor) by allowing longer path for the oncoming air through casing and divert the hot gases flow away from the wall. From the previously mentioned goals and constrains, the dilution air has a design of JICF with low-to-average r value.

(a)
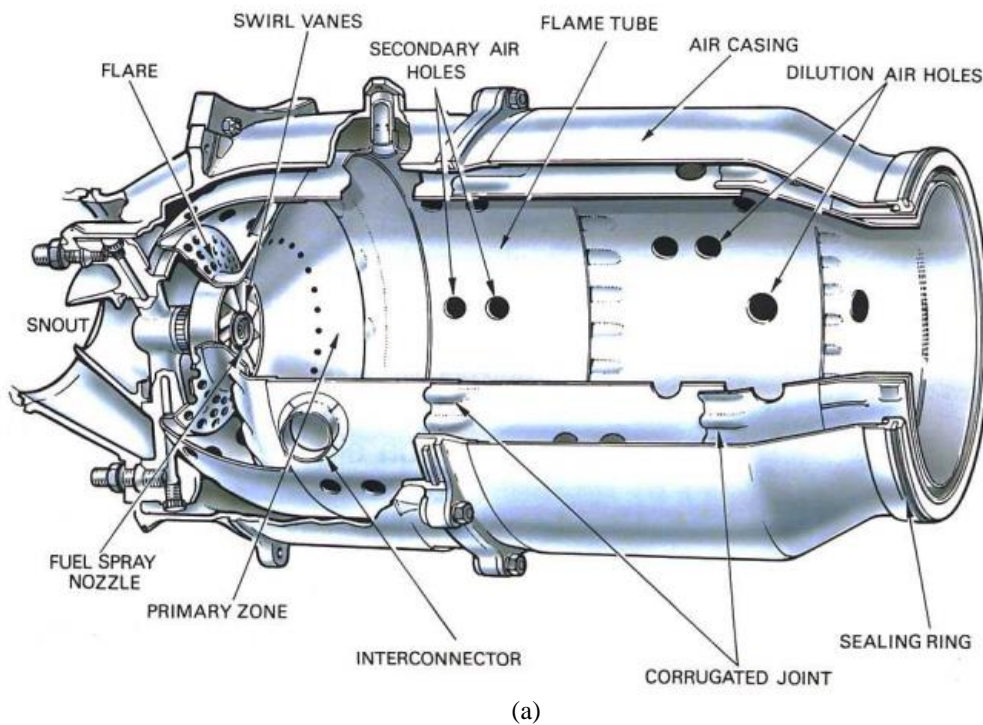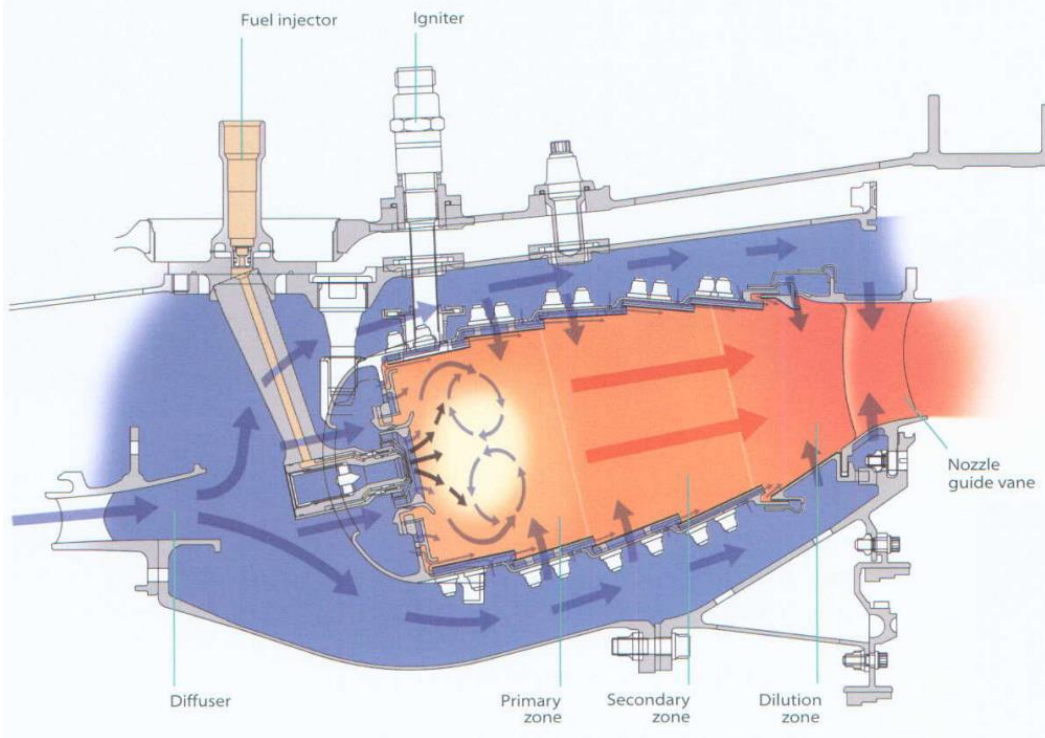
(b)

Figure 2-6: (a) Scaled drawing of combustion chamber design (b) Schematic of air (blue), fuel (yellow), and combustion gases (red) flows through an annular combustion chamber. Primary, secondary, and dilution holes are demonstrated by vertical blue arrows[42]

Experimental and numerical researches were carried out to explore the features of the dilution jets and manipulate the number of related variables to achieve the homogeneity required in mixing with the hot gasses. Previous experimentation about jets size and spacing with respect to a rectangular duct height was done at different r and density ratios, and results of dimensionless temperature with 3-D coordinates showed that superiority of r over density ratio for mixing profiles[43]. An earlier work for the same author with similar conditions deduced that better mixing outcome can be attained at each r from a specific spacing to duct height proportionality[44]. In 1990, a 3-D simulation of small dilution zone targeted reducing the non-uniformity "pattern factor" at the exit plane, and it was found that the pattern factor has non-linear relation with "jet spacing/ duct height" ratio and increase with jet inlet turbulence[45].

21

Experimental and empirical studies investigated the flow field in the dilution zone in a combustion chamber with single row of round-jets in a straight duct, then an extensive study included realities of a combustion chamber such as: variation in the main-stream temperature, jet shape and arrangement, and wall convergence streamwise. The investigations on the temperature distribution sustained the importance of momentum-flux ratio and jet-orifice spacing (especially when equals the dividing-radius to even annulus areas) to the mixing control, meanwhile the cross-section area contraction and jet diameter were not much effective to the required uniformity[46]. Other studies and patents were introduced to improve the design and performance of the dilution zone in various combustors[47]-[52]. Finally, recent work by Gupta *et al.* on the exact test-rig in the dissertation tested the attachment of jet deflectors (i.e. guide vanes) on the holes to direct the jet into the crossflow with an angle varying from 0° (full penetration counter flow) to 90° (full swirl transverse flow)[53]. Experiments on different Re gave the advantage to the 30° orientation for generating 30% more temperature uniformity than staggered wall holes mixing chamber with 1% additional pressure drop. Another investigation conducted by Gupta *et al.* is the insertion of the streamlined body (American football) to divert the primary flow towards the inject jets. Following the same procedures of guide vanes experimentation accompanied with LES simulations, the streamlined body enhanced the mixing with a low-pressure drop[53].

2.3 Cavitation Phenomenon:

The second engineering application is the turbomachinery (e.g. turbines and pumps). The discussion will introduce the cavitation nature and discuss its side effects on turbo-machines.

2.3.1 Phenomenon Description

Cavitation is a term representing a phenomenon happening to liquid fluid that partially transforms into vapor due to difference in pressure. When the absolute static pressure of liquid drops to the vapor saturation pressure (P_v) corresponding to the medium temperature, the inter-molecular spacing starts to widen and a phase-change to vapor state occurs. Locally in the fluid, the low-pressure zone expands by tensile forces, tearing the liquid and form the vapor gap (i.e. cavity). Though cavitation be related to any liquid fluid, the expression is linked to the water most of the time because of the variety of hydraulic applications. Cavitation and boiling have similar consequence of phase-change and features of the generated bubble; however, the nature of boiling (superheating the liquid, and exciting the molecules with more kinetic energy) and its operating circumstances (temperature increase at constant pressure) make the two phenomena quite different. Figure 2-7 exhibits the two phenomena on a pressure-temperature diagram of water. The boiling is a red horizontal line representing a constant-pressure heating process leaving the liquid phase to the vapor, while the cavitation is a vertically downward state change process from liquid to vapor.
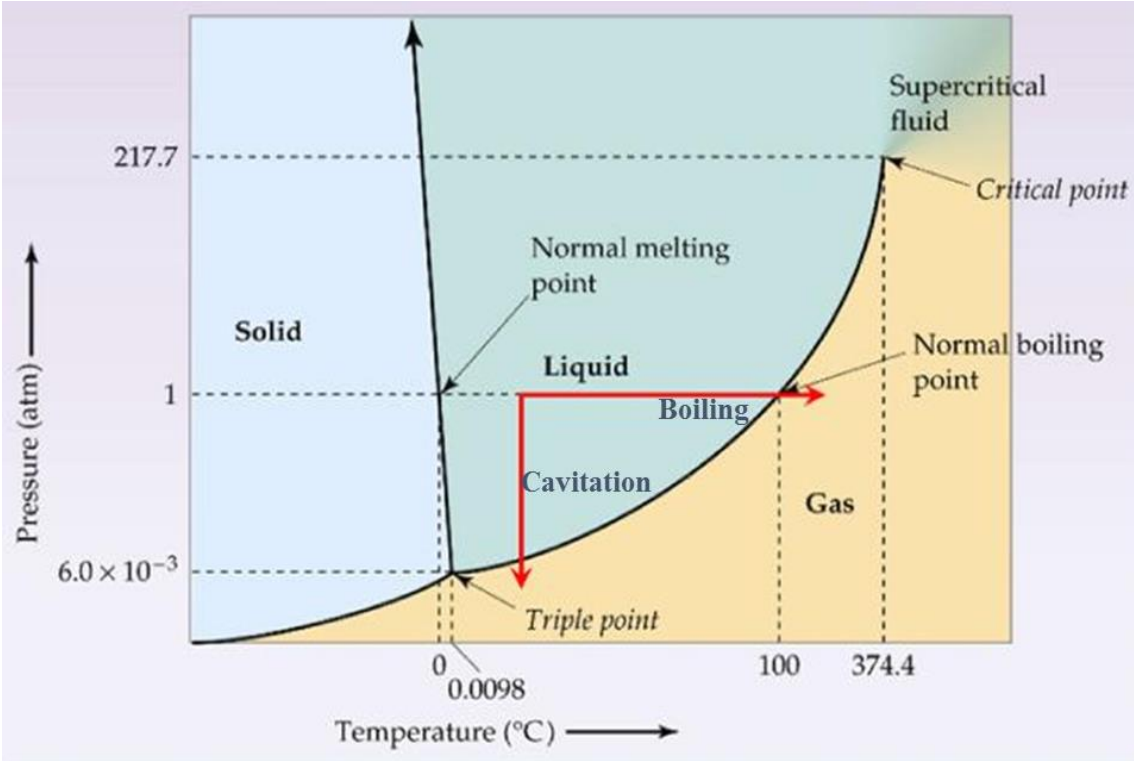
Figure 2-7: Phase diagram of water with boiling and cavitation illustrations[54]

2.3.2 Bubble Growth and Collapse

At the cavitation location, vapor bubble first forms as a nucleus (mostly on a solid surface) which grows to be a visible bubble of a diameter around 0.5mm on average. By this stage, the buoyancy force overcomes the surface tension, and the bubble detaches from the surface as illustrated in Figure 2-8.
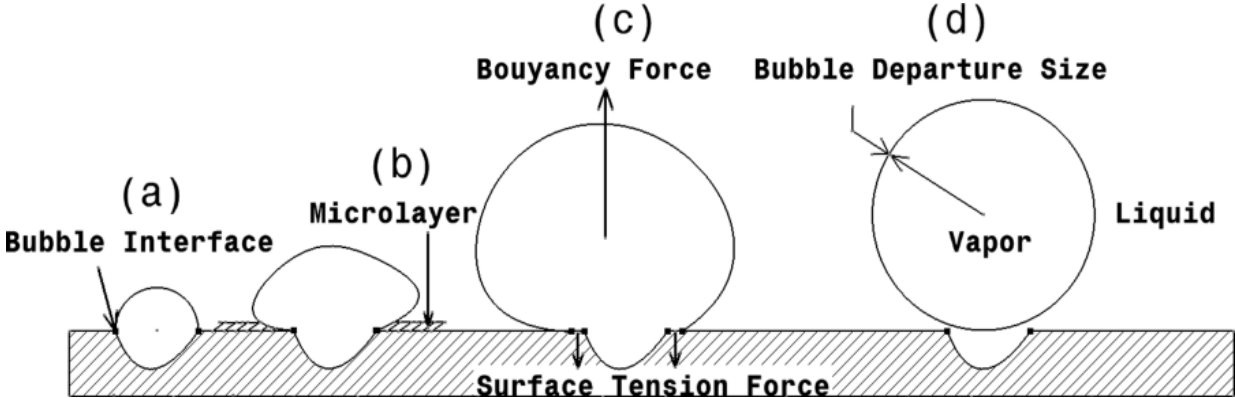
Figure 2-8: Vapor bubble growth and detachment from solid surface[55]

The travelling bubble either continues the enlargement (beyond 1 mm in diameter) if the local pressure is highly lower than P_v, or it coalesces with other bubbles to form a larger embodiment called (vapor cloud) depending on the flow conditions (i.e. bubble size, local velocity, recirculation, and geometrical constraints). A good descriptive image for the bubble growth progress over a NACA 4412 hydrofoil is shown in Figure 2-9. Smaller bubbles initiate near the leading edge, the diameter gets bigger, and the merged cloud happens by moving further downstream. The duration of a growth, detachment, and coalescence process could be in the order of tens to hundreds micro-seconds (μs) [56].
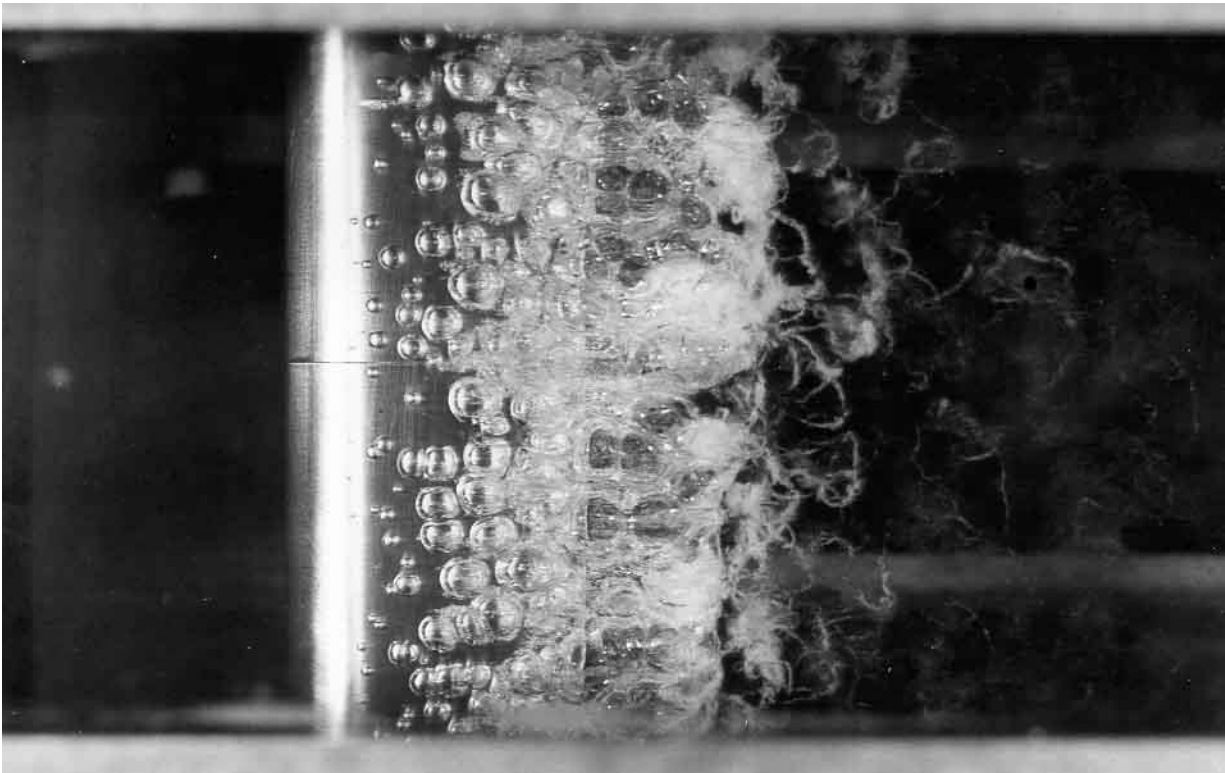
Figure 2-9: Cavitation over NACA 4412 hydrofoil at zero incidence angle and upstream velocity (from left)[57]

The bubble growth rate (dR/dt) mechanism is best explained by the non-linear second order ordinary differential "Rayleigh-Plesset" equation[58],[59] which accounts for the viscous (v_L) and surface tension (γ) effects besides the primary inertial forces driven by the pressure difference

between the bubble pressure (P_b but sometimes it is assumed to be equal to P_v) and the surrounding liquid pressure (P_∞). The correlation written in equation (2-2) is considered the most general. A simpler form shown in equation (2-3) is introduced by Sauer in 2000[60], and it omits the viscous and surface tension because of their diminished influence in most applications.

$$\frac{P_v(t) - P_s(t)}{\rho_L} = R\frac{d^2R}{dt^2} + \frac{3}{2}\left(\frac{dR}{dt}\right)^2 + 4\frac{v_L}{R}\frac{dR}{dt} + \frac{2\gamma}{\rho_L\,R} \tag{2-2}$$

$$\left(\frac{DR}{Dt}\right)^2 = \frac{2}{3}\left(\frac{P_v(t) - P_s(t)}{\rho_L}\right) \tag{2-3}$$

Such that ρ_L is the density of the liquid, t is time, and $\frac{DR}{Dt}$ is the total derivative of the bubble radius with time.

The bubble sustainability depends on the surroundings, especially pressure. Once the absolute static pressure rises around the bubble walls, the liquid compresses the interface to downsize it after the growth. With different collapse scenarios, the asymmetric collapse (microjet) and shockwave can produce high speed jets (100 m/s and above) and pressure waves (1 GPa) to the surrounding liquids and the nearby solid boundaries[61].
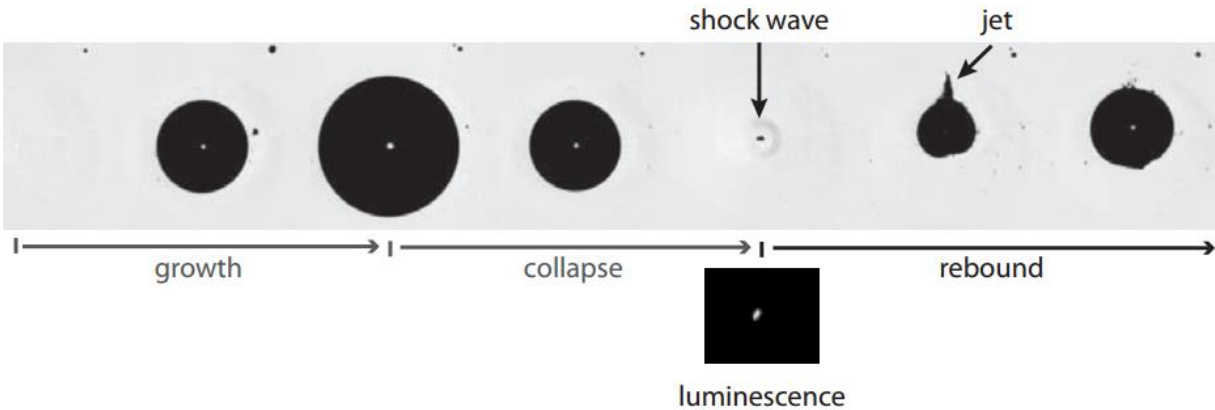
Figure 2-10: Cavitation bubble growth and collapse progress[61]
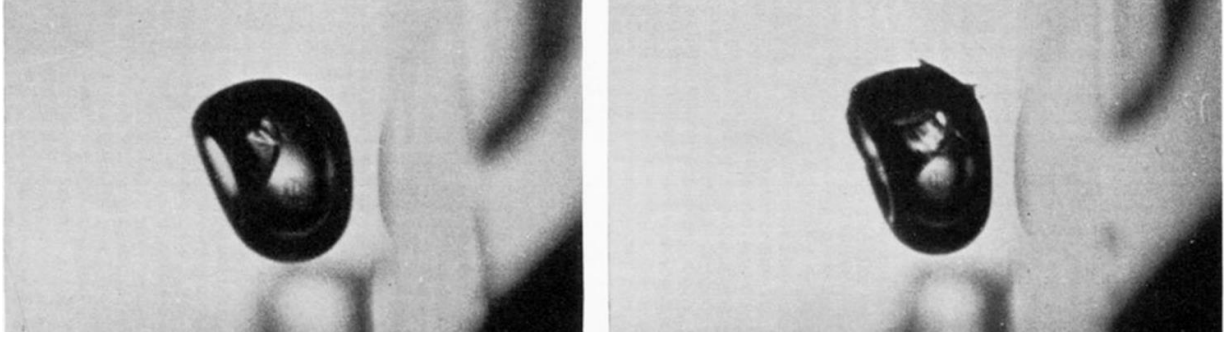
Figure 2-11: Horizontal microjet collapse near a vertical solid wall at 9 and 10ms (left and right)[62]

2.3.3 **Cavitation in Hydraulic System**

In hydraulic systems, Bernoulli's equation correlates the flow total energy along streamline with the consideration of losses due to viscous shear effect. Equation (2-4) shows that the static pressure is coupled with the dynamic pressure (resulted from the velocity, V) and the height from a datum (Z), forming a total pressure which is constant along the streamline.

$$P_1 + \frac{1}{2}\rho V_1^2 + Z_1 = P_2 + \frac{1}{2}\rho V_2^2 + Z_2 + \text{Losses} = \text{Constant} \tag{2-4}$$

Following this correlation at a same level flow (or negligible height difference), the static pressure decreases with area contractions (i.e. higher velocity). Two non-dimensional numbers, pressure coefficient (C_P) and cavitation number (σ), relate the upstream dynamic pressure (driven by upstream velocity, V_∞) to the pressure difference between the upstream pressure of the non-disturbed flow (P_∞) and the local (P) and vapor pressure (P_v) respectively. The mathematical definitions of the two number are written in equations (2-5) and (2-6).

$$C_P = \frac{P - P_\infty}{\frac{1}{2}\rho_L V_\infty^2} \tag{2-5}$$

$$\sigma = \frac{P_\infty - P_v}{\frac{1}{2}\rho_L V_\infty^2} \tag{2-6}$$

While the local pressure changes by the space coordinates (e.g. x), C_P does the same, and it could reach a minimum value called (C_{Pmin}). The meaning of C_{Pmin} becomes more significant when its absolute value matches the cavitation number ($|C_{Pmin}| = \sigma$) or becomes higher than it as depicted in Figure 2-12. At the matching level, the cavitation could be initiated with an infinitesimal nucleus that withstands and starts the growth depending on some other factors like residence time, water temperature and quality, Reynolds number (Re), and the availability of solid boundaries and their roughness state[63]. If fluid and flow conditions allowed the cavitation to happen, the cavitation number is called inception cavitation number (σ_I).
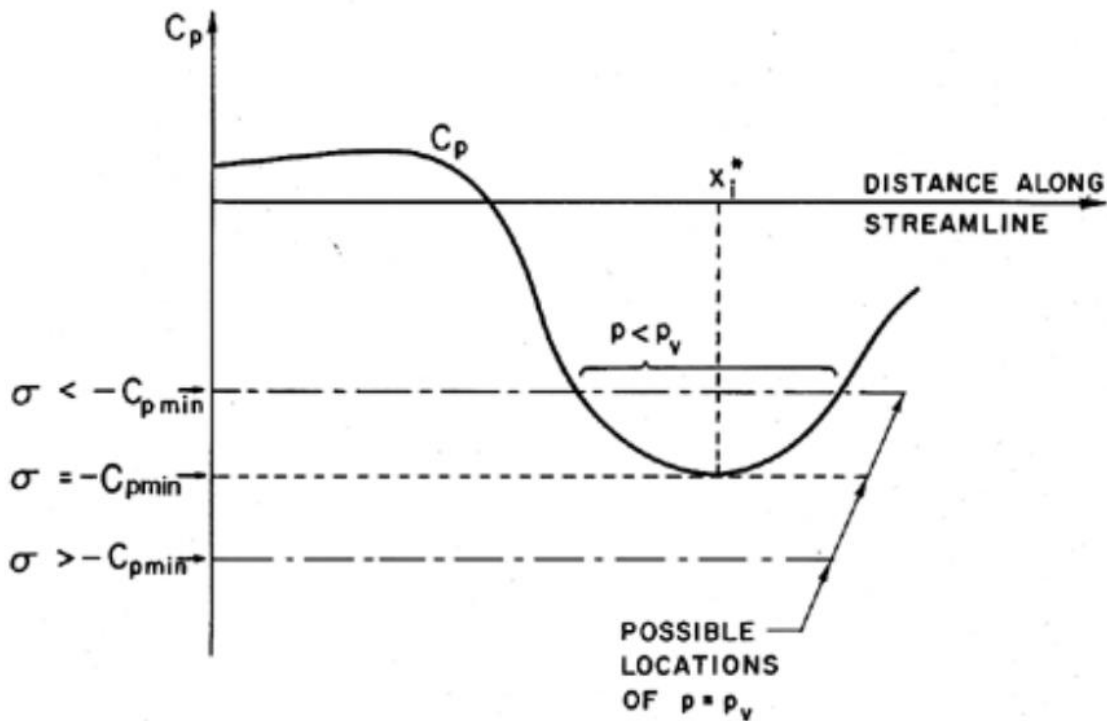
Figure 2-12: C_P variation along the streamline and comparison with σ[63]

Hydraulic systems encounter cavitation can be classified into: (1) dynamic flow-static boundaries (such as pipes with contractions and expansions), or (2) dynamic flow and boundaries (like hydrofoils, hulls, propellers, pumps and turbines). Because of the aftermath of the collapse, cavitation is an aggravating problem in fluid flow applications. Detrimental effects are ranging

from high amplitude noise and vibrations parallel the cavitation structure[64] to material erosion (as shown in Figure 2-13 and Figure 2-14) and full system efficiency drop[65], [66]. Such consequences could cost much in maintenance[67] or complete replacement of the damaged body. In turbomachinery, especially in turbines, cavitation is also a limiting factor for utilizing the total available energy[68].

Figure 2-13: Severe cavitation erosion effect on Francis runner blades[68]
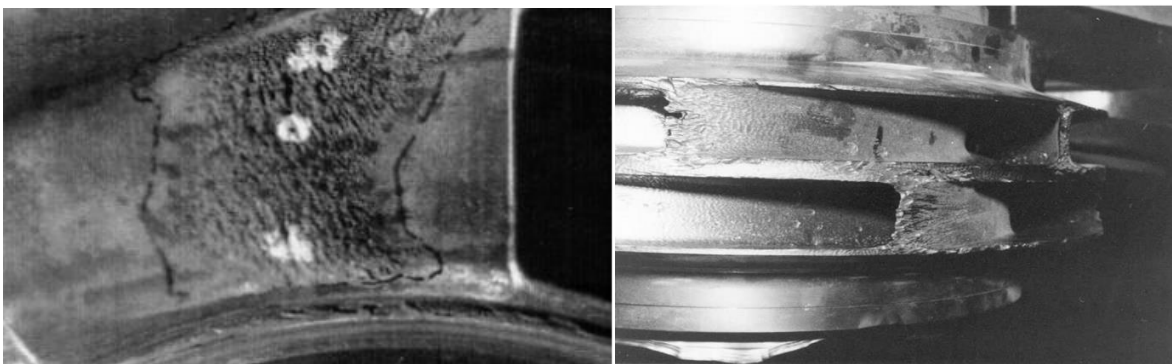
Figure 2-14: Cavitation erosion effect on pump impellers[69]

2.3.4 **Aeration Treatment**

Introduced air into a non-cavitiatng is a technique used to avoid the occurrence of happening at sections of low static pressure. Though it is not a common treatment, supplying air started to be explored for cavitaing elimination in hydraulic systems. Zhi-yong *et. al.* [70] investigated experimentally and theoretically the cavitation control by aeration at the flow velocity range of $V=$ 20-50 m/s. The experimental results show that aeration remarkably increases the pressure in cavitation region. Meanwhile, the work presented a semi-cubical parabola relation between flow velocity and least air concentration to prevent cavitation erosion. In 2016, Tomov *et. al.* [71] conducted an experimental comparison for aerated and non-aerated cavitation in a transparent horizontal venture nozzle by using a high-speed camera. Aerated cavitation was done by injecting air bubbles for three different regimes; sheet cavitation, cloud cavitation, and super-cavitation. It was observed that the symmetrical cavitation structures were partially broken for sheet and cloud cavitation regimes, and it was completely disappeared when super-cavitation regime was reached. Lately, and with a similar idea to the current work, Rivetti *et. al.* [72] studied pressurized air injection in an axial hydro-turbine (Kaplan). Air injection is found to mitigate the erosive potential of tip leakage cavitation, and decreases the level of vibration of the structural components. Slightly reduction in the turbine efficiency was the sole expense.

CHAPTER 3 - THERMAL MIXING EXPERIMENTAL SETUP AND WORK PROCEDURES

3.1 Mixing Chamber:

Annular type test rig, Figure 1-5, generates two thermally segregated airflows in two coaxial ducts (d_{cf}= 40 cm, d_{Ann}= 60 cm). The main airflow, before split, is driven by a forced draft fan coupled to 3 HP motor. Hand operated gate damper is placed after the fan to control the flow rate, and another damper is located at the dividing section for regulating the secondary stream compared to the primary. Once divided, the primary air flows in the center duct and heated by a set of electric heaters distributed as (4 x 1950 W and 4 x 3700 W) and operated using multiple switches, while the cold air is kept at the room temperature. The coaxial ducts are insulated by packing to minimize losses and prevent mutual heat exchange, and they are long enough to ensure fully developed condition for both streams.
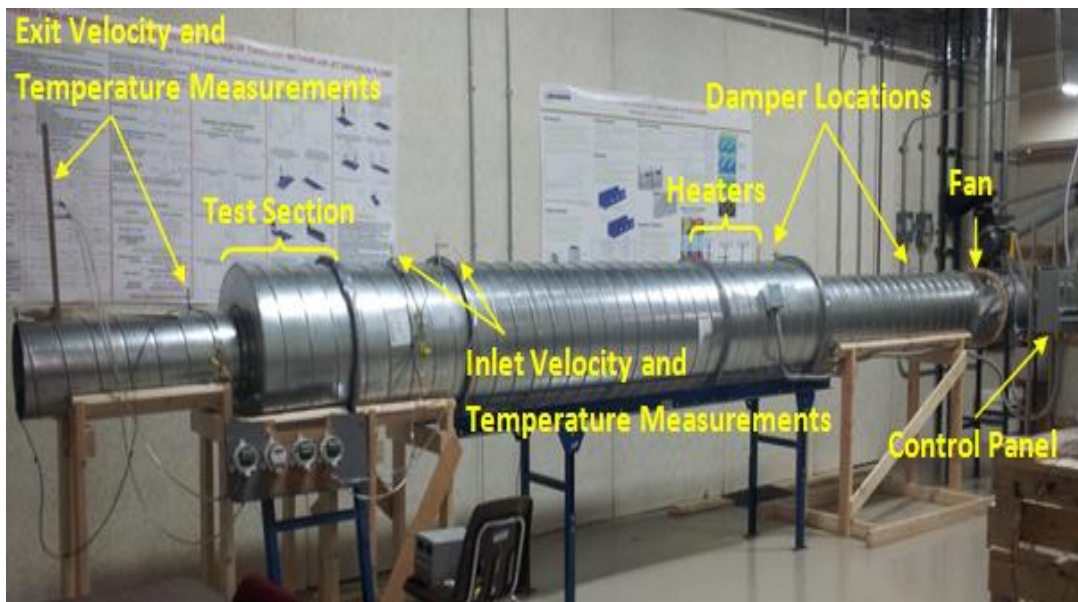
Figure 3-1: Built test setup[53]

Mixing chamber illustrated in Figure 3-2 is constructed as a jet-in-crossflow (JICF) where the cold stream is injected radially through rows of holes into the axially flowing hot air. The design is made in correspondence to the combustion chamber of gas turbines where air enters at different stages for better mixing with sprayed fuel besides film cooling the liner. The cylinder is connected to the primary duct and extends to 20 cm, while the frustum is 20 cm long with start and end diameters matching the primary and exit ducts (d_{ex}= 30 cm). Jet holes have a circular projection of 5 cm on the cylinder and 2.5 cm on the frustum. The smaller holes and converging part are meant to maintain the jet effectiveness after the decrease of mass flow rate of the cold air at the first two rows.

Figure 3-2: Staggered Arranged Mixing Chamber

Before the chamber inlet, the temperatures of the two streams are measured by a group of Ni-Cr K-type thermocouples of ±2.2 ⁰C standard uncertainty. Six sensors are linearly spaced by 3.8 cm along the radius of the primary duct as shown in Figure 3-3, and one sensor was measuring the

cold isothermal air. The thermocouples are connected to NI-DAQ which converts the millivolts readings into data interpreted to temperature values on the computer using the calibrated InstaCal® software. Similarly, static pressure and axial velocity measurement are conducted for the primary and secondary air using sliding pitot-static tube which is connected to FLUKE® 922 differential pressure flow meter, Figure 3-4, of accuracies determined as $\pm 1\% + 1$ Pa in pressure and $\pm 2.5\%$ in velocity. Same measurement configurations are also considered at the exit duct after mixing with thermocouple radial spacing of 2.5 cm starting from the center. It is worth mentioning that the data at the duct surface are assumed to be non-slip and perfectly insulted for velocity and temperature respectively, leading to the estimation of zero velocity and consistent surface temperature with the closest measuring point. Measurements were taken three times at the same conditions within a short time; then the final value is averaged to minimize any variability error. Repeatability standard deviation was kept as low as possible (i.e. outliers were re-measured) to verify precision.
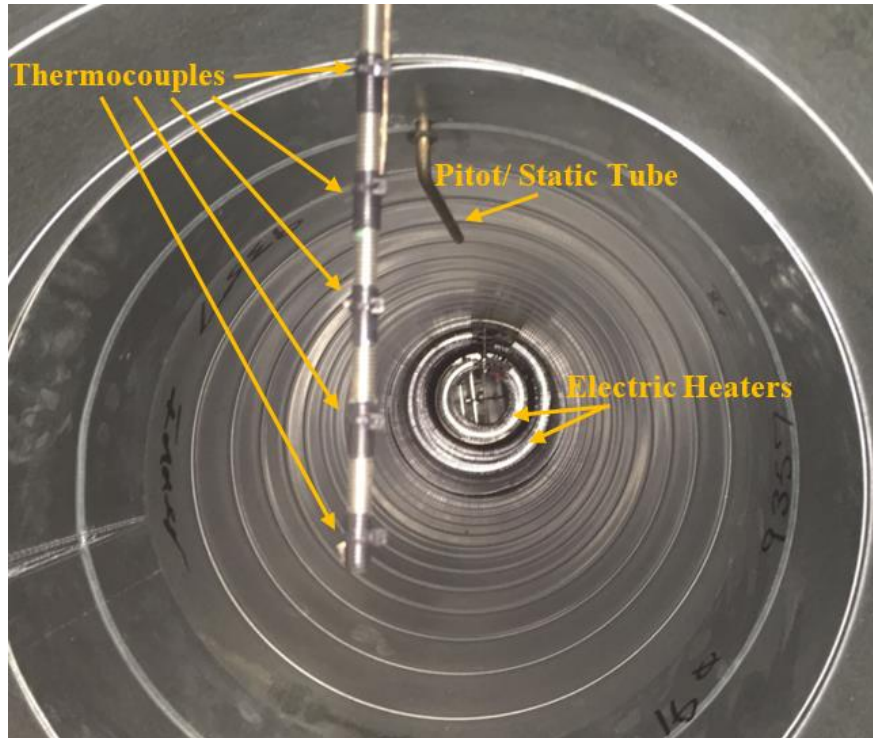
Figure 3-3: Flow and Heat Controls and sensors
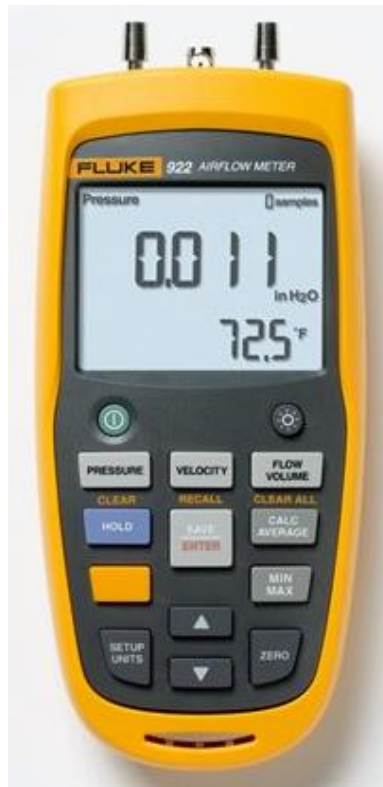
Figure 3-4: Buttons Interface and Digital Screen of FLUKE 922 Air Flow Meter

3.2 Passive Mixing Enhancers:

The term "Passive Enhancer" is meant for the technique which is set once in system to always respond (i.e. enhance) under different operation circumstances. At the first stage of the experimentation, the focus was on introducing three streamlined bodies 3D printed of Acrylonitrile Butadiene Styrene (ABS) thermoplastic polymer, in addition to a football shape previously fabricated (d=0.075 m) to improve the mixing with the least pressure drop (ΔP) possible [53]. The first new streamlined body had the same football shape (scientifically named prolate spheroid) tested before but with an enlarged diameter (d=0.1 m). Additionally, two new teardrop forms (aka piriform surfaces) were made; the first had the same diameter and length dimensions (d=0.075 m, L=0.3 m) of the football shaped bodies, and the other had the same length and a larger diameter (d=0.1 m, L=0.3 m). Figure 3-5 displays the four manufactured streamlined bodies and their characteristic dimensions while their aspect, profile and blockage ratios (AR, PR, and BR respectively) are defined in Eqs. (3-1), (3-2) and (3-3) below:

$$AR = L_{body}/d_{body} \qquad (3\text{-}1)$$

$$BR = d_{body}/d_{Mixing\ chamber} \qquad (3\text{-}2)$$

$$PR = \frac{Projected\ Side\ Area|_{body}}{Projected\ Side\ Area|_{Mixing\ chamber}} \qquad (3\text{-}3)$$
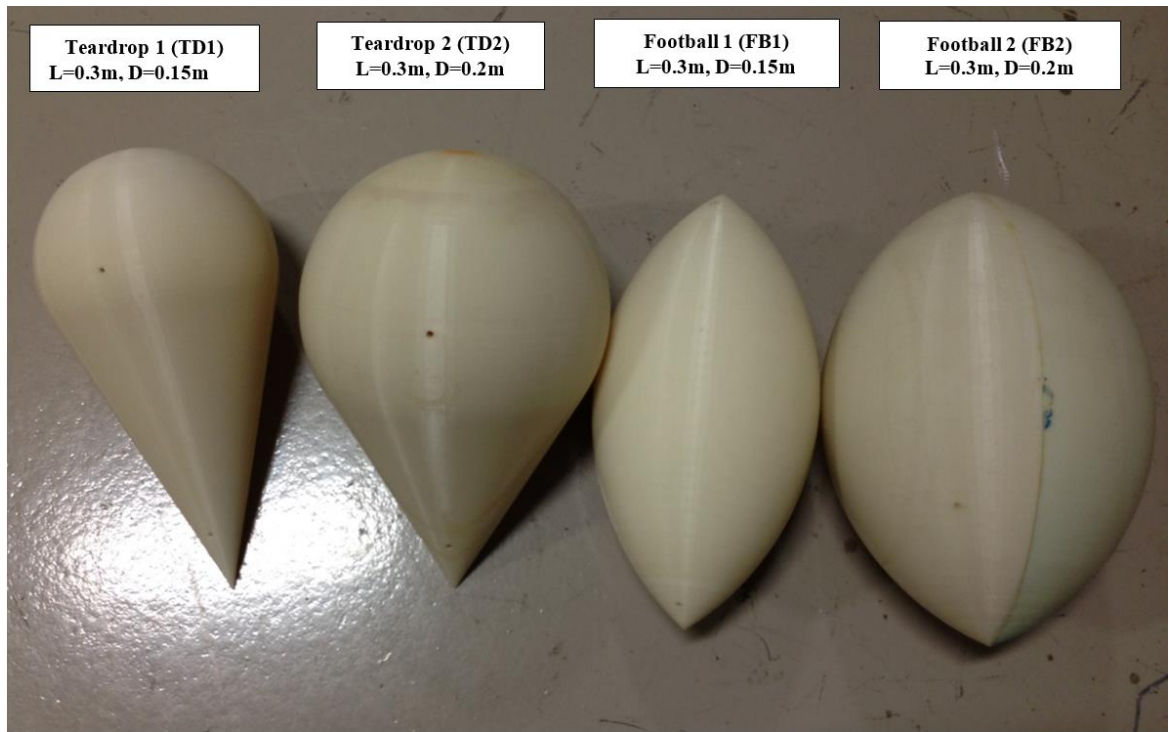
Figure 3-5: Streamlined Bodies of Different Dimensionless Parameters

The experiments consisted of each solid body being tested at the center of the dilution (i.e. mixing) zone at two different Reynolds Numbers determined by fixing the air volume damper at two different positions: fully open (i.e. angle= 0°), and half-open (angle= 45°). The results were compared with baseline case (i.e. without passive enhancer) at the same conditions. There are 10 experiments to compare and analyze, whereas every experiment needed at least three runs at the same flow rate and heating power to satisfy the statistical conditions mentioned in section 3.1, which results in a minimum of 30 total trials detailed in Table 3-1.

Table 3-1: Experimentation on the Proposed Streamlined Bodies

Case	Staggered Holes (SH)	Football 1 (FB1)	Football 2 (FB2)	Teardrop 1 (TD1)	Teardrop 2 (TD2)
AR	-	2	1.5	2	1.5

BR	-	0.37	0.49	0.37	0.49
PR	-	0.2	0.28	0.17	0.25
# flowrates	2	2	2	2	2
# runs	3	3	3	3	3

3.3 Swirling Fins (Swirlers):

Based on the latest assessment of passive enhancer insertion, additional twisted fins (swirlers) were proposed to generate a rotational flow within the chamber for a better mixing process. Four short rectangular swirlers were 3-D printed of the (ABS) material and attached circumferentially to the centrally placed football as shown in Figure 3-6. Three cases of mixing were done at the average flow rate (i.e. same Reynolds number): a) Staggered Holes (SH), b) Plain Football (FB), and c) Football with 4 Short Rectangular swirlers (F4SR). After that, lower flow rate was set for testing F4SR to check the performance at lower flow rates. It is important to mention that this stage of experimentation was conducted after a computational fluid dynamics (CFD) analysis of the effect of swirlers variables (dimensions, number, and shape) on the thermal uniformity of the outcoming mixture [73]. Further details on the numerical modelling are presented in Chapter 4 -. The F4SR design was recommended for the uniformity/ pressure loss balance introduced.
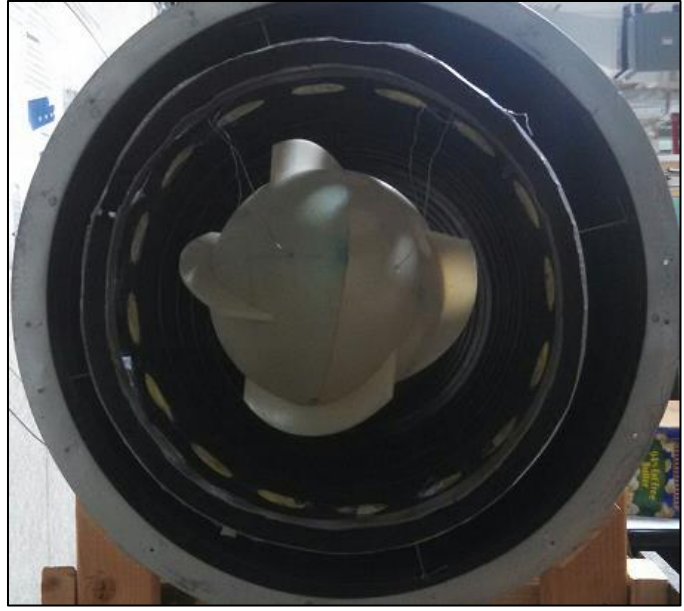
(a)   (b)

Figure 3-6: 3-D Printed Streamlined Body (a) after Attaching Swirlers, and (b) in the Mixing Chamber

CHAPTER 4 - THERMAL MIXING NUMERICAL MODELLING (CFD)

4.1 Geometrical and Boundary Conditions:

The main geometrical design for simulation is like the experimental setup: two coaxial ducts with a perforated mixing zone ending with a mixing exit pipe. Hot (central) and cold (annular) air flows start from the segregated entrance at the mixer inlet, go through the jet mixing section, and the mixed flow converges and departs at the exit section as seen in Figure 4-1. CAD is made using PTC Creo and imported to STAR CCM+ 9.06 and 11.04 to simulate the fluids motions and interactions in an unsteady run.
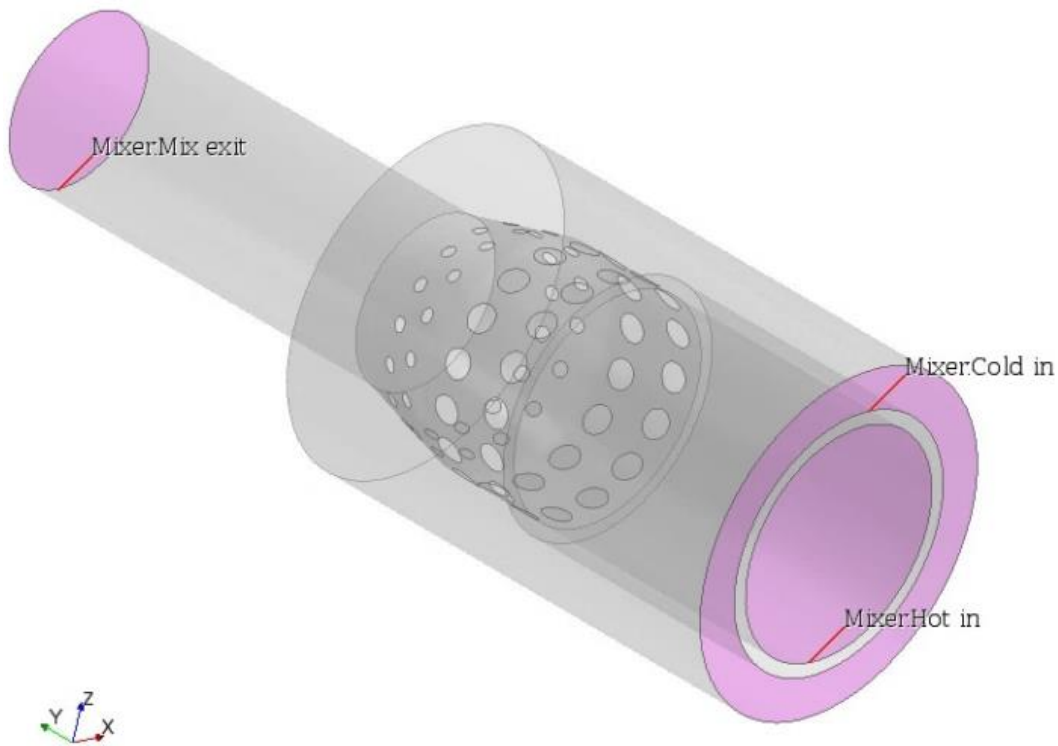
Figure 4-1: 3-D CAD Model of Mixer with Prescribed Boundaries

Boundary conditions were defined by the axial velocity (V_z) and temperature (T_{avg}) at the two inlets (cold and hot streams) and by pressure at the outlet. Duct walls were insulated and applying

non-slip condition. Constant properties over the cross-sections were assumed and set from the data recorded experimentally, Table 4-1 shows the values at the primary (central) and secondary (annular) ducts. Axial velocity and temperature of the hot air were averaged algebraically from the approximation of the integral relations of the mass and energy flow rates written in Eqs. (4-1) and (4-2). Ideal mixture velocity and temperature are directly calculated from the Eulerian form of mass and energy conservation equations of displayed in Eqs. (4-3) and (4-4) respectively.

Table 4-1: Boundary Conditions at the Entrance Zones

	Axial velocity V_z (m/s)	Temperature, T_{avg} (^{0}C)
Primary (hot) air	3.7	49
Secondary (cold) air	2.1	25.5
Ideal mixture exit	10.3	40.6

$$\dot{m} = \iint \rho \, \vec{V}.\vec{n} \, dA_p \approx 2\pi\rho \sum_{r=0}^{r=R_p} u \,.\, r \,.\, \Delta r = \rho \, V_a \, \pi \, {R_p}^2 \tag{4-1}$$

$$\dot{E} = \iint \rho \, C_p \, T \, \vec{V}.\vec{n} \, dA_p \approx 2\pi\rho \, C_P \sum_{r=0}^{r=R_p} u \,.\, T.r \,.\, \Delta r = \rho \, V_a \, \pi \, {R_p}^2 C_P \, T_{avg} \tag{4-2}$$

$$A \, V_a|_p + A \, V_a|_c = A \, V_a|_m \tag{4-3}$$

$$A \, V_a \, T_{avg}\big|_p + A \, V_a \, T_{avg}\big|_c = A \, V_a \, T_{adb}|_m \tag{4-4}$$

Where $\dot{m}$ and $\dot{E}$ are the mass and energy flow rates through the primary duct, ρ and C_p are the air density and constant pressure specific heat, u is the normal velocity which is the dot product of the velocity vector $\vec{V}$ and the normal vector $\vec{n}$ of the primary (crossflow) duct cross-section A_{cf}. r,Δr and R_p are the arbitrary radius, radial spacing, and primary duct radius respectively.

4.2 Inserted Streamlined Bodies:

Seven simulations represent the flow over the different swirling patterns attached to the streamlined "American Football" shape discussed to be effective in the quality of mixing. Swirlers shapes, numbers, and dimensions are varied over the same base body to study their effect on the mixing uniformity and total pressure drop occurring by the exit from the chamber. Cases can be arranged as follows:

a) Plain Football (**FB**), AR=1.5, BR=0.49, PR=0.28

b) Football with 4 Short Rectangular swirlers (**F4SR**),

c) Football with 8 Short Rectangular swirlers (**F8SR**),

d) Football with 4 Tall Rectangular swirlers (**F4TR**),

e) Football with 8 Tall Rectangular swirlers (**F8TR**),

f) Football with 4 Short Airfoil swirlers (**F4SA**), and

g) Football with 4 Tall Airfoil swirlers (**F4TA**).

Figure 4-2 depicts the CAD drawings of all proposed passive enhancers. Swirlers height defines the terms "short and tall" such that the short is 1.25cm and the tall is the double of that height.

(a) (b) (c)
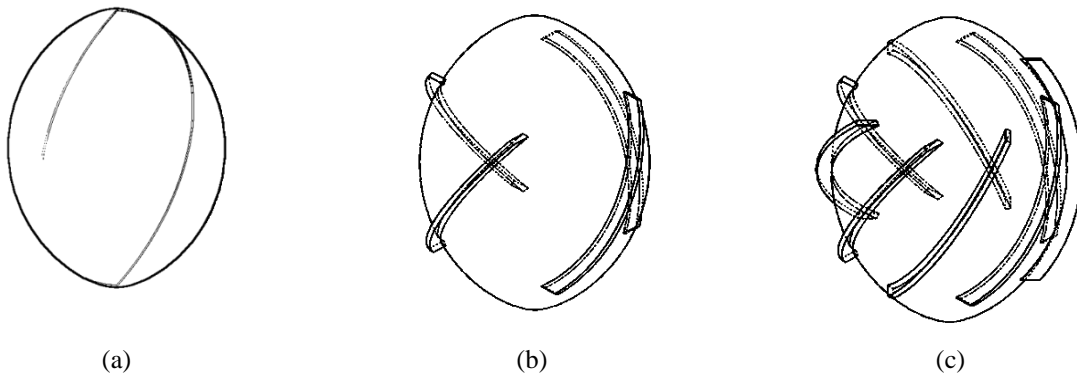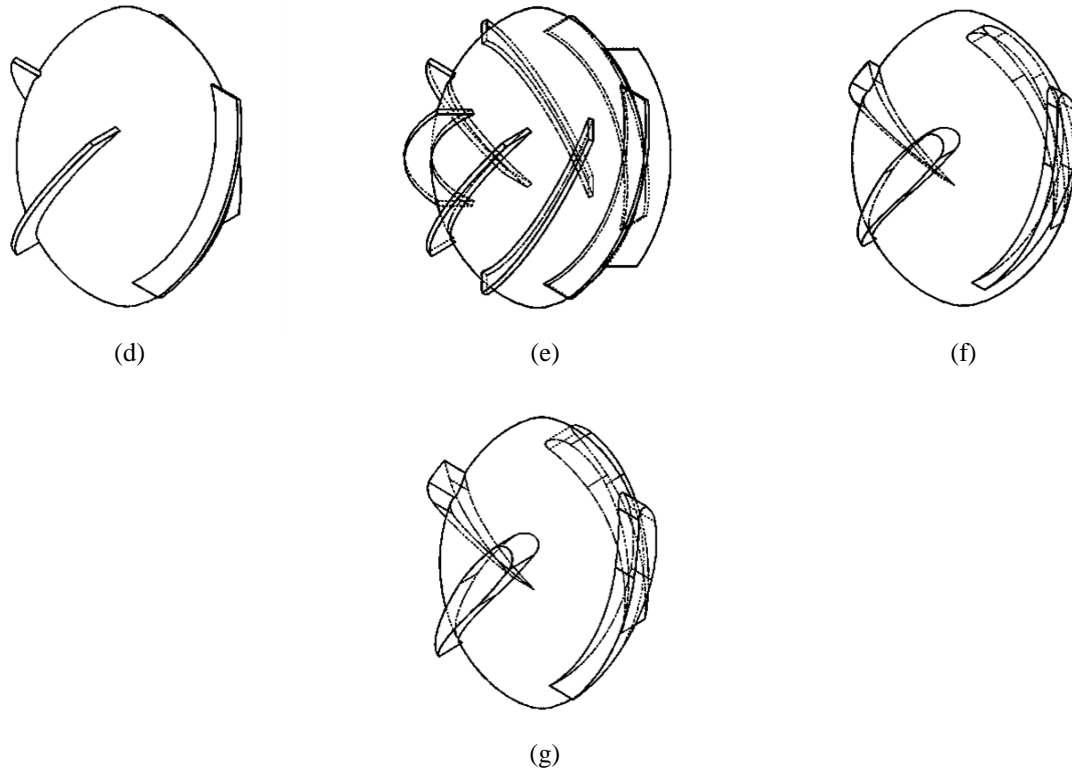
Figure 4-2: Streamlined American Football Equipped with (a) No Swirlers FB, (b) 4 Short Rectangular Swirlers F4SR, (c) 8 Short Rectangular Swirlers F8SR, (d) 4 Tall Rectangular Swirlers F4TR, (e) 8 Tall Rectangular Swirlers F8TR, (f) 4 Short Airfoil Swirlers F4SA, and (g) 4 Tall Airfoil Swirlers F4TA

4.3 Simulation Running Models and Parameters:

4.3.1 Spatial discretization

Domain meshing is 3-D with unstructured polyhedral cells which are more adaptive to the geometry with all its complexities by the arbitrary sized and distributed cells, and well responsive in the situations of flow components change. Prism layers are applied to the surfaces to activate the (viscous sub-layer, buffer layer, law of the wall) calculations for accurate boundary layer modeling. Jet holes and football edges showed finer cells to capture physics of swirl, tumble, wake region, and stagnation. Three optimization cycles redistributed the cells and managed the different sizes with homogeneity, achieving cell quality between 0.4-0.8 and cell face validity of 1. Total

42

number of cells are 1.2-1.3 million with 10 prism layers on the solid surfaces (i.e. walls and streamlined body), which result in independent exit values for temperature and velocity, and a wall distance function (y^+) in the range of 1 to efficiently model the viscous sub-layer. Different views for the 3D mesh of the mixing chamber can be seen in Figure 4-3a, Figure 4-3b, and Figure 4-3c, while the y^+ values for both the football and the system walls are shown in Figure 4-3d.

(a)   (b)

c)

43
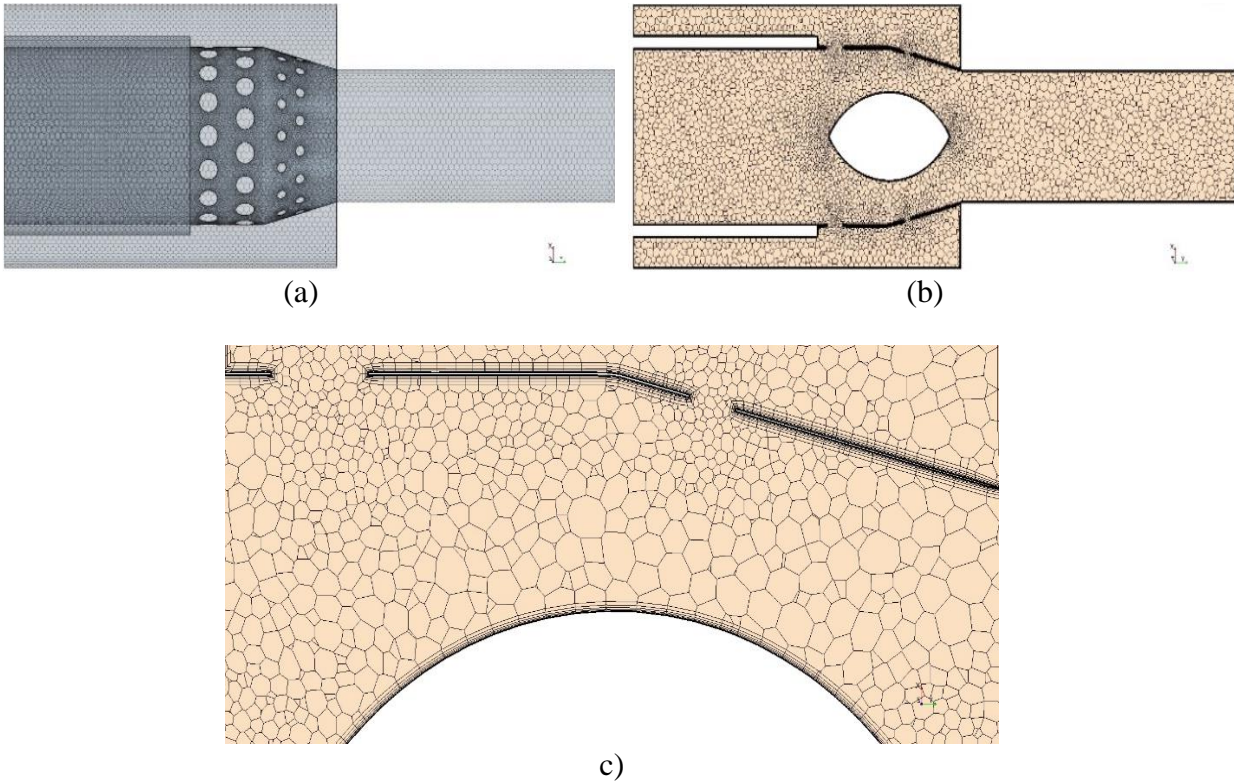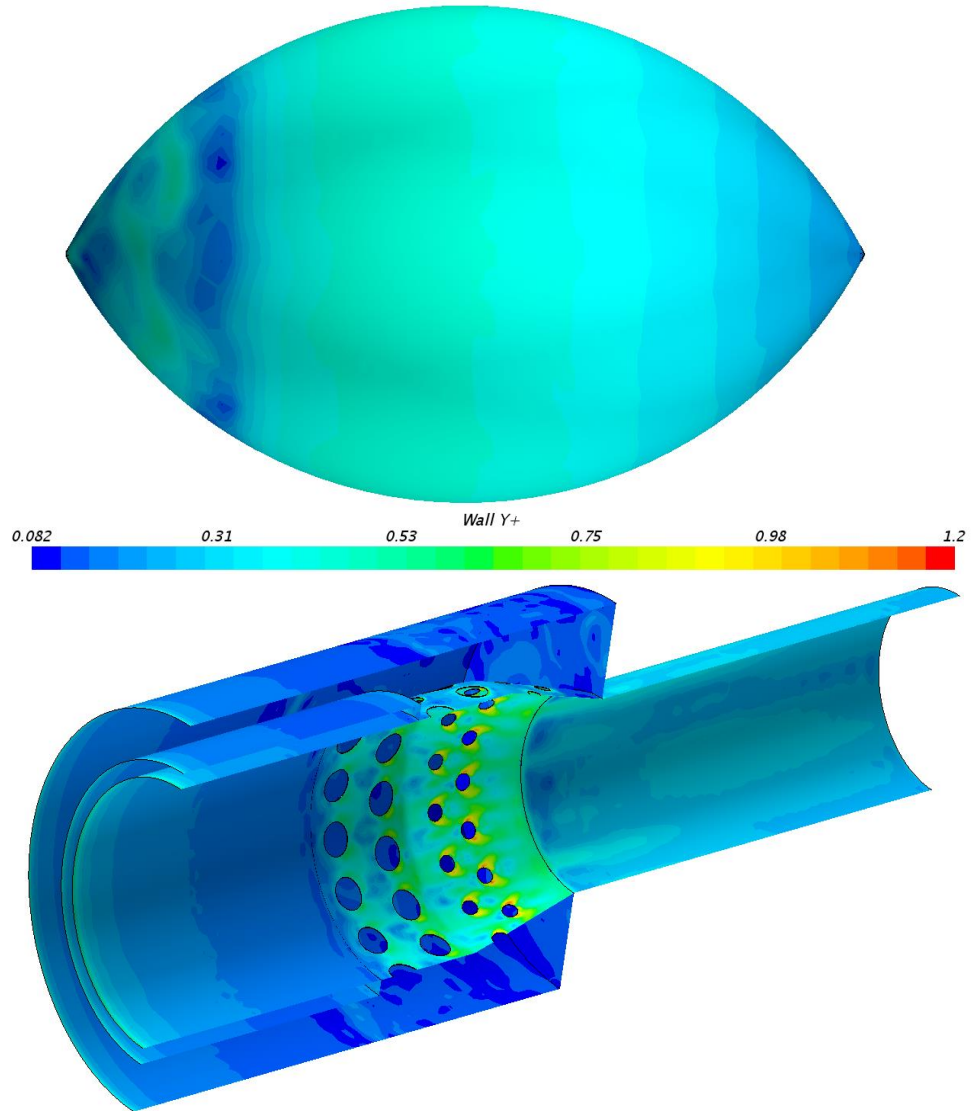
d)

Figure 4-3: Meshed Domain: (a) Surface Polyhedral Cells, (b) Section Volume Mesh, (c) Boundary Prism Layers and Finer Mesh at Jet Inlet, and (d) y^+ distribution over the surfaces (football and walls)

4.3.2 **Temporal discretization**

For time marching, time step (Δt) was 10^{-4} s which satisfies low convective Courant number which is still recommended even with the selection of implicit temporal computation. Because of the calculation depends on the initial guess, a solution of each time step is iterated five times to

converge with proper accuracy. Total physical time in simulation is 4s (corresponds to 200,000 iterations), which is found to be enough for statistically stabilizing the flow field properties (especially the exit temperature and velocity). Running simulation lasts on High Performance Computing (HPC) cluster for 14 hours using 96 Intel® Xeon E5-2450 v2 processors and 2560 Mb memory.

4.3.3 **Solution Methodology**

STAR-CCM+ employs Finite Volume (FV) numerical method for solving the governing equations (mass, momentum, and energy). Algebraically transformed partial differential equations are solved separately and in sequence (i.e. segregated flow) such that the continuity is firstly solved then followed by the three momentum equations for estimating the components of velocity and pressure at the cell under interest and ending by the temperature calculation through the energy equation. Segregated flow is known to be a better method than the couple flow approach in the subsonic flow cases.

Large Eddy Simulation (LES) is used for unsteady turbulence solution. Based on the principle of large eddies to be case related and the very small (Kolmogorov) eddies are always independent, LES solves the flow related eddies using the unsteady spatial-averaged Navier-Stokes (N-S) equations and depicts the filtered small ones near walls by Wall-Adapting Local Eddy (WALE) viscosity sub-grid scale (SGC) model. WALE is a recent model which exceeds the performance of the Smagorinsky SGS in formulating the turbulent viscosity (μ_{Turb}), and the accurate scaling near the wall without damping effects [74]. LES is more favorable than unsteady RANS in time-dependent numerical analysis.

4.4 Design of Experimentation and Optimization:

Following the concept of Analysis Led Design of the swirlers using the CFD, the research was directed to goals summarized in minimizing the uniformity number (x) and pressure drop (PD), choosing the most effective variables of the swirling prolate spheroid, and reaching the ideal feasible design(s). The strategy is purely numerical, and it can be stated as follows:

1) _Setting three geometrical variables:_ of the prolate spheroid (diameter: D, length: L, axial position with respect to the chamber center: *p*). For every variable, minimum and maximum bounds will be defining the study span. **Error! Reference source not found.** s hows some possibilities of manipulating the body variables.

(a)   (b)

(c)   (d)
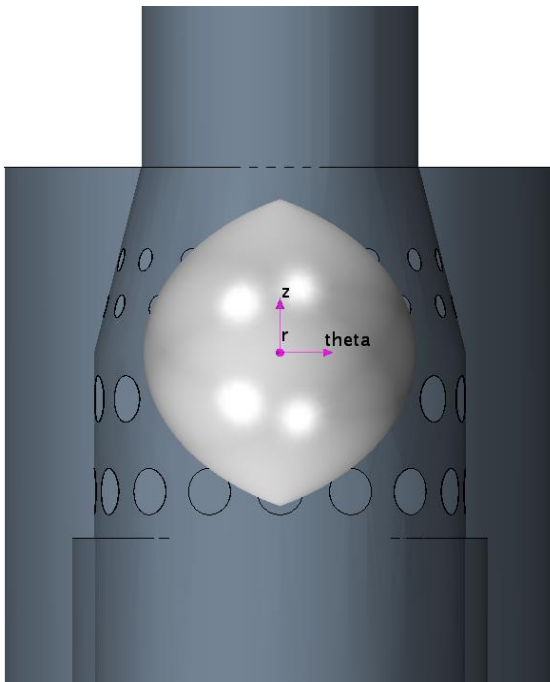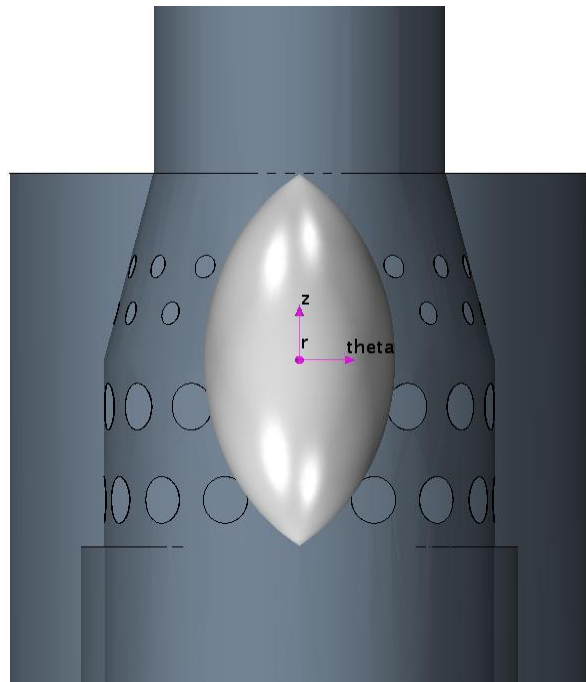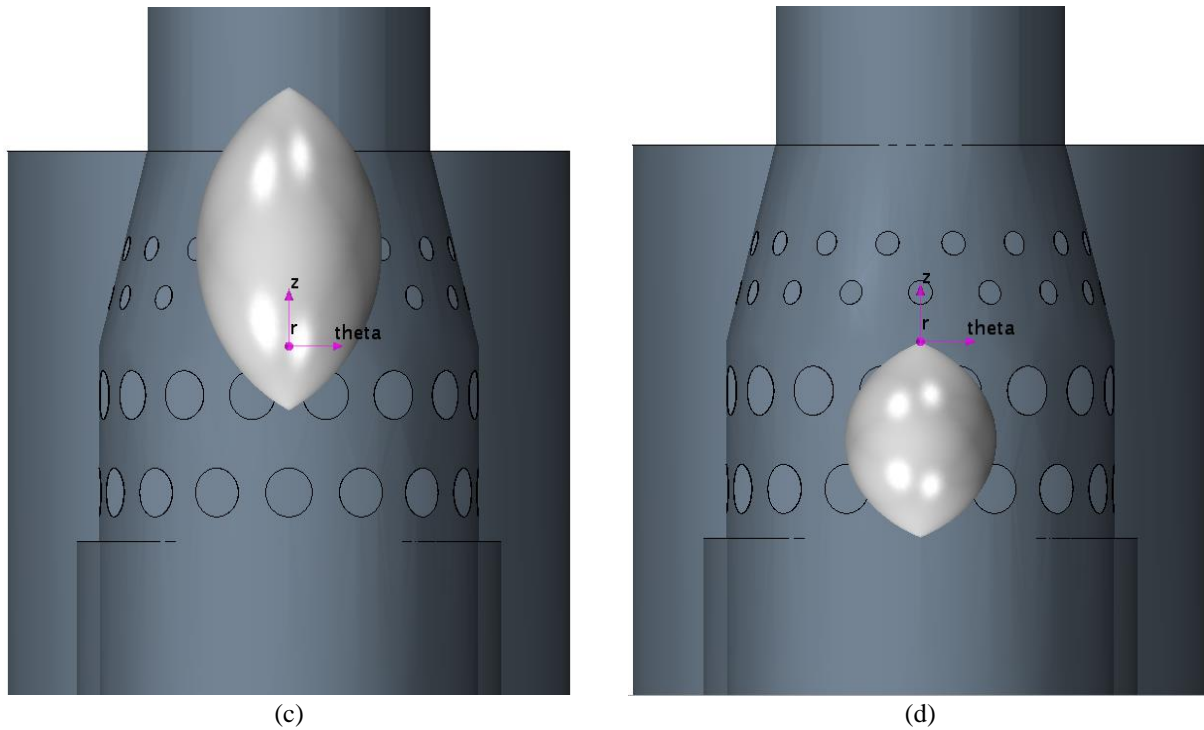
Figure 4-4: Possible changes in FB variables: (a) diameter only, (b) length only, (c) position only, (d) all variables together

2) _Arranging the initial design space:_ based on the three of variables and their proposed testing ranges. The arrangement will be based on the DOE approach: Uniform Latin Hypercube (ULH). ULH, described in 1993 [75], is a method of selecting the input variables values as a perfect sample reflecting the whole testing space. Generally, in sampling, each case study acquires dissimilar sets data inputs (e.g. D_1, L_1, p_1) than the others (e.g. D_2, L_2, p_2 or even d_1, L_2, p_1) to represent the wide design space. The sampling in ULH determines not only distinct sets, but also completely new values from the variables ranges (continuous or discrete). With M variables, ULH DOE generates a cube of M dimensions and divide the variables ranges equally such that the number of divisions is the same among all variables. It is ensured that each case occupies M different vectors (row and column in case of M=2) alone, and all vectors are used. Such step maintains

47

good distribution of the cases between the all the variables predefined extremes. The minimum number of studies/experiments (aka sample size) is recommended to be evaluated as in Eq. (4-5). The ULH is highly adopted these days in experimentation sampling.

$$Sample\ Size_{min} = \frac{(M + 1)(M + 2)}{2} \tag{4-5}$$

3) _Applying optimization algorithms_ to investigate more cases that narrows towards the optimum design. The work will be subjected to three popular optimization categories:

(a) **Local heuristic algorithm** effectively approaches the closest objective (set either minimal or maximal) to the start point. The outcome is a relative to the initial case study and search technique, and it is not necessarily the absolute optimum. This fast and robust kind of algorithms is good for tentative understanding of inputs-outputs relations, analyzing the strength of some variables, and making quick decision [76]. Generalized Reduced Gradient, GRG, is the currently suggested local algorithm which has a search technique based on linear approximation for the gradients of the output functions[77].

(b) **Global deterministic algorithms** overview the design space with investigating the solutions of well-distributed cases. Complete search process reaches the absolute optimum design with full realization of the design space response by the end [78]. However, it is a time-consuming type, because of the broader search technique. In the upcoming period, the global optimization is chosen to be Multi-Objective Genetic Algorithm-II (for short MOGA-II) which seeks the optimization in a similar way to

the evolution theory. Based on evaluating a parent generation (set of initial guess cases and usually arranged by ULH), characteristics improvements (i.e. objectives) of some cases are highlighted and weighted when happened. Subsequently, an automated process architects an offspring generation by combining the properties (i.e. variables values) of the best parents. After predefined number of generations or tolerance, the global optimal can be reached [79].

(c) Hybrid optimization algorithm is mainly a recursive method in which the big picture solution is a function of small solution zones. The importance of hybrid system lies on the ability of shifting methods per data size. The start usually is global over the design space, then the logic switches to local when the solution size converges towards the optimum solution. Classified as a hybrid, Simultaneous Hybrid Exploration that is Robust, Progressive, and Adaptive (SHERPA) [80] serves time efficiency and sometimes better solutions than global algorithms [81].

The work is supposed to introduce evaluation tools such as Response Surface Methodology (RSM), correlation matrix, scatter and parallel axes, and Pareto efficiency (i.e. optimality) curve between x and PD.

CHAPTER 5 - CAVITATION NUMERICAL STUDY

5.1 Introduction

In all the simulations and experimental tests, the cavitation treatment was investigated over a constant flow rate to preserve the same conditions generating the cavitation pattern. Meanwhile at the conventional constant head approach, the air injection chokes the cross-section area for the water flow which minimizes the flow rate over the rotor, and the cavitation pattern changes, so the treatment is not consistent.

5.2 Simulation Conditions and Tested Cases

5.2.1 All-Inclusive Model

Working on a CFD model of a 7.5-cm Kaplan turbine, cavitation was initially sought to identify the generating conditions and define an assessment criterion related to the cavitation phenomena in the system. The upstream side is a 15-cm diameter pipe with a fully-developed turbulent profile velocity inlet (V_{avg}= 2-2.54 m/s). The turbulent velocity profile is defined by the power law stated in Eq (5-1). With a power (n=8) for high Re flows, the V_{max}=1.2 V_{avg}.

$$V = V_{max} \, (1 - \frac{r}{R})^{\frac{1}{n}} \tag{5-1}$$

Next, the flow passes through a converging intake pipe confining the Pre-Swirl Stator (PSS), ending with the 7.5-cm rotor section. At the beginning of each simulation, the rotational speed (N) is pre-set for the rotational domain surrounding the rotor, and the value is selected from a range (1000-5000 rpm) with a 1000 rpm step. The downstream of the rotor is designed to be a diffuser (i.e. diverging frustum of 20-degrees half angle) for static pressure reclamation, then a straight

pipe of a 15-cm diameter extends towards a 90-degrees elbow where the outlet section is defined by the exit pressure. Such conditions were enough to drop the static pressure below the vapor pressure (P_v) and start the cavitation on the rotor components. The CFD model suits the two air injection methods (housing and hub) by adding the proper number of holes that will define the air injection locations and pressures. System configuration is depicted in Figure 5-1.
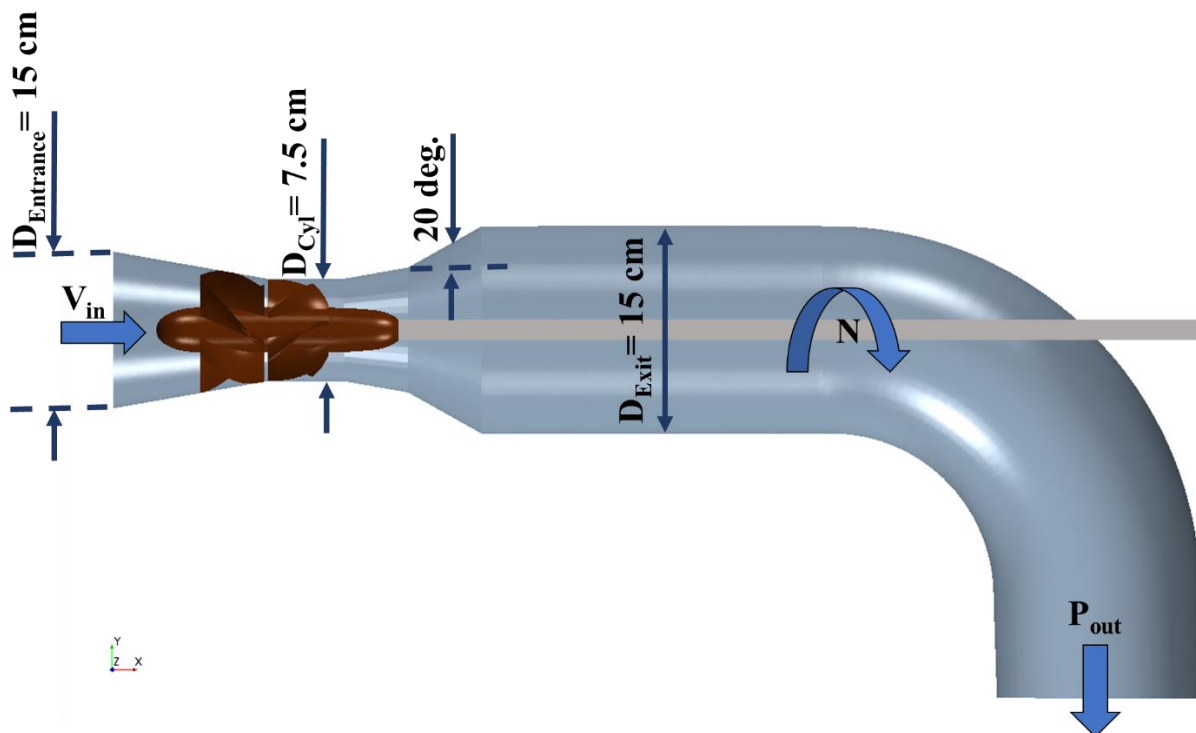
Figure 5-1: Numerical setup and boundary conditions of the cavitation in 3-inch Kaplan hydro-turbine

The numerical domain involves two regions of different computational natures:

1) <u>Stationary Region (SR)</u>: Solves the flow by the linear conservation equations within motionless cells during the entire solution time. The region encompasses the inlet, PSS, exit pipe/elbow/outlet, and a thin annular envelope around the rotor domain (i.e. rotational) to account for the static wall effect of the housing.

2) <u>Rotational Region (RR)</u>: is created around the rotor blades and hub only and includes a cylindrical and part of the slant sections. The mesh cells are in rotational motion set by

the predefined N parameter, so the flow is solved with respect to the tangential velocity and new positions of the cells updated every time step. A zoomed scene in Figure 5-2 shows the two distinct regions.
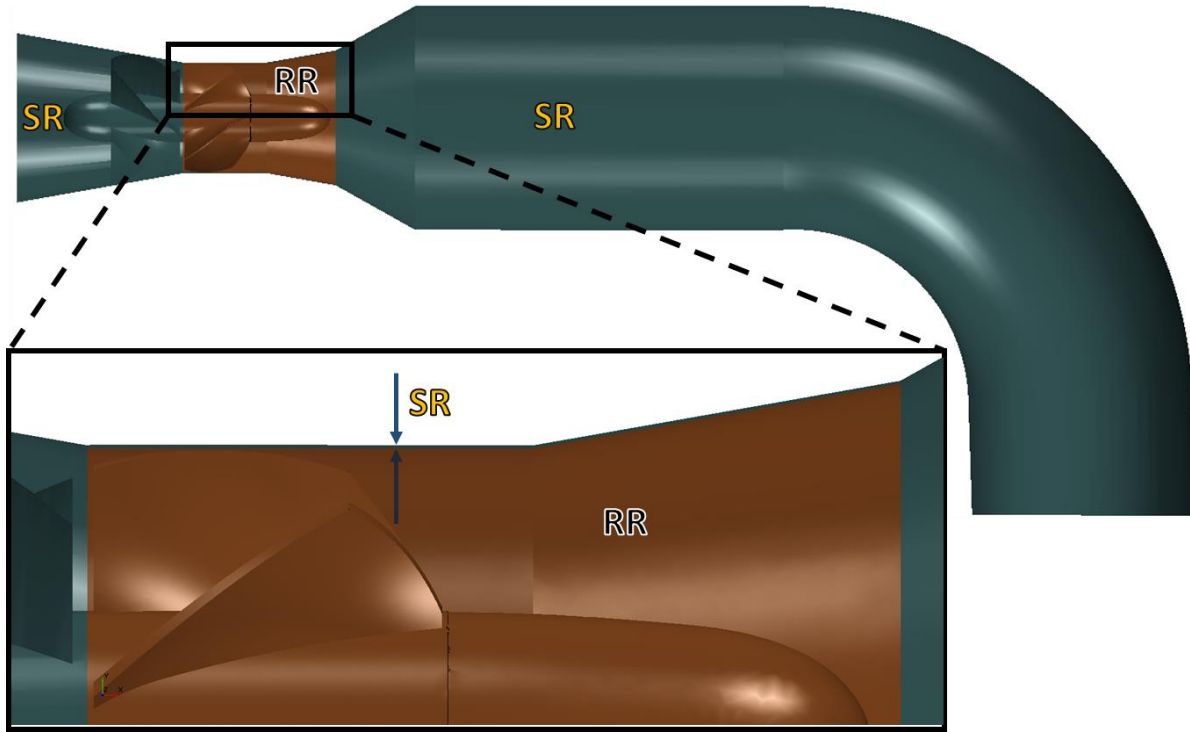
Figure 5-2: Zoomed scene of the two numerical regions (stationary and rotational) defining the model

5.2.2 Housing Air Injection

Attached to the internal wall of the housing, air is injected from 1-mm diameter circular holes arranged in different patterns (1 port, 12 circumferential ports, and 2 Blocks/ 3 Ports (2B3P): 6 ports divided into two axis-parallel linear groups separated by 180 deg.) as seen in Figure 5-3. Though the operation pressure around the rotor is low enough for an atmospheric pressure air injection, the pressurization of air is set to be slightly above the atmospheric pressure by 0.5-1 psi to guarantee the stability of the injection at the startup when the water pressure is still high around the turbine. Extra reason is the acting as a cavitation pre-cure by raising the absolute pressure at the zones prone to the vapor pressure.

<p align="center">(a)   (b)</p>
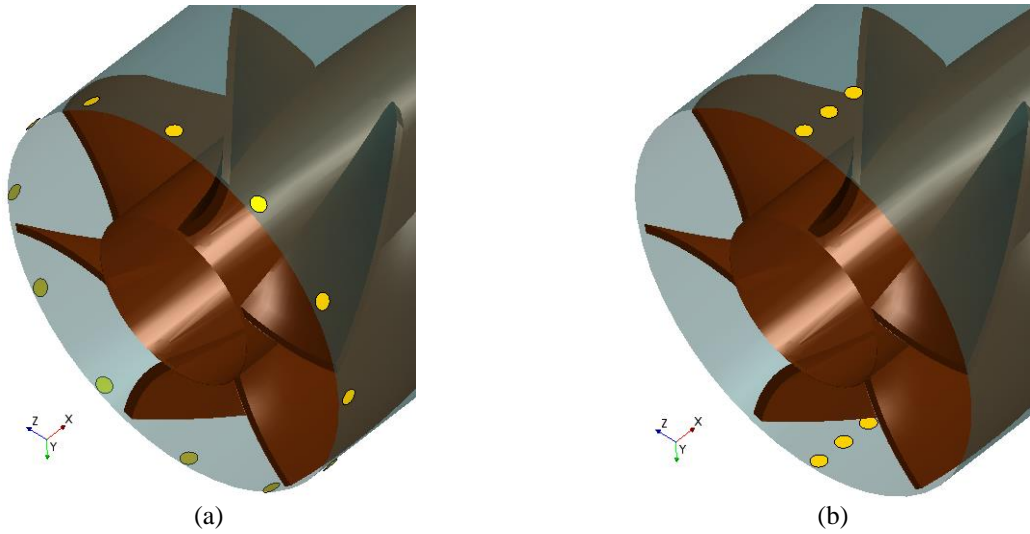
Figure 5-3: Air ports (Gold color) arrangements around the rotor blades: (a) 12 circumferential inlets, and (b) two linear groups of 3 inlets separated by 180 degrees

Another aspect was investigated subsequently to the 2B3P analysis, which is the port location relevance to the vapor content reduction. The proposed locations were those used in 2B3P and they are arranged as follows:

Port (1): At the blade's leading edge

Port (2): Downstream of the first port by 6 mm spacing (i.e. $2 \times d_{port}$)

Port (3): More downstream and almost at the mid of the blade's chord with the same spacing $(2 \times d_{port})$ from the second port.

Descriptive scene for the configuration is seen in Figure 5-4. The three locations were simulated alternatively (having one port open and the other two are closed). Operation conditions (water flow rate and air injection pressure) are maintained along with the same port diameter and rotational speed. For the sake of simplicity of the model, the simulations were done at one rotational speed (N=1000 rpm) and with one block instead (top) of two facing each other.
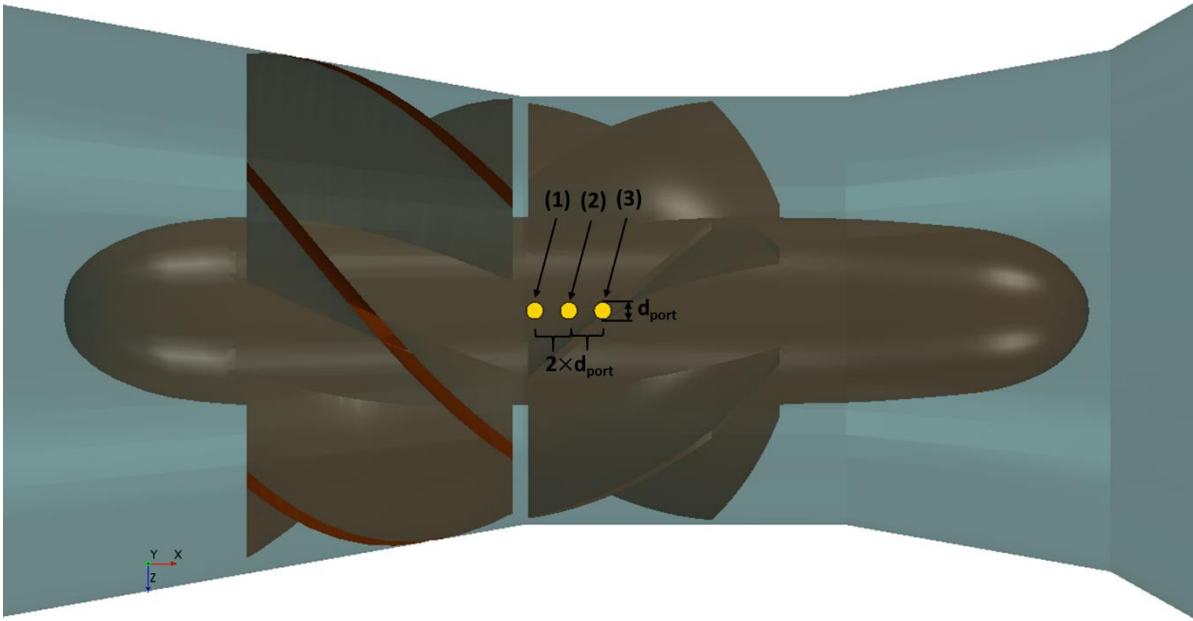
Figure 5-4: Three air ports order and position

5.2.3 **Hub Air Injection**

Considering a cavitation occurrence over the blade suction side, the hub air injection is proposed very close to the blade surface in four equally spaced locations from the leading edge until the trailing edge as shown in Figure 5-5. The holes are circular (d= 3mm) with pressure as high as 5 psi to ensure a good amount of air entering the system from each hole. While the design is tested collectively, the effect of each row of holes per blade was investigated as well by alternate opening at the same cavitation condition.
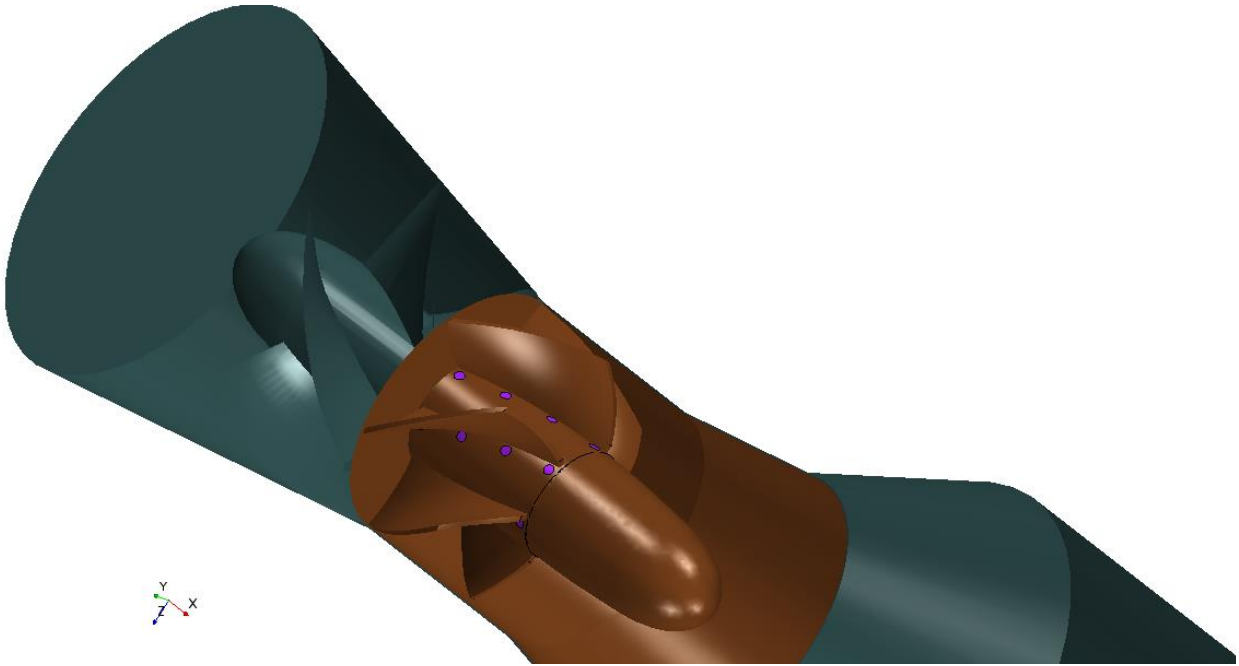
Figure 5-5: 3-D view for the turbine with the circular holes representing the hub air injection configuration

5.3 Selected Numerical Models

A case including three different fluids with distinctive densities (ρ) needs a multi-phase physics model to differentiate well between the phases (and components) available in the system and define the interactions between them during the flow. Because the case involves phase change and the cavitation shows in either a cluster of bubbles or a cloud, it was proposed that Volume of Fluid (VOF) be the multiphase model expressing the large volumes of the different fluids (liquid water and vapor, and even air later), and tracking the interface between them. VOF is efficient when dealing with large volumes and smaller contact areas between the phases. At every numerical cell, each phase/component is represented by a volume fraction (α), which is updated every time step by solving a corresponding transport equation. By the end, VOF gives a solution for all the properties as a weighted average of the constituents. In this simulation, the convection of diverse fluids is 2nd discretization which is sufficiently good in describing the distribution and interfaces.

55

Additionally, the case is turbulent (Re=3.4x10^5). Thus the unsteady random chaotic phenomena were simulated using Large Eddy Simulation (LES) which filters the large-scale eddies to be solved in Navier-Stokes (N-S) equations from the small-scale ones which are shaped by the Wall-Adapting-Local-Eddy viscosity (WALE) Sub-Grid Scale (SGS) model. LES is more favorable than unsteady RANS in time-dependent numerical analysis. Some previous CFD work on turbomachinery showed the reliability of the LES [82],[83].

The meshing cell is unstructured polyhedral, which is better than structured mesh in capturing physics like separation and wake region. After trying different mesh combination, ranging from 1.3 million to 12 million cells, mesh size is selected fine to form 9 million cells with 8-12 prism layers maintaining the first layer y^+ value less than 2.5 except for certain intentional regions (recommended 1-prism layer at the interfaces for proper data transference between the different regions and no prism layers at the air ports to be defined as stagnation inlets on the later stage of simulation). Mesh refinement is required not only for the solution accuracy and independence, but also for the optimal representation of the fluids' interfaces and propagation. Another reason for the small cell sizes is the LES recommendation of improved modelling when eddies volumes go to the universal Kolmogorov scale. A sectional plane of the meshed system is in Figure 5-6, while wall y^+ of the turbine is depicted in Figure 5-7.
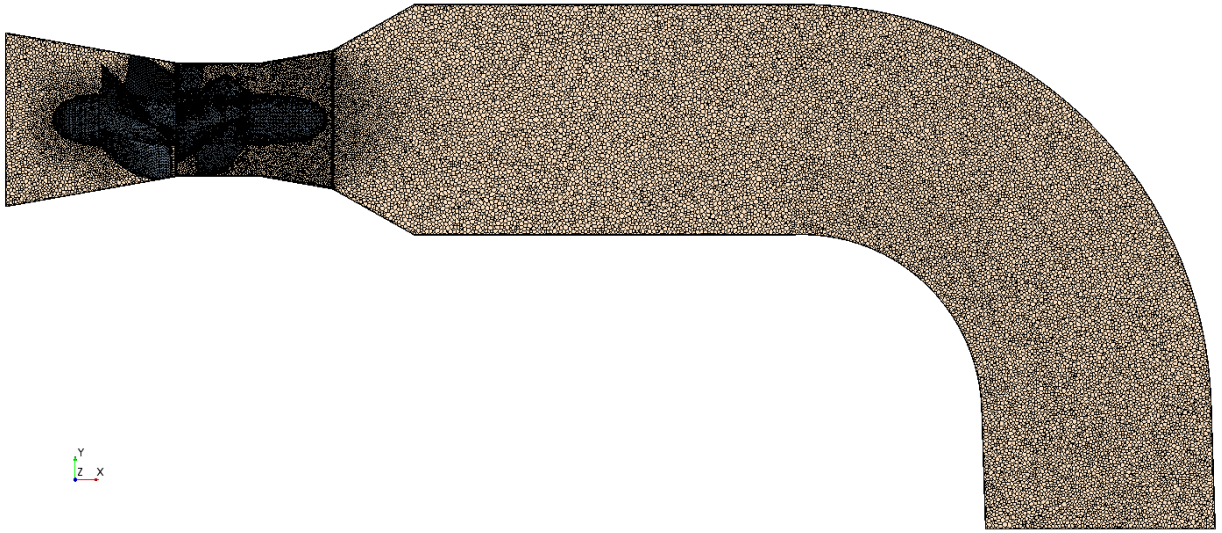
(a)
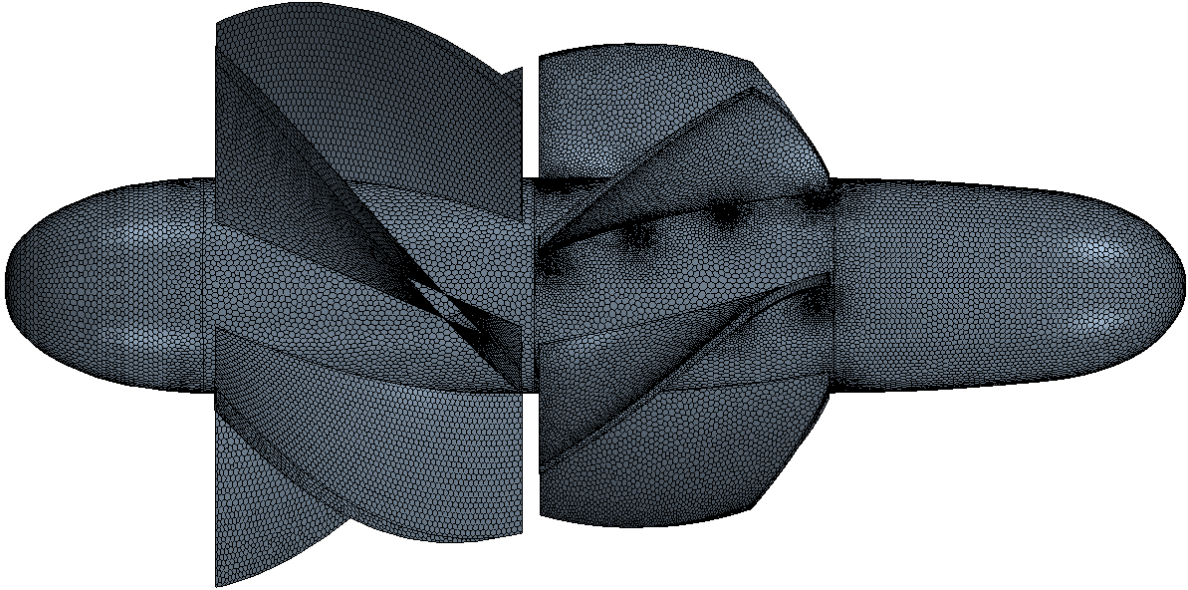
(b)

Figure 5-6: Meshed hydro-turbine system with 6 million polyhedral cells: (a) whole model, (b) turbine parts
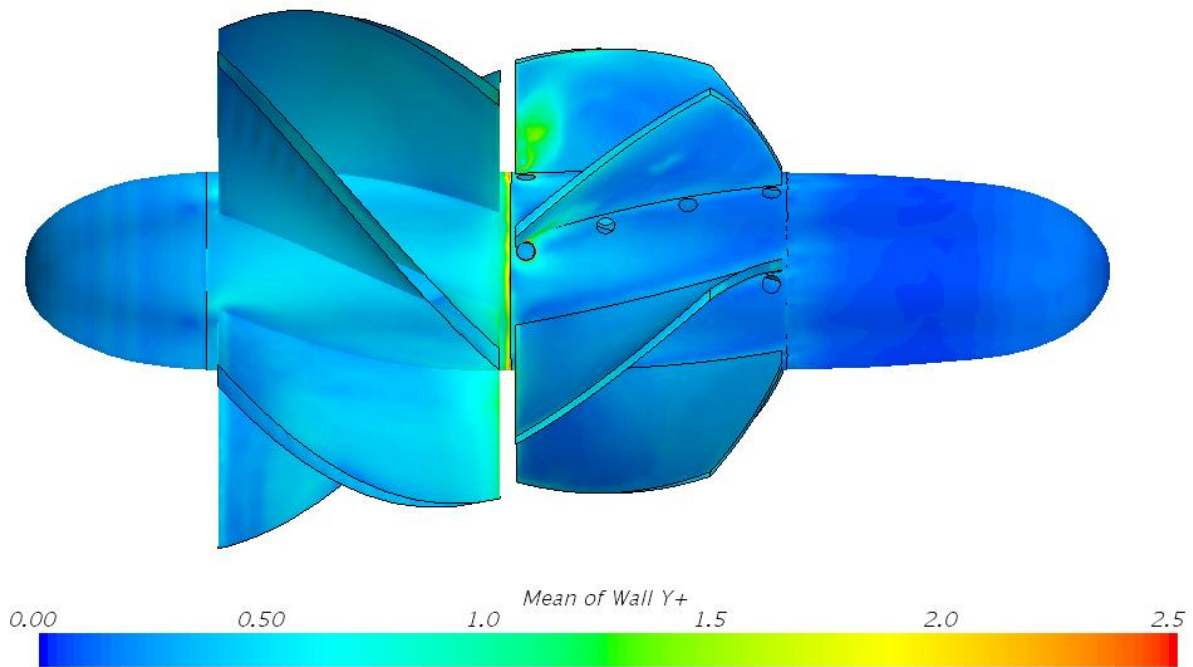
Figure 5-7: Wall y^+ function over the hydro-turbine

Time marching in the case studied was essential to capture the development of the vapor on the surfaces and its propagation within the liquid water. The time step was based on the rotation because it defined a smaller time scale and higher effect on the cavitation pattern than the axial flow velocity. Temporal discretization was adjusted for every N to be less than the 1 deg. of turbine rotation (i.e. maximum time step is 10^{-4} s for the 1000 rpm case and the minimum is 3×10^{-5} s for the 5000 rpm). The solution accuracy was 1st order type which was preferable over the 2nd order accuracy because of the faster performance and the granted stability for the computational process. The simulation ends after 12 turbine cycles to ensure the achievement of the steady state. Total computation time for one simulation is 3 days on 240 High Performance Computing (HPC) cores.

5.4 Flow Physical Equations

5.4.1 Volume of Fluid

VOF was firstly introduced briefly in 1976 Noh and Woodward's conference paper [84] which was followed by a full method description by Hirt and Nichols in 1981[85]. In such approach, the co-existed (n) fluids are accounted as a global one phase of fluid and flow properties calculated as an averaged sum based on the presence percentage of each phase in the computation cell by volume ratio ($\frac{\forall_l}{\forall_c}$). Accordingly, the $(l)^{\text{th}}$ phase volume fraction (α_l), and any equivalent property (ϕ) are calculated every time step as in Eq. (5-2) and (5-3) respectively.

$$\alpha_l = \frac{\forall_l}{\forall_c} \tag{5-2}$$

$$\phi = \sum_{l=1}^{n} \alpha_l \, \phi_l \tag{5-3}$$

Since the system is always conserved, the volume fractions of the phases are also maintained in balance by solving the transport equation (also known as continuity) of each volume fraction as shown in Eq. (5-4). The equation considers the phase motion relative to the reference frame motion $(V - V_g)$, interface update, and phase addition/reduction due to source/sink (φ_{α_l}) existence.

$$\frac{\partial}{\partial t} \int_{\forall} \alpha_l \, d\forall + \int_{A} \alpha_l \, (V - V_g) \, dA = \int_{\forall} (\varphi_{\alpha_l} - \frac{\alpha_l}{\rho_l} \frac{D\rho_l}{Dt}) \, d\forall \tag{5-4}$$

In situations of rapid phase change, like in cavitation, the global density varies temporally and locally in a high rate, and the source/sink term dominates. Meanwhile, the unsteady term exhibits a similar behavior and becomes difficult to be solved by the segregated flow method. To bypass the computational challenge, Eq. (5-5) is a simplified but non-conservative equation is derived from Eq. (5-4).

$$\int_A^{\cdot} \alpha_l \, (V - V_g) \, dA = \sum_l \int_\forall^{\cdot} (\varphi_{\alpha_l} - \frac{\alpha_l}{\rho_l} \frac{D\rho_l}{Dt}) \, d\forall \tag{5-5}$$

In a consecutive computational step, the motion of the global phase (i.e. mixture) is solved by the compressible-flow momentum differential equation with the consideration of the isothermal and Newtonian fluid conditions as expressed in Eq. (5-6).

$$\frac{d(\rho\vec{V})}{dt} + \nabla.\left(\rho\vec{V}\,\vec{V}\right) = \rho\vec{g} - \nabla P + \nabla.\left[\mu\left(\nabla\vec{V} + \nabla\vec{V}^T\right)\right] \tag{5-6}$$

Where $\vec{g}$ is the gravitational acceleration affecting in the downward vertical direction (i.e. negative y-direction as it can be figured in Figure 5-1) with a constant value 9.81 m^2/s.

5.4.2 **Large-Eddy Simulation**

Turbulence is solved and modelled by LES, the method utilizes a filtration function to the field property (ϕ) to block the values lower than a certain spatial and temporal scales. Filtration shown in Eq. (5-7) results in a separation between the pass field scale ($\bar{\phi}$) (i.e. those in large eddies) and the blocked one (ϕ') (i.e. small eddies) as in Eq. (5-8). The resultant N-S equation for the filtered field scale is expressed in tensor form in Eq. (5-9).

$$\overline{\phi(x,t)} = \int\!\!\!\int_{-\infty}^{\infty} \phi(\tilde{x},\tilde{t}) \, G(x - \tilde{x}, t - \tilde{t}) \, d\tilde{x} \, d\tilde{t} \tag{5-7}$$

$$\phi = \bar{\phi} + \phi' \tag{5-8}$$

$$\frac{\partial\overline{u_i}}{\partial t} + \frac{\partial(\overline{u_i u_j})}{\partial x_i} = -\frac{1}{\rho}\frac{\partial\overline{P}}{\partial x_i} + 2\nu\frac{\partial S_{ij}}{\partial x_j} \tag{5-9}$$

whereas $S_{ij} = \frac{1}{2}(\frac{\partial\overline{u_i}}{\partial x_j} + \frac{\partial\overline{u_j}}{\partial x_i})$ is the strain rate tensor of the fluid flow.

With the difficulty of the calculation of the filtered advection term ($\frac{\partial(\overline{u_1 u_j})}{\partial x_i}$) because of the need to include the interaction of the filtered large-scale eddies with the unfiltered small ones. Leonard related the filtered advection term to the multiplication of the filtered velocities by adding a residual (or sub-grid scale) turbulent stress tensor (τ_{ij}^r) expressed in Eq. (5-10) [86].

$$\frac{\partial(\overline{u_1 u_j})}{\partial x_i} = \frac{\partial(\overline{u}_1\,\overline{u}_j)}{\partial x_i} + \frac{\partial(\tau_{ij}^r)}{\partial x_i} \tag{5-10}$$

By defining (τ_{ij}^r) using Boussinesq's hypothesis[87] of linking the turbulence stress to an artificial turbulent viscosity (μ_{Turb}) which needs an SGS model to identify. Equations (5-11) and (5-12) are outlining the formulation for τ_{ij}^r (general and descriptive forms) based on the strain rate (S_{ij}) and turbulent kinetic energy (k).

$$\tau_{ij}^r - \frac{1}{3}\tau_{kk}\delta_{ij} = -2\mu_{Turb}S_{ij} \tag{5-11}$$

$$\tau_{ij}^r = 2\mu_{Turb}S_{ij} - \frac{2}{3}\left(\mu_{Turb}\nabla\cdot\vec{V} + \rho k\right)I \tag{5-12}$$

Such that (I) is the identity matrix of unity diagonal (i.e. $i=j$) with zeros at the rest elements.

With WALE model, μ_t is defined in terms of the length scale which is usually set at the half of $\forall_c$ near the wall, and the deformation parameter which is a non-linear function consisting of the gradients of the filtered velocities as the building unit[72],[88].

CHAPTER 6 - CAVITATION EXPERIMENTAL INSTALLATION AND PROCEDURES

6.1.1 System Configuration

The hydro-system is designed to run a horizontally oriented 7.5-cm Kaplan turbine from a relatively low water height (9 ft. maximum level) between the head and sink. Since the system was set in a lab, it was planned to be a closed system by flowing water from a head tank to the turbine, discharging to a sink tank, then pumping the water again from the sink tank to the head one. The installed setup appears in Figure 6-1. Pump was selected of power 10HP/60 Hz operated by a Variable Frequency Drive (VFD). Below the tank, a ball valve regulates the water flow rates for different conditions testing and system steadiness along with the pump applied frequency.
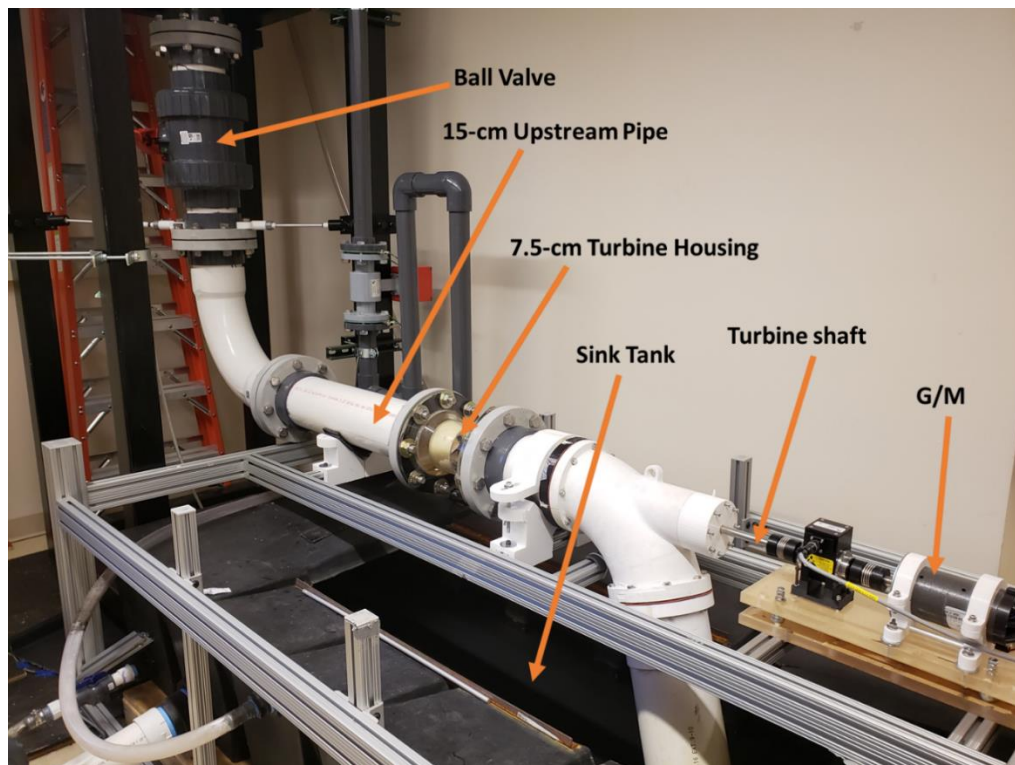
Figure 6-1: 9 ft. closed hydro-system: full setup, and turbine housing with and emerging shaft coupled to a generator/motor

The turbine stator and rotor blades are 3-D printed of NGen, sanded, and painted to have a smooth surface. Specifications like number of blades (9 for stator/ 6 for rotor), blade aspect ratio ($\frac{span}{chord}$=0.68), blade thickness-chord ratio (0.05), and others were chosen after extensive CFD study for a built 12-inch turbine on Bark river in Rome town, WI [75], [83]. A close-up image of the turbine is presented in Figure 6-2. The turbine is seated inside a clear Acrylic housing shaped in three sections from the inside: (a) nozzle intake tube with 15 and 7.5 cm start and end diameters, it is where the shrouded stator stays, (b) 7.5-cm straight cylindrical section confining the rotor, and (c) diffuser-like draft tube diverging to a 15-cm downstream exit pipe.
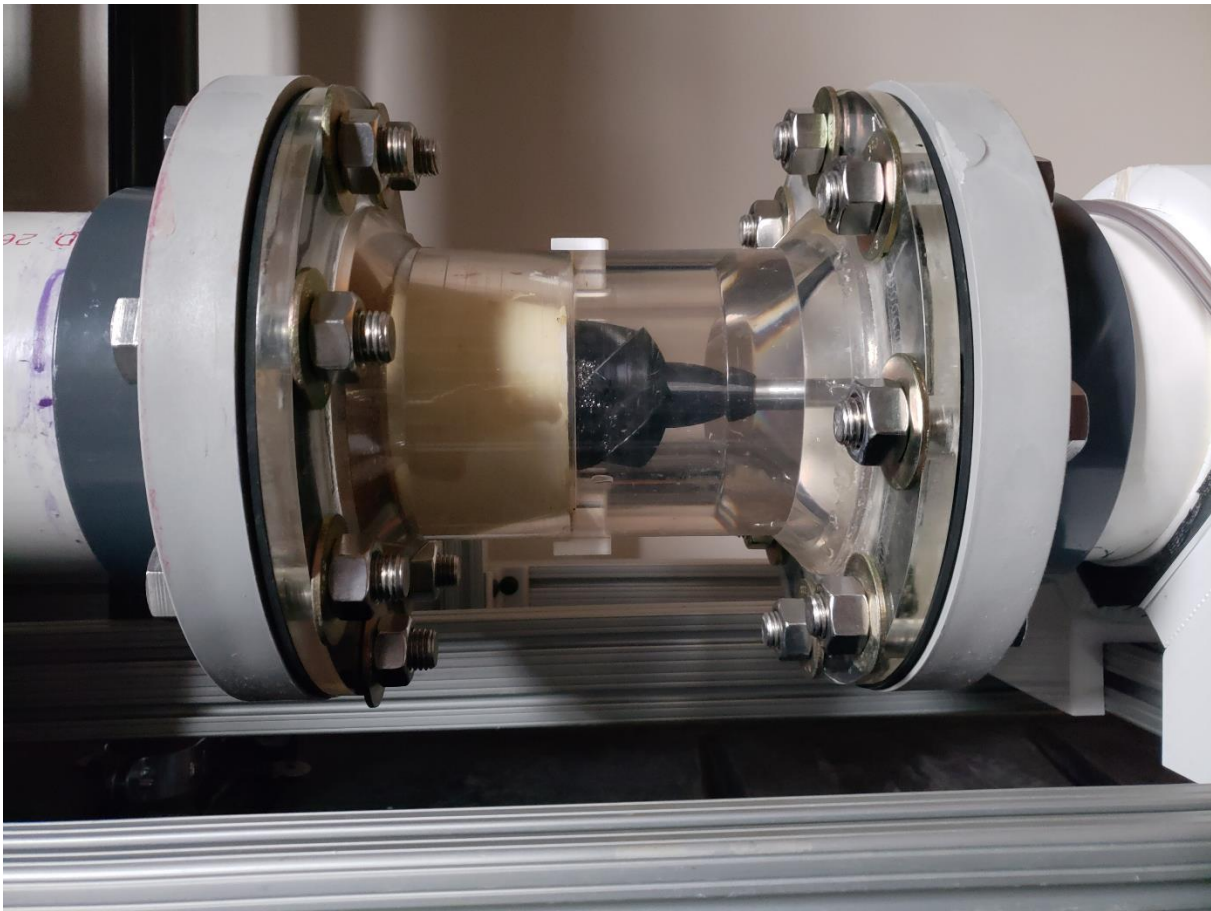
Figure 6-2: 7.5-cm turbine and transparent housing configuration for a head driven flow (from left to right)

The turbine shaft is connected to a 2.25Hp, permanent magnet, DC motor that can be turned to a generator by merely letting the shaft rotate by the effect of water flow. A voltage signal controller is wired to the motor to change the output speed (maximum free spinning= 6000 rpm). The MM501U dual-voltage single quandrant SCR drive, shown in Figure 6-3, controls 90 or 180 VDC SCR brush-type motors ranging from 1Hp through 5Hp. The core idea of having motor besides the generator is to 1) increase the speed, and 2) reverse the rotation if the normal conditions are not enough to generate the cavitation on the rotor blades.

(a)   (b)

Figure 6-3: (a) motor and (b) controller at the load side of the turbine

System pipes, turbine housing and motor are stabilized at the suggested height by a T-slot assembled table and set of supports seen in Figure 6-4. The table gives the flexibility of adding or removing of crossbars and supports whenever needed. The table length and height can be adjusted according to the length of the crossbar used. The pipe supports are shaped like V-blocks which are two angled blocks cut from 2x4 wood boards and placed on a crossbar. A threaded rod will join the two and allow for adjustment by twisting the rod. Wooden pegs at the block lower side guide the blocks along the slotted profile. One block will have a threaded insert hammered in to allow it

to be pulled when twisted. Rubber layers line the surface of each block to cushion the load. The motor is loaded on 2 Acrylic sheets cut to the casing diameter, while the base is another two sheets bolted together to dampen any vibrations.

Power transmission between the turbine shaft (3/8-inch diameter) and motor/generator (5/8-inch diameter shaft) is secured by a coupling for better efficiency and less complicated design. The metallic coupling encompasses both shafts with a threaded connection to the motor shaft at one side and a pin key to the turbine shaft at the other.
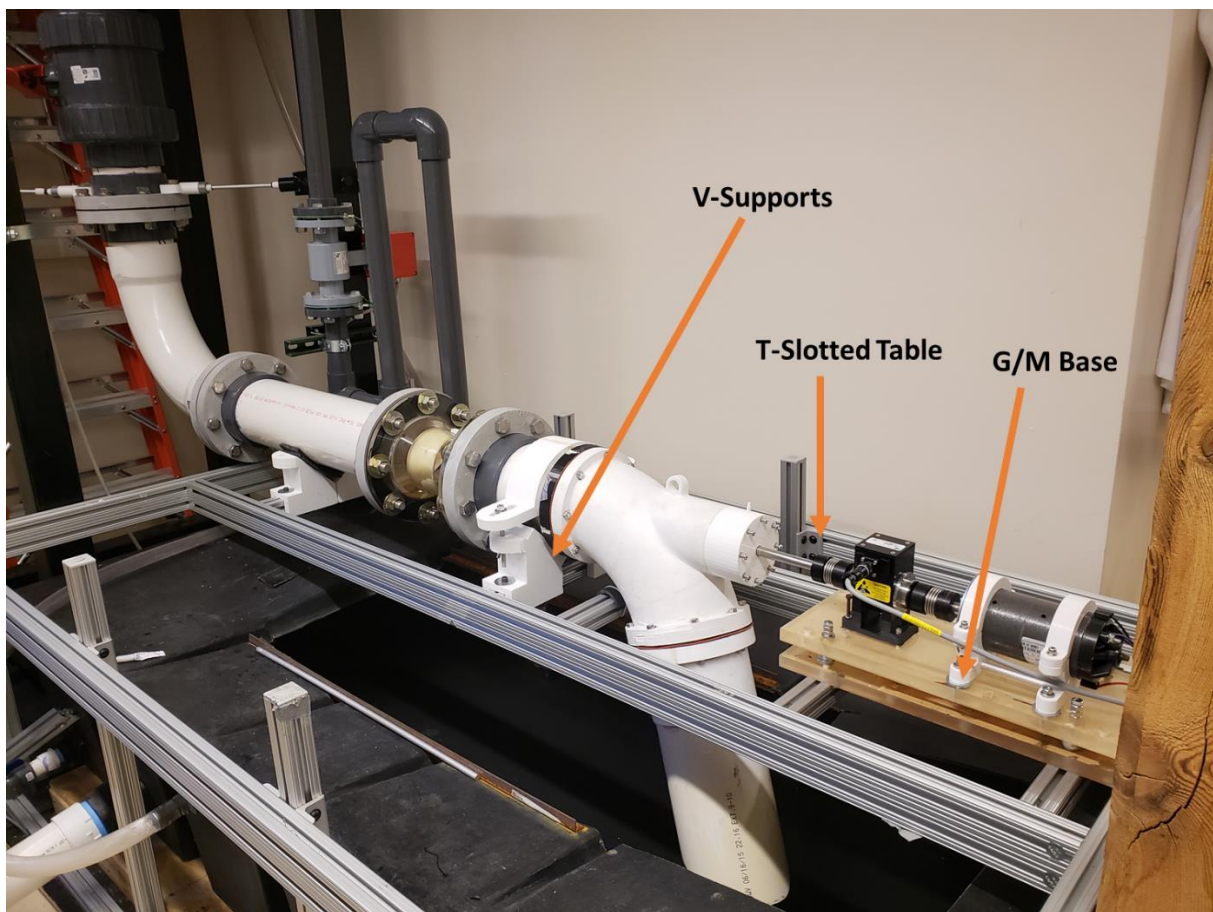
Figure 6-4: Built T-slot table and V-blocks supports

Flow is captured by a high-speed camera, so the generated video and pictures can reveal the flow behavior around the turbine under different running conditions. The camera was intended to be in a straight plane, facing the clear turbine housing with no inclination. Aperture and focal point

were always adjusted to the perfect view. The images are recorded, analyzed, and saved by Photron FASTCAM Viewer (PFV) software. 1000 W lights were placed nearby to supply the turbine with a good amount of light (Figure 6-5).

Figure 6-5: Another view for the setup camera and the 1000 W lights are in the background

6.1.2 Air Injection Addition

(A) **Housing Air Injection:** Six air injection ports were grouped in two opposing blocks (3 at each). The blocks are 3D printed using NGen (Figure 6-6), inserted in drilled holes at the two and bottom of the housing, and locked in place by a small screw (Figure 6-7). The blocks are connected by 6 hoses to an air distributor which is primarily clamped to a pressurized air supply tap (up to 80 psi). The connections arrangement of the air injection is illustrated in Figure 6-8. It is worth mentioning that the port's diameter has been enlarged 3 times (i.e. Area has increased 9 times at each injection port) to accommodate more air mass flow rate.
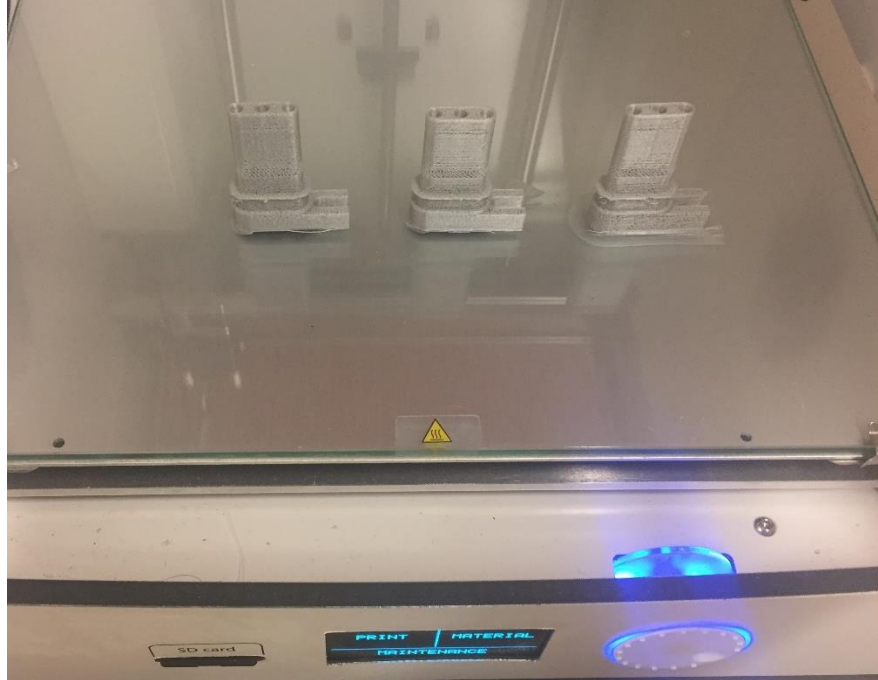
Figure 6-6: 3D printed air injection blocks
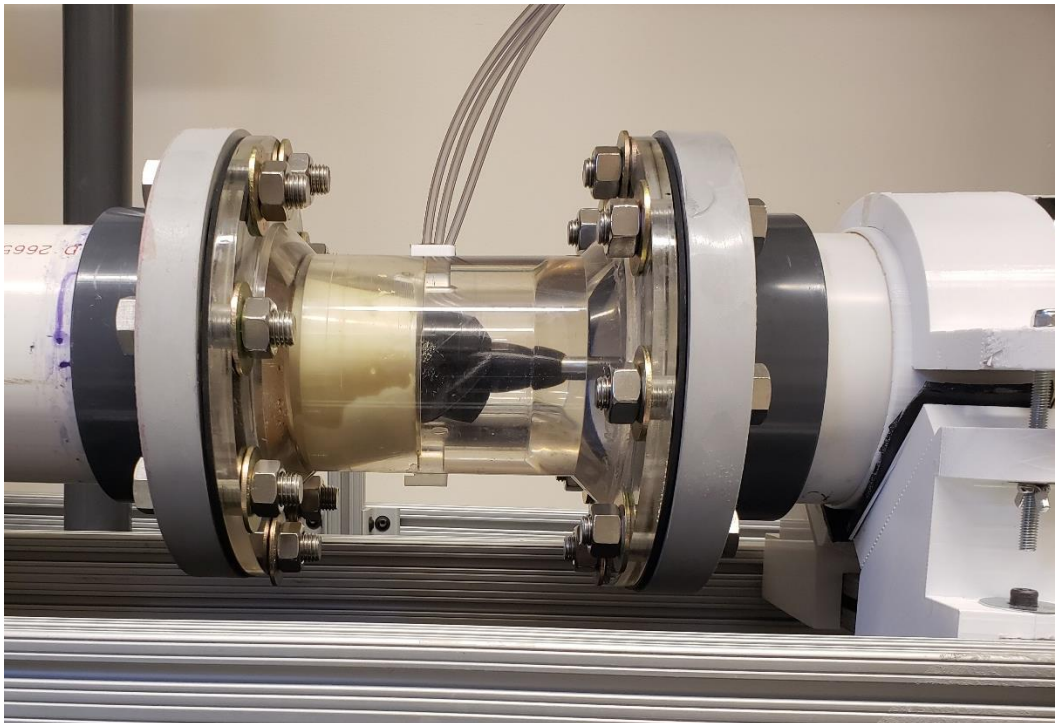
Figure 6-7: The top air injection block connected to 3 supply hoses
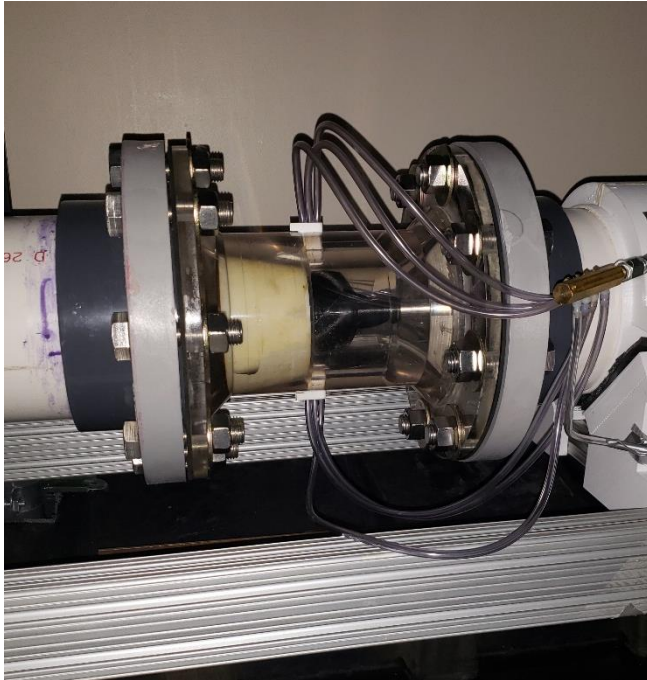
<table>
<tr><td>(a)</td><td>(b)</td></tr>
</table>

Figure 6-8: (a) Hoses of the jets connected to the distributor, (b) Distributor hose clamped to the air tap

(B) <u>Hub Air Injection:</u> In such configuration, the air goes through a central passage in the shaft ending with an internal cavity in the rotor hub. The cavity is connected to superficial holes behind the blades (four per blade) to guarantee air injection very close to the cavitation initiation areas on the blades (i.e. leading edge, intersection with hub, highest suction side curvature, and trailing edge). Air is primarily supplied from the tap to an "air chamber" which is a sealed compartment that allows air to enter the rotating shaft. Figure 6-9 is demonstrating the setup system and the new rotor design as a 3D print. The "air chamber" is 3D printed and screwed to the exit elbow, and it embraces two bearings on the two sides to have well sealing besides the free shaft rotation.
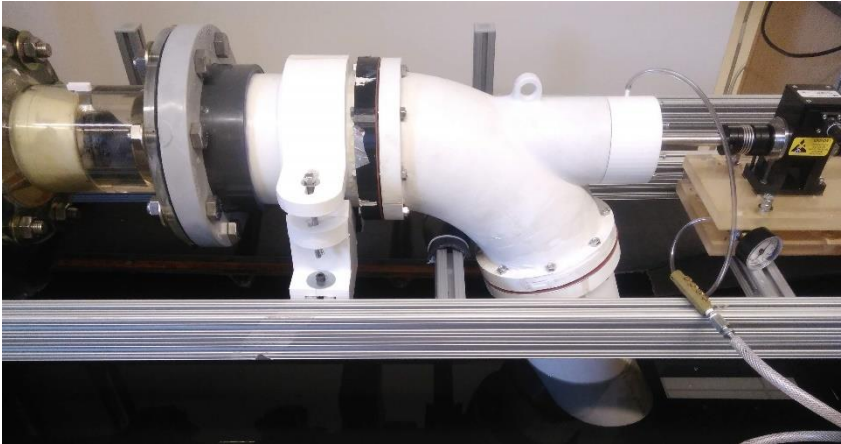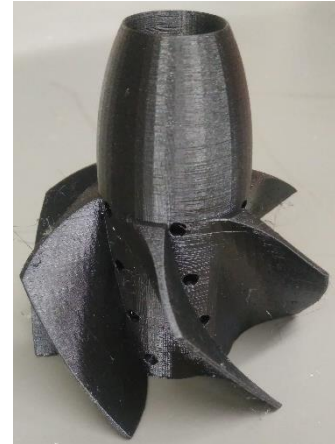
<div align="center">(a)   (b)</div>

Figure 6-9: (a) Supply air hose is connected to the "Air Chamber", (b) Distributed injection holes on the hub

6.1.3 **Measurement Procedure**

(A) <u>**Quantitative Evaluation**</u>: The procedure involves checking the conditions of inducing cavitation (e.g. flowrate controlled by the regulating valve opening and the rotation speed managed by the set load on the generator/motor). Once cavitating flow is generated, the following will be conducted:

- *Assessing the turbine performance* during a cavitation case by recording the readings of head, flowmeters, tachometer and torque meter. The case will be documented as a baseline for comparison. Figure 6-10 illustrates the measuring devices that are added lately.
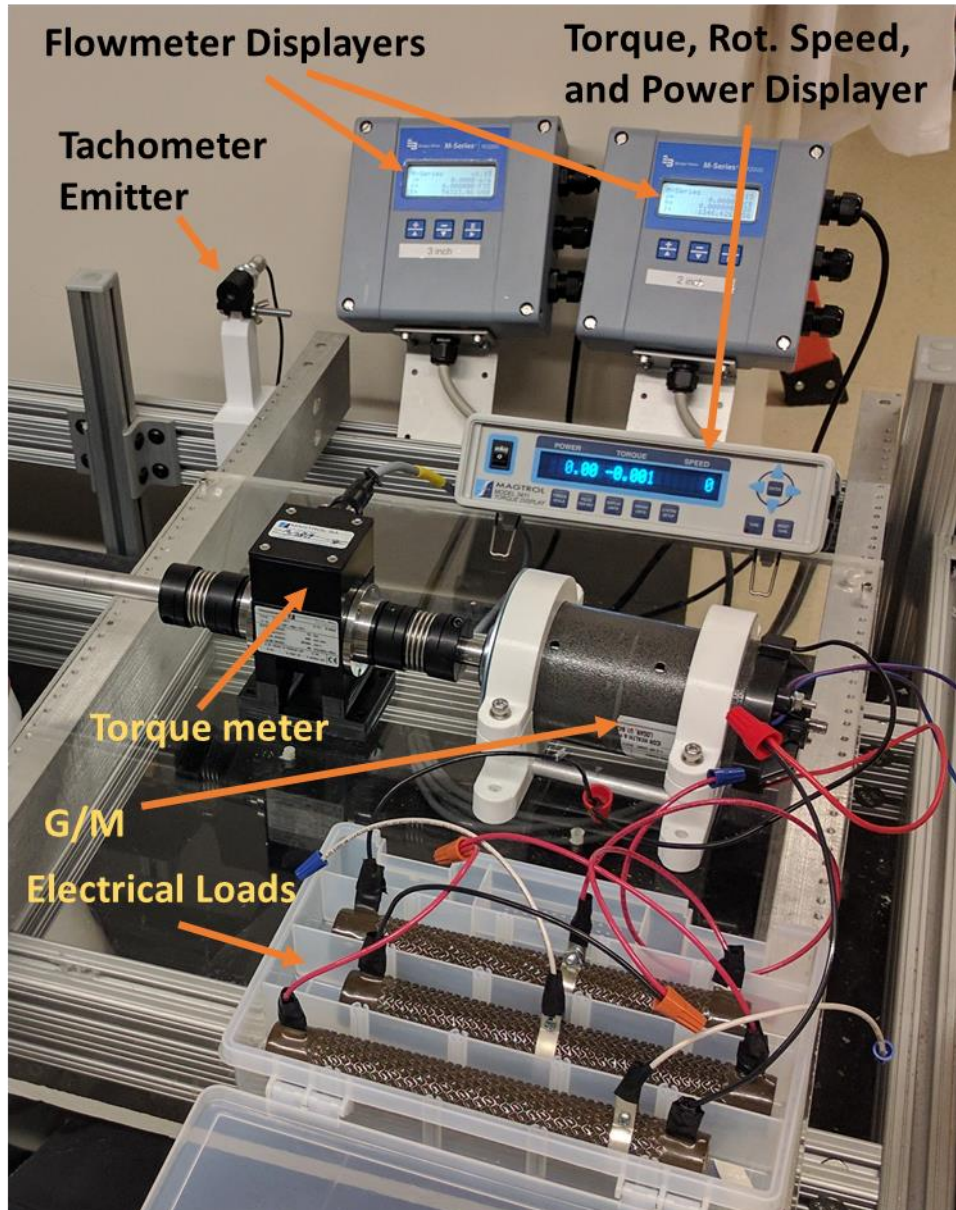
Figure 6-10: Arrangement of hydro-turbine measuring devices

- *Injecting air through 2B3P design* into the cavitating flow. With keeping the water flow rate constant, air is to be supplied with different pressures. For each case, visual imaging and rotor performance are going to be recorded. While the CFD proposed an atmospheric pressure for the air, the injection will be done on higher levels (i.e. 20.5, 41, and 82 kPa

at the supply tap) to overcome the pressure loss and the opposing centrifugal force and see the effect of the air addition into the cavitating system.

- ***Injecting air through the hub injection design*** in a similar way to the previous procedure, the pressurized air hub-injection will be made through the four holes per blade after generating the baseline case earlier.

(B) <u>**Image Processing:**</u> Additional section entails image processing for emphasized visual comparison between the experimental and the CFD works. To identify the percentage of cavitation around the turbine blades, the camera images taken where converted from grayscale images to binary images. The goal was to convert an image in such an obvious way that the cavitation is the only part of the image visible after conversion based on visual observation by the user. The first step in this process was setting up a loop to run through the entire directory of images recursively (effectively applying the same image processing to each image) and store any data taken from the images in a single matrix. From there two image processing techniques where applied, a histogram adaption and an image adjustment. To do this, the function "adapthisteq" was used. The function enhances the contrast of the grayscale image by transforming the values using contrast limited adaptive histogram equalization. Basically, this technique breaks an image into "tiles", then enhances each of the tiles contrast. The other contrast enhancement function used was 'imadjust". This function maps the intensities of the grayscale image by saturating the bottom 1% and top 1% of all pixel values, basically making the darker spots of the images darker and the lighter spots, lighter, effectively enhancing the images contrast.

From here, the image was deemed ready for conversion from grayscale to binary. The function "imbinarize" was used to do this. "Imbinarize" uses binary code to represent an image, using 1 as logical true and 0 as logical false for each pixel. To determine which threshold value should be

71

used, an iteration for values around 0.5 could be a good start, then the appropriate one is selected after some comparisons for the cavitation cloud size. Alternatively, the value chosen was 0.6 using the adaptive method. The adaptive method uses locally adaptive image threshold using local first order image statistics around each pixel to calculate the given threshold value. Once the image was converted to binary, the image was cropped to the area of interest, which was around the turbine blades and just below a glare in the image. It is important to note that the cavitation was represented as logical true (1) statements in the image.

With the image cropped around the area of interest, the total area was then determined by the size of the image in pixels. To determine the area of cavitation, the function "bwarea" was used, which gives a sum of all logical true (1) statements in the image. To determine a percentage, the area of cavitation found (in pixels) was divided by the total area of the image (in pixels) and multiplied by 100. A mean was determined by finding the average of all the percentages calculated from the recursive images of one case.

To help visualize the cavitation propagation, the same image contrast enhancement techniques were applied to a range of images. It is important to note that after 10 images, the placement of a turbine blade seemed to repeat itself, so the following colormap application only was applied to 10 images. After the image contrast was enhanced, a custom crop was applied around the turbine blades. This was accomplished using "impoly" which utilizes a draggable GUI (guided user interface) to select the area of interest in the image. From there, the area was able to be saved, and then the selected area was extracted from the image. For clarity, the selected custom crop, was cropped to get rid of an unnecessary black border outlining the image's upper and lower sided. To make the cavitation more visible, particularly so that the cavitation touching the next turbine blade, color was added to the image. Now sense the images were originally taken in grayscale it is

impossible to convert the image to a truecolor image without the aid of an artist. Therefore, a colormap or a "range of colors to represent gray values" was applied to the image using the function "ind2rgb" and "gray2ind". The specific colormap applied was a Jet colormap. The highest intensity value defined for the grayscale color was 255. Meaning that at 0, the image is black with no color and at 255, the image is white. 255 was chosen because in the typical range for a truecolor image (or RGB image) is 255 for each red, green and blue pigment in each pixel. Different values, lesser values to match the colorbar given in the CFD images, where tested but didn't make any changes as compared to using 255.

CHAPTER 7 - RESULTS

7.1 Thermal Uniformity:

7.1.1 Mathematical Relations

The temperature at a local radial point is termed as a dimensionless number called (mixture fraction, f) which relates the temperature difference between the measured point at the exit plane and the dilution jet (i.e. $T_i - T_J$) to the maximum temperature difference between the two streams ($T_{cf} - T_J$) as written in Eq. (7-1). The benefit of depending on dimensionless numbers is clarifying the ratios of the outcomes to the minimum and maximum limits of the physical domain and generalizing the investigated case to fit the scaling process to other studies.

$$f = \frac{T_i - T_J}{T_{cf} - T_J} \tag{7-1}$$

Likewise, an additional fraction is outlined by the theoretical energy balance exit temperature expressed in Eq. (7-2). Equilibrium mixing fraction, f_{eq}, mentions the ideal mixing as a fraction of the maximum temperature difference in the system (Eq. (7-3)).

$$V_{avg,cf}\, A_{cf}\, T_{avg,cf} + V_J\, A_J\, T_J = V_{avg,ex}\, A_{ex}\, T_{eq} \tag{7-2}$$

$$f_{eq} = \frac{T_{eq} - T_J}{T_{cf} - T_J} \tag{7-3}$$

Where $V_{avg,cf}$ and $V_{avg,ex}$ are mass-averaged velocities by area integral, $T_{avg,cf}$ is the energy-averaged temperature by area integral, while A_{cf}, A_J and A_{ex} are the areas of hot/crossflow, cold jet and exit ducts respectively.

Another number in Eq. (7-4) is the normalized mixture fraction, f^*, which relates the difference of measured temperature to the equilibrium state. Finally, Eq. (7-5) is used to find the

uniformity factor, x. The uniformity factor compares the proximity of the mixture to equilibrium state. Temperature profile uniformity prevails in lower x. The notion is based on the discretized integration of f^* on the radial axis.

$$f^* = \frac{f - f_{eq}}{f_{eq}} \qquad (7\text{-}4)$$

$$x = \frac{\sum(|f - f_{eq}|.dr)}{R} \qquad (7\text{-}5)$$

Total pressures are gauged at the inlets (crossflow and annular) and exit boundaries of the test section to determine the amount of drop occurring, which consequently will specify the rise in compressor/fan power consumption to keep the same level of the flow rate in a GT. Both uniformity factor and pressure drop of the tested patterns will be expressed as a percentage of baseline results (initially SH), whereas references to other comparisons will be stated later in each case. The general form of relative percentage difference is given by Eq. (7-6).

$$\%diff = \frac{\phi_{case} - \phi_{ref}}{\phi_{ref}} \times 100\% \qquad (7\text{-}6)$$

7.1.2 Graphical Representation of a Mixture

Figure 7-1 depicts the radial variation of the normalized mixture fraction, f^*, of the thermally mixed flow using SH at Re=1x10^5. The horizontal zero line (i.e. r/R axis) represents the ideal state based on the complete homogeneity of the mixture at the ideal mixture temperature (T_{eq}). Meanwhile, curves of the 7 experimental sensors and 20 monitors at the exit deviate from the ideal line due to imperfect uniformity. The main concept lies in getting as flat and close as possible to the horizontal axis to achieve better outcome from the proposed pattern. Non-uniformity is quantified by considering the absolute differences (rise or decline) at all points, and the total is

75

averaged along the radial coordinate to get the constant x. Each case is denoted by its unique uniformity number.
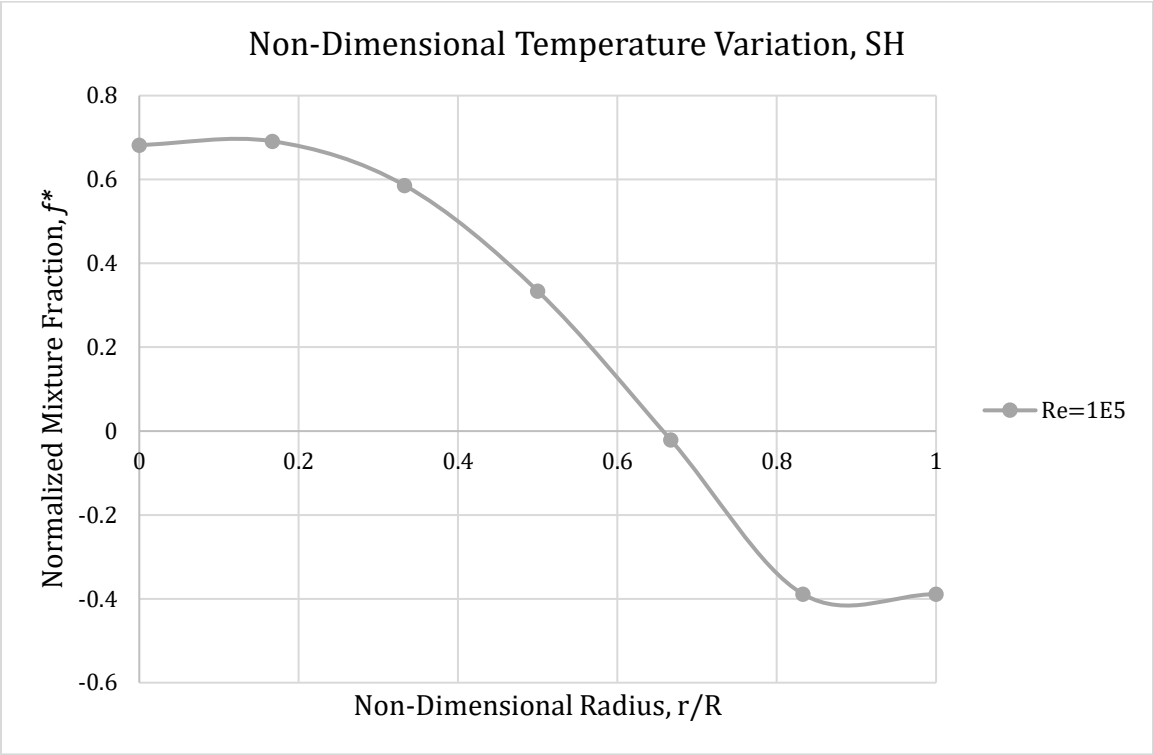
(a)
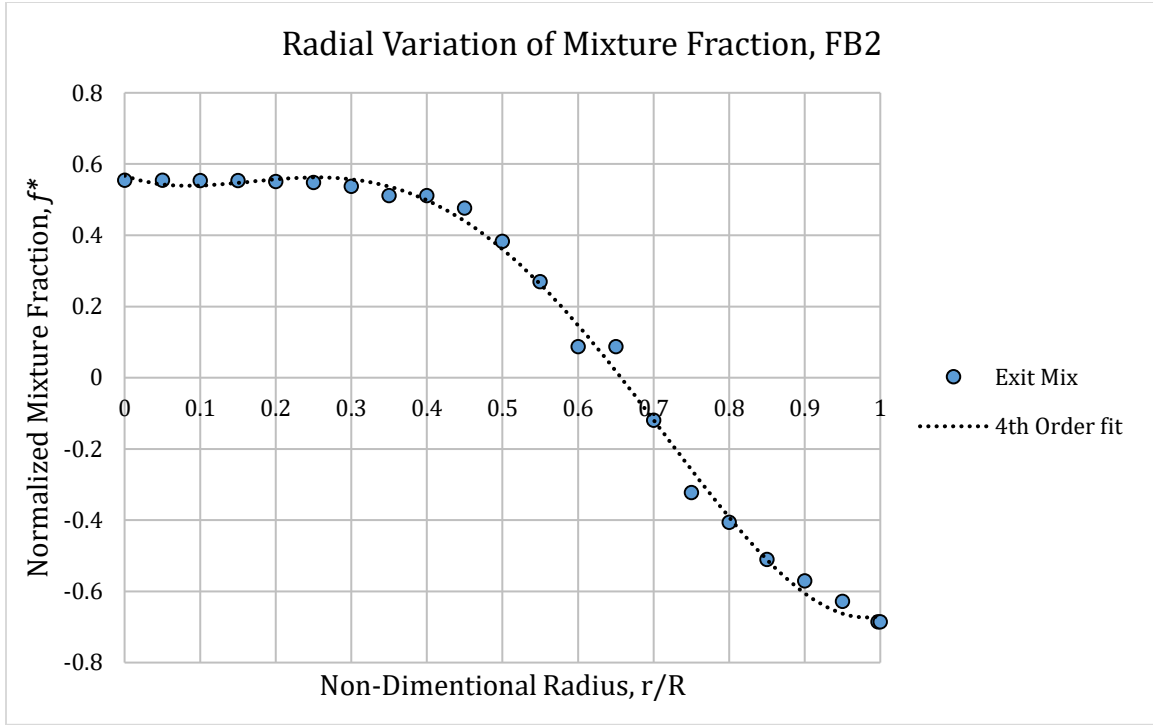
(b)

Figure 7-1: Radial Variation of the Normalized Thermal Mixture Fraction at Re=1×10^5 in (a) Experimental SH Mixer and (b) Numerical SH Mixer with plain FB2

7.1.3 **Passive Mixing Enhancers**

(A) Reynolds Number

Two Reynolds numbers are based on the velocity of the total flow before splitting to ensure the turbulence condition for each stream. In turn, Reynolds numbers after flows division are also checked according to the hydraulic diameter of the crossed duct. Table 7-1 links the two damper positions with corresponding Reynolds number before streams split. It is worth mentioning that each Re value is the average of the range calculated for all bodies.

Table 7-1: Re values related to the damper position		
Damper Angle	**0º (Fully Open)**	**45º (Half Open)**
Re	1×10^5	0.7×10^5

Effect of variable Re values at each geometrical model is seen in Figure 7-2. Both curves have temperature distortions with horizontal-axis intersections ranging between (r/R= 0.35-0.5) for Re=0.7 x10^5 and (r/R= 0.5-0.65) for Re=1 x10^5. Furthermore, all cases exhibit a similar feature of (Re=1 x10^5) superiority over (Re=0.7 x10^5) in $f*$. At the positive side, higher-Re curve has longer vertical distances from the ideal line, and a wide gap from the low-Re points. On the negative side, the opposite happens but with less difference between the two curves.

(a)

Non-Dimensional Temperature Variation, FB1

(b)

Non-Dimensional Temperature Variation, FB2

(c)

Non-Dimensional Temperature Variation, TD1

(d)

Non-Dimensional Temperature Variation, TD2
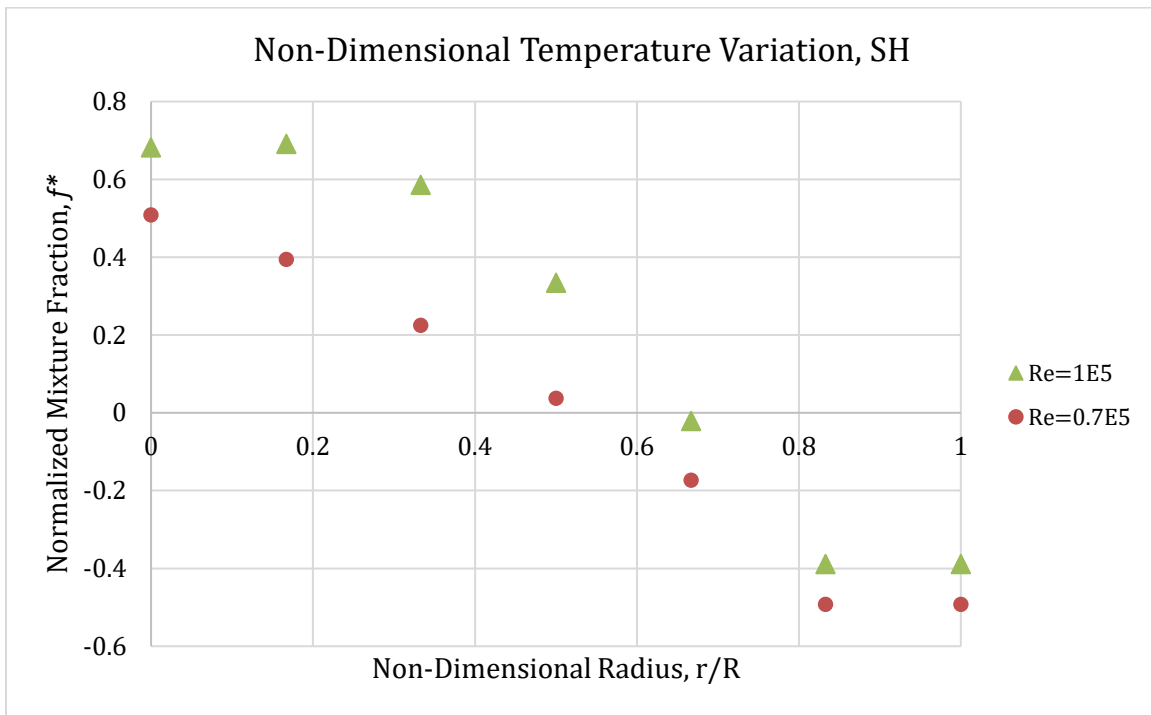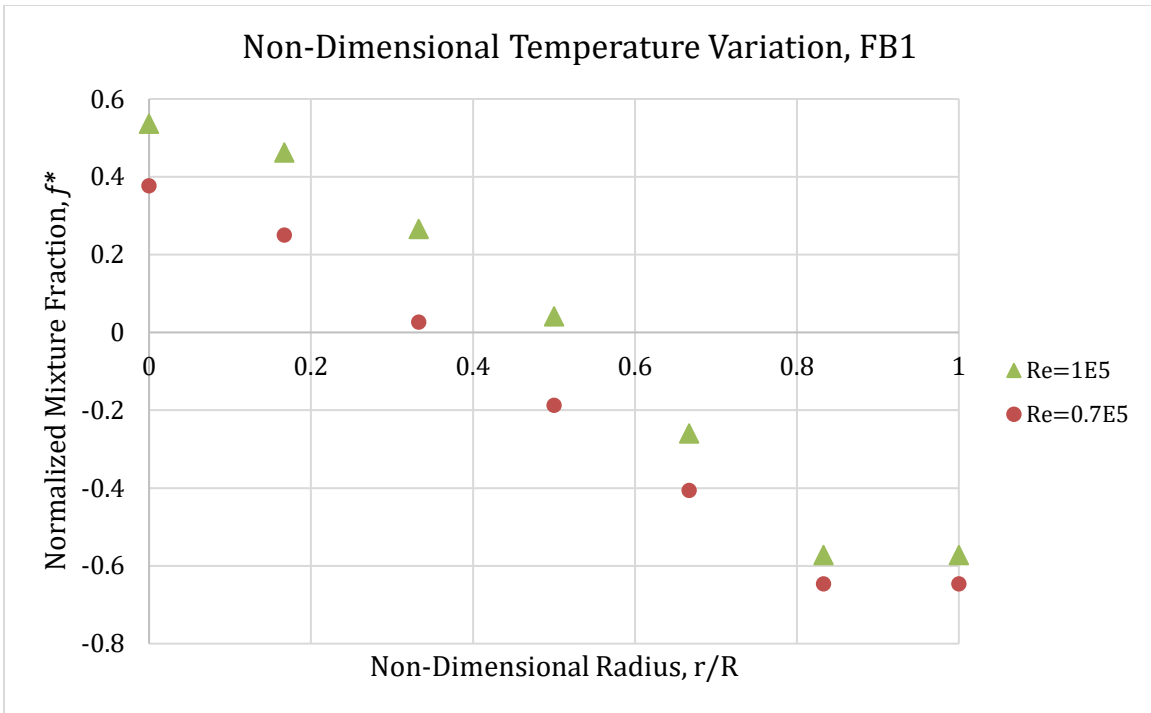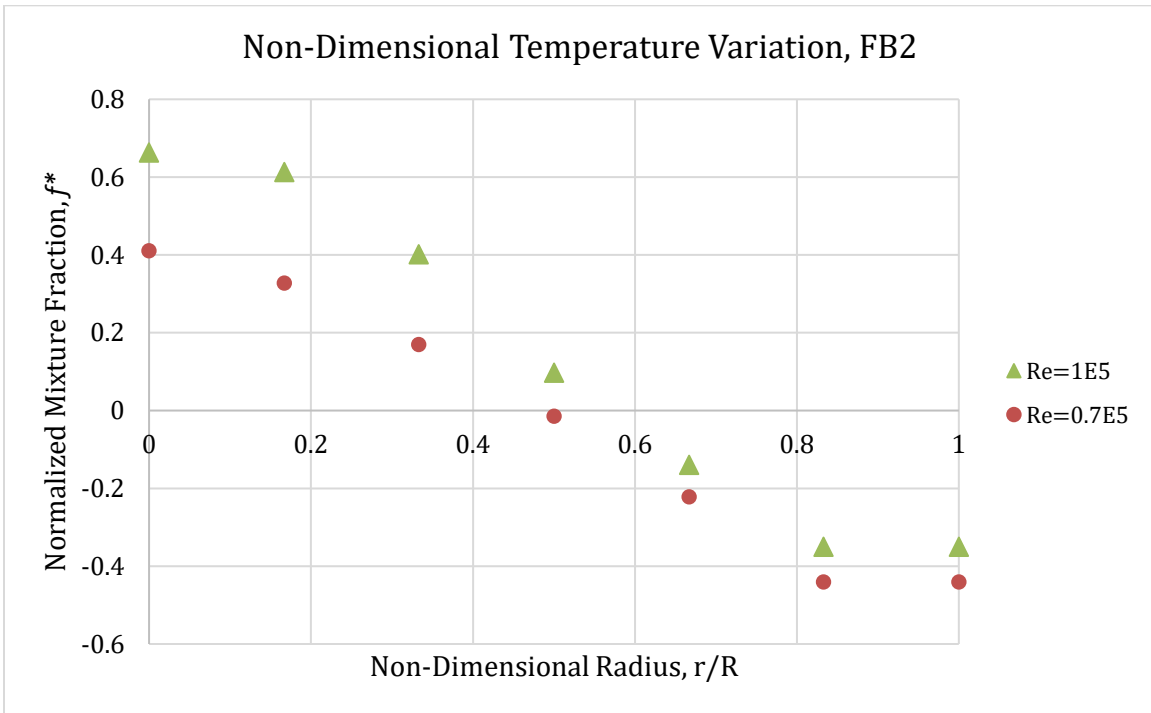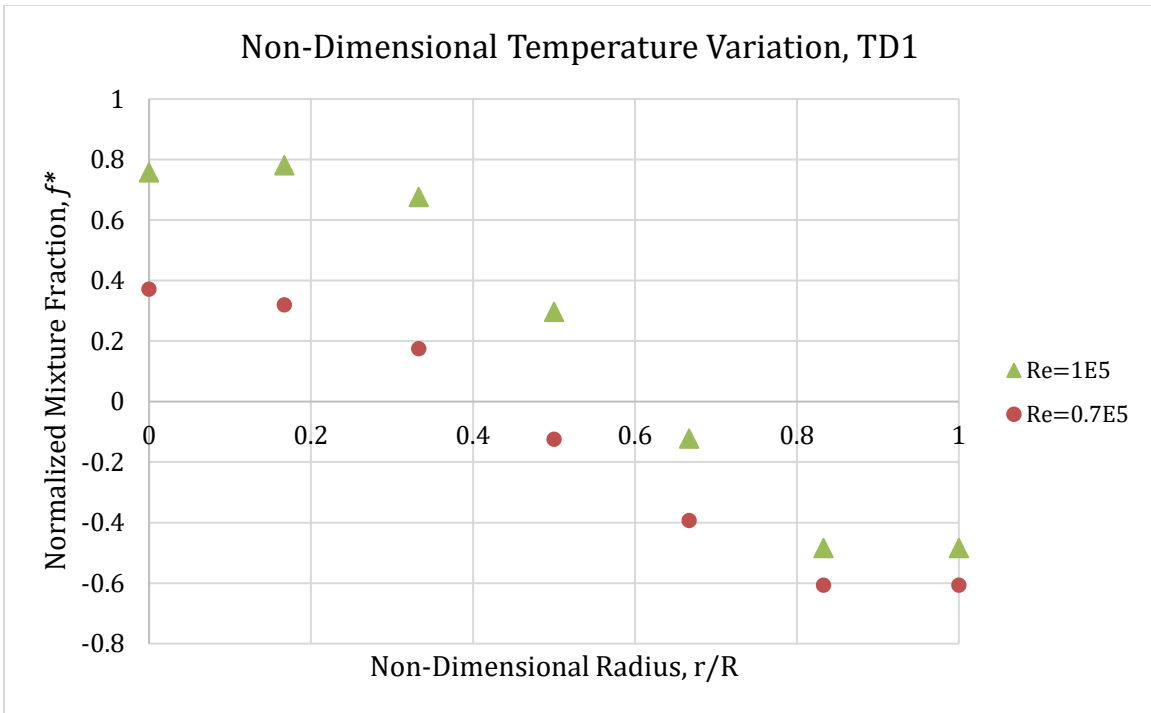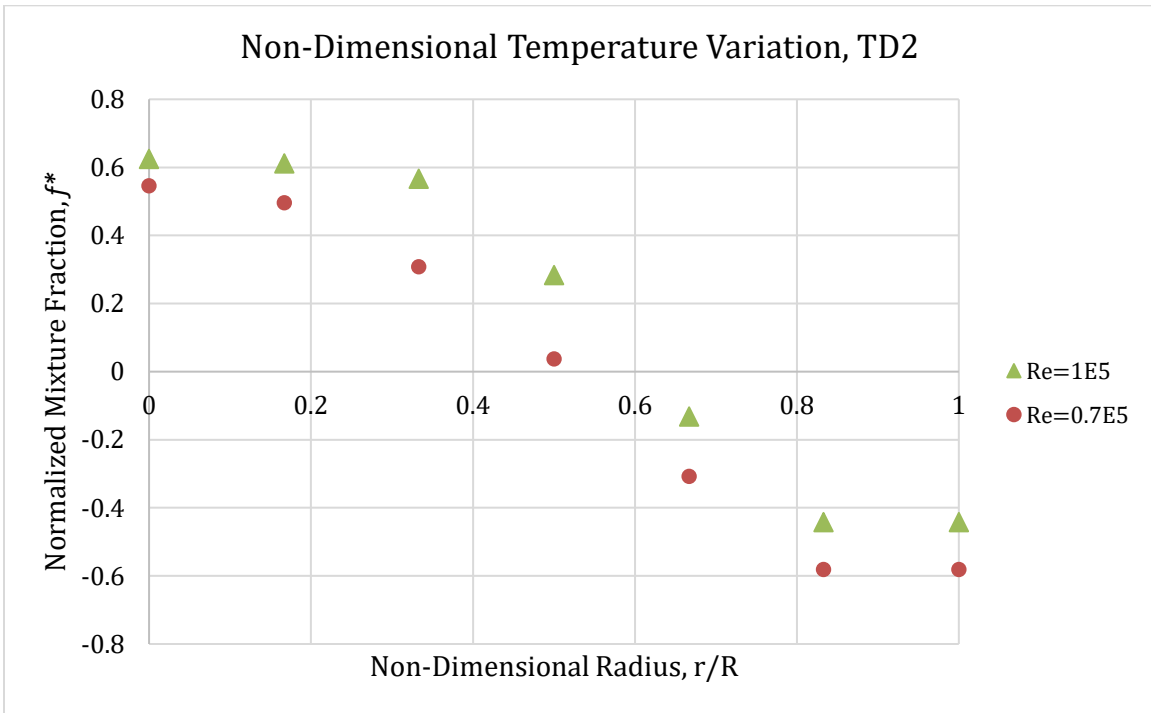
(e)

Figure 7-2: Re and dimensionless radial variations of the exit temperature: (a) SH, (b) FB1, (c) FB2, (d) TD1, (e) TD2

Uniformity number, x, describe the discrepancy between the two Re-curves for each geometrical case. Table 7-2 arranges the resulted x in rows of geometries and columns of Re. Low-Re always has low x values, which mean better and more ideal mixing. Through low-Re values indicates more heating time (from heating or combustion), it also gives crossflow (i.e. hot stream) time to interact and cool down by jets. High-Re flows are having greater sweeping motion (i.e. axial velocity, V_z) than penetrating (i.e. radial velocity, V_r), and this ratio makes the mixing nature more diffusive than dispersive, even with the existence of streamlined body.

Table 7-2: Uniformity, x, of distinct geometries at two Re

Case	Re=0.7×105	Re=1.0×105
SH	0.27	0.32
FB1	0.25	0.31
FB2	0.2	0.26
TD1	0.25	0.31
TD2	0.23	0.3

Streamlined Body Insertion

Graphical representations in Figure 7-3 and Figure 7-4 illustrate the normalized mixture factor along the radius of the exit duct for the two different Re. Some curves are not performing well like the baseline, and their corresponding x are high as it is already shown in Table 7-2. Superior effectiveness is associated to FB2 design, while TD2 has a very inferior uniformity. Possible reason is the nature of the FB and TD shapes. Generally, the slope of the TD after the maximum diameter is higher than the FB, and separation angle (measured from the stagnation point) is smaller. Having a larger separation zone, TD designs have a recirculation zone of low pressure

81

and velocity (i.e. least interaction). The result is preserving the potential core unaffected by diffusion/dispersion. A quick view at the figures below, the central part (r/R= 0, and 0.167, and 0.333) of TD1 and 2 are always at elevated f^* level than FB1 and 2 respectively.

Non-Dimensional Temperature Variation, Re=10^5
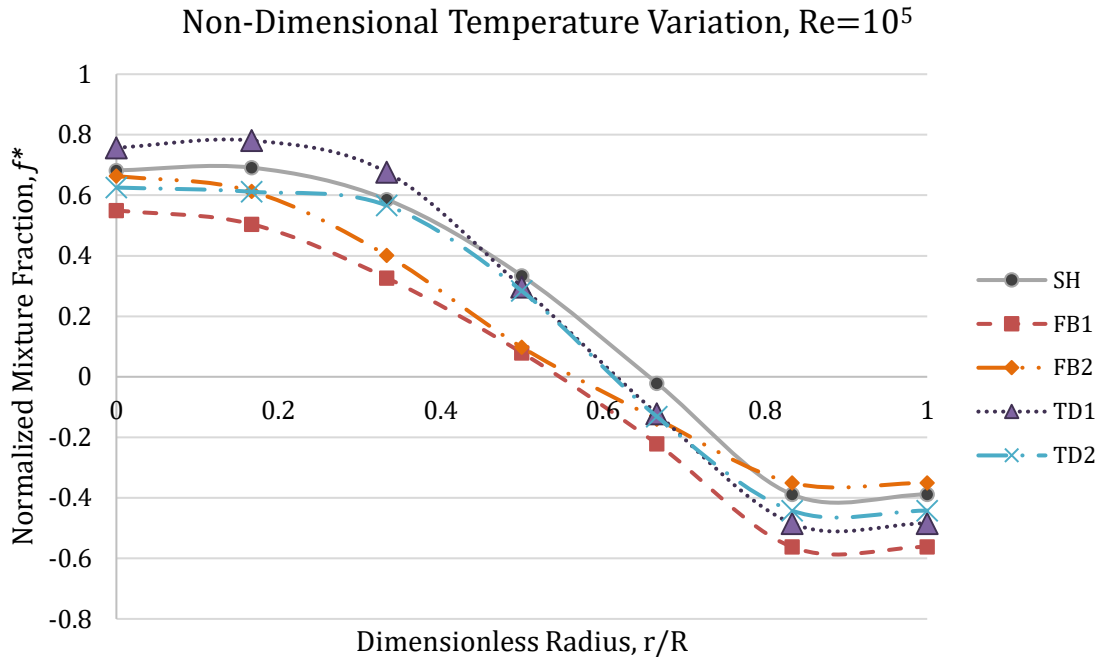
Figure 7-3: Dimensionless radial variation of temperature at exit duct (Re=1x10^5)
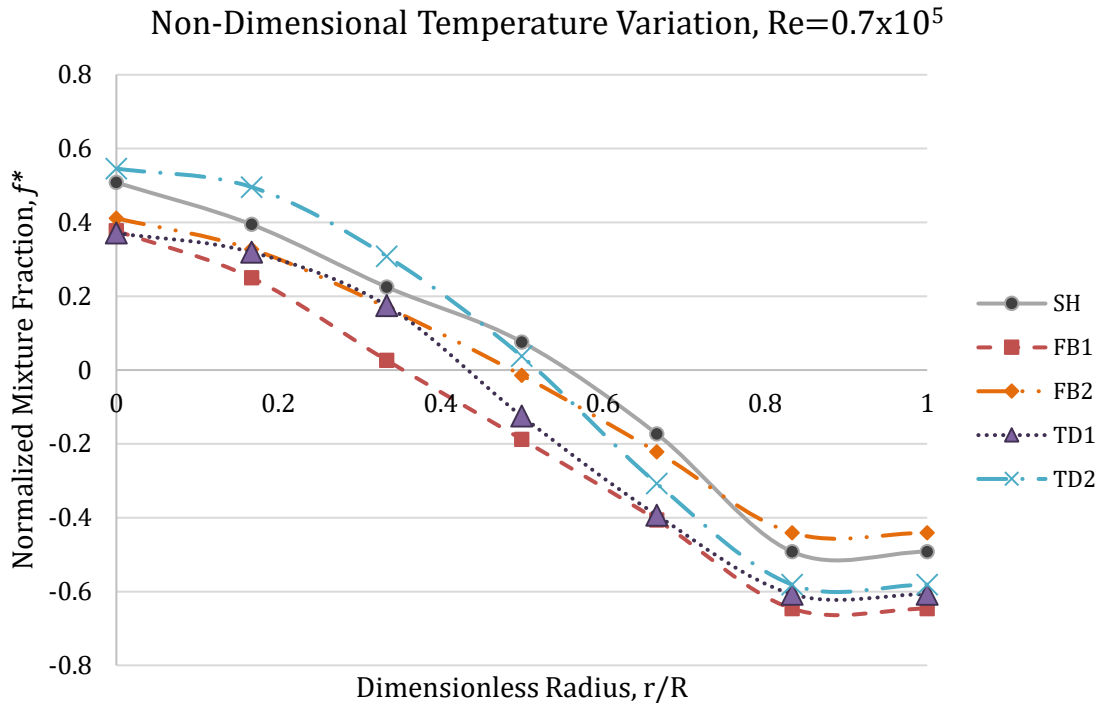
Figure 7-4: Dimensionless radial variation of temperature at exit duct (Re=0.7 x10^5)

(B) **Blockage and Aspect Ratios**

For each geometry, the following Table 7-3 and Table 7-4 are displaying the uniformity and pressure drop values of the two sizes as percentages of the reference results as stated before. Positive percent means more non-uniformity and pressure drop (i.e. bad influence). Better uniformities were attained with the two shapes (FB and TD) at the two Re values. FB2 (BR=0.49, AR=1.5) has an improved the uniformity outcome (i.e. low *x*) more than FB1 (BR=0.37, AR=2) at the two tested Re because of the continuous increase in body diameter for the same length allowing more radial movement and consequently higher chances of interaction between the streams (hot and cold). For a 32% increase in BR (based on FB1 size), FB2 uniformity was 18.8% and 25.9% better than the staggered holes at Re=1 × 10^5 and 0.7 × 10^5 respectively. The same positivity can be observed with the teardrop bodies, in which TD2 (BR=0.49, AR=1.5) was better

than TD1 (BR=0.37, AR=2) in gaining a rise in uniformity by 14.8% and 6.8% compared with SH outcomes at low and high Re respectively.

At each Re, the pressure loss is decreasing marginally with the reduction of AR (i.e. higher diameter and BR). In the meantime, high Re (more turbulent) lowers the pressure drop in the four bodies as the separation point shifts towards downstream reducing the wake region behind the bodies. Moreover, it seems that at high flow rates, cold jets apply momentum pressure over the deviated hot stream and delay the separation point that, therefore, minimize the loss.

Table 7-3: Uniformity and Pressure Loss for Football Bodies at Various Re (Bold Black for Poor Result, While Bold Red for Best Ones)

	Re= 0.7×10^5		Re= 1.0×10^5	
	FB1	FB2	FB1	FB2
x (%)	-7.4	-25.9	-7.4	-25.9
ΔP (%)	2.5	2.7	2.5	2.7

Table 7-4: Uniformity and Pressure Loss for Football Bodies at Various Re (Bold Black for Poor Result, While Bold Red for Best Ones)

	Re= 0.7×10^5		Re= 1.0×10^5	
	TD1	TD2	TD1	TD2
x (%)	-7.4	-14.8	-7.4	-14.8
ΔP (%)	2.8	4	2.8	4

(C) Profile Ratio

The four bodies have different PR, which strongly affected the results. One reason is the larger PR of football than those of cones of same AR and BR, which indicates the more existence of the solid body at the central zone of the total dilution space. Greater PR due to large diameter forces the hot stream bulks to stay closer to the cold jets and accordingly boosts mixing. Figure 7-5

represents the relation between PR and percentage increase in uniformity at Re=1x10^5; the trend is decreasing (third order polynomial) through the negative zone (i.e. more ideal). As expected, the best case (FB2) has the highest PR while the lowest output was from TD1 (PR=0.17), acquiring homogeneity ranged from 7.4% to 25.9%. For pressure (Table 7-5 and Table 7-6), and at high Re (i.e. Re =1x10^5), large PR raised the loss happening along the body for the same BR and AR. Low Re (0.7×10^5) showed a random behavior, and correlation is not clear.
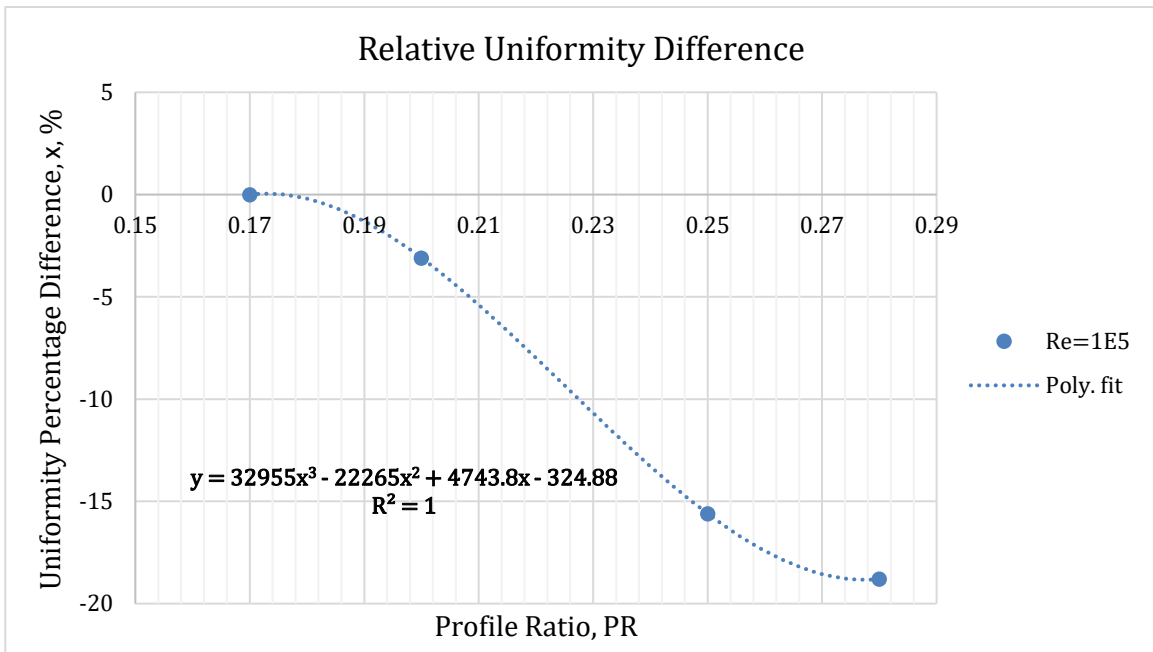
Figure 7-5: Uniformity Variation as a Function of Profile Ratio

Table 7-5: Pressure Loss Comparison at Different PR (FB1>TD1) at Same BR and AR				
	Re= 0.7 × 10^5		Re= 1 × 10^5	
	TD1	FB1	TD1	FB1
ΔP (%)	1.4	2.1	1.4	2.1

Table 7-6: Pressure Loss Comparison at Different PR (FB2>TD2) Same BR and AR

	Re= 0.7×10^5		Re= 1×10^5	
	TD2	**FB2**	**TD2**	**FB2**
ΔP (%)	2.3	2.5	2.3	2.5

7.1.4 **Central Swirlers**

(A) Mesh Independence and Validation

Different mesh refinements were explored to select the optimal mesh cell size based on the precision of outcomes and time consumption criteria. The total number of cells ranged between 2 million cells to 5 million cells for the staggered holes case (SH). Figure 7-6 shows non-significant deviation in the exit temperature curves of the different meshes. With slight change in the temperature curve of the coarse mesh (i.e. 2 million cells), an exclusion is made for calculating the averages.
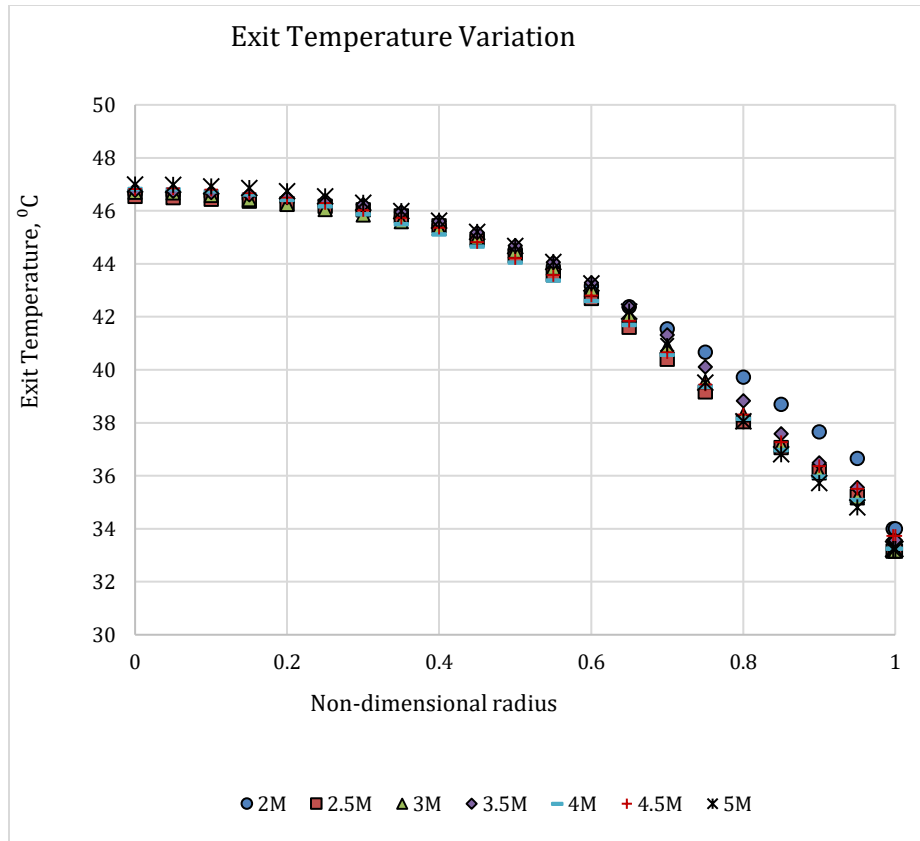
Figure 7-6 Mesh Independence Test on Exit Mix Temperature

For each mesh size, the relative differences from the averages are estimated for the uniformity and pressure drop as tabulated in Table 7-7. The values of the 3.5 million cells mesh are the closest to the average, and it is chosen based on such precision.

Table 7-7: Mesh Independence Uniformity and Pressure Loss Relative Difference

x_{avg}= 0.208, ΔP_{avg}= 109.2 Pa		
	x Relative difference (%)	ΔP Relative difference (%)
2.5M	-1.22	0.65
3M	-0.53	0.23

3.5M	0.05	-0.02
4M	-1.67	-0.33
4.5M	-2.04	-0.31
5M	5.41	-0.22

Another confirmatory stage is the validation with experimental results at same operating conditions as displayed in Figure 7-7. With an average magnitude error of 6.3%, the 3.5M numerical model predicts the mixing performance in a good way.
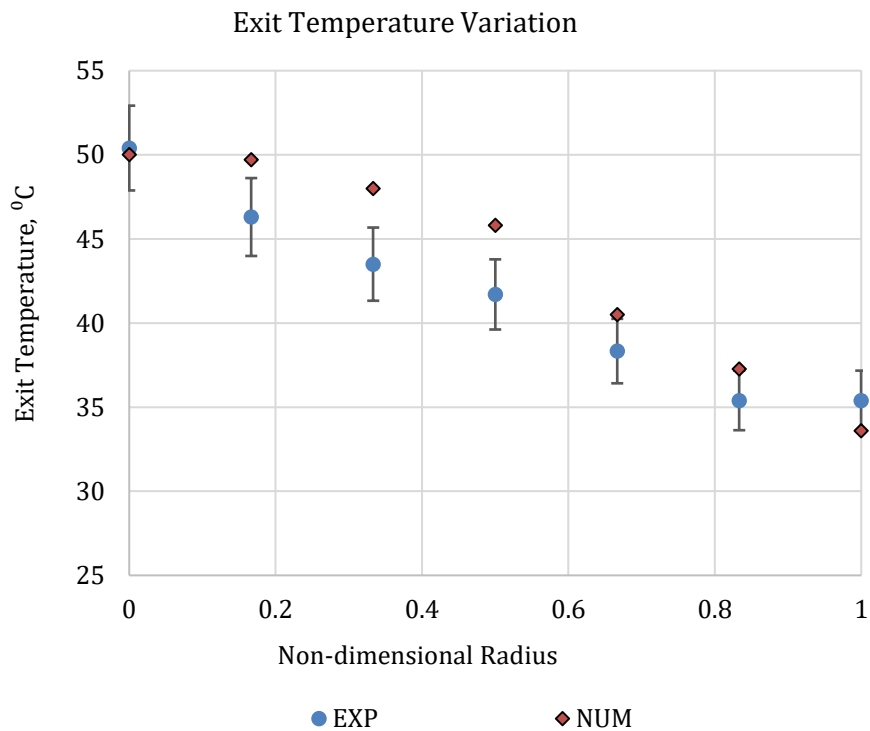
Figure 7-7: Experimental and Numerical Radial Variation of the Exit Temperature

(B) Primary Numerical Outcomes

Numerical solutions are attained and analyzed to set a recommendation for the experimental testing. Running time was 4 s which was sufficient for the exit flow properties to stabilize in all cases. Reynolds number (Re) was fixed at 10^5 in all cases due to the same inlet conditions. Momentum ratio, r, varies between 0.34 and 1.56 at the wide and smaller holes respectively. Jet height is relatively low as demonstrated in Figure 7-8 which is tracking the jets central streamlines. The jet penetration values (represented by the height perpendicular to the wall until the first bent in the central streamline) are normalized with the corresponding jet diameters d_{j1}, d_{j2}. The first jet could penetrate the cross-flow by 0.89 its diameter, while the second jet penetration height is 0.88 d_{j2}. Because of the chamber design, the downstream rows of jet and converging wall work in deforming the shape of the traveling jet. Features of JICF such as CVP and wake structures are not clear to be represented due to the abrupt change in the flow due to the injection from another row or the walls inward inclination.
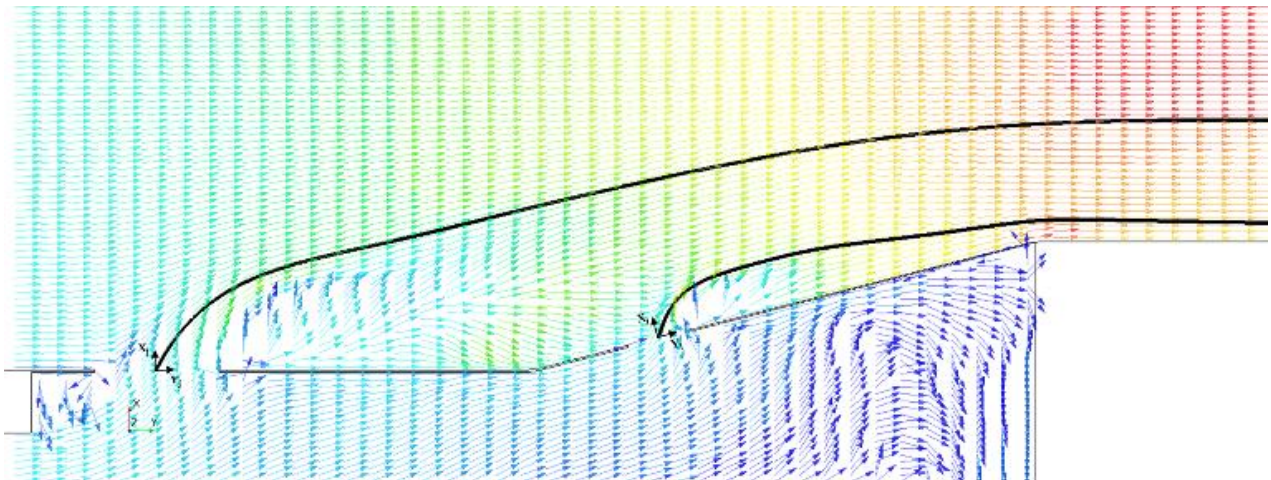
Figure 7-8: Vector Arrows Representation of JICF at low r, Jet Centerline is Graphed in Black

Figure 7-9 is a contour distribution of the radial velocity on the mid-plane after steady state. The football acts as a streamlined body which deflects the primary flow outwardly, adding radial component (V_r) to the axial velocity which helps closer interaction with the incoming jet. Due to

the opposing directions of the streams (i.e. positive radial flow around the FB, and the negative radially entering jet), the flow is counter flow thermal mixing in the radial direction. In the meantime, and rotational flow can be induced to enhance the mixing depending on the jet/main stream velocity ratio. The length of the radial interaction does not extend for longer distance after FB depending on the primary flow regime. The non-dimensional length (z^*) expressed in Eq. (7-7) shows that the interaction length is nearly 0.5 which is relatively low compared to a total pipe length of 2.53. Checking the tangential velocity, no substantial magnitude is induced by the FB due to the absence of external forces towards this component (i.e. swirlers). In the other designs, these two velocity components will be changed clearly, and they will play important role in enhancing the mixing process.

$$z^* = \frac{z - z_0}{d_e} \qquad (7\text{-}7)$$

Where z is the arbitrary axial distance, z_0 is the nominal distance of the exit pipe entrance from the universal system origin= 0.2 m, and d_e is the exit pipe diameter.

(a)

Radial Velocity (m/s)

| −8.0 | −6.0 | −4.0 | −2.0 | 0.00 | 2.0 |
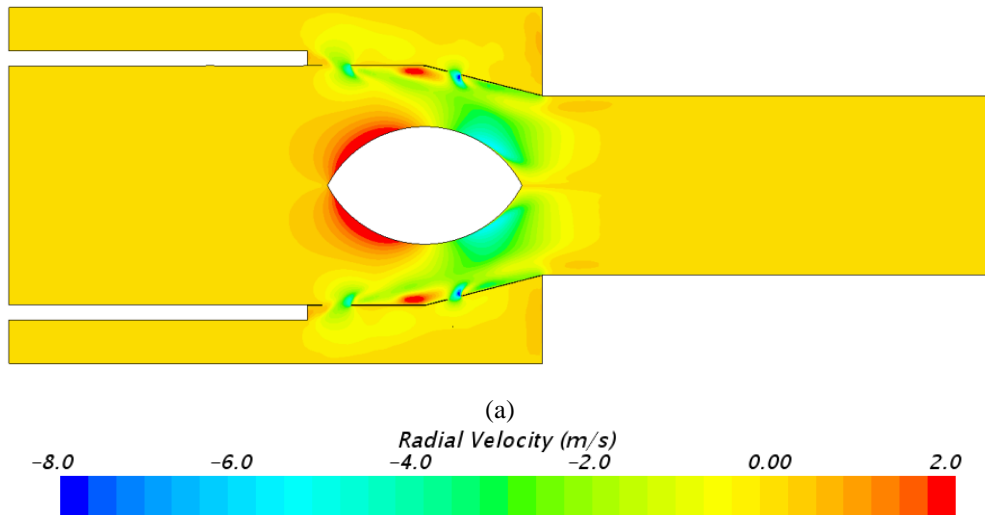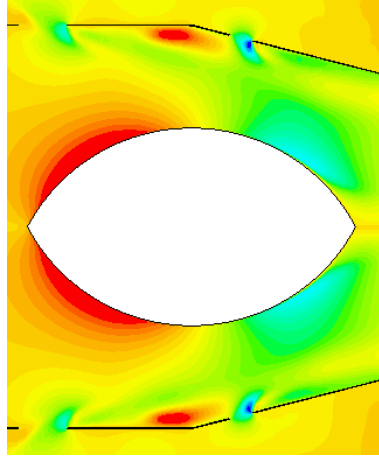
(b)

Figure 7-9: Steady State Radial Velocity Contours in the a) Whole System and the b) Mixing Chamber

(C) Swirlers Effect

As aforementioned, cases are characterized by different temperature output distribution resulting in sole uniformity profile and number. Final results are listed in Table 7-8 showing the calculated x and a relative change Δx % to the value of the plain football which is considered as a baseline. Negative numeric labeled in red bold font refers to better uniformity at the exit because of the suggested design.

Table 7-8: Uniformity Values of Different Geometries

Case	FB	F4SR	F4TR	F8SR	F8TR	F4SA	F4TA
x	0.25	0.21	0.12	0.15	0.08	0.23	0.13
Δx %	0.0	**-16**	**-48**	**-40**	**-68**	**-8**	**-48**

All 6 six cases of swirlers are exhibiting better mixing conditions. Installed swirlers worked on generating extra velocity component in the theta component (V_θ) which makes swirls perpendicular to the axial flow, transferring the divided bulks of the hot flow (depending on the

91

number of swirlers) into the jet. These passive curved protrusions boost the momentum mixing caused by turbulence. One cost can be detected is the pressure loss (ΔP) which is calculated by the subtraction of the exit total pressure from total pressure at the two inlets. The ΔP and $\Delta P\%$ values can be seen in Table 7-9, where positive values in black bold font expresses higher drop in pressure. Worst case of pressure loss was F8TR which resulted in more loss than FB by 54%, while the best after swirler design was F4SR with only 17% relative pressure difference from FB.

Table 7-9: Pressure Drop Values of Different Geometries

Case	FB	F4SR	F4TR	F8SR	F8TR	F4SA	F4TA
ΔP (Pa)	98	114.7	135.1	126.3	150.9	112	131.8
ΔP %	0	**17.1**	**37.9**	**28.9**	**54.1**	**14.4**	**34.5**

Unlike FB, all cases of swirling fins exhibited radial and tangential components in around the streamlined bodies, and these velocities kept existing with noticeable magnitudes after the mixing section until the outlet of the exit pipe ($z^*_{exit}=2.53$).

(D) Swirler Shape

Two shapes were compared, rectangular and airfoil geometries and the uniformity factor was evaluated to determine the superiority of the variable thickness fin over the constant one. Rectangular swirler acted on directing the flow to one direction, forming a particular pattern of swirl, unlike the airfoil fins which smoothly converges and diverges the passing flow leading to several swirling configurations in the mixing chamber. Figure 7-10 illustrates the difference in f^* of cases (F4SR and F4SA) and (F4TR and F4TA) with the consideration of concurrency of other parameters (number of fins and their height). At part (a), the dashes line (i.e. short rectangular swirlers) are closer to the idealism line at the hot (upper) and cold (lower) sides than the dotted

line (i.e. short airfoil swirlers). The resultant uniformity numbers expressed the superiority of F4SR (0.21 vs 0.23 respectively). By doubling the swirler height, part (b), the thermal uniformity curves of the two designs are trending similarly. On checking x, F4TR and F4TA give 92.3% alike values (0.12 vs 0.13 respectively).

(a)
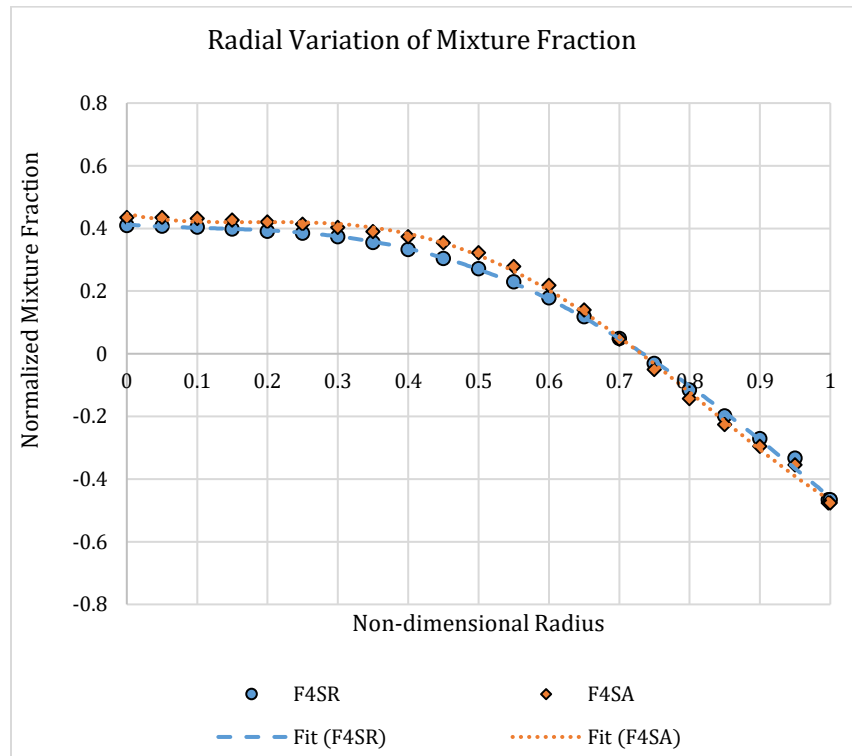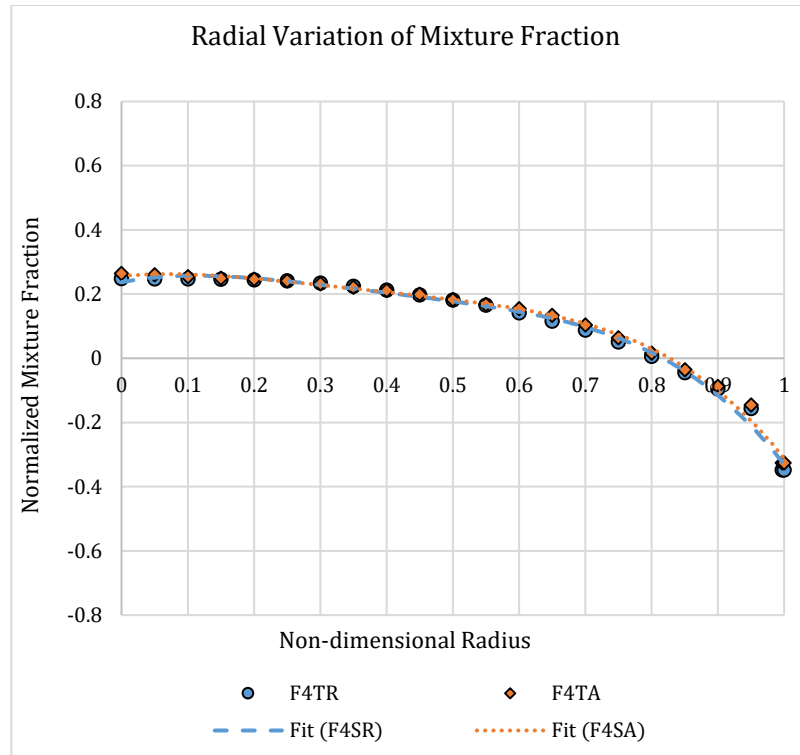
Figure 7-10: Radial Variation of the Normalized Thermal Mixture Fraction in Mixer with (a) F4SR vs. F4SA, and (b) F4TR vs. F4TA

Figuring out the developed velocity vector at the exit pipe after the mixing chamber, radial and tangential velocities appear as another two velocity components with the constant axial one. Figure 7-11 is focusing on the trend of the two generated velocity components (expressed as a non-dimensional percentage of the axial velocity) along the non-dimensional length of the exit pipe (z^*) due to the four short rectangular and airfoil swirlers. These velocities (V_θ and V_r) are relatively low with the magnitude of axial velocity (V_a). The tangential velocity is more dominant axially than the radial (4.5 and 9 times on average of short and tall swirlers respectively).

F4SR is having higher values for the entrance tangential velocities than F4SA, leading to the idea of the increased mixing momentum. By applying Eq. (7-8) for line integrating the absolute values along z^*, F4SR generates more tangential velocity than F4SA by 2%. The other graph,

Figure 7-12, shows a variation, especially at the tangential velocity, but with no clear superiority in the magnitude. It is calculated that F4TR has higher radial and tangential velocity magnitudes with 6.8% and 7.2% differences. This could give the reason of the better uniformity number for the rectangular swirlers.

$$\emptyset_{Linear\ Average} = \frac{\int_0^{z^*_{exit}} |\emptyset|\ dz^*}{z^*_{exit} - 0} \tag{7-8}$$

(a)
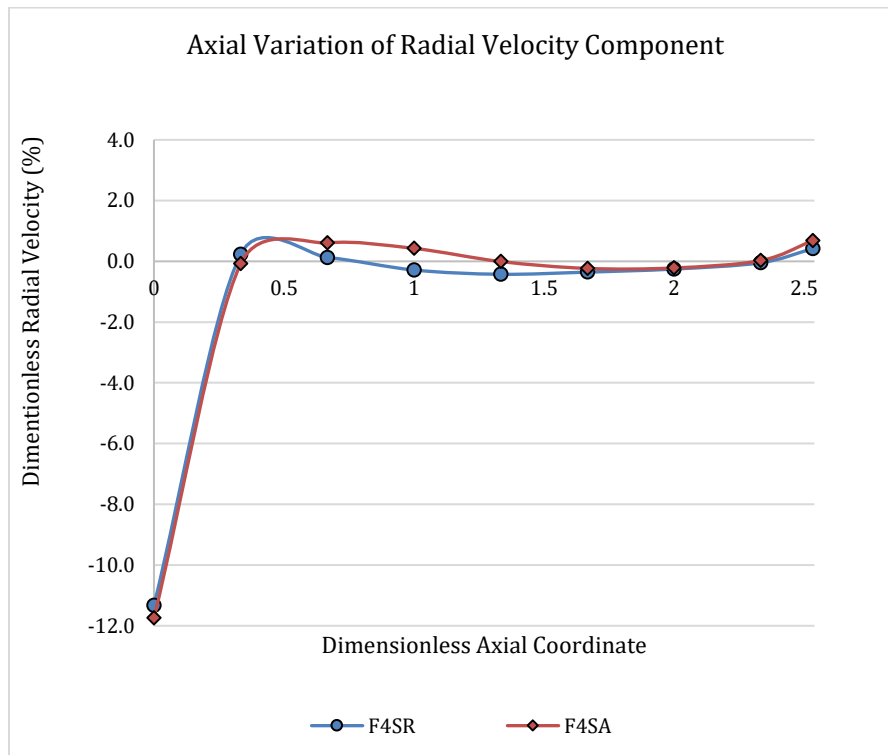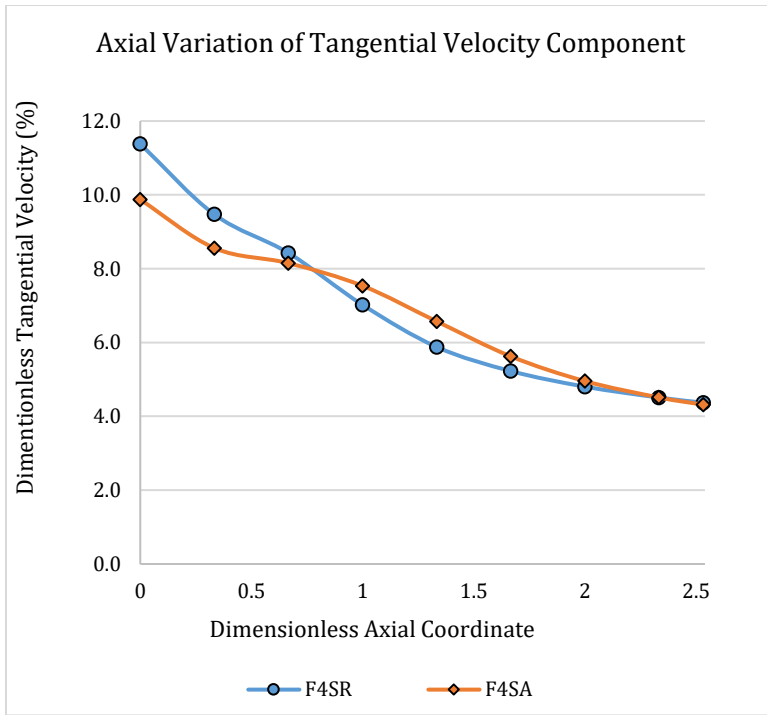
Figure 7-11: (a) Radial and (b) Tangential Velocities Variation along the Exit Pipe for F4SA and F4SR Cases
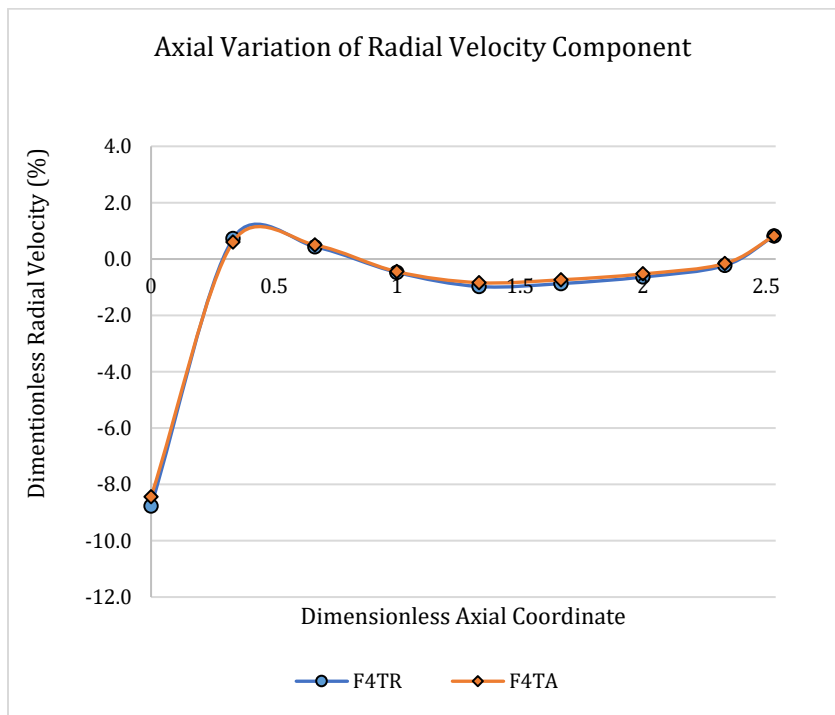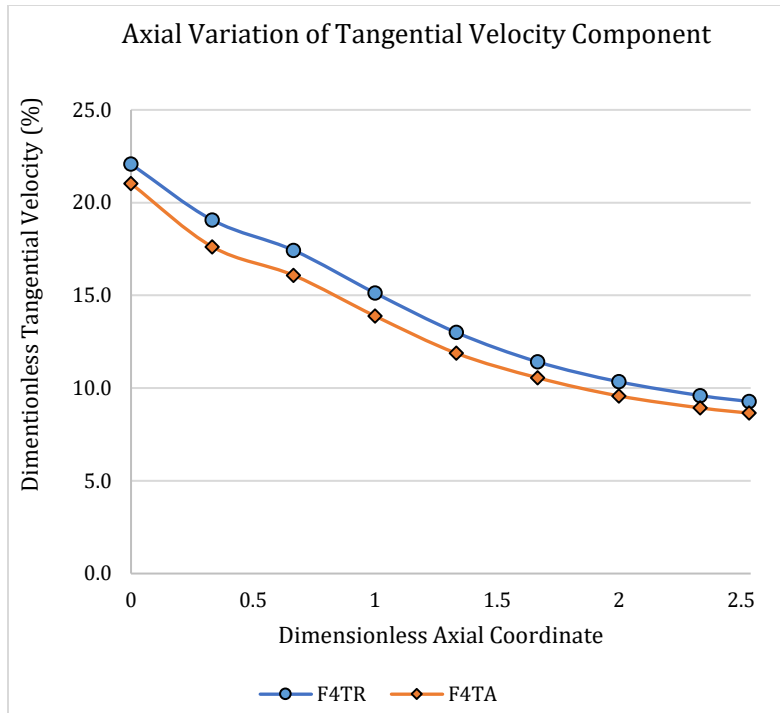
Figure 7-12: (a) Radial and (b) Tangential Velocities Variation along the Exit Pipe for F4TA and F4TR Cases

(E) Swirlers Height

From Table 7-8, and when comparing x of the short to tall swirlers, all the cases prove that taller swirlers can control the mixing in an optimal way. Larger amount of hot stream is divided by the tall fins and starts swirling in the chamber allowing better dispersion in the annular space around the central vortex. For showing, F4TR is 42.8% more uniform than F4SR, while F8TR has 46.7% uniformity than F8SR, and finally F4TA improves the performance of F4SA by 43.5%. Looking at the sub-graphs of Figure 7-13, short swirlers are performing in a similar but better way to FB, unlike the ones with taller fins which have closer thermal distribution to the ideal mixture in most of the radial range.

(a)

(b)

98
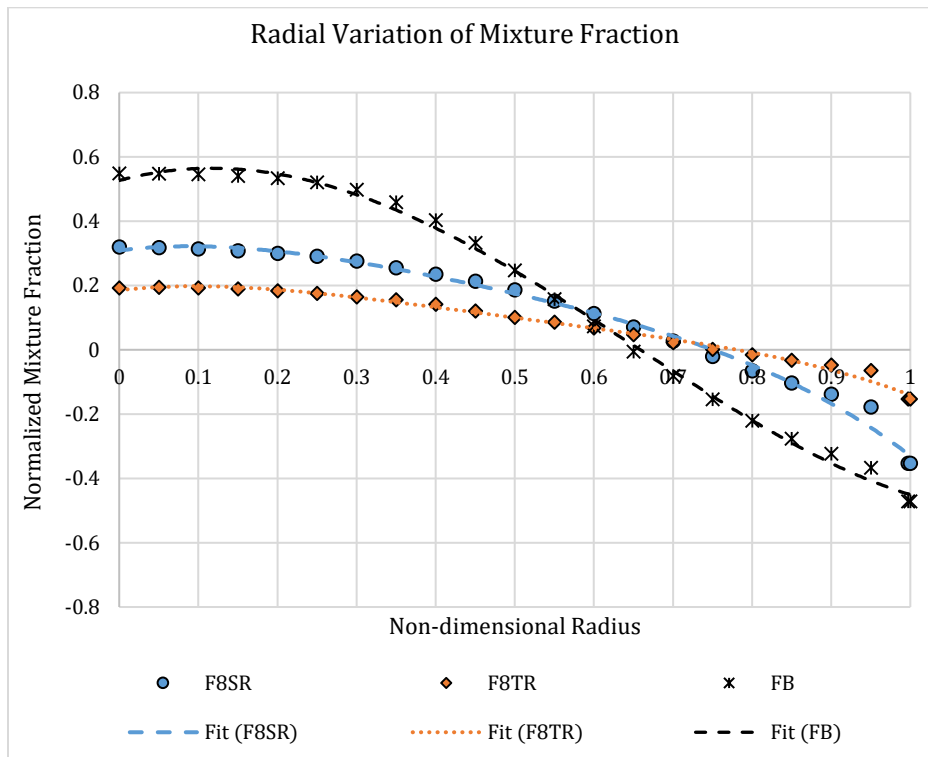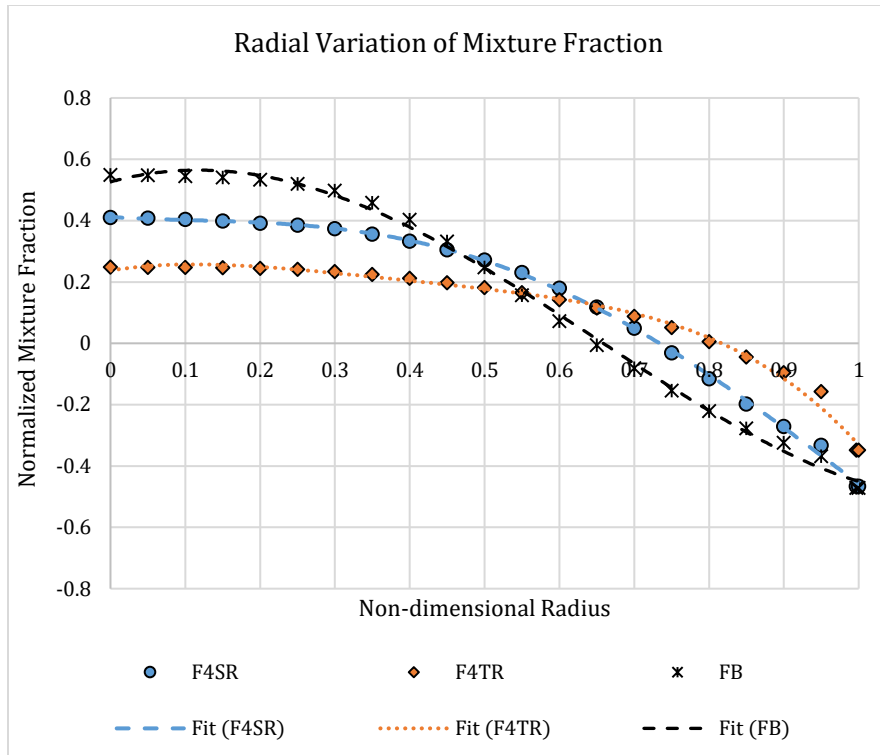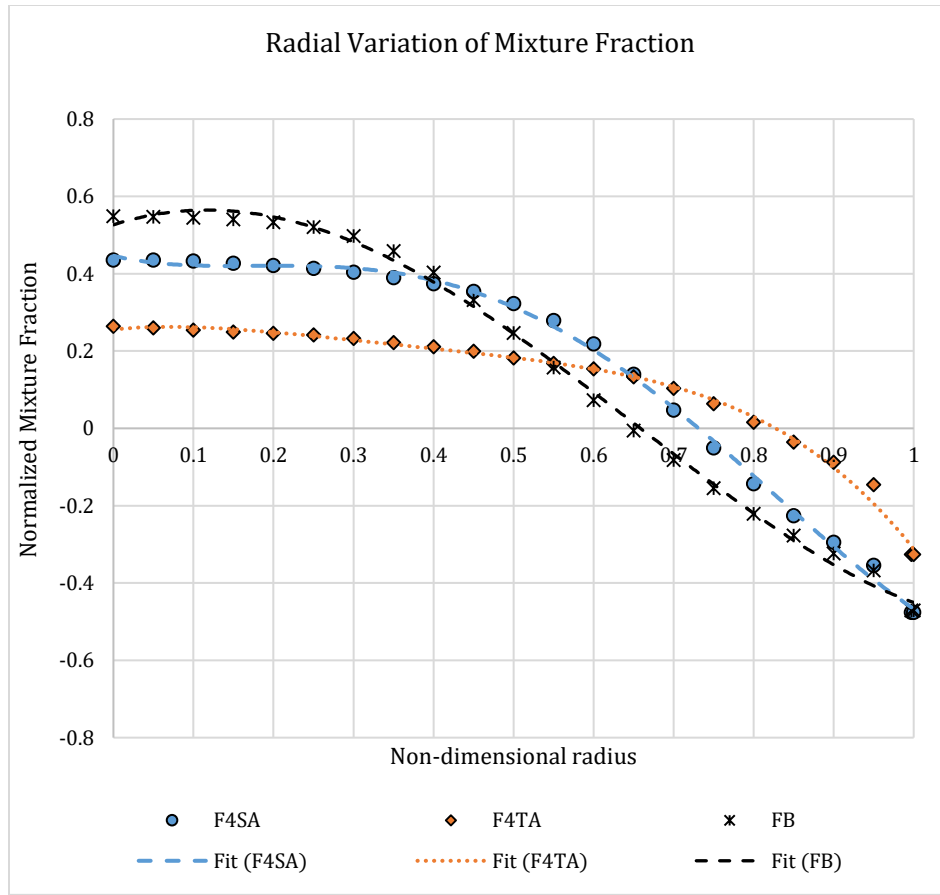
Figure 7-13: Radial Variation of the Normalized Thermal Mixture Fraction in cases: (a) FB-F4SR-F4TR, (b) FB-F8SR-F8TR, and (c) FB-F4SA-F4TA

Analyzing the temperature contours at the exit pipe, the core of hot stream can be tracked to its end to determine the extent of the thermal mixing of each pattern. Figure 7-14 is comparing between the end length of the hot flow thermal core in each pair of short and tall geometries (a) 4 rectangular, (b) 8 rectangular, and (c) airfoil. Generalizing by non-dimensionalizing, the temperatures are represented by the dimensionless mixture fraction (f), while the hot core end lengths are expressed in terms of z^* to relate them to the exit pipe dimensions. It is seen that for each pair, z^* of the hot core in the short swirler case extends longer than its peer with the taller swirler. For the record, F4SR, F8SR, and F4SA have longer core than F4TR, F8TR, and F4TA by

54.4%, 16.2%, and 61.2% respectively. The longer the core, the less thermal mixing between the central hot and the inwardly injected cold streams.
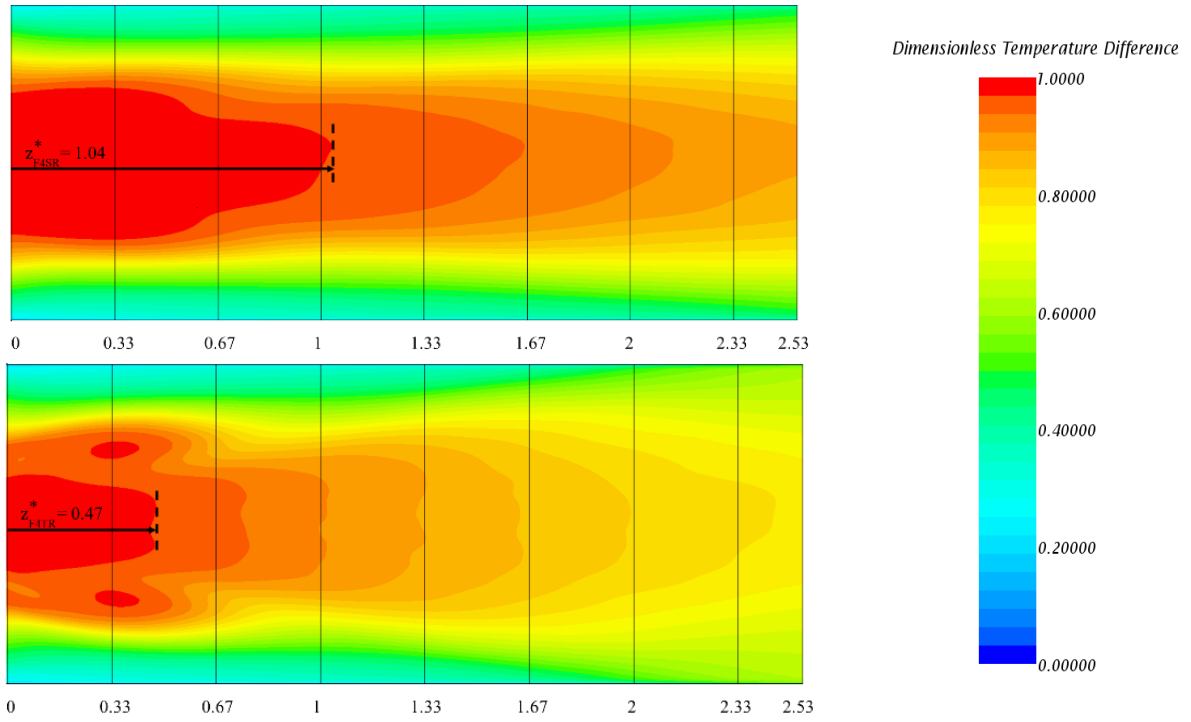
(a)
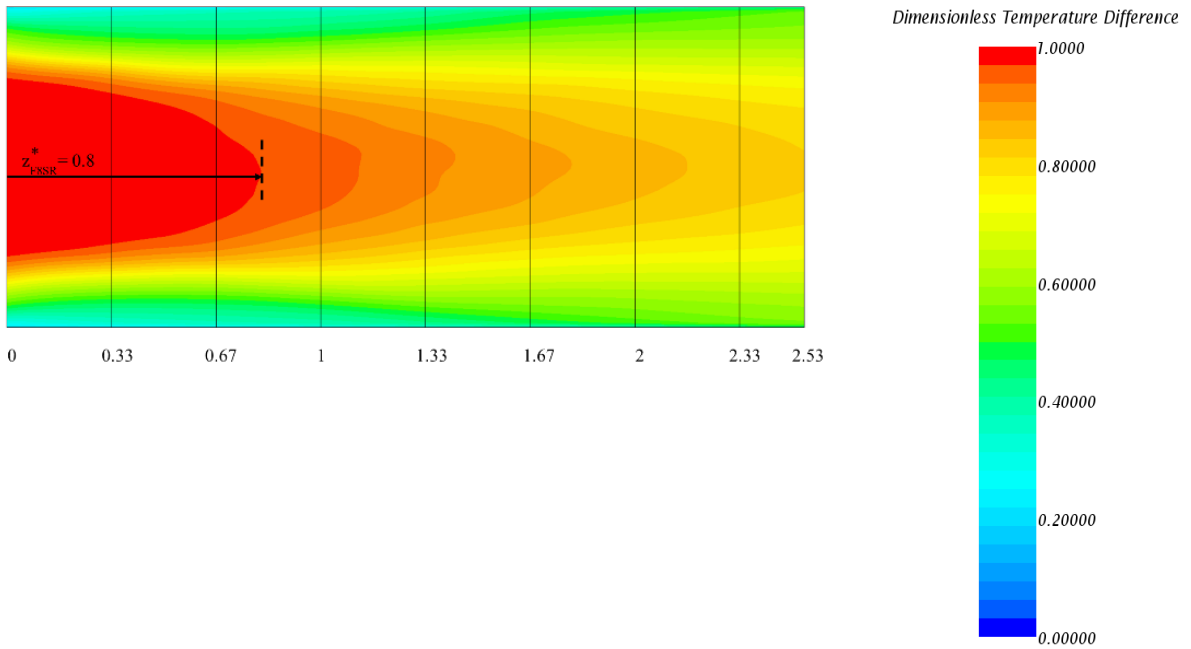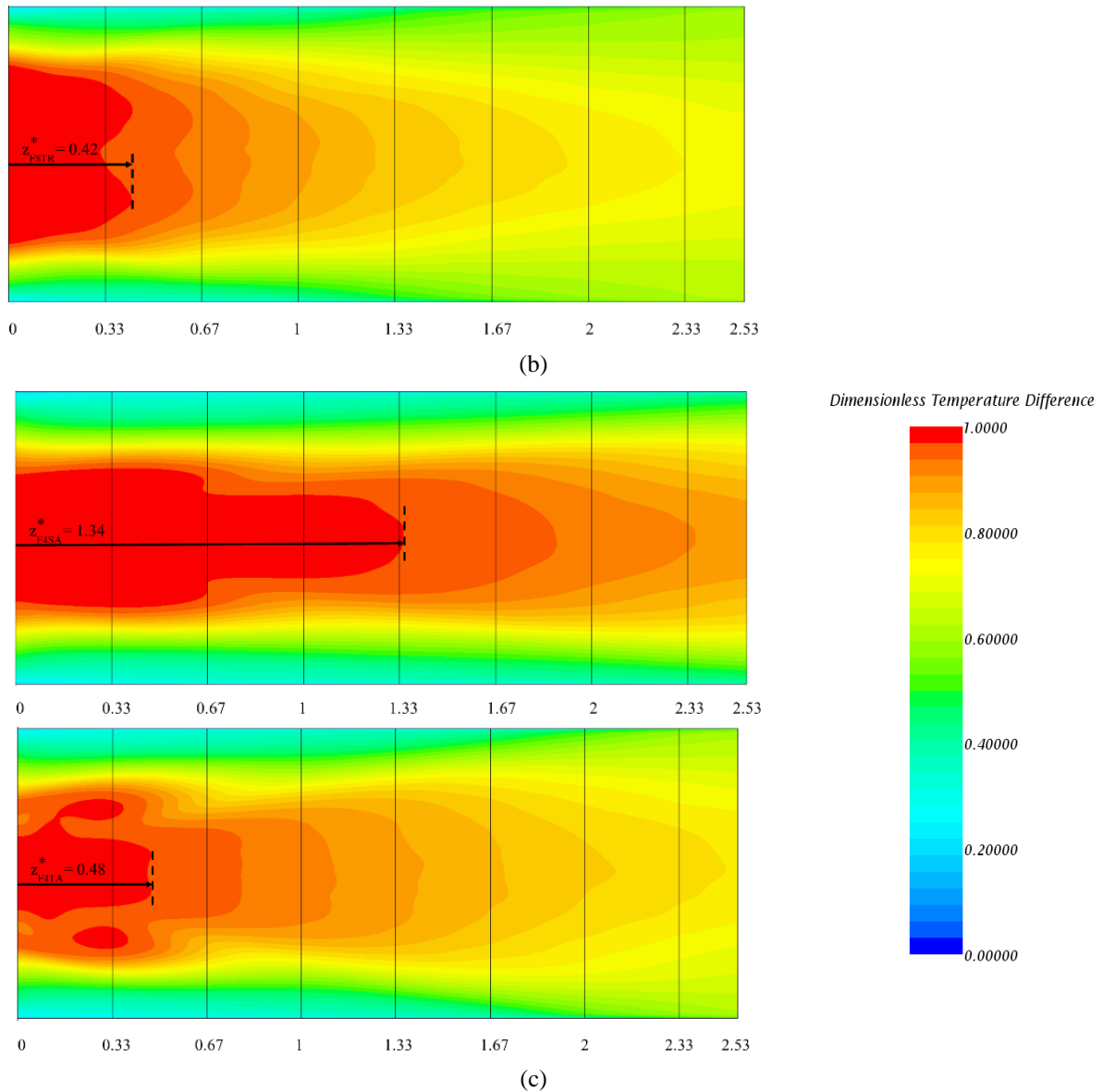
Figure 7-14: Temperature Contours of the Mixed Flow at the Exit Pipe in (a) F4SR (Up)/ F4TR (Down), (b) F8SR (Up)/ F8TR (Down), and (c) F4SA (Up)/ F4TA (Down)

(F) **Number of Swirlers**

F8SR and F8TR are improving the mixing outcome by partitioning the primary flow into N sections (8 in this case) and generating the large central swirl. More controlled rotational motion is achieved as the lump of air per swirler is reduced. By raising the number of spacing two times, the vorticity regions of almost the same magnitude distribution are doubled in a smaller surface

area as seen in Figure 7-15a, which shifts up the average vorticity of the whole streamlined body. Average vorticity magnitude over F8SR (Figure 7-15a: right side) surpasses the average of F4SR (Figure 7-15a: left side) by 6.4%. In case of F4TR/F8TR, the same principle applies even though a high vorticity concentration exists beside F4TR swirlers. F8TR (Figure 7-15b: right side) has higher vorticity than F4TR (Figure 7-15b: left side) by 5.3%.

(a)

Mean of Vorticity: Magnitude (/s)
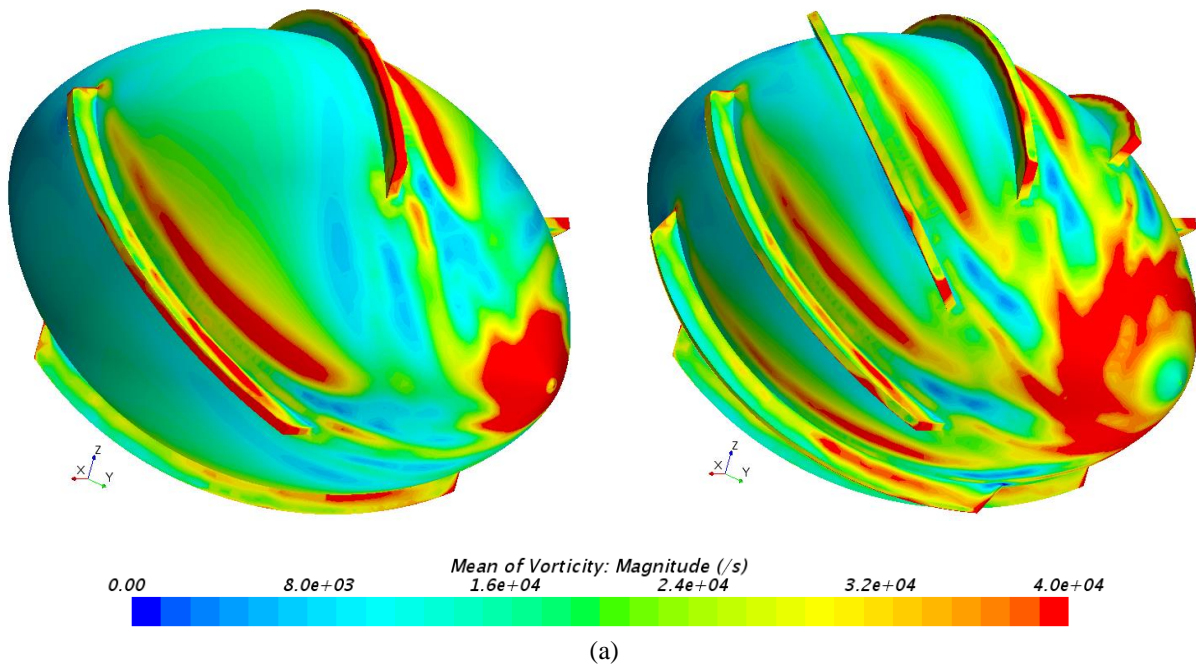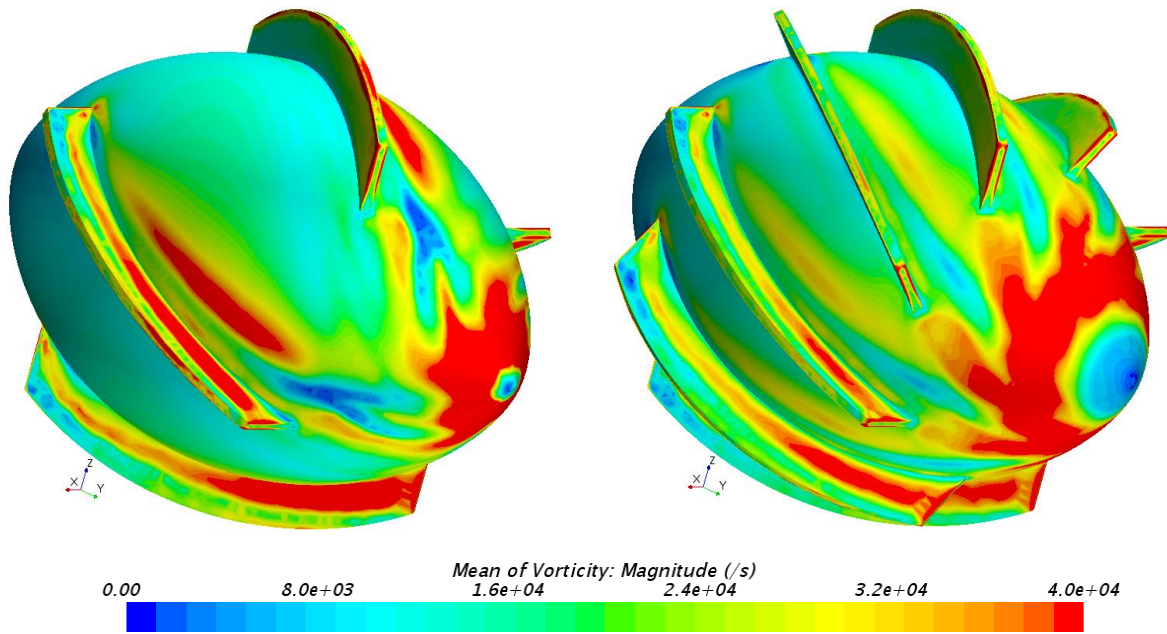
(b)

Figure 7-15: Vorticity Contouring Over Streamlined Bodies: (a) F4SR-F8SR, and (b) F4TR-F8TR

Following the downstream of the swirlers, two guidelines of bounding the core of the central vortex are defined behind after the finned footballs. The vortex patterns of F4SR and F4TR, appeared in the upper scenes of Figure 7-16a and Figure 7-16b, are clear to be clock wise formed around the central axis and maintain nearly constant diameter with intensity fading along the exit pipe length. On the other hand, F8SR and F8TR downstream vortices have a similar start, but the core rotation collapses and external vortex boundaries deviate towards the pipe outer surface after a shorter distance, named collapse length ($z^*_{collapse} \approx 0.54$ and 0.67 respectively), and exhibit a wide rotation pattern. In addition to the main vortex, an adjacent reversed rotation (i.e. counter-clock wise) appears externally. The reversed rotations of F4SR and F4TR are shifted forward, limiting the fast spread of the central vortices. Meanwhile, the reversed rotations are close to the swirlers and diminished in the case of F8SR and F8TR.

Furthermore, the bounds of central vortex core are thicker in the cases of the 8 swirlers. The ratios of the core thickness at one side to the exit duct radius (i.e. t/R) are estimated to be 0.28, 0.31, 0.37, and 0.41 for F4SR, F8SR, F4TR, and F8TR respectively.
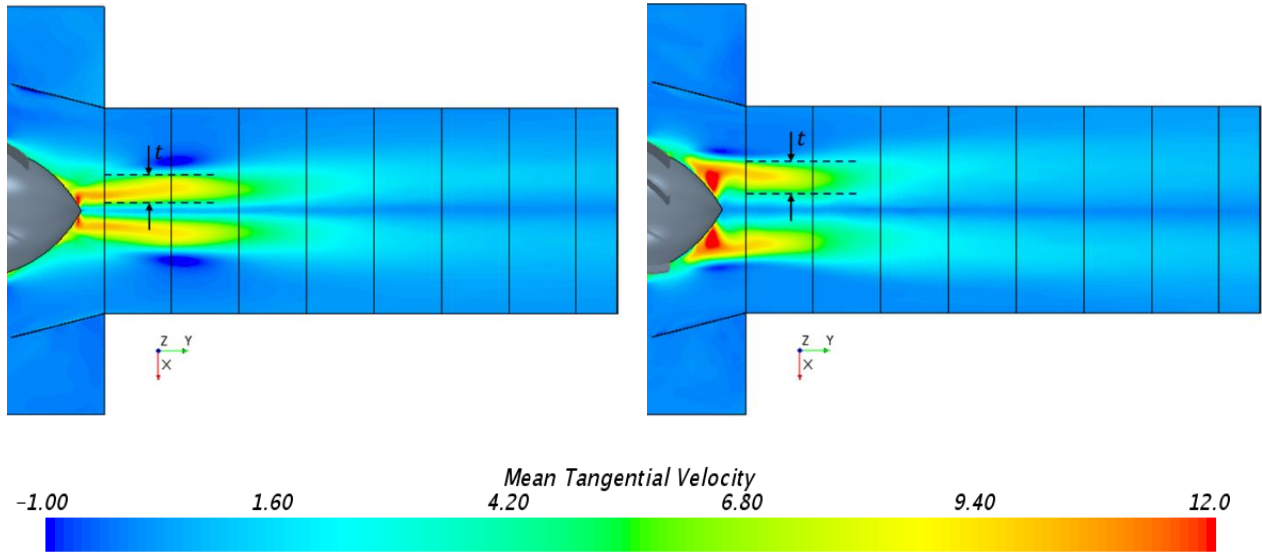
(a)
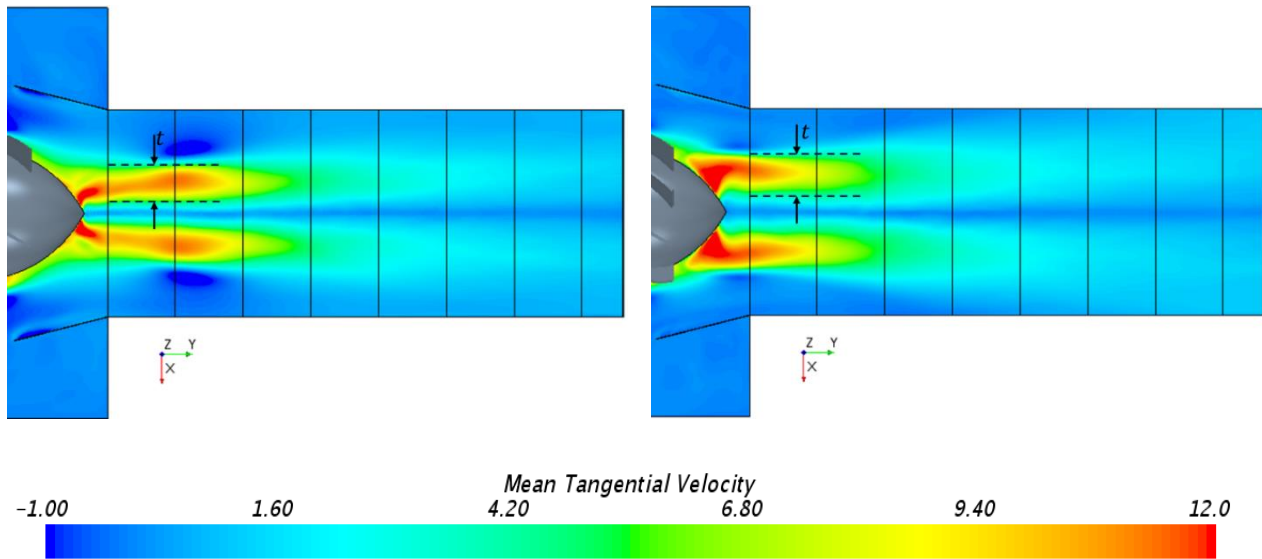
(b)

Figure 7-16: Tangential Velocity Distribution at the Exit Pipe: (a) F4SR-F8SR, (b) F4TR-F8TR

(G) Pressure Drop Analysis

With frictional and eddy flow, the energy in streamline encounters some losses (i.e. transformation to heat most of the time). Pressure is the property to be affected by the loss since the velocity maintains its value according to the continuity. Pressure loss (or drop) is an important monitor to understand how the suggested system will consume power for pushing the air into the jets. Tracking the surface averaged total pressure at different locations along the system enables the calculation of the pressure drop. On average, the mixing chamber with swirling body contributes with 96% to the total pressure drop in the system, leaving the rest 4% to the flow in exit pipe. From Table 7-9, the airfoil swirler can be preserving total pressure better than the rectangular one, which is a known advantage in the streamlined shapes. Observing the height and the number of swirlers, a larger wake region and re-circulations are accompanied to the taller and more swirlers, resulting in higher pressure drop.

In applications like Gas Turbine (GT), there is a linear relationship between the pressure losses and the output power drop. Being different per GT type, power output drop is ranging between 0.1-0.5% for every inch water of pressure loss [89], [90]. Compared to a GT with a regular SH dilution zone, the insertion of FB and F4SR could cost total pressure losses of 1.2 and 1.4 times respectively. As a result, the expected drop in the generated turbine power is in the range of 0.12-0.6% for the FB and 0.14-0.7% for the F4SR.

(H) Decision Making

In evaluating a technology, three criteria are primarily considered: usefulness efficiency, applicability (easiness and risk awareness), and cost efficiency (material and manufacturing wise). The usefulness efficiency (η), is formulated from the x improvement as an output over the fractional ΔP as the input as shown in Eq. (7-9).

$$\eta = \frac{\frac{x_{FB}-x}{x_{FB}}}{\frac{\Delta P - \Delta P_{FB}}{\Delta P_{FB}}} \times 100\% \qquad (7\text{-}9)$$

A drawback regarding the efficiency definition is irrelevance to the magnitude of the power loss represented by the ΔP which is important for the cost efficiency as well. A revised definition of the efficiency, η_{use} , considers another division over ΔP, so the final version looks like Eq. (7-10).

$$\eta_{use} = \frac{\frac{x_{FB}-x}{x_{FB}}}{\left(\frac{\Delta P - \Delta P_{FB}}{\Delta P_{FB}}\right)^2} \times 100\% \qquad (7\text{-}10)$$

With all data given about the designs, Table 7-10 summarizes the η_{use} for each case and gives an insight about maximizing the benefit by the greater number. Unlike the regular efficiency, the highest value has shifted from the F8TR to F4SR after counting the press loss as a critical value to the cost.

Table 7-10: Usefulness efficiency of different swirling cases

	F4SR	F4TR	F8SR	F8TR	F4SA	F4SA
η_{use} (%)	5.47	3.34	4.79	2.32	3.86	4.03

(I) Experimental Outcomes (Uncertainty Analysis)

Uncertainty estimation is based on statistical analysis of multiple measurements and calculations. Because of generating three readings for four major variables (inlet and exit temperatures and velocities), the total number of normalized mixture fractions (f^*) could reach 81 with a full factorial design of experiments. Saving time, a uniform Latin Hypercube Sampling is

proposed to reduce the number of computations for the uncertainty analysis to 24. The 24 experiments are uniformly selected to cover different measurements of the four variables, and a new f^* line is generated every time. Finally, a sample standard deviation is evaluated for each point on the f^* line, then an average value is made of the 7 points. The average standard deviation is found to be between 0.07-0.076 for all cases. A sample computation for the staggered holes case is added in Appendix I.

(J) Experimental Outcomes (Mixing Enhancers)

Figure 7-17 shows the f^* curves of SH, FB, and F4SR at Re=0.85×10^5 and Re=0.2×10^5. As expected, the highest deviation is attributed to SH system where the jet interaction is minimal with the axial primary flow. Streamlined body (FB) is improving the mixing outcome by producing a tumble in the whole domain due to the hot air diversion radially. F4SR showed effectiveness represented in more levelled curve and closer to the x-axis. Central swirl added more diffusivity in the third component (i.e. tangential). Table 7-11 compares between the 3 designs according to the uniformity factor x at the same Reynolds number (Re=0.85×10^5) and asses the latter two cases based on the first. FB and F4SR surpass SH performance by 31.8% and 47% respectively.

Radial Variation of Mixture Fraction
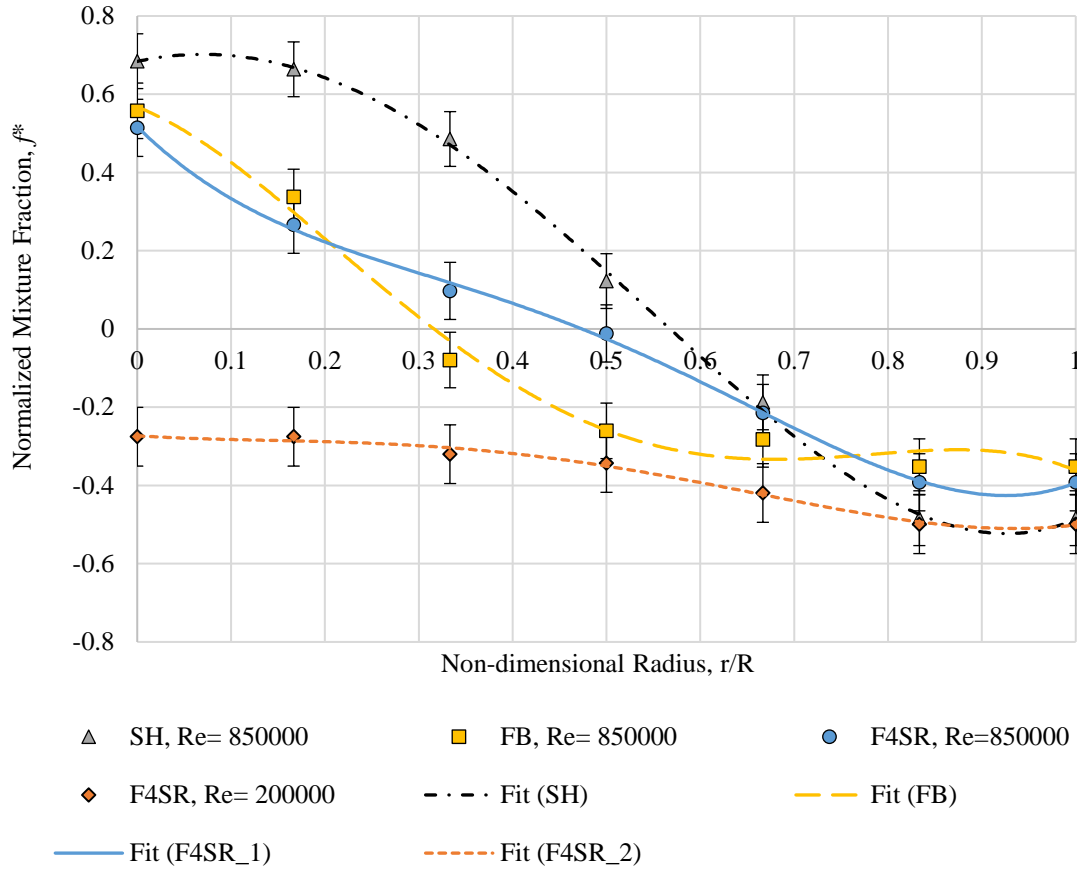
Figure 7-17: Experimental Radial Variation of the Normalized Thermal Mixture Fraction in cases: SH, FB, and F4SR

Table 7-11: Uniformity Values of Different Geometries Tested Experimentally

Case	SH	FB	F4SR
x	0.26	0.18	0.14
Δx %	0	**-30.8**	**-46.2**

(K) Experimental Outcomes (Reynolds Number)

With two different flow rates (i.e. Re=0.85×10^5 and 0.2×10^5), F4SR is set as the mixing

pattern in the chamber and a comparison is illustrated in Figure 7-17. Interestingly, though high

Re indicates more turbulence which supports the heat and momentum diffusion, it means low tangential-axial velocity ratio which is one of the main factors of the large-scale diffusion. Such behavior raises the advection mode against the dispersion. The 4 times drop in Re has regulated the outflow uniformity of F4SR system by 23.8%.

At low Re, the F4SR overcools the hot flow to below than the equilibrium temperature. All the points of the exit mixtures are lower than the ideal line, but closer than the central points of the Re=0.85×10^5.

7.1.5 DOE and Optimization of the Streamlined Body

Optimizing through total 18 designs, a scatter of the HYBRID design space can be seen in Figure 7-18 which shows the concentration of the points over a limited area because of the coupling between the global and local search methods which saves the computational energy and time. In the same figure, a Pareto front (i.e. optimal curve) minimizing the uniformity and the pressure drop is highlighted by red outline. The Pareto range is (x= 0.081-0.263) and (PD= 92.6-196.5 Pa). The baseline design, represented in a yellow circle, generates a uniformity and pressure drop of 0.254 and 109 Pa respectively, which does not nominate it to be an optimal solution.
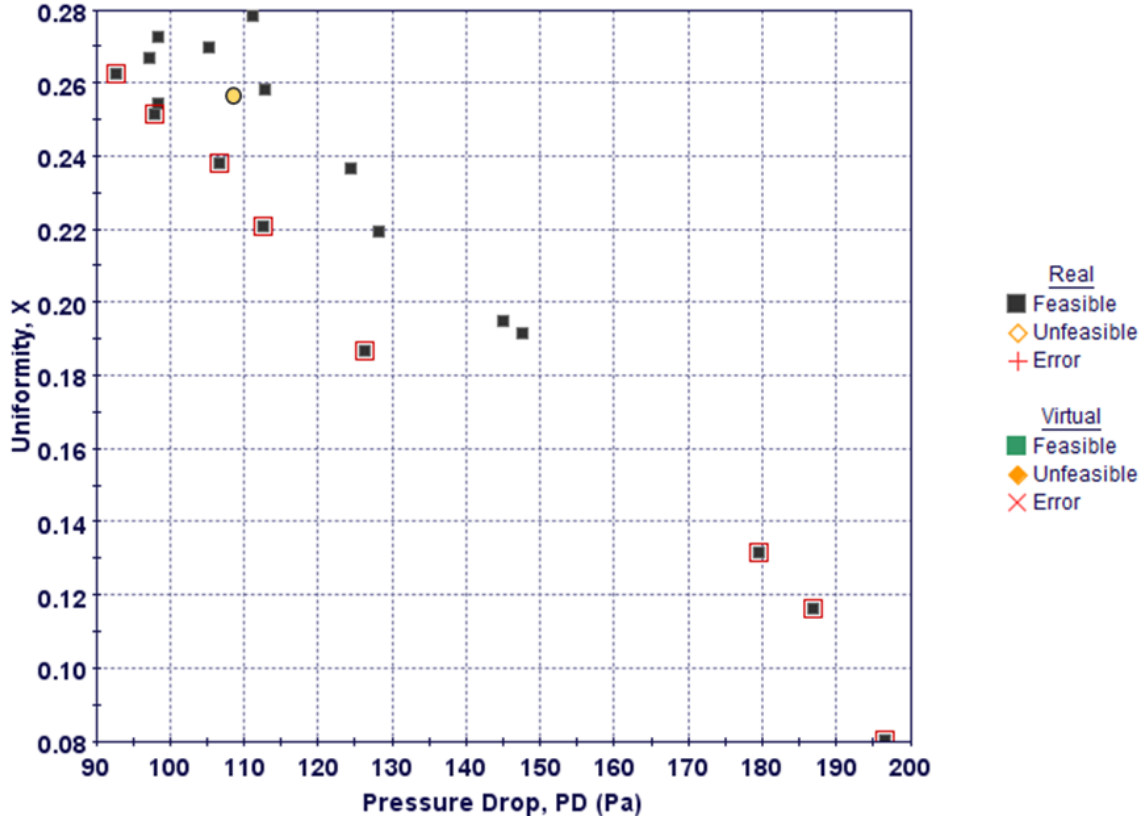
Figure 7-18: Scatter plot of the uniformity-pressure drop design space explored by the HYBRID optimization algorithm

In comparison with other methods, Pareto front of each exploration method (OLH DOE, MOGA II, and HYBRID) is plotted in Figure 7-18. OLH scatter are shifted towards higher uniformity and pressure drop values as a result of lacking an optimization algorithm. MOGA II, as an optimization method, developed variables that can improve the outputs based on the history of the earlier generation. Such evolution enabled a shift in the Pareto front towards the objectives. HYBRID algorithm advances over MOGA II by considering gradient-based method for local optimization which is reflected in focusing most of the designs at either low-PD or low-uniformity areas. The slope of HYBRID tends to achieve the objectives more than MOGA II as in Figure 7-19. As a result of superiority, further analysis is based on the HYBRID.
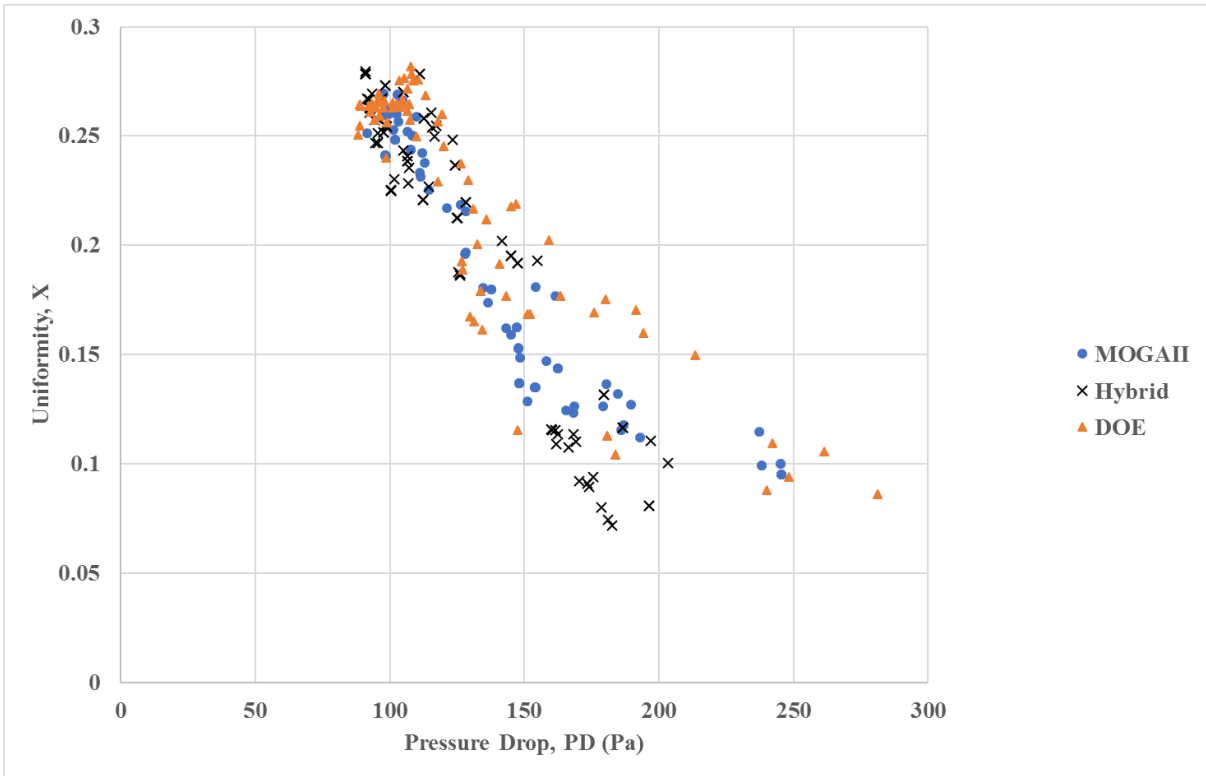
Figure 7-19: Scatter Pareto Front of OLH, MOGAII, and HYBRID
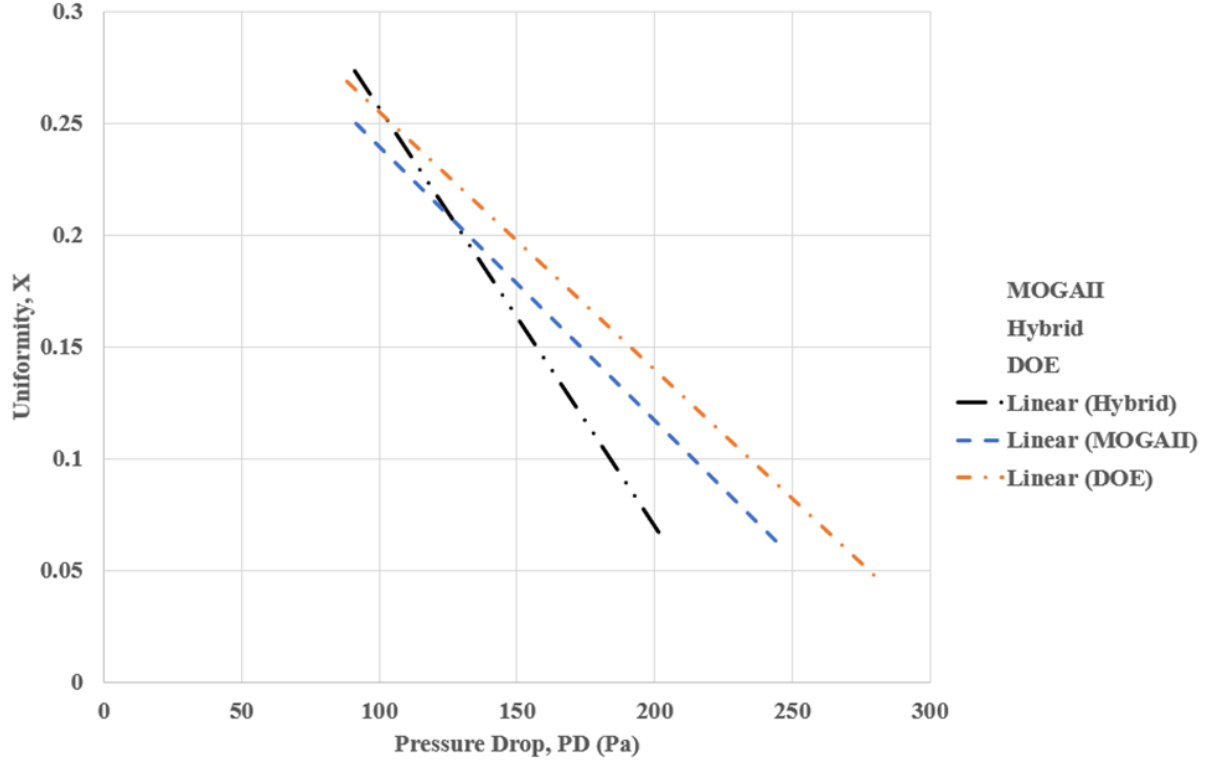
Figure 7-20: Linear Slopes of Pareto Front of OLH, MOGAII, and HYBRID

Based on the generated designs by HYBRID, the correlation between the inputs (D, L, P) and

the outputs (x, PD) is identified by the Pearson correlation, written in Eq. (7-11), which divides

the covariance between each two variables with their standard deviations to keep the final value

between -1 (i.e. Extreme inverse correlation) and 1 (i.e. Extreme direct correlation).

$$\rho_{X,Y} = \frac{COV\ (X,Y)}{\sigma_X\ \sigma_Y} = \frac{\frac{\sum_{i=1}^{N}(X_i-\overline{X})(Y_i-\overline{Y})}{N-1}}{\sqrt{\frac{\sum_{i=1}^{N}(X_i-\overline{X})^2}{N-1}}\sqrt{\frac{\sum_{i=1}^{N}(Y_i-\overline{Y})^2}{N-1}}} \tag{7-11}$$

The resulted correlation matrix in Figure 7-21 illustrates the correlation coefficients of all the

variables (inputs and outputs). The diameter (D) has a stronger correlation with the outputs more

than the other two input variables (L and P). The correlation of D is 88% negatively linear with x

which means the larger diameters are related to the required low uniformity levels. Considering

the PD, the D correlation is 94% positively linear which implies unfavorable increase in the pressure drop associated to the large diameter. Other input variables (L and P) are in either weak or no correlation with the outputs.
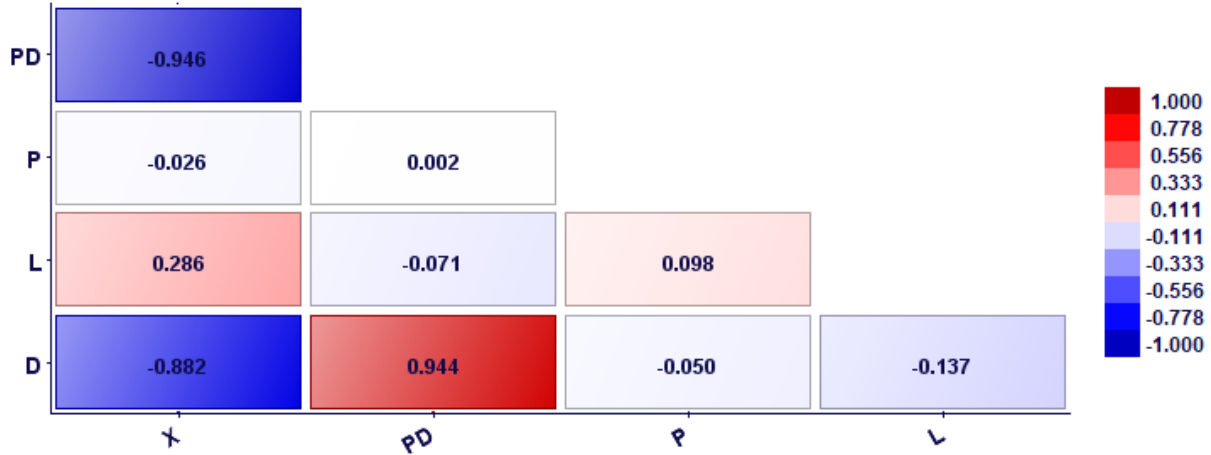
Figure 7-21: Correlation Matrix between the inputs (D, L, P) and outputs (x, PD) based on the HYBRID results

Input variables significance to the outputs is represented as pie charts in Figure 7-22. The change of diameter has an almost equal impact on x and PD. The significance of L is more associated to the PD than the uniformity number x, meanwhile any alteration in P leads to an effect in the x with inconsiderable amount on PD.
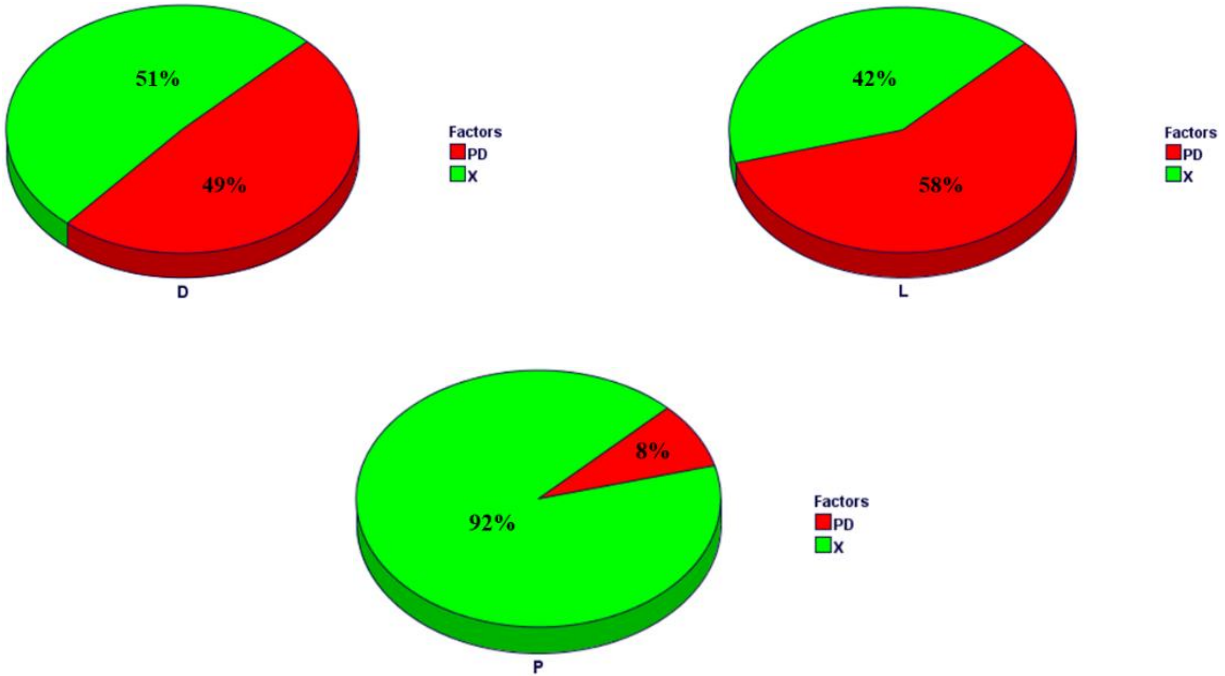
Figure 7-22: Significance pie charts for the three input variables

On an additional step, the design space is surveyed by a numerical approximation for understanding the correlation curves between the variables (inputs and outputs) and determining the unknown areas with no further real simulation (i.e. virtually). Response Surface Methodology (RSM) or Meta Model is created by defining the coefficients of proposed functions based on the known data from the investigated simulations. The explored designs are divided into training and validation categories. The training designs are maintained as many as possible to generate correct coefficients, while the RSM validation is done by 5-10% of the total designs number. Several RSM (Kriging, DACE-Kriging, Anisotropic Kriging, Gaussian Processes, and Radial Basis Functions) are checked using the current data from HYBRID, with 2 designs kept for validation. In Tables (Table 7-12) and (Table 7-13), the different RSM are listed ascendingly by the Mean Normalized Error of the uniformity and pressure drop respectively. The two tables endorse the supremacy of the Kriging (KR) model with a minimum Mean Normalized Error (1.41×10^{-15} and 1.72×10^{-15}).

114

Table 7-12: Uniformity RSM with errors

Name	Mean Absolute Error	Mean Relative Error	Mean Normalized Error
X_KR_0	2.79E-16	1.57E-15	1.41E-15
X_DACE_0	8.70E-15	3.67E-14	4.40E-14
X_AKR_0	4.28E-14	1.96E-13	2.17E-13
X_GP_0	1.95E-9	9.36E-9	9.85E-9
X_RBF_0	1.40E-7	7.56E-7	7.08E-7

Table 7-13: Pressure drop RSM with errors

Name	Mean Absolute Error	Mean Relative Error	Mean Normalized Error
PD_KR_0	1.79E-13	1.51E-15	1.72E-15
PD_RBF_0	6.13E-13	4.70E-15	5.90E-15
PD_AKR_0	2.87E-11	2.33E-13	2.76E-13
PD_DACE_0	1.06E-10	8.97E-13	1.02E-12
PD_GP_0	9.81E-8	7.52E-10	9.44E-10

With the advantage of the trained KR, HYBRID optimization is extended virtually to cover 72 new geometries in the design space. Such exploration gives the opportunity for reaching new limits and a better Pareto front. Figure 7-23 scatters the real (i.e. simulated) and virtual designs between the two objectives. By adding the virtual designs, the Pareto front is shifted diagonally towards minimum uniformity and pressure drop. The new ranges for the objectives are ($x = 0.0272$-0.278, PD= 91-183 Pa).
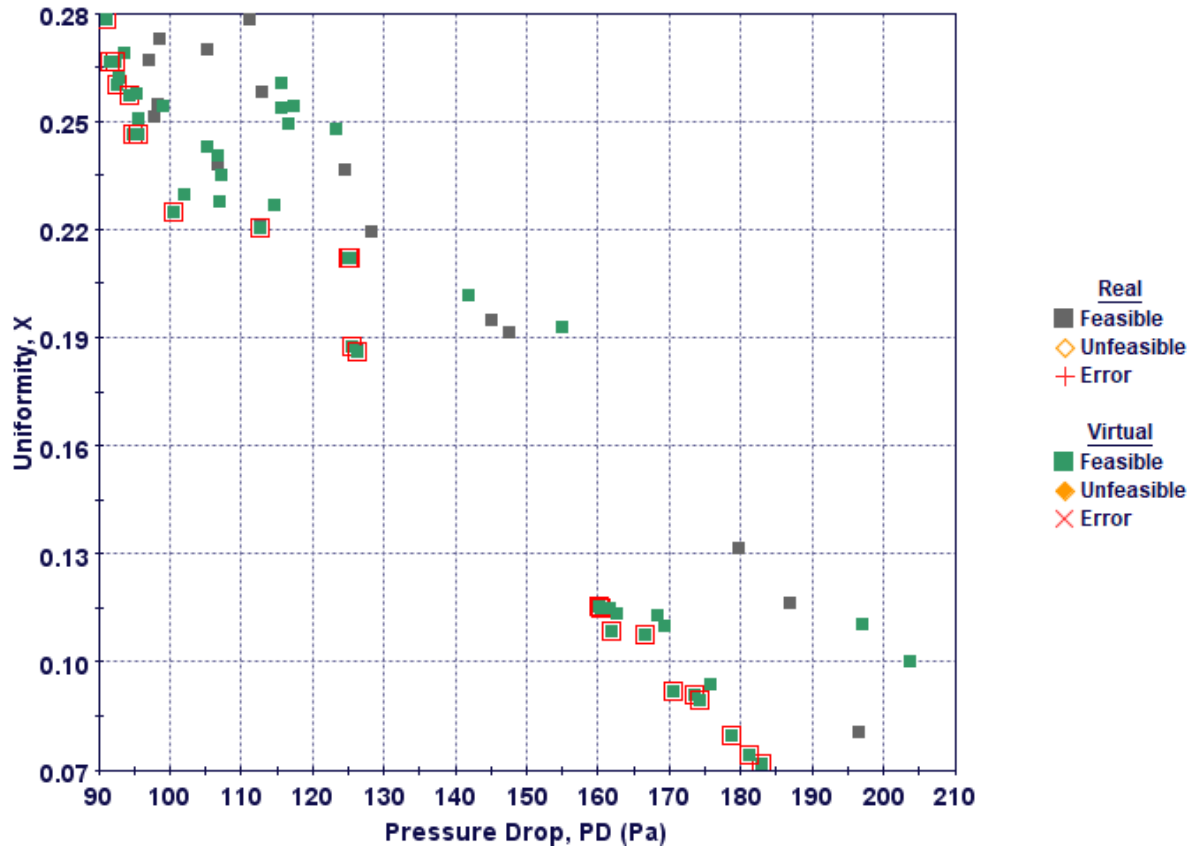
Figure 7-23: Scatter plot of the uniformity-pressure drop design space based on both methods: Simulation and Kriging RSM

Understanding the influence of the ranges of the inputs on the two outputs, parallel axes arrange the designs (represented by the connecting lines) according to their dimensions and the corresponding uniformity and PD values. Such graphs endorse the correlation concept and help in selecting effective ranges for the required objective, so the decision making could be easier. In Figure 7-24, D and L are affecting on x and PD in an inverse way which makes a comprise is highly needed. Meanwhile the high P (0.0063-0.024) achieves low values for both x and PD leading to a favorable shifting towards the exit pipe.
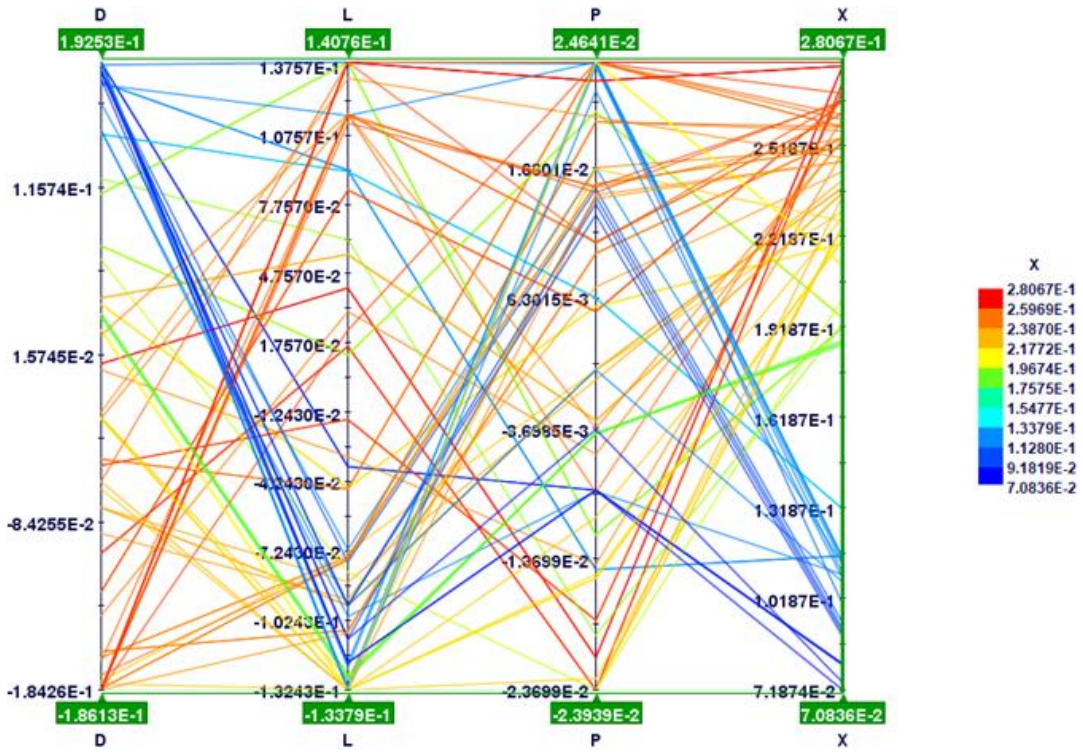
(a)
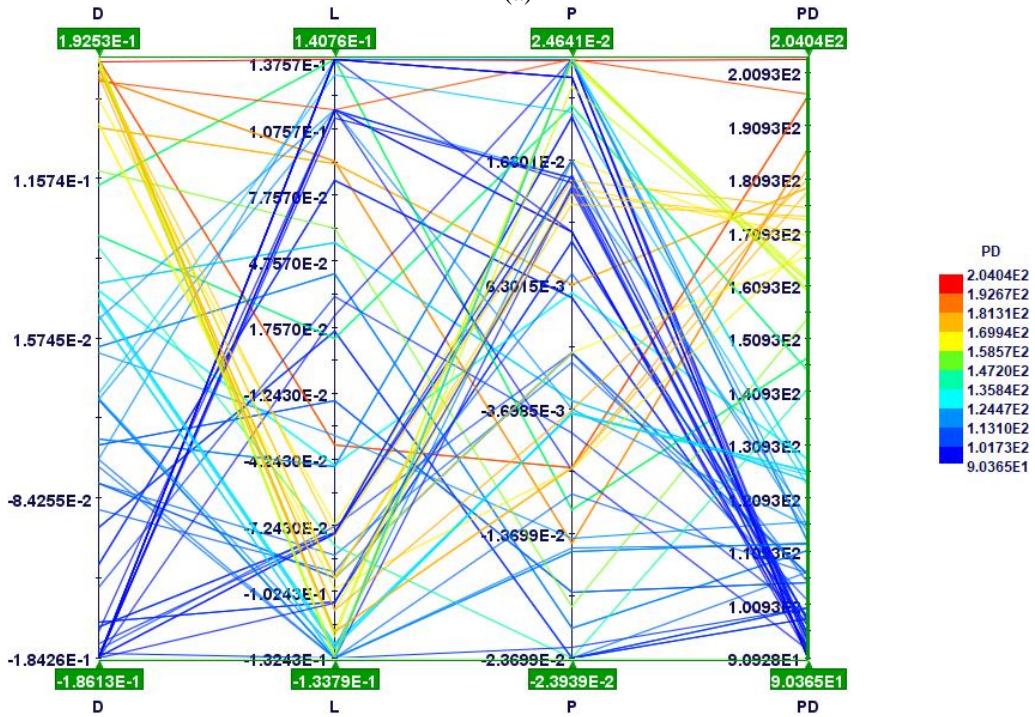
(b)

Figure 7-24: Parallel Axes between the Three Dimensions and: (a) Uniformity, and (b) Pressure Drop

RSM has 2D and 3D surface visualization for the entire design space of each output with respect to inputs. Figure 7-25(a) is the curve and surface correlation of D and L with x where the extremely low uniformity values (i.e. less than 0.11) are concentrated on the region (D= 0.175 to 0.2, L= -0.14 to 0.14). In Figure 7-25(b), the lowest uniformity numbers are bounded by the circular region (D= 0.175 to 0.2, P= -0.025 to 0.025). Same concept applies on the low pressure drop (i.e. less than 115) which lies in zone of (D= -0.02 to 0, L= -0.14 to 0.14, and P= -0.03 to 0.03) as shown in Figure 7-26 .

(a)
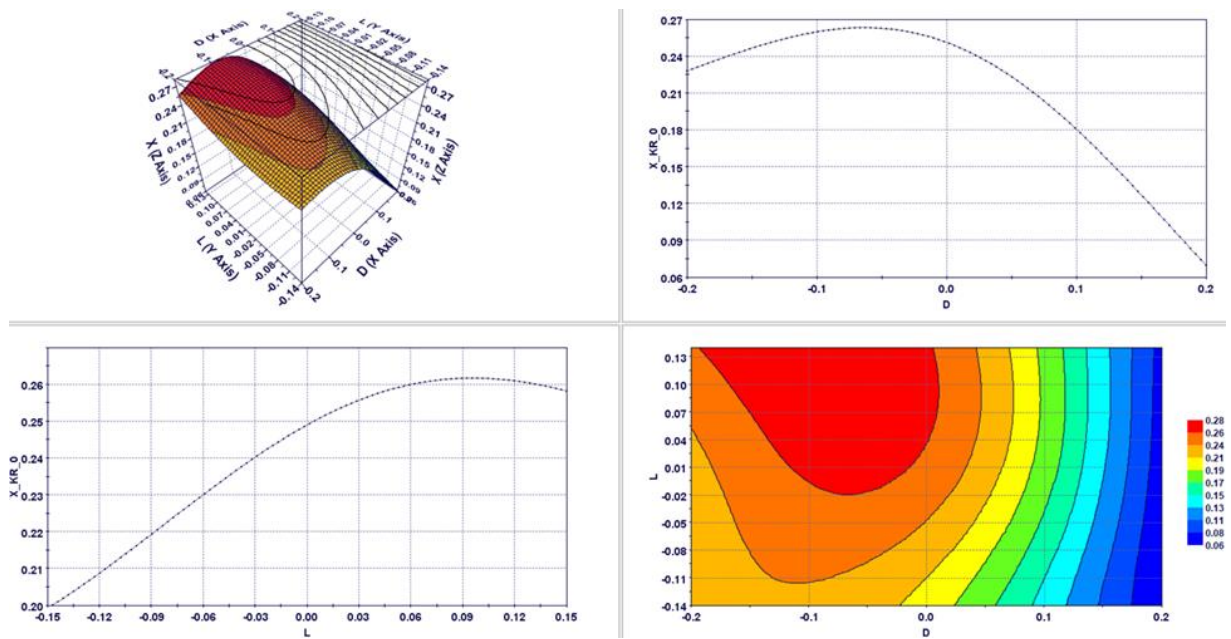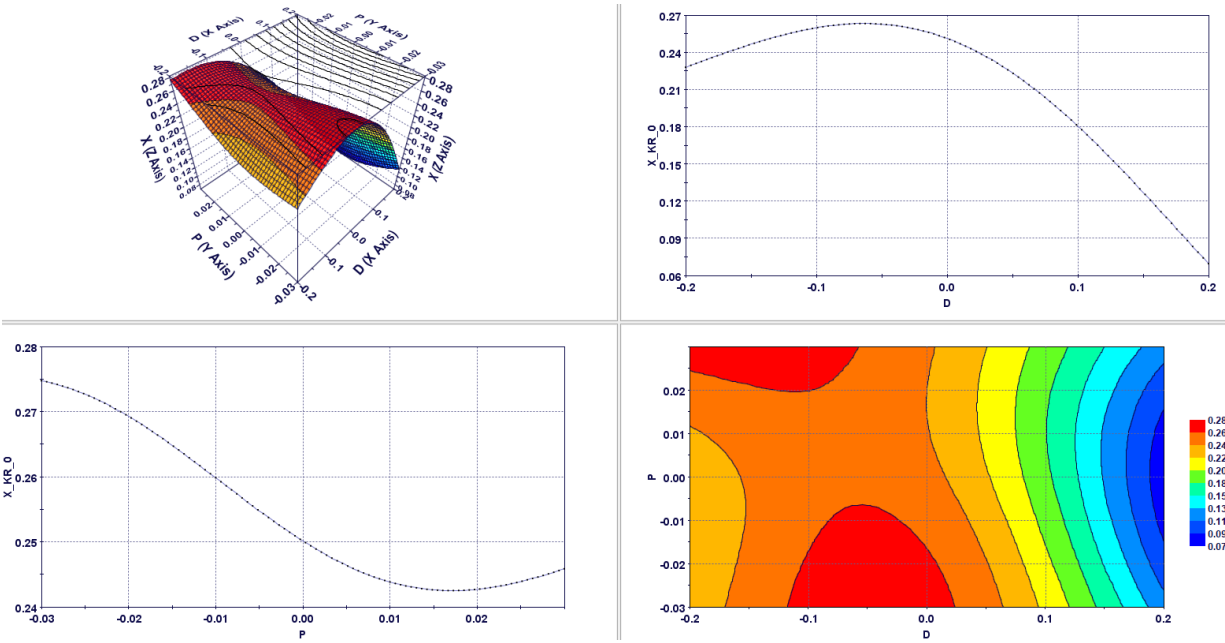
Figure 7-25: Kriging Response Surface Model for Uniformity with: (a) D-L, and (b) D-P
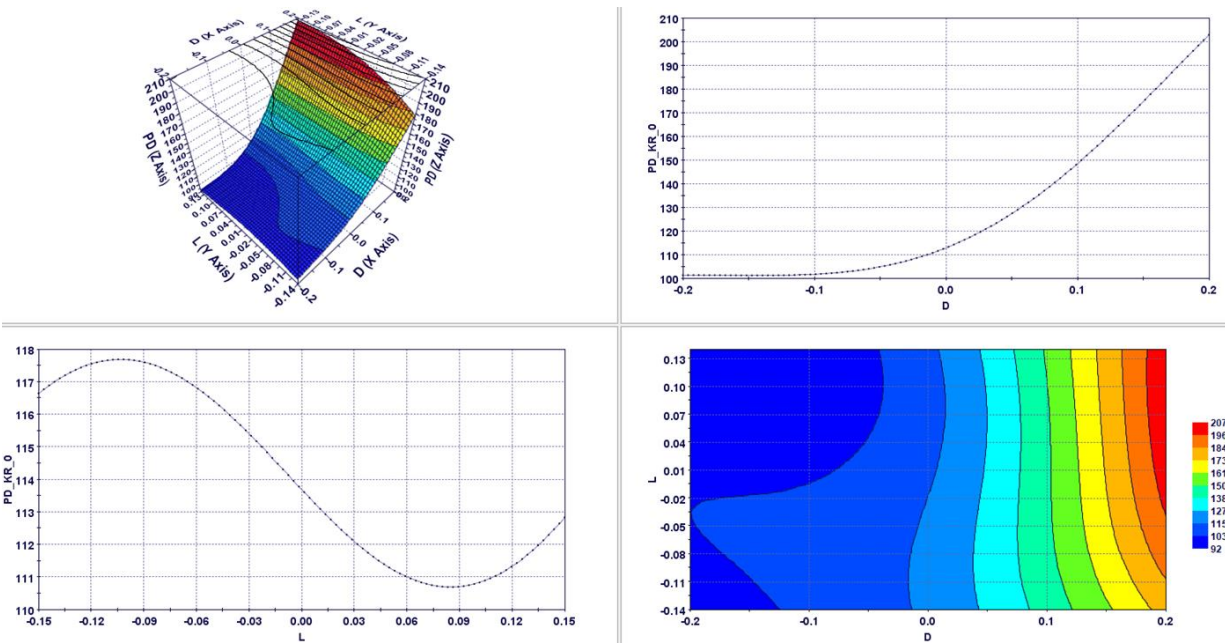
(a)
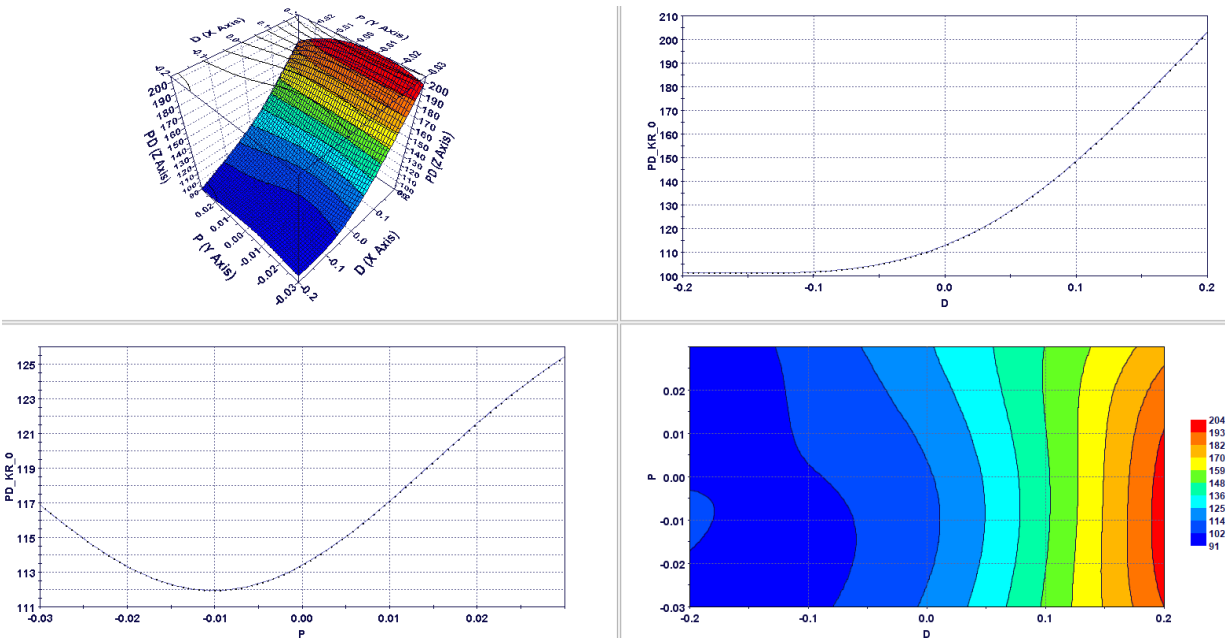
(b)

Figure 7-26: Kriging Response Surface Model for Pressure Drop with: (a) D-L, and (b) D-P

7.2 Cavitation Treatment

7.2.1 Research Roadmap

The CFD started earlier than the experimental setup, and it was intended to predict the cavitation patterns and optimize the proposed air injection treatment to minimize the cost and time of experimentation. Early numerical results showed that the cavitation in the 7.5 cm turbine will need a quite high flow rate (i.e. $V \geq 2$ m/s at the 15-cm inlet pipe, or $P_{out} \ll 0$ psi). Because of limitations in the setup space (especially the turbine elevation from the sink), cavitation was not attainable naturally (i.e. by the increased flow controlled by the head or the ball valve). The need to induce the cavitation led to a different path for the experimental work such that the rotor was operated by the motor for attaining high N and reversing the rotation direction. The two approaches reduced the pressure around the turbine and generated the cavitation sought to be examined and

120

treated. Because of the operation by a motor, the expected response with the cavitation treatment is to decrease the drawn power (P_{motor}) as the quantitative sign of performance improvement. Figure 7-27 is illustrating the two paths and compromising stage which was established to match some experimental cases (i.e. propeller) with especially set-up numerical simulations at the same conditions.
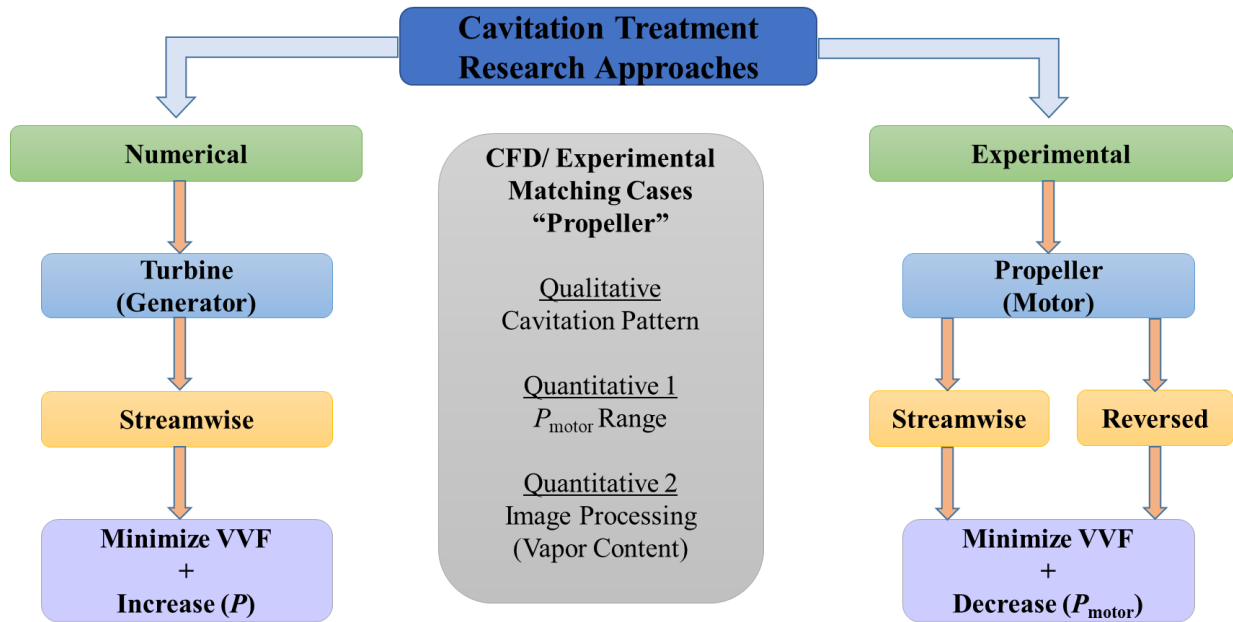
Figure 7-27: Numerical and experimental approaches used to investigate the cavitation treatment

7.2.2 Mesh independence test

The initial work investigated the relationship between six mesh cell counts (1.3, 3, 4.5, 6.1, 9, 11.8 million cells) and the value of the Vapor Volume Fraction (VVF) at the 5000-rpm case (i.e. extreme cavitation condition) as graphed in Figure 7-28. The study resulted in a disregarded mesh-dependent range for counts less than 6.1 million, followed by a solution convergence (around a VVF average= 0.223) for the larger counts (i.e. 6.1, 9 and 11.8 million cells) which appears in the smoothed line. In the converged range, the 5th case (9 million cells) was selected as the base refinement for the latter work because of the minimum deviation from the average (1.2 %), better

rotor y^+ representation than the 4th case (6 million cells), and the 68% less time consumption compared to the 6th case (11.8 million cells). Further analysis was based on the validation (visual, power consumption, and image processing) with some experimental cases as discussed in section 7.2.10.
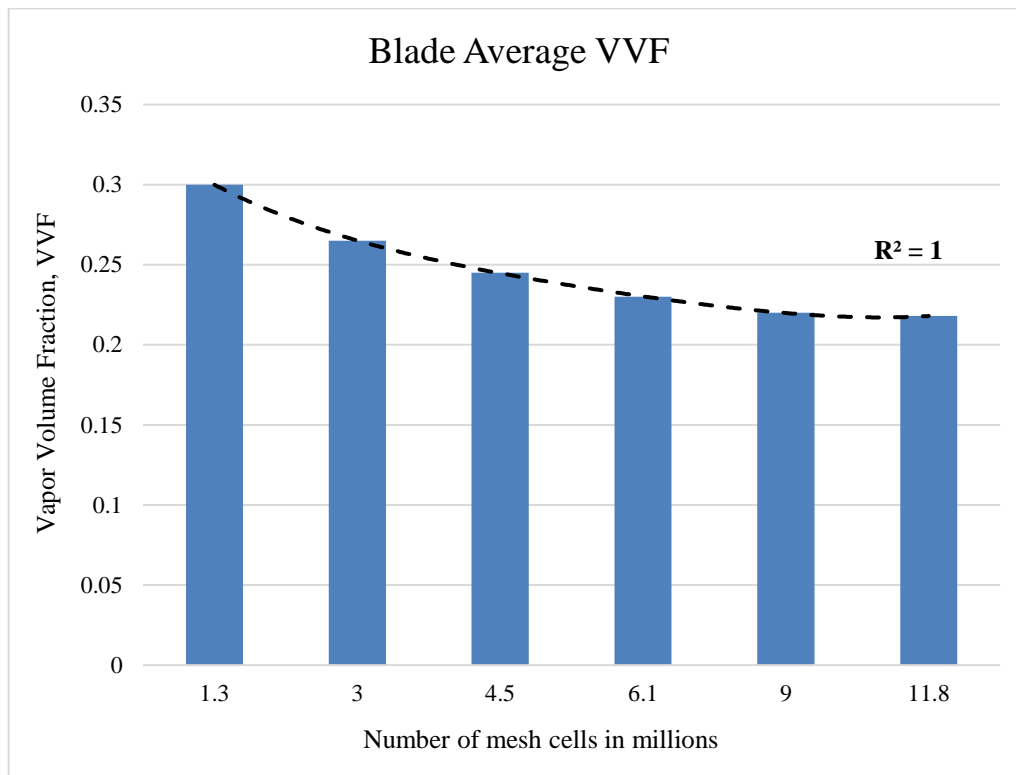
Figure 7-28: Mesh independence test based on the vapor volume fraction on the rotor blades

7.2.3 Preliminary CFD Results

(A) Turbine Cavitation

A very early work was done on small domain (only converging inlet, stator and rotor, and diverging outlet: 3.5 million cells) to quickly check the cavitation generation, propagation and stabilization (i.e. steady state), and for the first time, investigating the influence of injecting air around the rotor (housing injection more specifically). Also, the area averaging process of the

blades' and hub's Vapor Volume Fraction (VVF) was based on the total surface area of the blades and hub respectively as written in Eq. (7-12).

$$VVF_{Blades/Hub} = \frac{1}{A_{Blades/Hub}} \int VVF \, dA_{Blades/Hub}$$

(7-12)

A pure cavitation case (i.e. no air) showed that the steady state is reached after 3-6 complete cycles, At the latter times, the properties fluctuate around an average value that can be statistically averaged to give the steady state with the consideration of turbulence and cavitation natural stages (formation, expansion, separation and collapse). The minimum pressure coefficient and cavitation number, calculated from the inlet velocity and pressure, are found to be ($|Cp_{min}|$= 6.08, and σ= 6.04). Such status leads to the formation of vapor at two main locations: the rotor blade Leading Edge (LE) extending over the blade Suction Side (SS), and the hub-blades intersection where the vapor spreads over part of the hub and the span of the blades. Increasing the rotational speed (N) shifts the cavitation formation radially along the blades' span, such that it gets closer to the blades tip. At high N (i.e. 4000-5000 rpm), Tip Leakage Vortex (TLV) are noticed in addition to the SS cavitation. Cavitation behavior is randomly fluctuating because of the vapor cloud cyclic nature (formation, expansion, separation, and collapse), and the relative position of the blade to the incoming flow from the stator. Figure 7-29 can show the local and temporal variation in the distribution of the vapor volume fraction (VVF) at the rotor.

(a)   (b)

Volume Fraction of vap

0.00   0.20   0.40   0.60   0.80   1.0

(c)   (d)

124
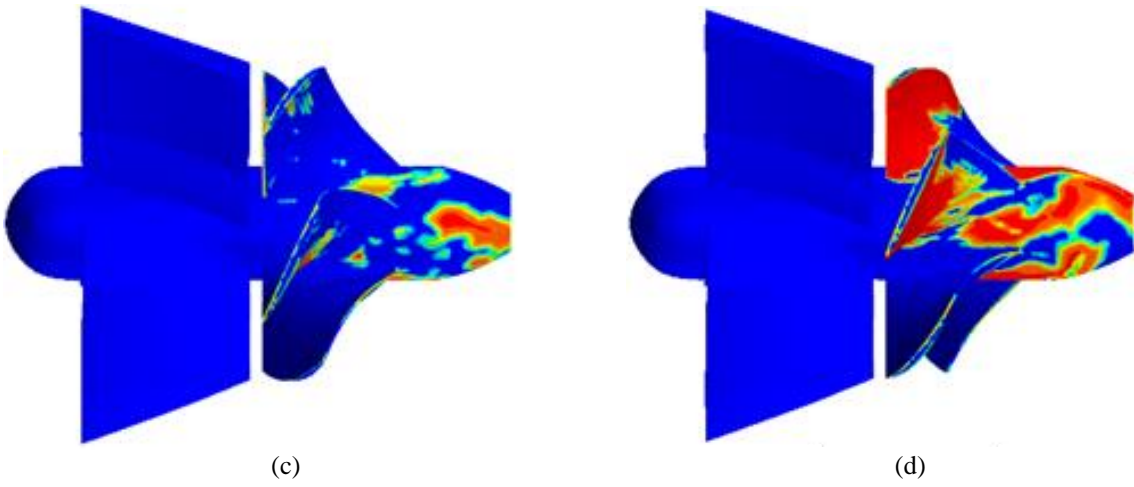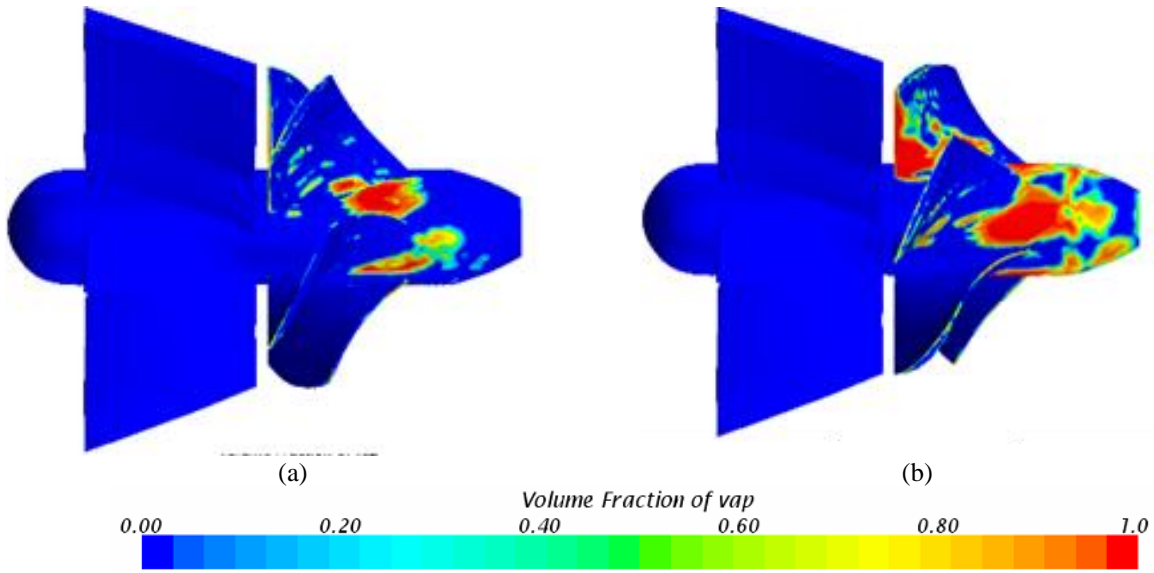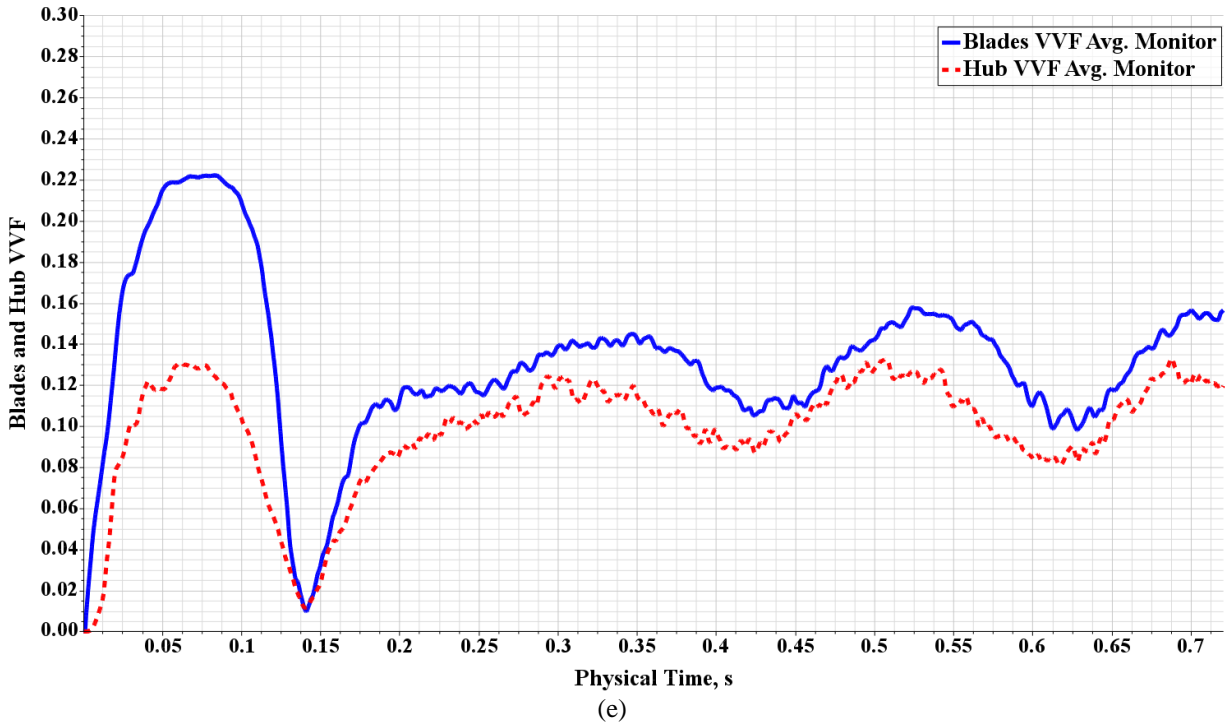
Figure 7-29: VVF distribution (non-Blue colors) at different times (a) 0.25s, (b) 0.35s, (c) 0.45s, (d) 0.55s, and (e) time history for the surface averaged VVF over the blades and the hub

(B) Effect of Air

When air enters the system like a jet, it is affected by the three motion components: radially inward (i.e. penetrating the other fluids towards the turbine axis) due to the pressurization, axial flow with the liquid water, and a rotational with the blades cycle. Accordingly, the location of air is variant with space and time. The air content is added as a factor in changing the shape of the vapor cloud on the rotor. Figure 7-30 displays the air and vapor volume fraction on a mid- sectional plane after reaching the steady state period. The domination of air at one location (e.g. dashed circles) diminishes the existence of vapor at the same place, which indicates the merit of air injection. This leads to further analysis about the reduction in vapor content.

125

(a)

(b)
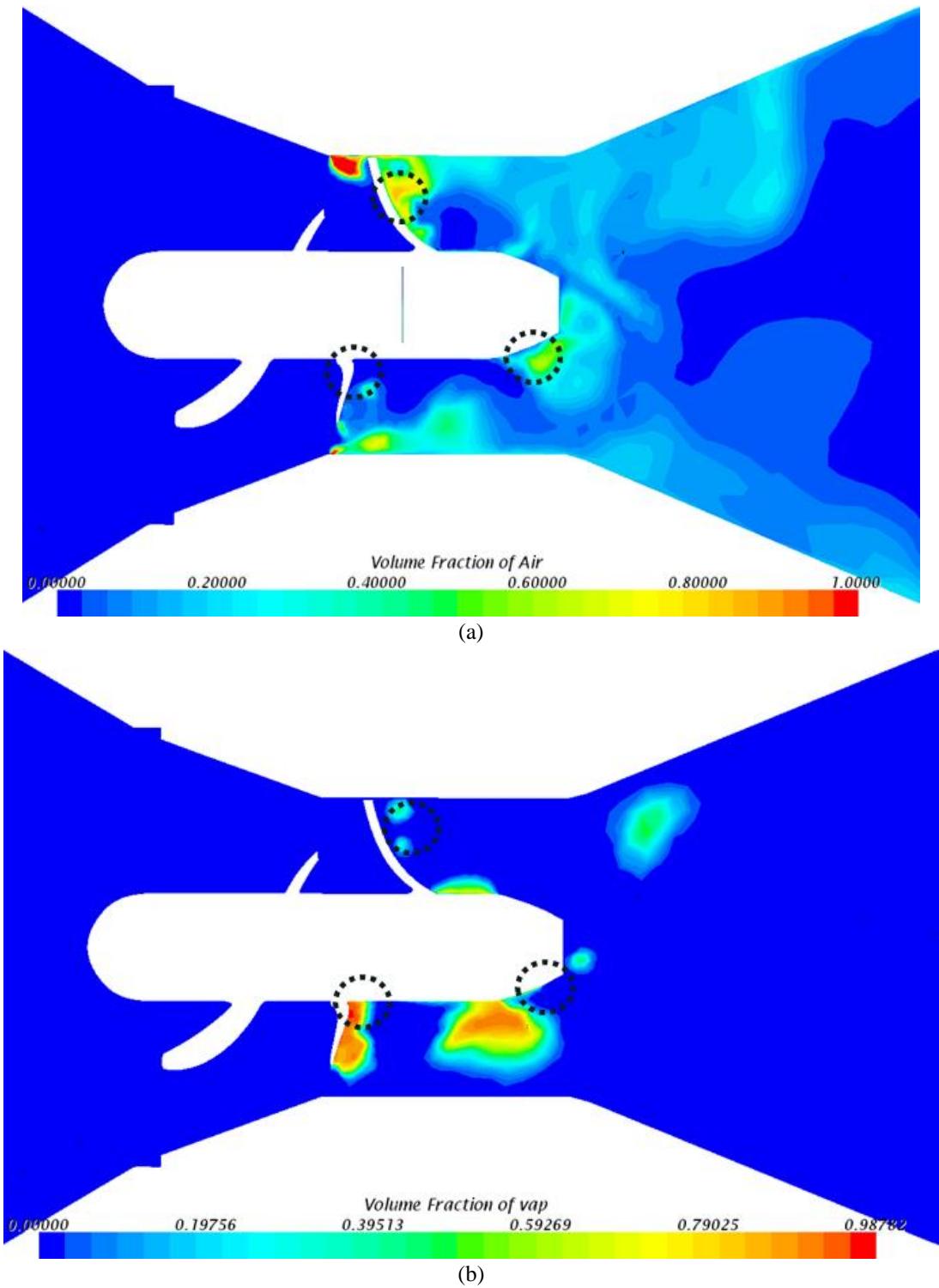
Figure 7-30: Volume fraction distribution for (a) air, and (b) water vapor after 0.18s. dashed circles show some locations of high and low vapor presence in relation with the air exsitence at the same place

By scaling up the minimum bound of the absolute static pressure to the vapor saturation pressure (P_v = 2338 Pa), the air-filled zones have a rise in pressure to be above the cavitation probability. Consequently, the vapor content at these areas is vanishing. A clear comparison is seen in Figure 7-31, specifically at the numbered locations behind the blade (1 and 2), and the converging section of the hub (3). The minimum absolute static pressure at these locations is in the range of the 17 kPa, which is 7.5 times over the cavitation limit.

(a)
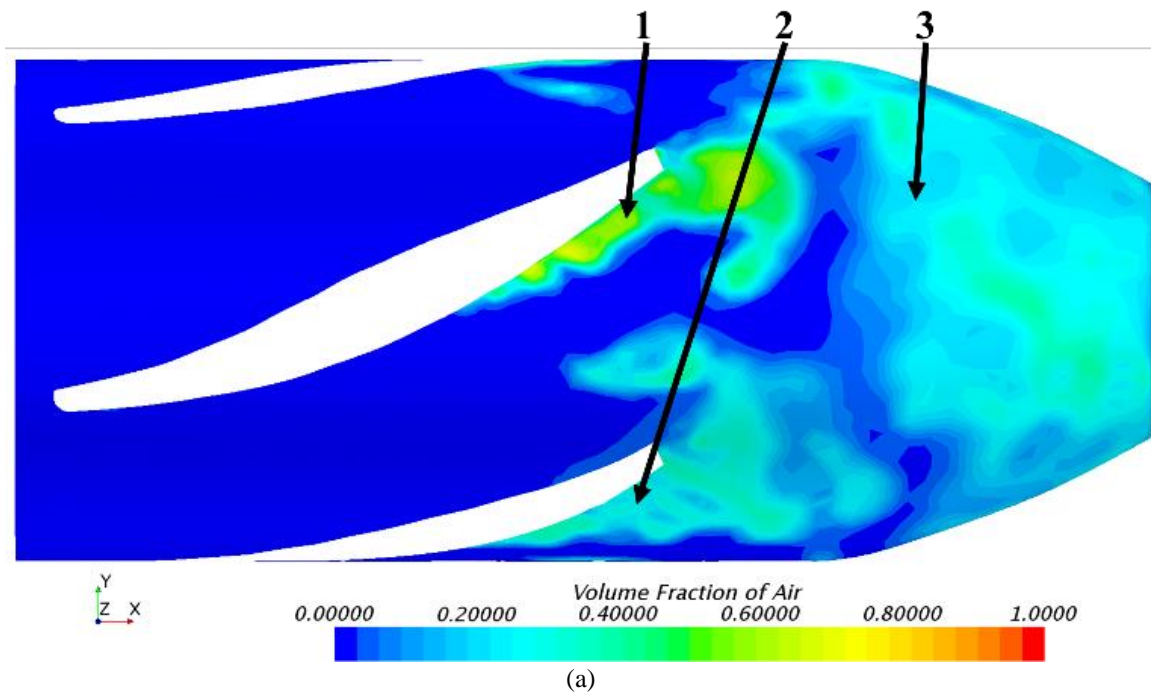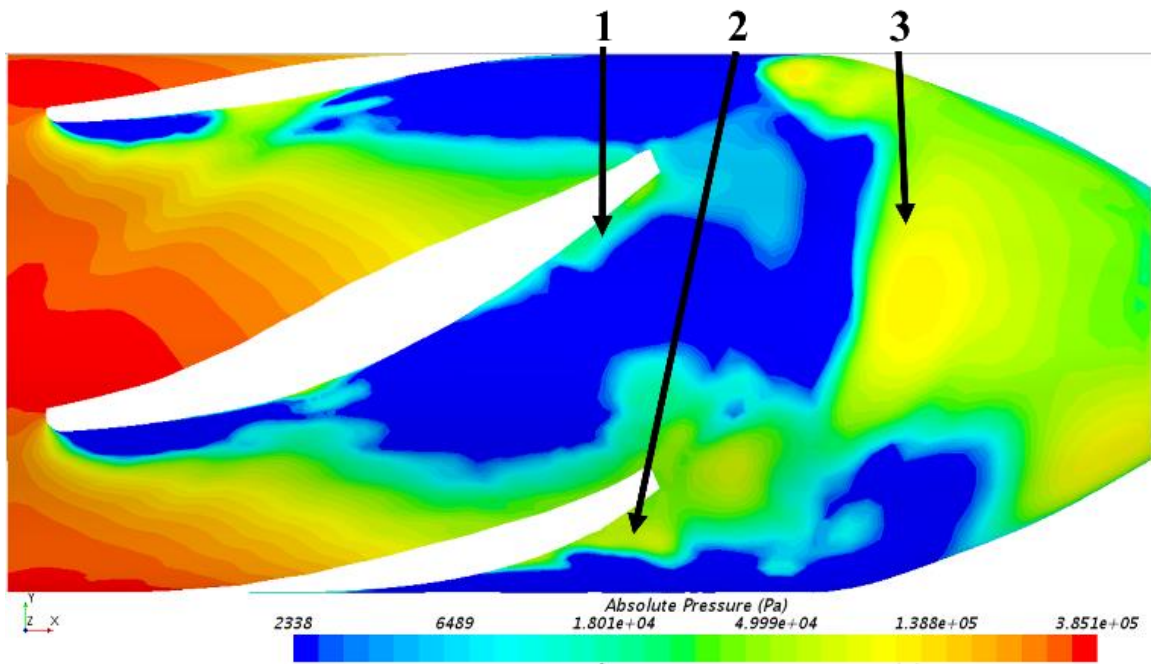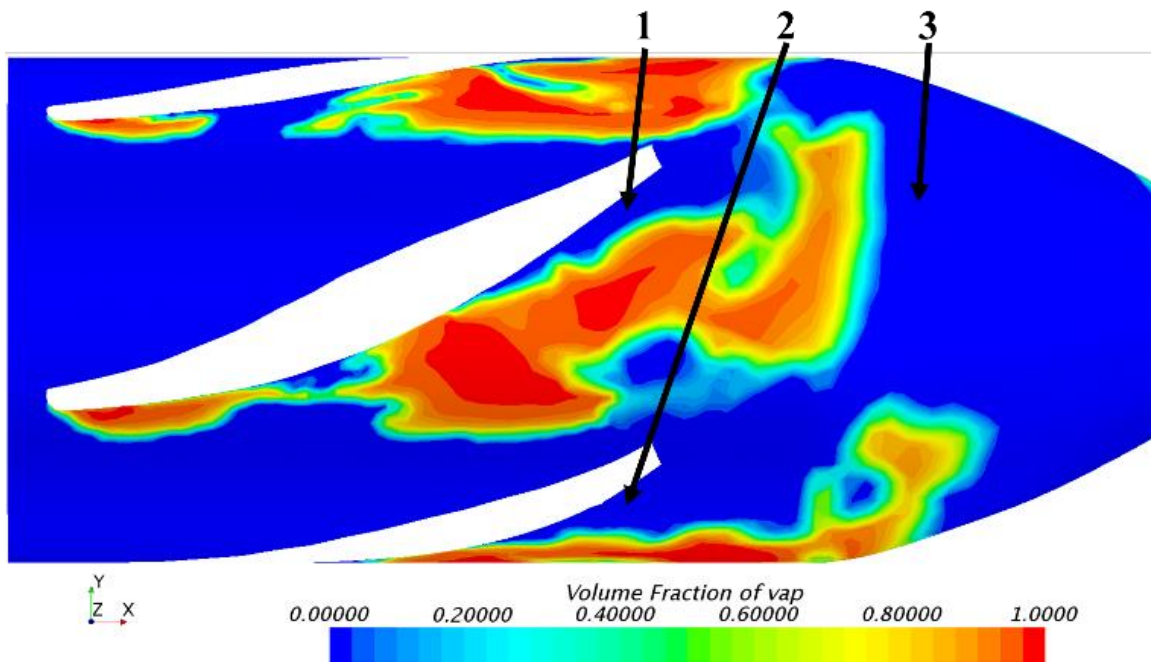
Figure 7-31: Distribution of (a) air volume fraction, (b) absolute static pressure (log scale), and (c) vapor volume fraction over the hub surface

Same concept applies on the suction side of the rotor blades. In Figure 7-32, pressure higher

than P_v is attributed to the present air on the blade surface besides some non-aerated locations (1,

2, 3 respectively). In the meantime, the absolute pressure reaches/crosses the vapor limit at zones lacking air, and cavitation persists (4 and 5).

(a)

(b)
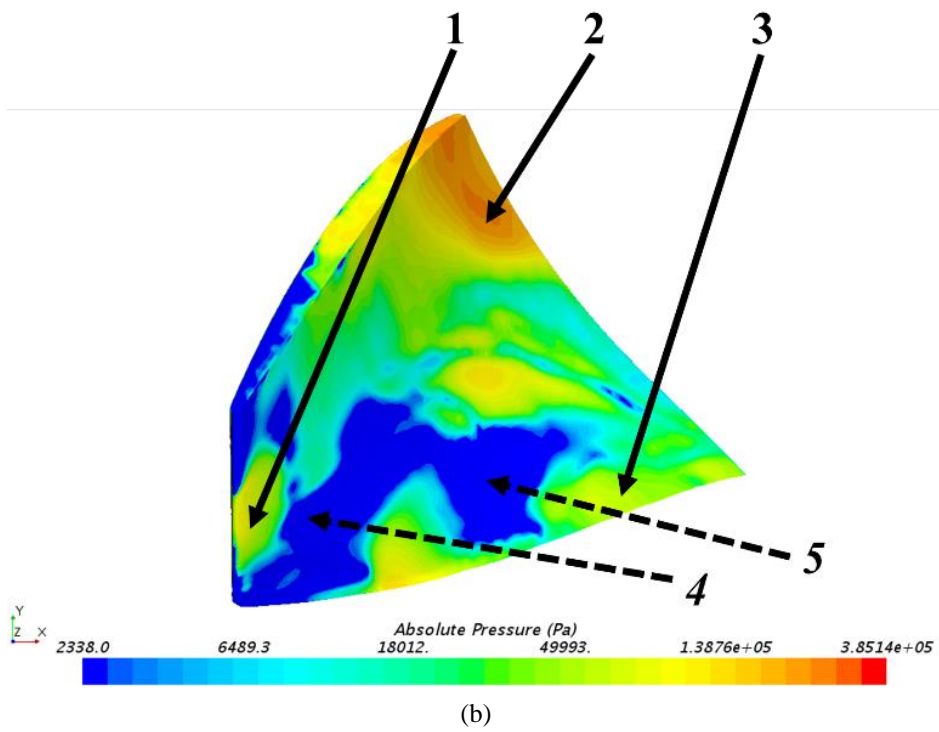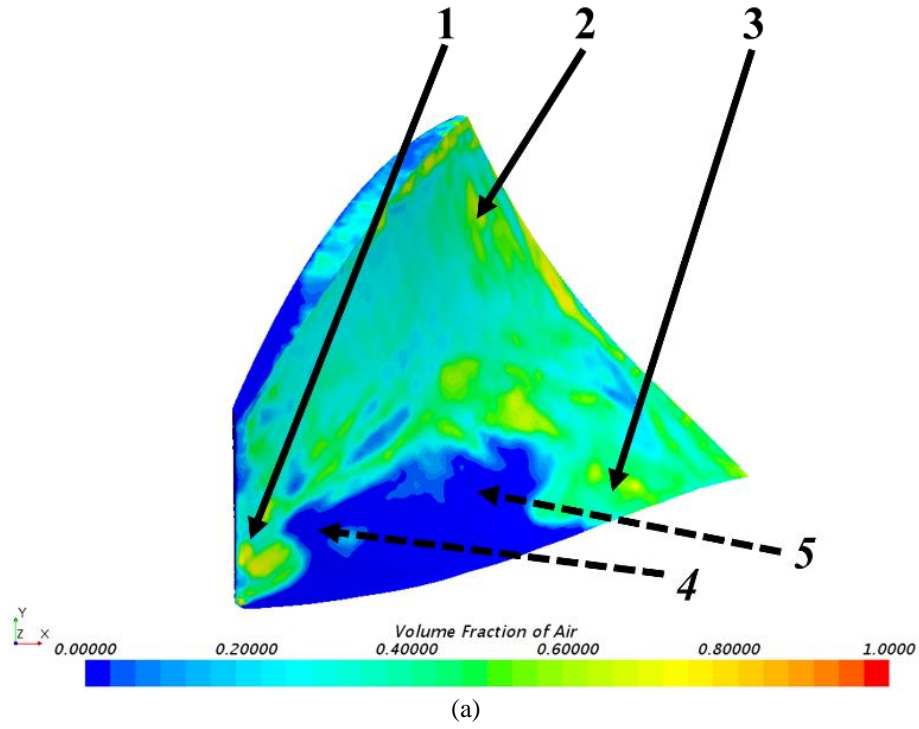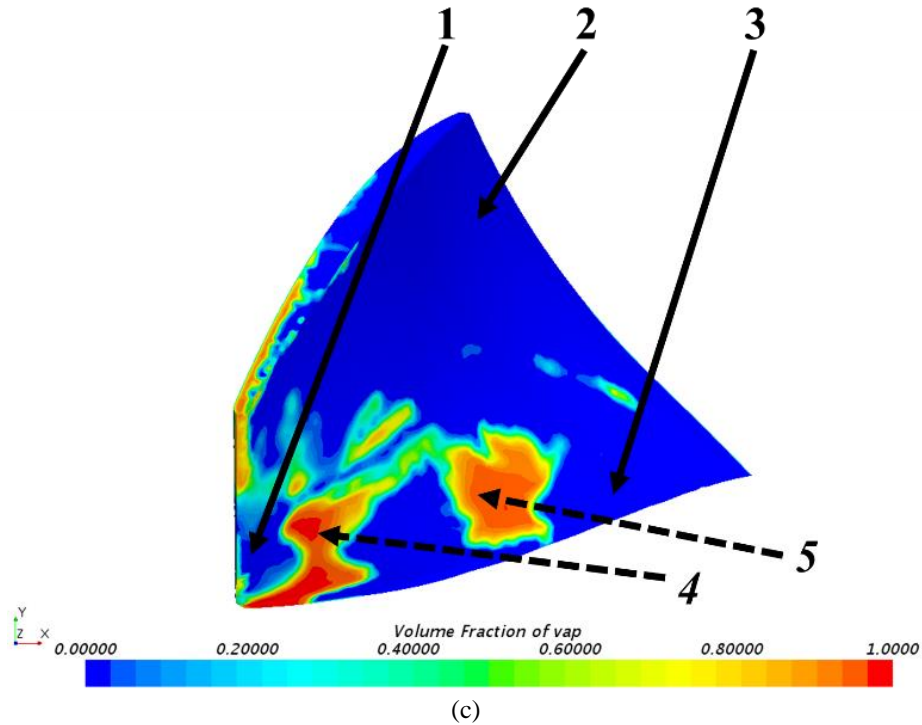
Figure 7-32: Distribution of (a) air volume fraction, (b) absolute static pressure (log scale), and (c) vapor volume fraction over the rotor blade suction side

(C) Vapor Content Comparison

Time averaging the VVF on the rotor parts gives a unique number for each case. The surface and time-averaged VVF number is directly related to flow behavior and the interaction of air distribution over the rotor. VVF is used to compare the amount of vapor created on the blades and hub in each case (no-air, 1 port, 12 ports, and 6 ports: 2B3P). Table 7-14 shows the VVF and expected mechanical power (P) for the cases of no-air, 1 air-port, and 12 air-ports. The percentage change (reduction in VVF and increase in P) is based on the no-air result as a reference. Air-water flow rate ratio (Q_a/Q_w) is calculated in each case to point to the effect of increase the amount of injected air.

Table 7-14: Air treatment outcomes compared to no-air case

Cavitation Case	No-Air	1 port	12 ports
Q_a/Q_w (%)		1.45	16.4
VVF (Blades, Hub)	0.23, 0.28	0.21, 0.26	0.12, 0.22
% VVF Reduction		9.25, 4.32	47.1, 20.1
P (W)	26.46	26.53	28.7
% P Increase		0.26	8.5

With results shown in Table 7-14, air works as a barrier between the solid surface and the low-pressure water on the blade suction side, minimizing the chances of nucleation. On another side, air increases the static pressure of the mixture, keeping the liquid phase stable. Consequently, the formation of vapor is reduced, leaving the liquid water (higher dynamic viscosity) to drive the rotor blades. It can be noticed that the increase of the mechanical power is directly related to the reduction in the vapor content around the rotor.

(D) 2B3P Evolution

Getting into a fitter design, the 2 blocks of 3-ports (2B3P) design (previously mentioned as the divided 6-ports design) is proposed for a better camera view of air distribution after injection in the experimental setup. Being tested in CFD, Table 7-15 lists the same values studied before (VVF and P) between the no-air as a reference and the 2B3P design. A reduction in VVF and rise in P are also documented for the 2B3P air injection pattern. In the regard of 1-port case, Q_a build-up by 5 times in 2B3P attenuates the vapor presence by 19% and 7.7% on the rotor blades and hub respectively. Meanwhile, P grows by 2.6% as an outcome.

Table 7-15: 2B3P air injection design compared to no-air case

Cavitation Case	No-Air	2B3P
Q_a/Q_w (%)		9.2
VVF (Blades, Hub)	0.23, 0.28	0.17,0.24
% VVF Reduction		25.6,14.4
P (W)	26.46	27.2
% *P* Increase		2.8

(E) Port Location Comparison (2B3P)

Finally, comparing with a cavitation only case, injection of each port is remedying the cavitation problem by reducing the vapor content, but in a distinctive magnitude than the others. Recorded data in Table 7-16 are showing the superiority of port (1) over the other two injection ports. Considering port (2) as a baseline since it is the lowest performer, ports (1) and (3) are had a relative reduction of 48% and 37% respectively.

Table 7-16: Air treatment outcomes of air ports at different locations with respect to the blade

Cavitation Case	Port (1)	Port (2)	Port (3)
Q_a/Q_w (%)	1.4	1.4	1.4
VVF (Blades, Hub)	0.14, 0.34	0.27,0.33	0.17, 0.33
% VVF Reduction	48, 0		37, 0
P (W)	1221.5	1193.6	1208.6
% *P* Increase	2.3		1.25

Using a proposed function on STAR-CCM+ for augmenting the volume fraction of each mixture component, the three fluids can be represented on one scene with a scale starting with 0 (complete air: blue color) and ends with 2 (complete water vapor: red color), while 1 is (complete water liquid: green). This kind of scales helps in understanding the distribution of the flows and shows almost perfect matching with the normal volume fraction of one component only. Figure 7-33a, b, and c are longitudinal mid-section scenes of the new scale (called 0_VF2) with a close-up to injection ports (1, 3, and 2 respectively) to comprehend the physics behind the difference in outcomes. The assessment is done at the same time which synchronizes a blade passing by the port under interest. In Figure 7-33a, port (1) gives the largest injection depth into the liquid water ($h_{air,1}$= 2.5 mm), pushing air to cover wider zone by the effect of the axial flow sweep and the blades rotation. Additionally, air reaches the leading edge (major cavitation part) after less than three cycles and works in limiting the vapor around. In Figure 7-33b, port (3) injection is disturbed by the blades rotation (i.e. less jet height) at one hand, but on the other hand, the port faces a thicker section of the passing blade which allows more contact time between the blade and jet and consequently higher chances of air slide to the blade suction side due to the two surfaces pressure difference (the reason behind tip vortex rotations). Lastly, in Figure 7-33c, port (2) is similar to port (3) in interrupting the incoming air jet, and the blade section is thinner (i.e. less contact time) which lead to more resistance against the aeration treatment.

(a)

(b)

134
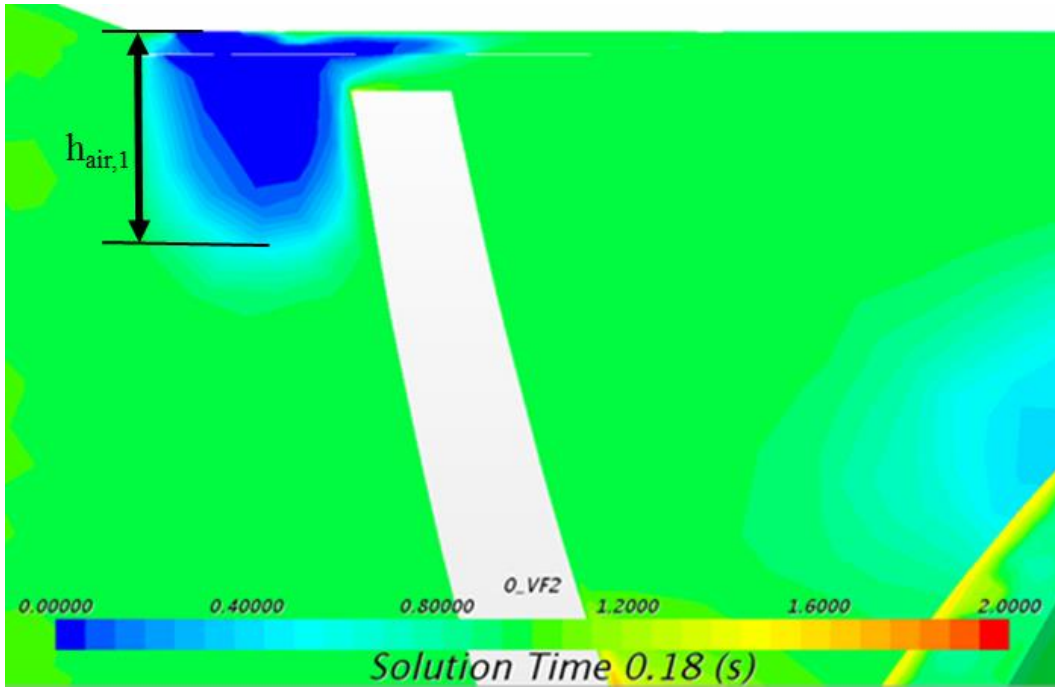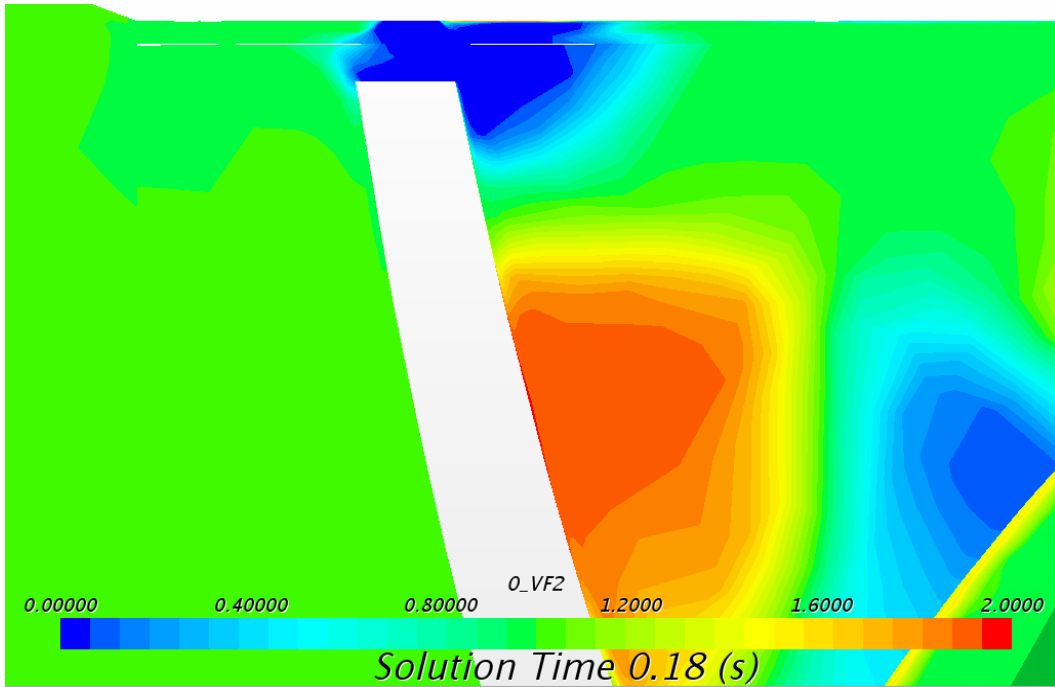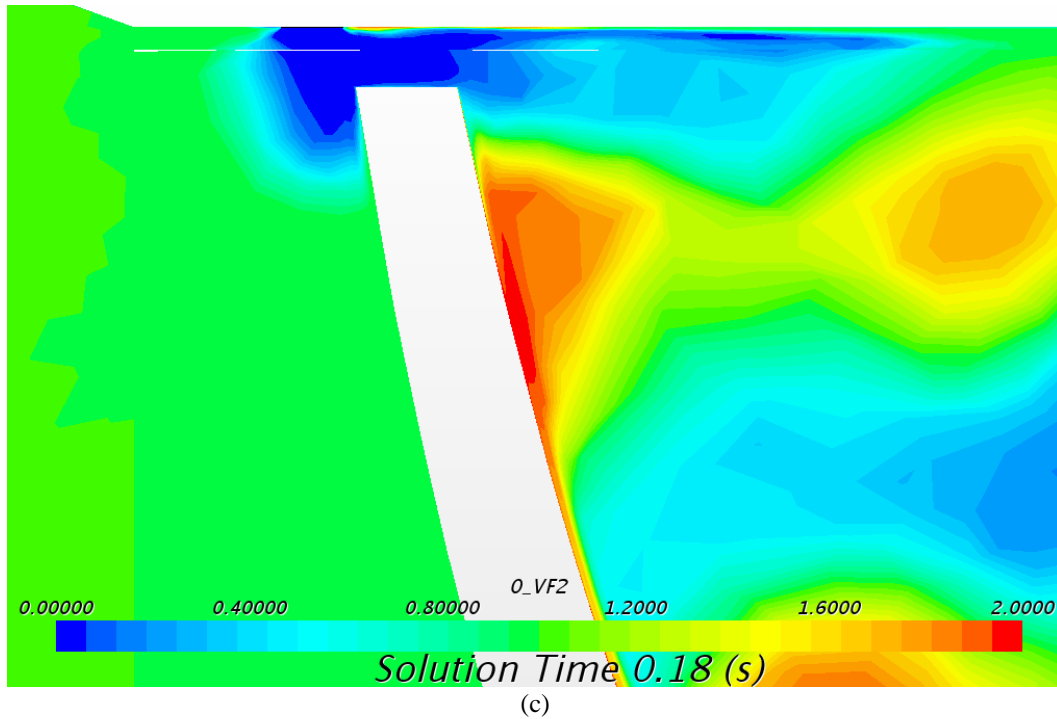
Figure 7-33: Volume fraction scenes of the three fluids (air jet: blue, liquid water: green, and vapor: red) with different air ports locations (a) port 1, (b) port 3, and (c) port 2. A blade section is the white region

A comparison between port (2) and (3) is done at the same transverse section downstream the ports (Figure 7-34). It was noted that the same section, the air from port (3) slides closer to the blade and it has a deeper distribution over the suction side, which is reflected on minimizing the VVF over the blades as viewed in Figure 7-35 and represented previously in Table 7-16.
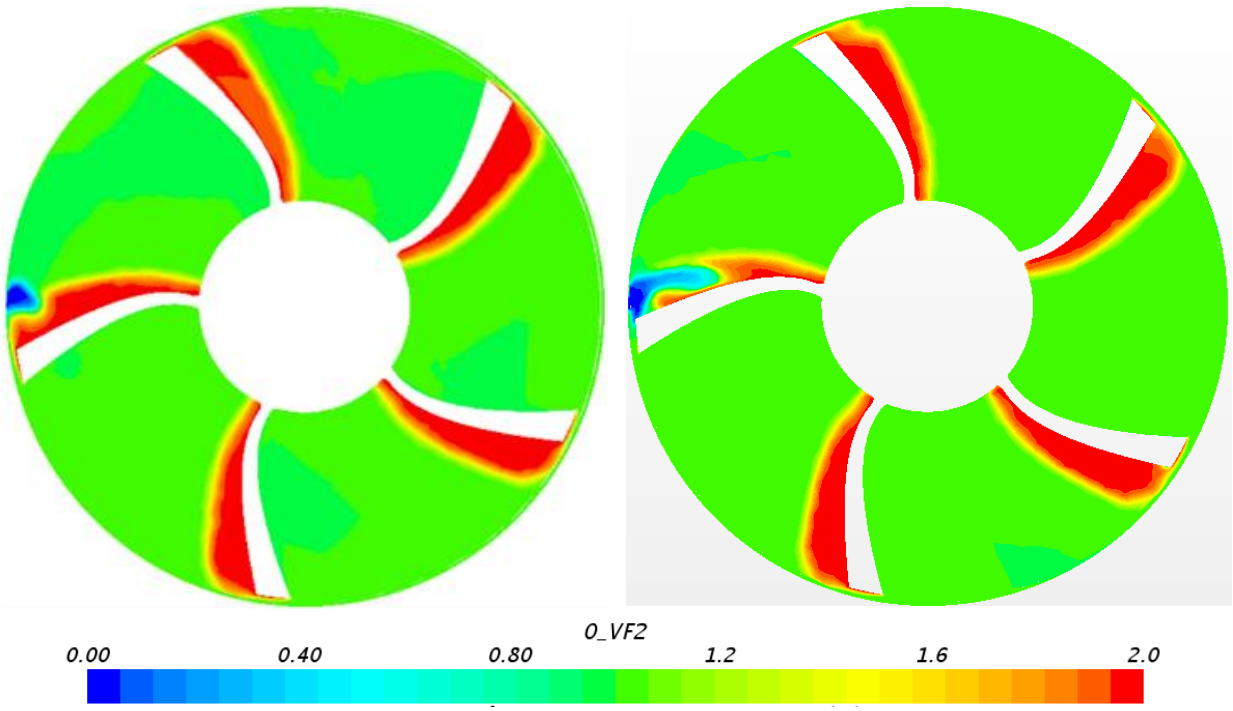
Figure 7-34: Volume fraction scenes of the three fluids (air jet: blue, liquid water: green, and vapor: red) at a section downstream the ports (2: left) and (3: right)

Volume Fraction of vap

0.00   0.20   0.40   0.60   0.80   1.0
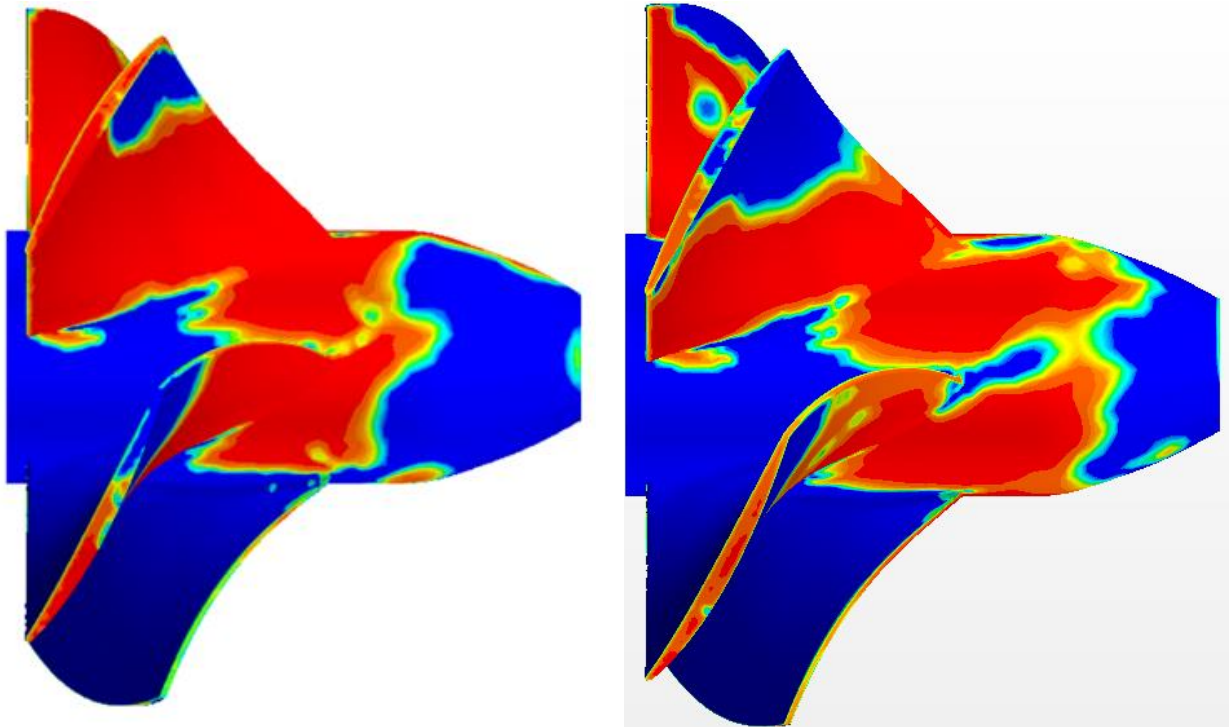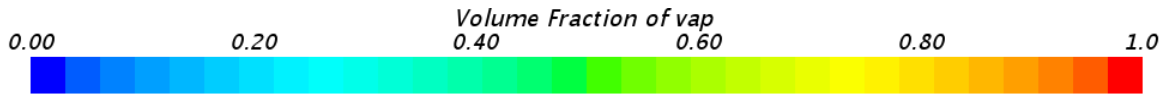
Figure 7-35: VVF variation over the rotor (blades and hub) in cases: port (2: left) and port (3: right)

7.2.4 Advanced Housing Air Injection

The work here expanded the domain to include the all-inclusive turbine system (i.e. 9 million cells). In addition to the change in the computational domain, the inlet boundary considered the turbulent inflow as mentioned previously in Eq. (5-1). Finally, seeking a common denominator for the area averaging, the blades and hub VVF are divided by the total rotor surface area (A_{rotor}).

(A) Turbine operation range (2B3P)

Expanding the work on the 2B3P, the turbine was tested over the operation range (1000-5000 rpm) to fully understand the treatment effect on the turbine at the different conditions, and more importantly, the highest power/efficiency point where the turbine is supposed to be operating around. First, the VVF plot in Figure 7-36 demonstrates the reduction of the vapor content in the different operation cases while preserving the cavitation trend (except for N=3000 rpm as the maximum reduction point).

137
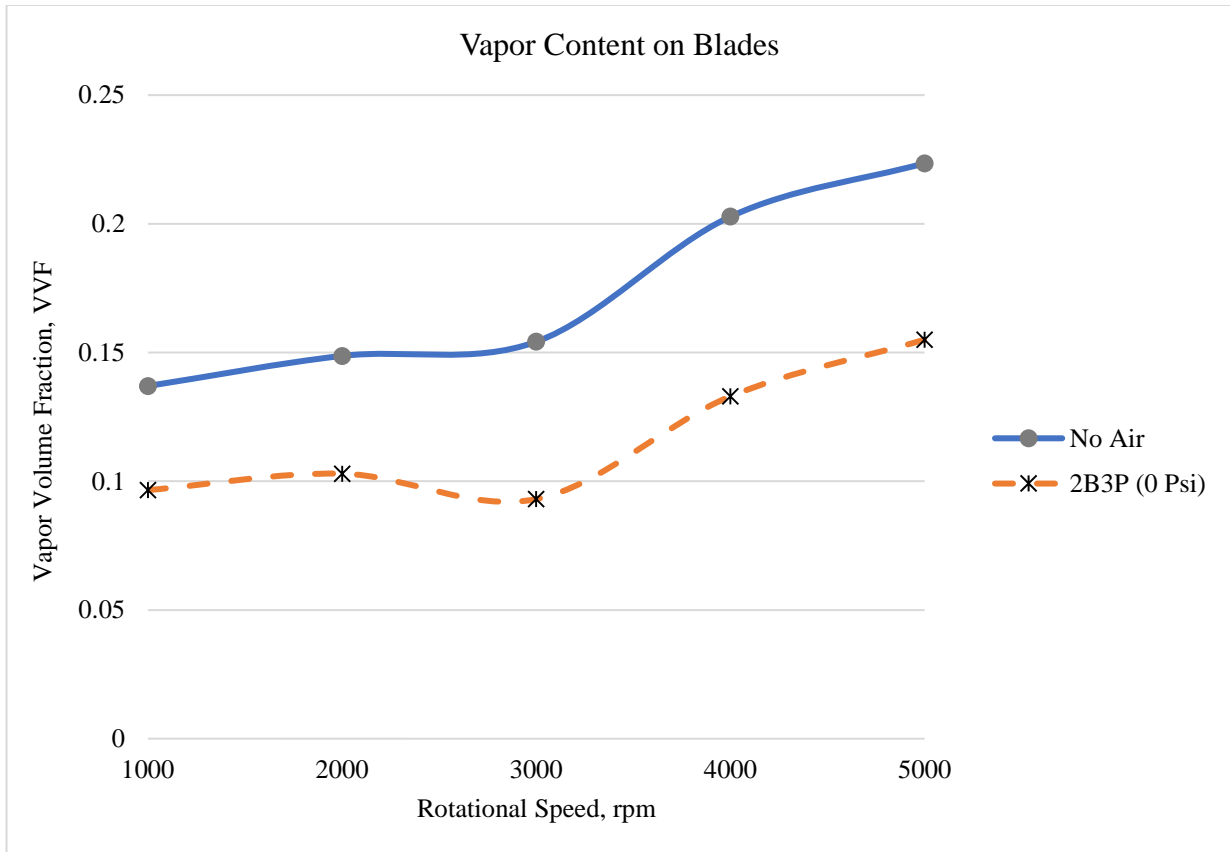
Figure 7-36: Blades VVF trends with turbine rotational speed: no-air and 2B3P treatments

Quantitative analysis in Table 7-17, the amounts of (Q_a/Q_w) are decreasing until a minimum of 5% at 4000 rpm because of the direct proportionality between Q_w and N. At 5000 rpm, the ratio rises again because the pressure around the turbine highly drops below the atmospheric pressure, allowing large Qa to enter the system. Second, the same Table 7-17 is defining the VVF values and percentage changes for every examined rotational speed. The reduction peaks with 40% at the 3000 rpm which is close to the highest power point (i.e. 4000 rpm), then the reduction go to lower levels as the rotational speed increases.

Table 7-17: 2B3P air injection design compared to no-air in a turbine operation range

Cavitation Case	No-Air					2B3P (0 psi)				
	1000 rpm	2000 rpm	3000 rpm	4000 rpm	5000 rpm	1000 rpm	2000 rpm	3000 rpm	4000 rpm	5000 rpm
Q_a/Q_w (%)						7.1	6.2	6	5.7	6.3
VVF (Blades)	0.14	0.15	0.16	0.2	0.22	0.1	0.1	0.09	0.13	0.15
% VVF Reduction						29.5	30.8	39.6	34.4	32.9

To understand the ineffectiveness of the increased Q_a on vapor content reduction, the scenes of Figure 7-37 illustrate migration of the air (iso-surfaces) away from the blade SS to be closer to the blades tip and the housing than blades/hub zone. The increase of N tends to interrupt the air injection and blocking it, leading to sweep the air with the liquid water in the axial direction rather than radially-inward jet. Moreover, once the air jet gets into system, it is influenced by the radially-outward centrifugal force with is a direct function of N.

Average Volume Fraction of Water Vapor

(a)

Average Volume Fraction of Water Vapor

0.000   0.200   0.400   0.600   0.800   1.00

(b)

Average Volume Fraction of Water Vapor

0.000   0.200   0.400   0.600   0.800   1.00

(c)

Average Volume Fraction of Water Vapor

0.000   0.200   0.400   0.600   0.800   1.00

(d)

Average Volume Fraction of Water Vapor

0.000   0.200   0.400   0.600   0.800   1.00
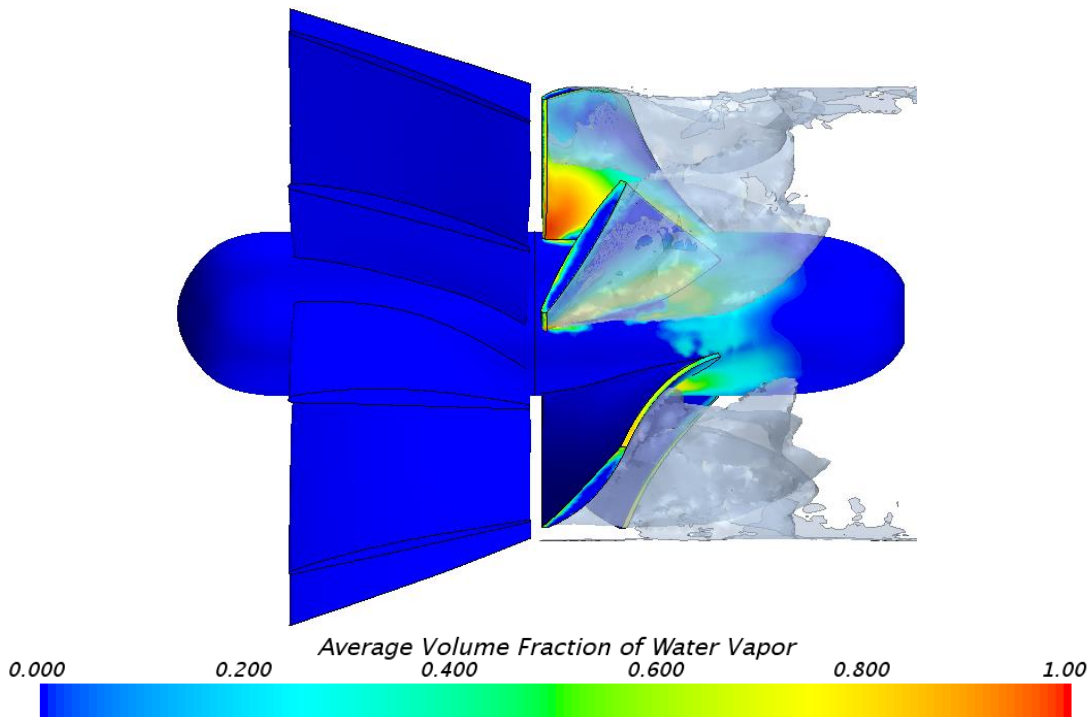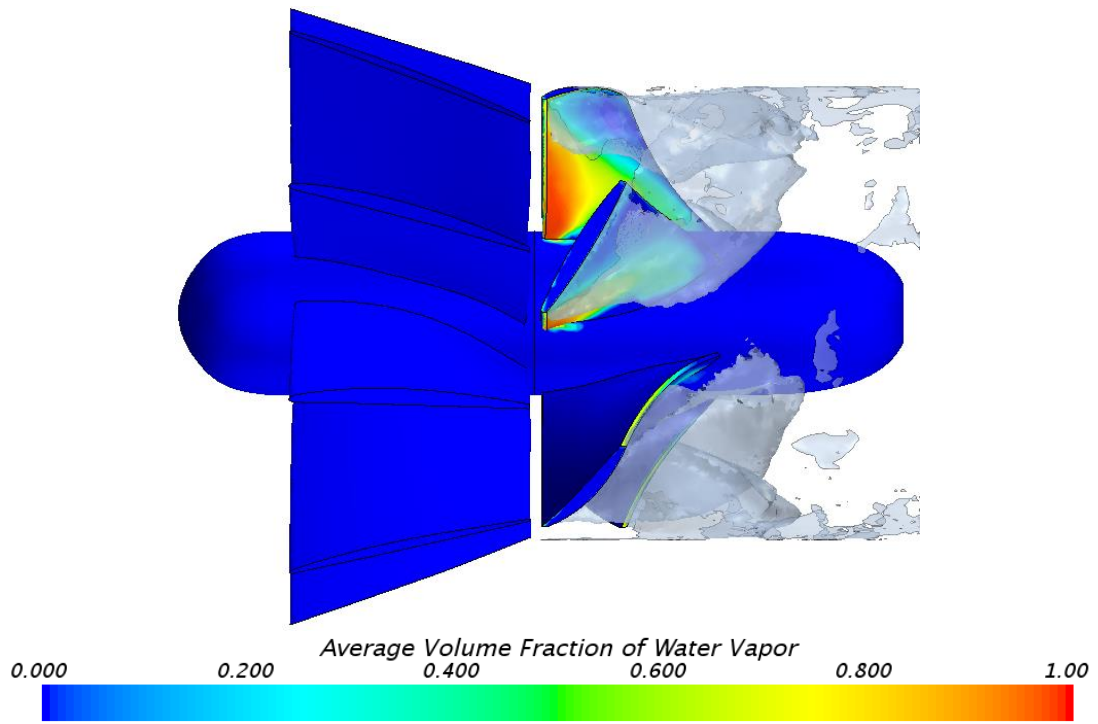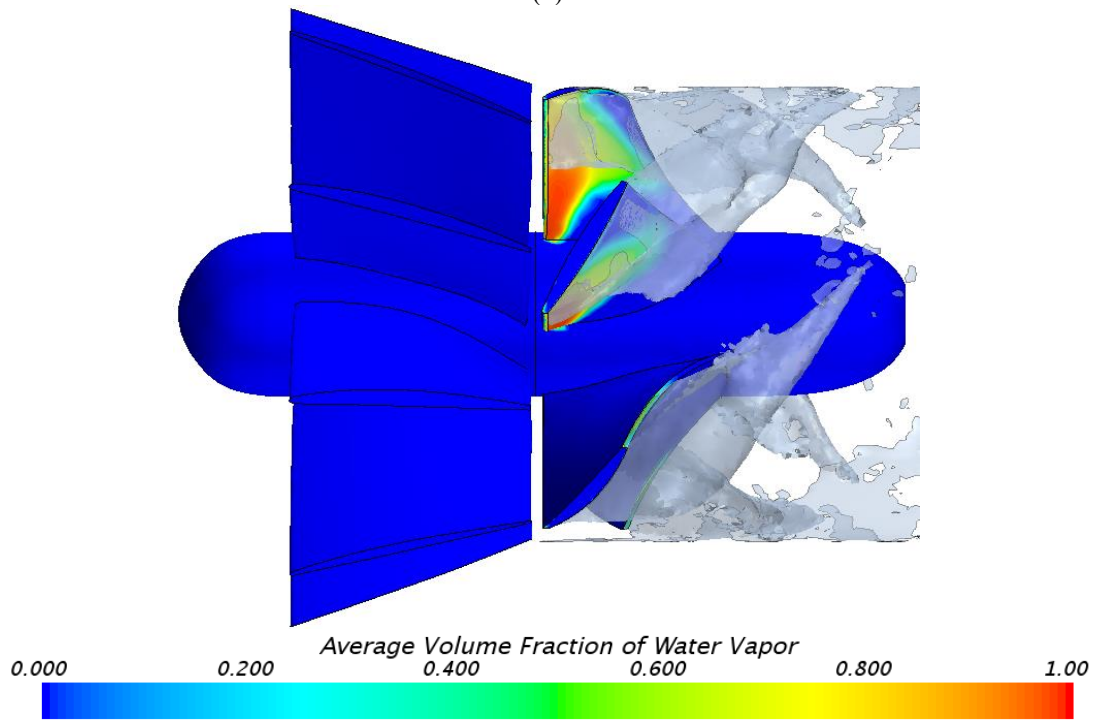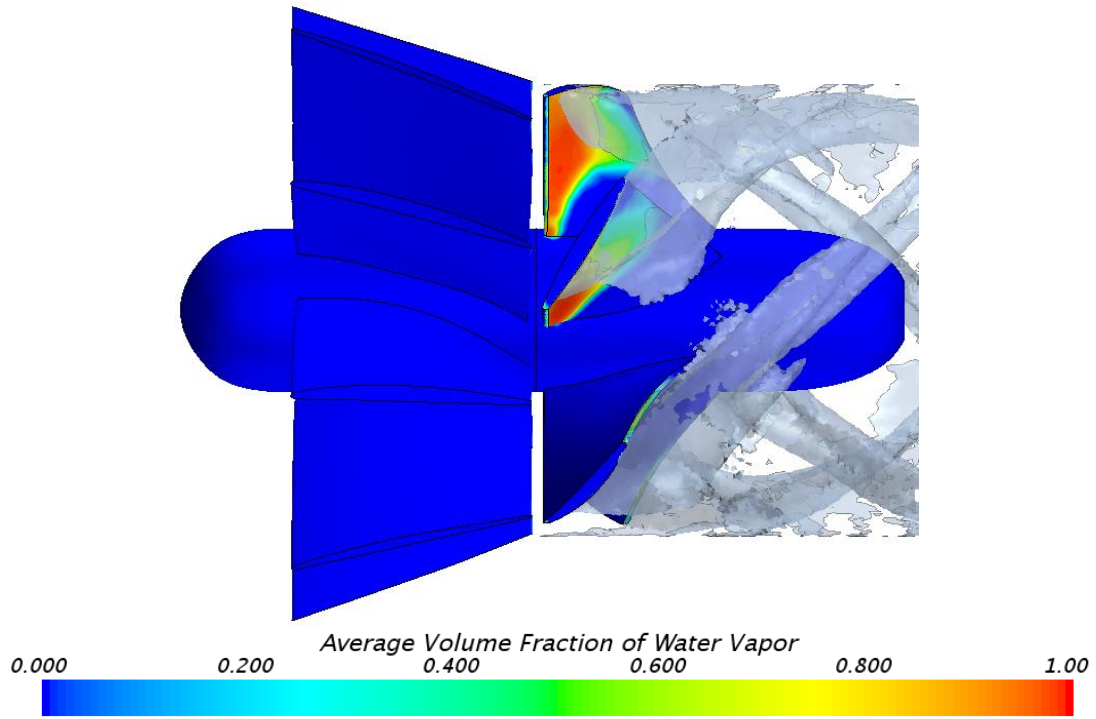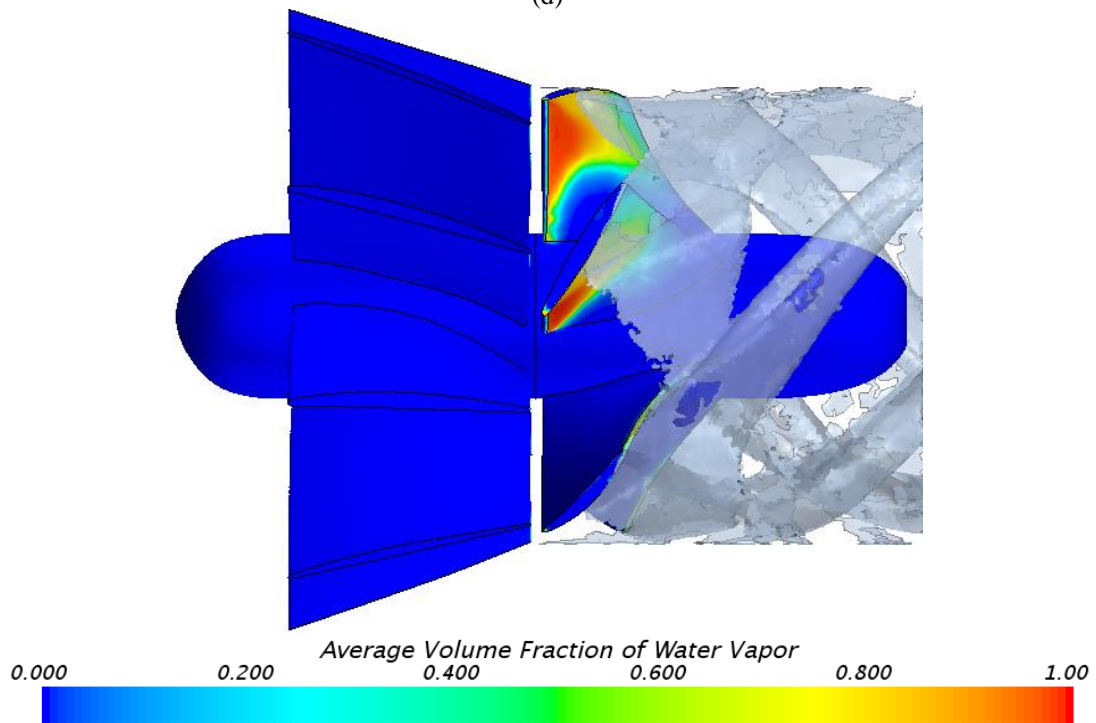
(e)

Figure 7-37: VVF and air cloud variation over the rotor (blades and hub) in cases: (a) 1000 rpm, (b) 2000 rpm, (c) 3000 rpm, (d) 4000 rpm, (e) 5000 rpm

Checking the cases before and after the air injection, two operation curves are drawn for the turbine performance as shown in Figure 7-38. While the performance could be improved by the air injection at the low N (e.g. 1000 and 2000 rpm), the improvement starts to be diminished, nullified at 2500 rpm, then turns to be a performance decline at higher N (3000-5000 rpm). This is related directly to the increase of the pressure difference (i.e. P_{air} - P_{rotor}) allowing more air to enter the system. Excess air starts to dominate the system (non-condensable gas) and does not help in treating the cavitation because of radially-outward shifting at the high N.
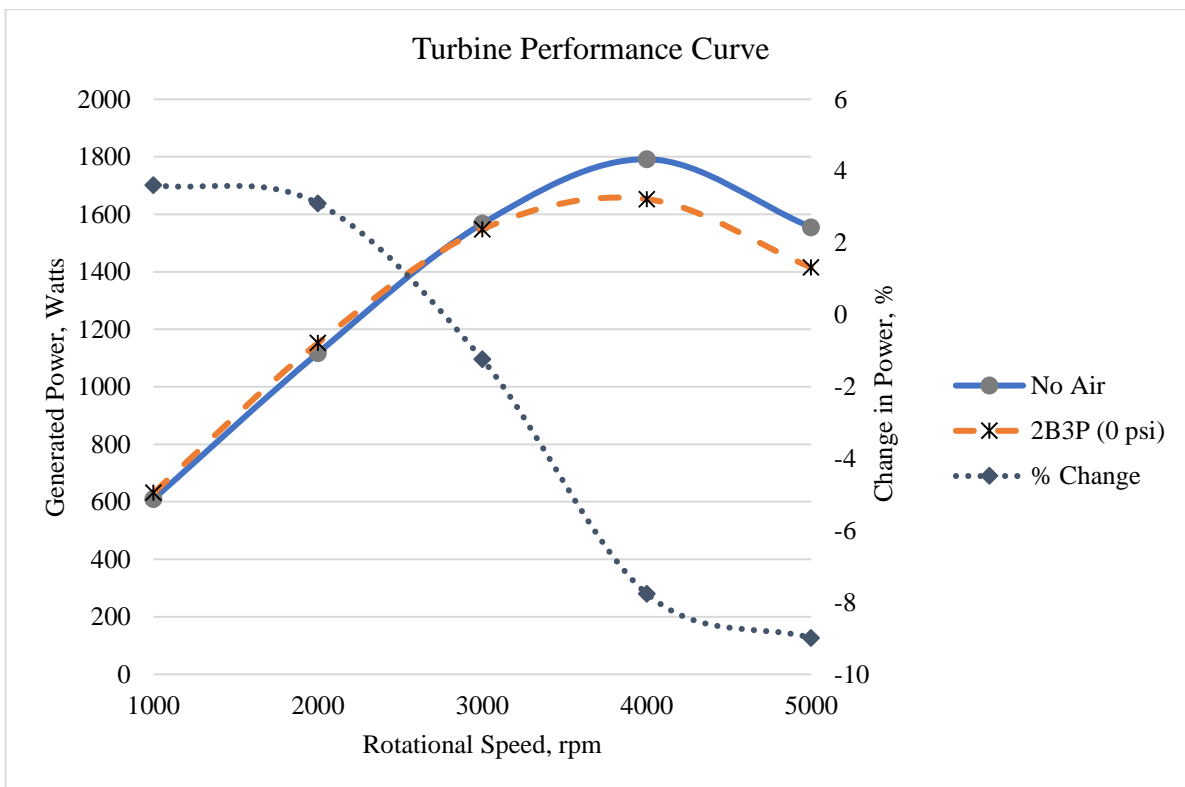
Figure 7-38: Operation curves of the 7.5-cm turbine under two circumstances: cavitation only and 0 psi (2B3P) air injection

7.2.5 2B3P Experimental

To test the effectiveness of air injection system, the experimentation was conducted on both cavitation patterns (cloud and TLV) of a motor-driven propeller with same turbine design. At each

case, the injected air was compared to no-air case at same propeller rotational speed (N) and water flow rate (Q_w). The comparison is based on the consumed power ($\boldsymbol{P}_{motor}$) by the motor driving the turbine. Earlier constant-head experimentation proven that when air is injected, it contracts the cross-section area, ending with less water flow. To stabilize Q_w with air injection, the recirculation pump was kept at the same supply frequency, so the water level in the head tank rises and Q_w reaches the rate before the injection. As a result, the water head had risen at the different injection stages from 2.3 m to 2.38 m. It is worth mentioning that constant flow rate experimentation is more recommended than constant water head for treating the same cavitation circumstances besides impartially comparing the propeller characteristics at the same flow velocity.

For the reversed propeller, the cavitation cloud was induced firstly at no presence of air, and output data such as (N, P, and Q_w) were documented with a visual recording for the cavitating rotor in action. In a following step, air is injected at three different pressures (3, 6 and 12 psig) with considering the outcomes from each pressure. The results are tabulated in Table 7-18, and the comparison endorsed the concept of less drawn motor power at same operating conditions of speed and flow rate. All the air injection cases exhibit improvements expressed by reductions in the drawn power compared to "No-Air" case. At Q_w=0.0088 m³/s and $N_{reversed}$= 950 rpm, air injection at the three different pressures reduced $\boldsymbol{P}_{motor}$ by 7.7%. The second main observation is the increase of the improvement by increasing the air pressure, but the improvement increase reaches a peak at 6 psi (% reduction in $\boldsymbol{P}_{motor}$= 10.4%), then there is a declination in the improvement by pressurizing with higher pressures (i.e. 3.4% performance declination at 12 psi).

Table 7-18: Experimental 2B3P air injection under different injection pressures with flow and motor variables (reversed propeller)

Cavitation State	No-Air	Air (P=3 psi)	Air (P=6 psi)	Air (P=12 psi)
Q_w=0.0088 m³/s	P_{motor} (W)	P_{motor} (W)	P_{motor} (W)	P_{motor} (W)
(V= 2m/s)	62.5	59	56	58.1
N= 950 rpm	ΔP_{motor} %= 0	ΔP_{motor} %= 5.6	ΔP_{motor} %= 10.4	ΔP_{motor} %= 7

Similarly, the streamwise propeller generated TLV cavitation at N=2500 rpm by the force of motor; exceeding the non-cavitating no-load speed (N=1900 rpm) of the turbine. The same conditions of air injection were maintained at the same pressures as the previous case. Table 7-19 illustrates the effect of air injection on the consumed motor power at Q_w=0.0114 m³/s and $N_{streamwise}$= 2500 rpm. Generally, the outcomes from the three air pressures are variable, and they are considerable when compared to motor power of the "No-Air" cavitation case (5.9% less P_{motor} in average). The performance improvement because of air injection increase by the air pressure until peaking at 6 psi (9.5% reduction in P_{motor}), then declines again at 12 psi.

Table 7-19: Experimental 2B3P air injection under different injection pressures with flow and motor variables (streamwise propeller)

Cavitation State	No-Air	Air (P=3 psi)	Air (P=6 psi)	Air (P=12 psi)
Q_w=0.0114 m³/s	P_{motor} (W)	P_{motor} (W)	P_{motor} (W)	P_{motor} (W)
(V= 2 m/s)	280	270.8	253.3	266.4
N= 2500 rpm	ΔP_{motor} %= 0	ΔP_{motor} %= 3.3	ΔP_{motor} %= 9.5	ΔP_{motor} %= 4.9

Another type of experimentation was run at a constant air pressure (6 psi) and flow velocity (2.5 m/s at the 7.5-cm pipe) while speeding up the propeller rotation streamwise from 1000 to 2500 rpm (maximum achieved by the motor) with a 500-rpm step. As shown in Figure 7-39 , the motor

144

power is increasing with the rotational speed, and the air injection treatment is showing an improvement in all studied cases. Despite the improvement, the reduction in power is decreasing at fast-rotational speeds. Doubling the rotational speed (from 1000 to 2000 rpm), the improvement by P_{motor} reduction declined rapidly from 6.7% to 1.4%.
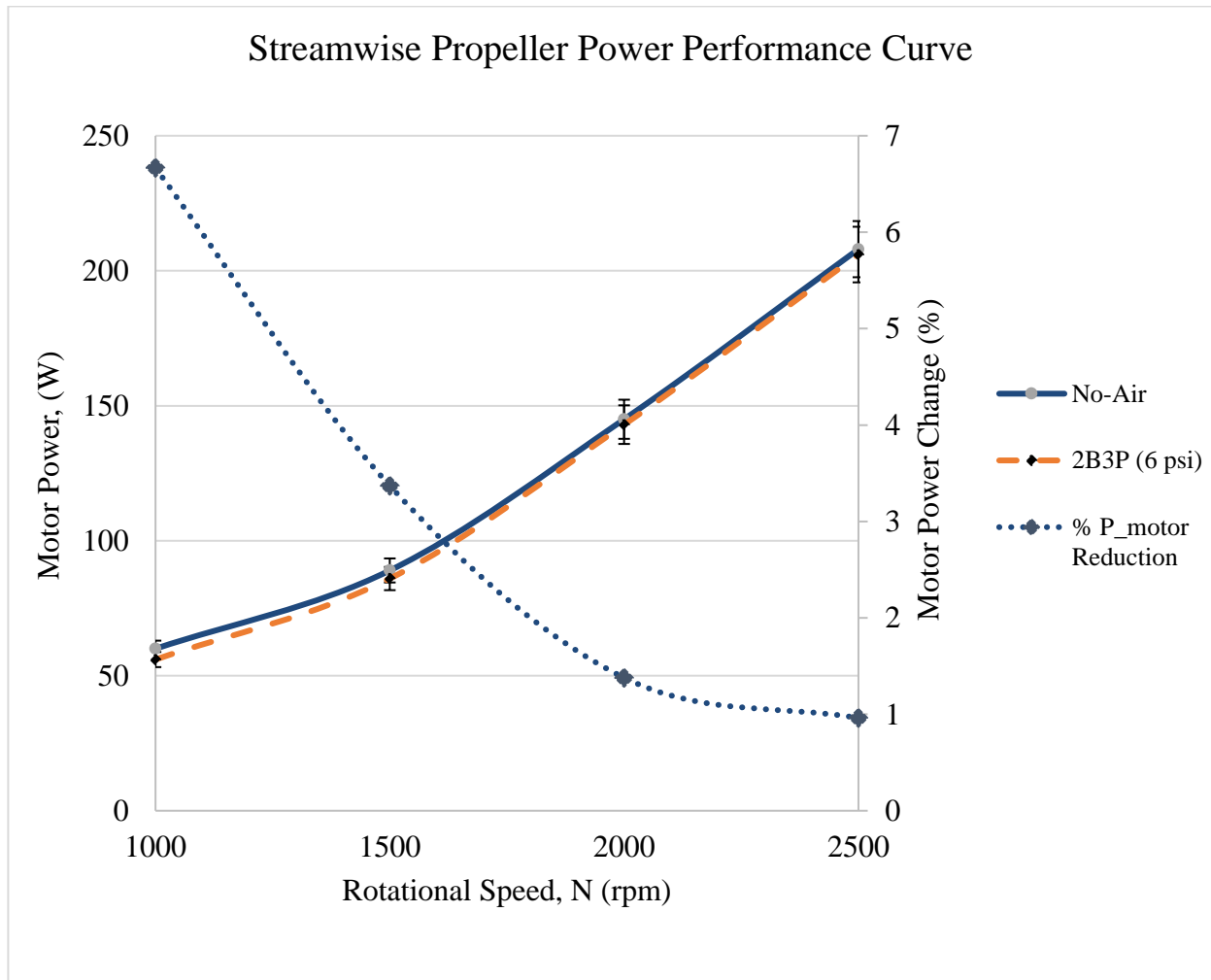
Figure 7-39: Operation curves of the 7.5-cm streamwise propeller under two circumstances: cavitation only and 6 psi (2B3P) air injection

7.2.6 **Hub Air Injection**

The proposed design is targeting the blade SS by injecting pressurized air. The diameter (dj= 3 mm) and pressure (P_{air}= 5 psi) are selected based on previous and corresponding researches that

involved parametric studies for the hub air-injection optimization. Ordering the results in columns as in Figure 7-40, each N has four air injection treatments representing the rows of holes behind the blades (symbolled by R1, R2, R3, and R4). First of all, the air injection from any row is effective in reducing the vapor content generated at the no-air case (i.e. first column). Second, though cavitation starts at the leading edge, R1 injection (i.e. the closest to the cavitation location) shows the least effectiveness compared to the other rows.
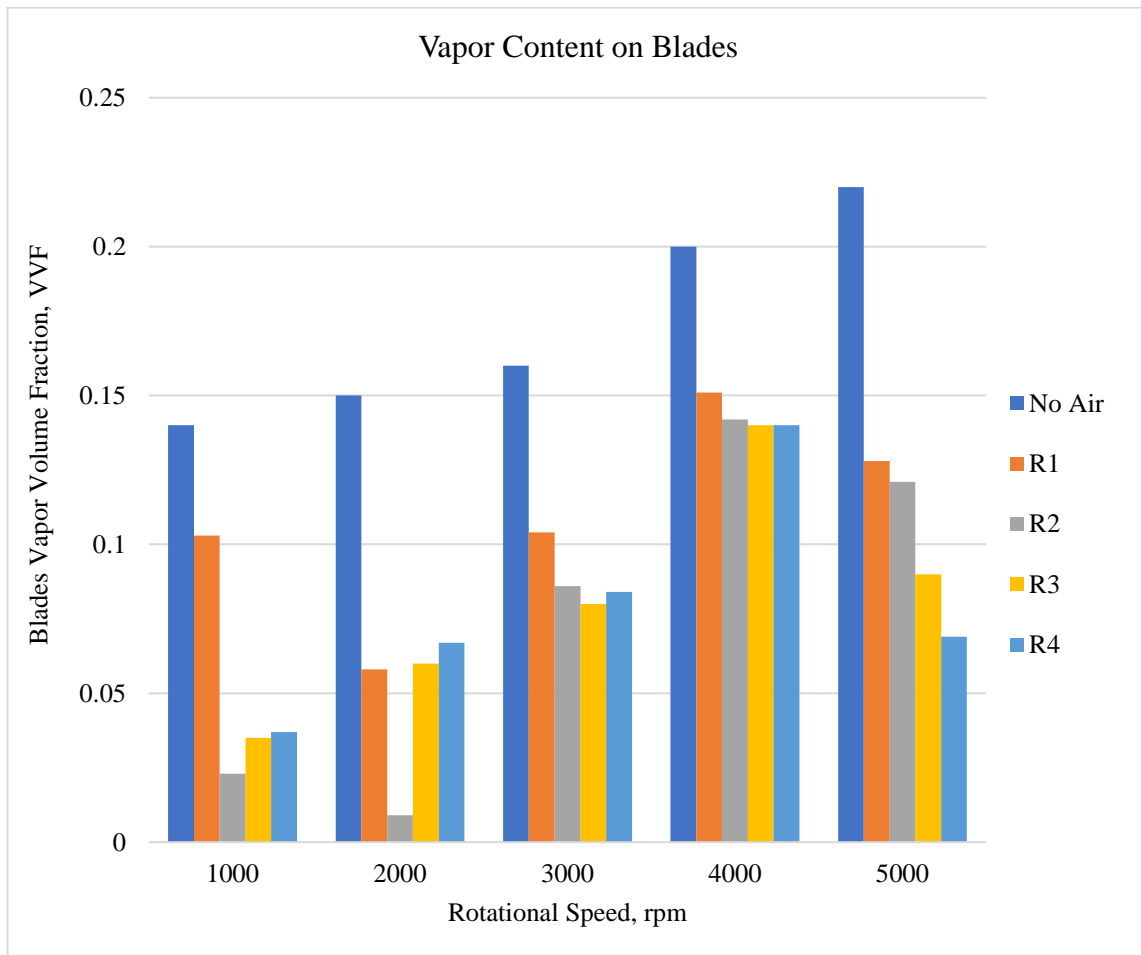
Figure 7-40: Blades VVF in the cases of No-Air and air injection from Rows 1, 2, 3, and 4

Table 7-20 is listing the percentage reduction from the VVF of the no-air case at each N. With a red font at the most reduction at each rotational speed, R2 injection has an effective cavitation

146

mitigation at the low speeds (i.e. 1000 and 2000 rpm), meanwhile the effectiveness shifts to the R3 and R4 with the increase of the rotational speed.

Table 7-20: VVF values and percentages of different cavitation cases during the operation ranges

	VVF Before Air Injection	VVF Air Injection (5 Psi)				Percentage Change (%)			
RPM	VVF	R1	R2	R3	R4	R1	R2	R3	R4
1000	0.14	0.103	0.023	0.035	0.037	26.7	83.3	75.0	73.3
2000	0.15	0.058	0.009	0.06	0.067	61.5	93.8	60.0	55.4
3000	0.16	0.104	0.086	0.08	0.084	34.8	46.1	49.4	47.2
4000	0.2	0.151	0.142	0.14	0.140	24.7	28.9	32.0	29.9
5000	0.22	0.128	0.121	0.09	0.069	42.0	45.0	58.8	68.7

For the power change, the curves in fig show that the air injection from R1 was not favorable in regaining power lost due to cavitation. Compared to the no-air case, R1 injection led to more power loss, unlike the other air injection locations (R2, R3, and R4). For R2, and while the VVF reduction was the best at this location, the power regain was either not noticeable or adverse. At higher N, R2 was able to recover power at higher N (3000-5000 rpm). The latter locations, R3 and R4, are always beneficial in regaining some of the lost power with an average of 10.2% and 5.7% over the whole operation range.
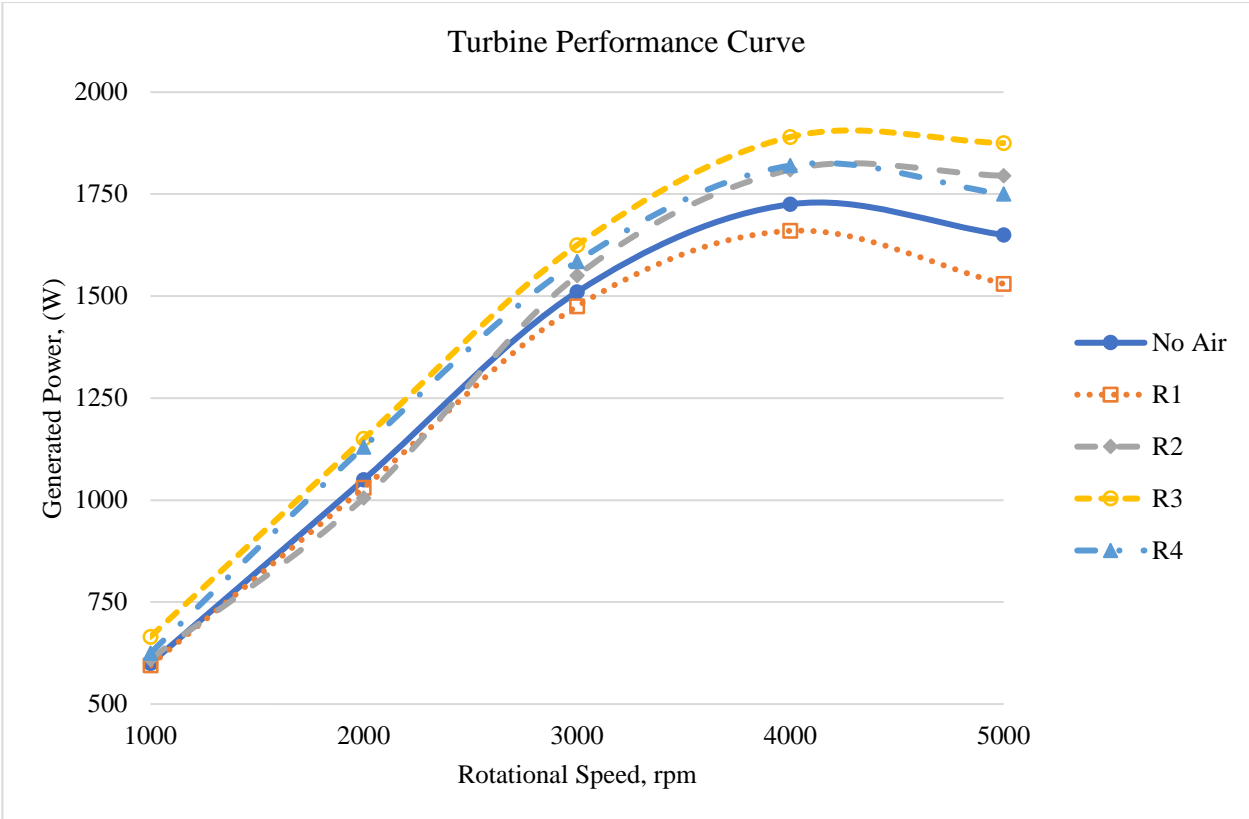
Figure 7-41: Turbine performance curves under the conditions of: No-Air and air injections from rows: 1, 2, 3, 4

7.2.7 Cases Matching and Image Processing

As mentioned in the research roadmap, the certain cases were built based on the experimental propeller test. Three measures were set to determine the matching level between the CFD models and the experimental cases: The cavitation pattern, the motor power, and the cavitation area percentage in the images/CFD scenes. The first case was taken for a streamwise turbine at 2000 rpm and inlet flow velocity of 0.45 m/s in the 15 cm pipe. Figure 7-42(a) shows the instantaneous cavitation formation on two turbine blades after the entering steady state phase. After the comparison of different time frames, the blades walls (dashed lines) and cavitation boundaries (solid line) were tracked and defined in each frame for as illustrated in Figure 7-42(b). With such definition, the matching with the CFD scene was easier. The cavitation starts from the blade

leading edge and extends upwards to touch the pressure side of the succeeding blade then declines while going downstream to join a merging zone after the blades. The same phenomenon can be interpreted from the time-averaged cavitation cloud (white formation on the brown rotor) seen in Figure 7-42(c).
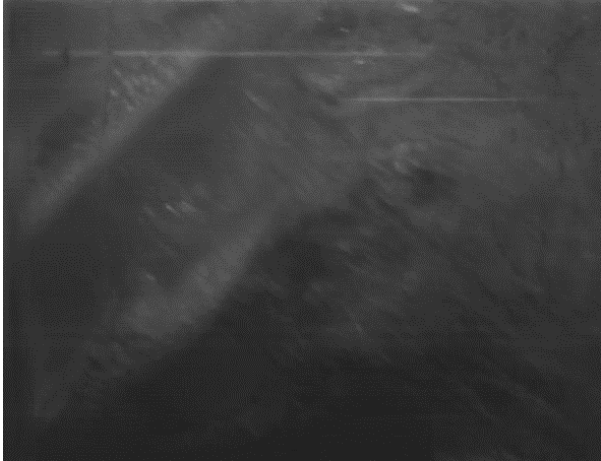
(a)
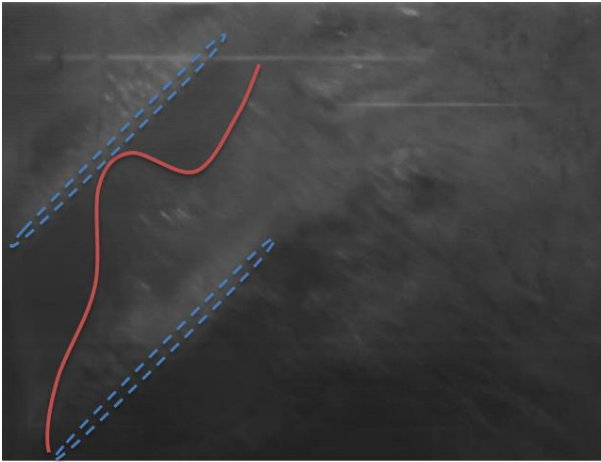
(b)
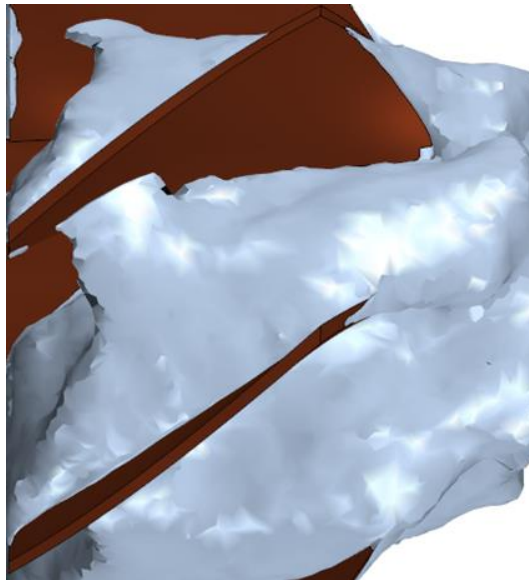
(c)

Figure 7-42: Cavitation formation around 2000 rpm streamwise propeller: (a) Timeframe image, (b) Timeframe image with the defined blade and cavitation boundaries, (c) Time-averaged cavitation based on CFD

Further investigation involved the image processing that worked on cropping the image to the intended area (two blades), enhanced the contrast, and converted the new image into either the RGB (Red, Green, Blue coloring system) or the binary logic (1= white and 0= black, according to a threshold value to differentiate between the contrast of the different pixels) as illustrated in Figure 7-43.
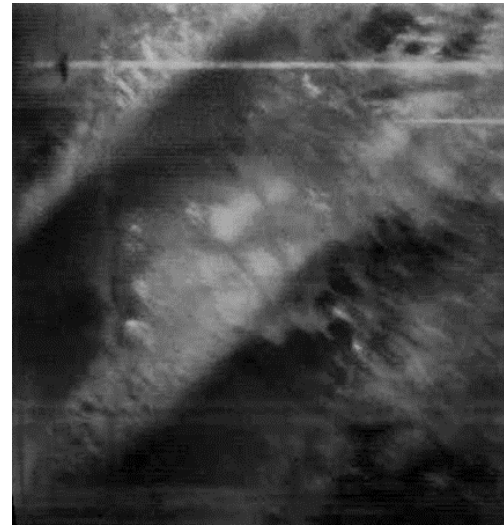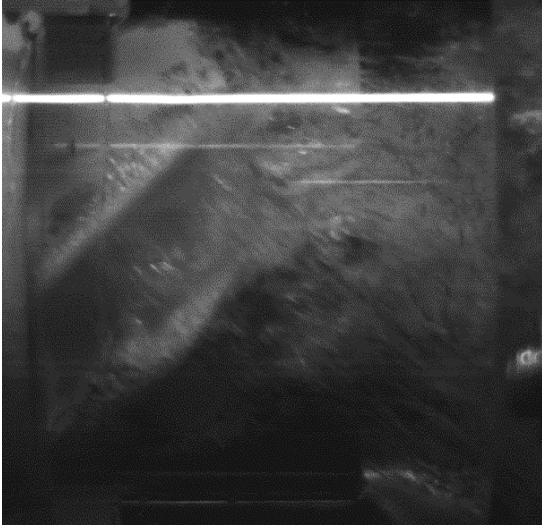
(a)
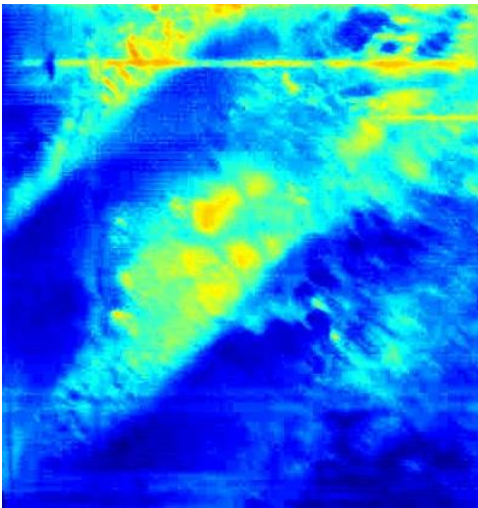
(b)

Figure 7-43: Image processing for the high-speed camera images, (a) Left: Original image for the rotor; Right: Cropped around two blades and contrast is enhanced, and (b) Left: RGB coloring; Right: Binary contrast

The RGB coloring added a clarification for the cavitation propagation. As shown in the figure above, the dark blue area is a no cavitation zone, while the others represent the vapor existence. The visualization leads to the realization of the cavitation extents once generated and detached from the blade. A better agreement with the CFD scene from Figure 7-42 can be noticed. For the binary image, the white pixels (representing the cavitation) are added and divided to the total

151

number of pixels (black and white) to give a ratio. This is compared to the binary scene from the CFD where the cavitation is distinguished easily based on rotor elimination from the scene (A baseline scene with no cavitation helps in defining the rotor extents which can be subtracted from the cavitation scenes), then a grey scaling step followed by a binary conversion take place with the advantage of setting black background and white cavitation in the scene properties. The scene treatments are represented in Figure 7-44.

(a)
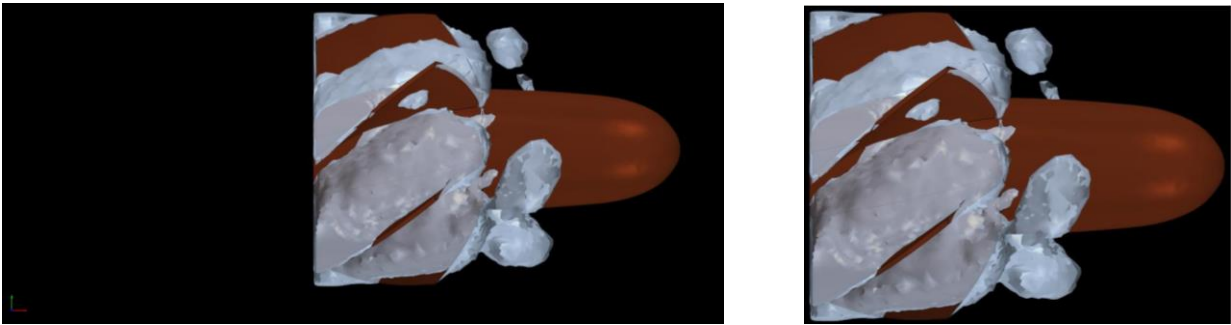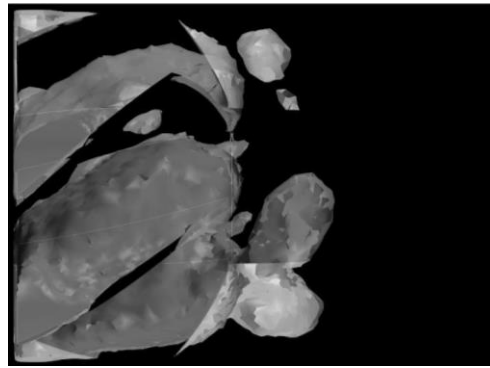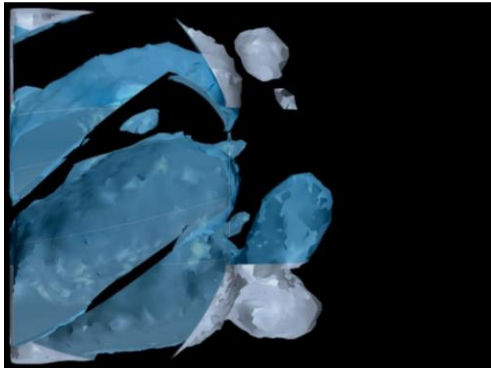
Figure 7-44: Image processing for the CFD scenes, (a) Left: Original image for the whole rotor; Right: Cropped to the rotor extents, and (b) Left: Rotor subtraction; Right: Grey-scale; Down: Binary conversion

The resultant binary image/scene are used to calculate the area based on the white-pixels ratio. The final result shows a very close data from the high-speed image (44% cavitation area) versus the CFD scene (47% cavitation area).

The third approach evaluates the motor's power to spin the rotor shaft under the flow and cavitation conditions. For the case of the (V= 0.45 m/s N= 2000 rpm), the power drawn in the experimental setup watts $55\pm5\%$ Watts, while the CFD resulted in a 70 Watts from the torque calculation on the blades. The CFD result did not change by any further mesh refinement, and it was accepted as the closest to be offered result by the numerical models used (i.e. VOF, LES, RBM).

A second case stepped up the rotational speed to N= 3000 rpm, and consequently, the inlet velocity increased to V= 0.56 m/s in the 15-cm pipe. The image processing lead to a cavitation percentage of 56% for the experimental imaging and 59% for the CFD, and the motor power was found to 197 and 220 Watts. It is worth mentioning that the CFD simulations were able to predict the power type (i.e. consumption) by generating a negative sign. A group of image processing illustrations (binary conversion) is seen in Figure 7-45.

(a)

(b)

Figure 7-45: Image processing for the high-speed camera images (left) and CFD scenes (right): (a) V=0.45 m/s, N= 2000 rpm, and (b) V=0.56 m/s, N=3000 rpm

CHAPTER 8 - RESEARCH CONCLUSIONS AND FUTURE WORK RECOMMENDATIONS

8.1 Thermal Uniformity:

8.1.1 Conclusions

Passive mixing-enhancement methods can be engineered for staggered holed dilution system by inserting streamlined bodies at the centerline of the mixing section. Uniformity number, x, is defined to quantify the temperature distortion and deviation from ideal situation, and it was used for comparing each case because of its uniqueness. Streamlined bodies like prolate spheroid and piriform introduce better mixing outcomes than staggered-holes (SH) chamber by 18.8% and 15.6%. Design ratios like aspect, blockage and profile ratios (AR, BR, and PR respectively) are important to the degree of uniformity required by controlling the amount of induced radial flow at certain Re. Doubling BR and halving AR by just increasing the shape maximum diameter at the same running conditions can result in 10 times uniformity number improvement on average, with less pressure drop. Meanwhile, PR has proved to be a good expression for every design, and it has a 3rd order polynomial with the uniformity change from the basic SH. Prolate spheroid (i.e. American football, FB) of larger diameter (AR=1.5, BR=0.49, PR=0.28) is selected to be the best design for boosting the crossflow mixing.

The addition of swirling fins was the primary interest to increase the vorticity in the flow and enhance dispersion. Flow and temperature fields with the seven swirling patterns were numerically simulated, analyzed and represented in graphical and calculated data, ending with one geometry

selected for experimentation. F4SR was endorsed because of acceptable uniformity factor (16% better output than plain football FB) resulted from fixed fin thickness and smaller wake region generated behind (i.e., low-pressure drop), allowing big central dispersive eddy in addition to the small ones from the jet entrance. The anticipated 16% increase in the pressure loss is not significant in the power generation applications (maximum condition is 0.7% power drop per inch water pressure loss).

A good agreement was realized between the results of the simulated and experimented cases of F4SR even with the little difference in Re. The performance of F4SR topped those of SH and FB configurations by 47% and 24% respectively. Another impressive result was the quality operation of F4SR at lower Re which can reach 24% improvement at 4 times drop in the value of the Reynolds number.

At the final stage of the research, design of experiments and two optimization algorithms were used to understand the effect of the dimensions (diameter and length) and the position of the swirling prolate spheroid inside the dilution section. Numerical techniques of Uniform Latin Hypercube, Multi-Objectives Genetic Algorithm, and HYBRID offered 54 designs (18 for each technique) to solve and optimize the spheroid aspects based on minimizing the uniformity number and the pressure drop. Understanding the elitism between the contradicting objectives, HYBRID introduced a more optimal slope than the other two techniques, and some designs from the Pareto curve are exhibiting better values than the baseline design by 69% and 15% in uniformity and pressure drop. Generating a correlation matrix, the diameter is the highest influencer with strong inverse and direct coefficients (i.e. magnitudes close to 1) with the uniformity and pressure drop respectively. An extended study is being done by creating the Response surface Methodology which explores the design space by formulating the correlation between the inputs and the outputs

156

from the data of the 18 designs. While Kriging method was the minimal in error, the depicted surfaces showed that the combination of the ranges (0-50% diameter, $\pm$100% length, and $\pm$30% position) is the effective to reach the required objectives. Finally, the 72 virtual designs optimized by Kriging shifted the Pareto curve towards the objectives with more designs at the front.

8.1.2 Future Work Recommendations

The dissertation research focused on the deflection of the hot main stream (i.e. cross flow) towards the cold jets by the aid of central and swirling streamlined body. Revision the whole mixing technique, the cold jets can be controlled and directed by installing guide vanes on the holes. The vanes shapes, sizes, orientation with respect to the cross flow (parallel, orthogonal, and counter), and even the internal versus external installations are different aspects that can be investigated for the thermal uniformity enhancement with the consideration of the pressure drop generated for each case.

Methodologies like the Analysis Led Design and DOE/Optimization are very valuable and time saving for such investigations. Evaluation matrix could be reduced by a third and running expenses of experimentation are saved for the final iterations only. Decision making with contradicting objectives can be easier by unifying them into one variable reflecting the significance/weight of each objective.

8.2 Cavitation Treatment:

8.2.1 Conclusions

An air injection treatment is proposed for the cavitation problem occurring at the rotational zone of a hydro-turbine. The phase change is mainly induced because of the static pressure drop of liquid water phase and the existence of a solid surface for nucleation start. Computational case

study was proposed of cavitating flow over a turbine, and air was added to the solution domain as jet-in-crossflow. Direct injection of at the rotor section allows the substitution of vapor at the low-pressure locations (blade suction side and hub). Air increases the static pressure to be above the vapor saturation pressure and acts a protective layer from cavitation initiation at the blade surface. Records observed less or no vapor occurrence at the zones of high air presence and a general vapor reduction in the whole system. Tracking the vapor content over area and time, averaged vapor volume fraction (VVF) gave a distinct number for each case studied. VVF showed better performance of the turbine when air is used. Because of aeration, less VVF and more output power was retained from the rotating parts. Air-to-water flowrate ratio (Q_a/Q_w) was proved to be an affecting factor by mitigating the cavitation by 47% when reached 16.4%. The work outcomes encouraged in developing a more realistic system (2B3P) that can achieve the objective with less cost. Arranged longitudinally than circumferentially, 2B3P sets 6 orifices linearly at two blocks with 180⁰-separation angle to reduce the setup costs and target the blades prone areas than just one row of ports can do. The 2B3P effectively did a 25% reduction in VVF and nearly 3% power recovery.

Further analysis lead to a recommendation of injection at either before the blade leading edge (but with much cost because of high pressure difference required for injection), or most importantly, in front of the largest thickness of the blade. Considering the second choice (i.e. the maximum thickness) for cost-effectiveness, it allows more contact time for the injected air with the blade which takes the advantage of the tip leakage vortex to sweep over the tip and suction side. Injection at thick part introduces 37% less vapor content and around 2% power buildup than a case of aeration at a thin tip.

The expansive use of the 2B3P over the turbine operation range showed that the air injection, though helping in vapor reduction, might be has some limitation after the peak power. The treatment effectiveness of vapor reduction and power regain decline considerably at the high rotational speeds because of the domination of the centrifugal force which shifts the air towards the tip gap. The power regain nullifies slightly before the peak power, then the air injection works on vapor reduction with more power loss than the no-air case. Understanding such fact aids in effective operation and decision making for the turbine longevity versus the demand at the time.

Additionally, the experimental work on the propeller mode proved the two concepts: 1) effect of air injection in improving the performance (i.e. less motor power consumption) compared to pure cavitation (i.e. no-air case), and 2) the adverse effect of increased amount to air (by more injection pressure) on reducing the improved performance.

Another air injection technique (i.e. hub air injection) was adopted to take the advantage of the centrifugal force in giving the jets additional height and be a convenient solution for no-housing/shrouds systems (i.e. propeller). The invention was proposed as a good approach for the marine industry, but it also competes with the housing air injection because of taking the advantage of alignment with the blades curvature, negative pressure of the rotor rotation, and outward injection with the centrifugal force. Meanwhile, the challenges of the hub injection may be accounted for the complexity of the production. Collaborating with another research, the pressurized air was found beneficial for the vapor reduction and with less power loss than the atmospheric air injection. Beginning from this point, the air injection was sought over four different rows (one port behind each blade) starting from the leading edge and ending at the trailing edge. Similar to the housing air injection, the first row (i.e. closest ports to the leading edge) was the lowest among the four rows in vapor reduction. The optimum reduction goes through the

second row to the fourth row in a direction correlation with the rotational speed. Even though there is no contact between the air and vapor cloud in the cases of the injection from the third and fourth rows, the reduction roots for the major influence from the raised pressure over the cavitation limit. Looking into the power, the other rows than the first proved to improve the performance by average reaching 10% in some cases. However, the power regain may be cut by the compression power for pressurized air.

Finally, and despite the imposed conditions for changing between the turbine and propeller modes, the CFD modeling showed a promising match with the experimental cases on the basis of the formed cavitation pattern and motor power drawn. Moreover, image processing codes built in MATLAB (enhanced contrast, RGB, binary conversion, and object identification/subtraction) improved the high-speed images and CFD scenes for better realization of the vapor/air contents against the liquid water. With only 3% difference, the gaseous phases were captured in area percentages of the CFD scenes as exact as the experimental images. Such advanced codes can be developed and used later in the multiphase imaging analysis for better interface tracking (e.g. Fast-Fourier Transformation).

8.2.2 Recommendations for Future Work

At the beginning, dimensional analysis and similarity is very good tool to reflect the model (experimental and CFD) on large-scale applications (i.e. turbines and propellers). While the current 7.5-cm model was based on low-head (i.e. less than 3 m) Kaplan turbines of smaller diameters (h < 3 m and $D_{turbine} = 0.3 - 1$ m), a recommended section for the similarity with larger sizes and heads (i.e. 100 m heads, 50-100 m diameters, and power of 300-3000 hp) is recommended to emphasize the worth of the proposed technologies.

With exploring the effect of the pressure and ports arrangements (linear vs circumferential) and locations importance. Many trials can be done for optimizing the ports' diameters (larger than a minimum value), number, and the spacing between them. This can be done with the consideration of keeping the compression pressure/ flow rate as minimal as useful (i.e. regained power versus the compression power). A Factor to be considered, especially in CFD, is the thermal effects of the cavitation initiation and implosion because of the energy being released or drawn from the liquid water. Air injection, whether at the same or different from the water temperature, will affect the cavitation behavior to an extent worth studying. The stability of the solution will be a challenge, but a good understanding of the mesh blending will help to keep the work done with high accuracy too.

Another development idea is to get the air injection the closest to the cavitation location; this can be achieved by designing the film air injection on the turbine blades. A preliminary design of a row of holes on the suction side and right after the leading edge (ending with a hole at the blade tip) was suggested, and 3D printed to take the advantage of the air supply through the shaft already made. The idea is driven from the gas turbine blades cooling, and it could be quite effective in suppressing the cavitation initiation.

Finally, aeration effectiveness could be leveraged by adding flow regulators and pulsation modulation, so the ports location and rate of air being adjusted according to the rotational speed and inlet water flow rate. Air temperature might also be a good factor such that the colder air injection decreases the chances of early cavitation.

161

REFERENCES

[1] Walker, A. S., U.S. Patent "Thermostatic mixing valve," No. US1954903 A, filed 7 Oct.1932, issued 17 Apr. 1934.

[2] Vishwakarma, S., Top 8 unbelievable Points in the World Where Two Water Bodies Merge Together, Travel To World, published: April 18, 2016, date accessed: March 14, 2017.

[3] Carlowicz, M., Zambezi River Delta, NASA Earth Observatory, published: December 12, 2013, date accessed: March 14, 2017.

[4] Stevenson M., Popocatepetl Volcano covers Mexico City in Volcanic Ash, The Christian Science Monitor, published: July 12, 2013, date accessed: March 14, 2017.

[5] Sánchez, A.L., Urzay, J. and Liñán, A., 2015, The role of separation of scales in the description of spray combustion, *Proceedings of the Combustion Institute*, 35(2), p.1549-1577.

[6] OSHA Directorate of Technical Support and Emergency Management, Anesthetic Gases: Guidelines for Workplace Exposures, Occupational Safety and Health Administration (OSHA), United States Department of Labor, published: July 20, 1999, revised: May 18, 2000, date accessed: March 14, 2017.

[7] Suthersan, S.S., 1997. *Remediation engineering: design concepts*. Ch.2. CRC-Lewis Publishers.

[8] Pennathur , S., 2008. Flow control in microfluidics: are the workhorse flows adequate?. *Lab on a Chip*, 8(3), pp.383-387.

[9] Agbonzikilo, F.E., Owen, I., Stewart, J., Sadasivuni, S.K., Riley, M. and Sanderson, V., 2016. Experimental and Numerical Investigation of Fuel–Air Mixing in a Radial Swirler Slot of a Dry Low Emission Gas Turbine Combustor. *Journal of Engineering for Gas Turbines and Power*, 138(6), p.061502.

[10] Cooper, C. D., & Alley, F. C. (2011). Air pollution control: A design approach. (4 ed.). Long Grove, IL: Waveland Press, Inc.

[11] Han, J.C., Dutta, S. and Ekkad, S., 2012. *Gas turbine heat transfer and cooling technology*. CRC Press.

[12] Ai, T., Masada, J. and Ito, E., 2014. Development of the High Efficiency and Flexible Gas Turbine M701F5 by Applying "J" Class Gas Turbine Technologies. *Mitsubishi Heavy Industries Technical Review*, 51(1), p.1.

[13] Smith, S.H. and Mungal, M.G., 1998. Mixing, structure and scaling of the jet in crossflow. *Journal of fluid mechanics*, 357, pp.83-122.

[14] Fric, T.F. and Roshko, A., 1994. Vortical structure in the wake of a transverse jet. *Journal of Fluid Mechanics*, *279*, pp.1-47.

[15] Srinivasan, S., Pasumarti, R. and Menon, S., 2012. Large-eddy simulation of pulsed high-speed subsonic jets in a turbulent crossflow. *Journal of Turbulence*, (13), p.N1.

[16] Coelho, S.L. and Hunt, J.C.R., 1989. The dynamics of the near field of strong jets in crossflows. *Journal of Fluid Mechanics*, *200*, pp.95-120.

[17] Pratte, B.D. and Baines, W.D., 1967. Profiles of the round turbulent jet in a cross flow. *Journal of the Hydraulics Division*, *93*(6), pp.53-64.

[18] Keffer, J. and Baines, W.D., 1963. The round turbulent jet in a cross-wind. *Journal of Fluid Mechanics*, *15*(04), pp.481-496.

[19] Gopalan, S., Abraham, B.M. and Katz, J., 2004. The structure of a jet in cross flow at low velocity ratios. *Physics of fluids*, *16*(6), pp.2067-2087.

[20] Terzis, A., Kazakos, C., Kalfas, A.I., Zachos, P.K. and Ott, P., 2012. Swirl jets in crossflow at low velocity ratios. *Journal of Mechanics Engineering and Automation*, *2*(EPFL-ARTICLE-177670), pp.256-266.

[21] Gupta, A., Ibrahim, M.S. and Amano, R.S., 2016. Effect of jet-to-mainstream momentum flux ratio on mixing process. *Heat and Mass Transfer*, *52*(3), pp.621-634.

[22] Salewski, M., Stankovic, D. and Fuchs, L., 2008. Mixing in circular and non-circular jets in crossflow. *Flow, Turbulence and Combustion*, *80*(2), pp.255-283.

[23] Huang, W., Liu, J., Jin, L. and Yan, L., 2014. Molecular weight and injector configuration effects on the transverse injection flow field properties in supersonic flows. *Aerospace Science and Technology*, *32*(1), pp.94-102.

[24] Mi, J., Nathan, G.J. and Luxton, R.E., 2000. Centreline mixing characteristics of jets from nine differently shaped nozzles. *Experiments in Fluids*, *28*(1), pp.93-94.

[25] Zhang, Y., Liu, W., Wang, B., Zhao, Y. and Zhang, D., 2015. Investigation of injectant molecular weight effect on the transverse jet characteristics in supersonic crossflow. *Acta Astronautica*, *114*, pp.101-111.

[26] Saarlas, M., 1987. Steam and gas turbines for marine propulsion. Naval Inst Press.

[27] Bhargava, R.K., Bianchi, M., De Pascale, A., di Montenegro, G.N. and Peretto, A., 2007. Gas Turbine Based Power Cycles-A State-of-the-Art Review. In *Challenges of Power Engineering and Environment* (pp. 309-319). Springer Berlin Heidelberg.

[28] Brandt, D.E. and Wesorick, R.R., 1994. GE gas turbine design philosophy. *GE Power Generation Marketing No. GER-3434D*.

[29] Yuri, M., Masada, J., Tsukagoshi, K., Ito, E. and Hada, S., 2013. Development of 1600 C-class high-efficiency gas turbine for power generation applying J-Type technology. *Mitsubishi Heavy Industries Technical Review*, *50*(3), pp.1-10.

[30] Carter, T.J., 2005. Common failures in gas turbine blades. *Engineering Failure Analysis*, *12*(2), pp.237-247.

[31] Padture, N.P., Gell, M. and Jordan, E.H., 2002. Thermal barrier coatings for gas-turbine engine applications. *Science*, *296*(5566), pp.280-284.

[32] L'vov, G.I., Lysenko, S.V. and Gorash, E.N., 2008. Creep and creep-rupture strength of gas turbine components in view of nonuniform temperature distribution. *Strength of materials*, *40*(5), pp.525-530.

[33] Wang, R., Jing, F. and Hu, D., 2013. In-phase thermal–mechanical fatigue investigation on hollow single crystal turbine blades. *Chinese Journal of Aeronautics*, *26*(6), pp.1409-1414.

[34] Mazur, Z., Luna-Ramirez, A., Juárez-Islas, J.A. and Campos-Amezcua, A., 2005. Failure analysis of a gas turbine blade made of Inconel 738LC alloy. *Engineering failure analysis*, *12*(3), pp.474-486.

[35] Błachnio, J. and Pawlak, W.I., 2011. *Damageability of gas turbine blades-evaluation of exhaust gas temperature in front of the turbine using a non-linear observer*. INTECH Open Access Publisher.

[36] Reyhani, M.R., Alizadeh, M., Fathi, A. and Khaledi, H., 2013. Turbine blade temperature calculation and life estimation-a sensitivity analysis. *Propulsion and power Research*, *2*(2), pp.148-161.

[37] Vardar, N. and Ekerim, A., 2007. Failure analysis of gas turbine blades in a thermal power plant. *Engineering Failure Analysis*, *14*(4), pp.743-749.

[38] Mattingly, J.D., 2002. *Aircraft engine design*. AIAA.

[39] Logan Jr, E., 2003. *Handbook of turbomachinery*. CRC Press.

[40] Błachnio, J., 2010. Examination of changes in microstructure of turbine vanes with the user of non-destructive methods. *Journal of Polish CIMAC*, *5*, pp.17-27.

[41] Povey, T., Chana, K.S., Jones, T.V. and Hurrion, J., 2007. The effect of hot-streaks on hp vane surface and endwall heat transfer: An experimental and numerical study. *Journal of Turbomachinery*, *129*(1), pp.32-43.

[42] Rolls Royce, 2015. *The jet engine*. 5th ed. John Wiley & Sons.

[43] Holdeman, J.D., Srinivasant, R. and Berenfeld, A., 1984. Experiments in dilution jet mixing. *AIAA journal*, *22*(10), pp.1436-1443.

[44] Holdeman, J., Walker, R. and Kors, D., 1973, November. Mixing of multiple dilution jets with a hot primary airstream for gas turbine combustors. In *9th Propulsion Conference* (p. 1249).

[45] SMITH, C., 1990, July. Mixing characteristics of dilution jets in small gas turbine combustors. In *26th Joint Propulsion Conference* (p. 2728).

[46] Holdeman, J.D., 1993. Mixing of multiple jets with a confined subsonic crossflow. *Progress in Energy and Combustion Science*, *19*(1), pp.31-70.

[47] Hoke, J.B., Mountz, D.B., Olsen, H. and Sonntag, R.M., United Technologies Corporation, 2000. *Low emissions can combustor with dilution hole arrangement for a turbine engine*. U.S. Patent 6,101,814.

[48] Lenertz, J. and Lawrence, K., AlliedSignal Inc., 2001. *Combustor dilution bypass method*. U.S. Patent 6,178,737.

[49] Prière, C., Gicquel, L.Y., Gajan, P., Strzelecki, A., Poinsot, T. and Bérat, C., 2005. Experimental and numerical studies of dilution systems for low-emission combustors. *AIAA journal*, *43*(8), pp.1753-1766.

[50] Morris, R.M., Snyman, J. and Meyer, J., 2007. Jets in crossflow mixing analysis using computational fluid dynamics and mathematical optimization. *Journal of propulsion and power*, *23*(3), pp.618-628.

[51] Simons, D.W., Gupta, A.K. and Romoser, C.E., General Electric Company, 2008. *Turbine combustor transition piece having dilution holes*. U.S. Patent 7,373,772.

[52] Ding, G., He, X., Zhao, Z., An, B., Song, Y. and Zhu, Y., 2014. Effect of dilution holes on the performance of a triple swirler combustor. *Chinese Journal of Aeronautics*, *27*(6), pp.1421-1429.

[53] Gupta, A., Ibrahim, M.S. and Amano, R.S., 2015. Experimental study of novel passive control methods to improve combustor exit temperature uniformity. *Heat and Mass Transfer*, *51*(1), pp.23-32.

[54] Glenn Machado, "Polymeric Solution for Pumps Suffering from Cavitation", Pumps and Systems, Cahaba Media Group, Published Oct 8th, 2009, Accessed Dec 22nd 2016.

[55] Gupta, M.K., Sharma, D.S. and Lakhera, V.J., 2016, Vapor Bubble Formation, Forces, and Induced Vibration: A Review, Applied Mechanics Reviews, 68(3), p.030801.

[56] Mørch, K.A., 2015, Cavitation inception from bubble nuclei, Interface focus, Vol. 5 (5), p.20150006.

[57] Kermeen, R.W., 1956, Water tunnel tests of NACA 4412 and Walchner Profile 7 hydrofoils in non-cavitating and cavitating flows, Calif. Inst. of Tech. Hydro. Lab. Rep. 47-5.

[58] Rayleigh, L., 1917, On the pressure developed in a liquid during the collapse of a spherical cavity, Phil. Mag., Vol. 34, pp. 94–98, doi:10.1080/14786440808635681

[59] Plesset, M.S, 1949, The dynamics of cavitation bubbles, ASME J. Appl. Mech. Vol. 16, pp. 228–231.

[60] Sauer, J., Instationaer kavitierende Stroemungen - Ein neues Modell, basierend auf Front Capturing VOF und Blasendynamik, Dissertation, universität Karlsruhe, Germany, 2000.

[61] Tinguely, M., 2013, The effect of pressure gradient on the collapse of cavitation bubbles in normal and reduced gravity (Doctoral dissertation, ÉCOLE POLYTECHNIQUE FÉDÉRALE DE LAUSANNE).

[62] Benjamin, T.B. and Ellis, A.T., 1966, The collapse of cavitation bubbles and the pressures thereby produced against solid boundaries, Philosophical Transactions of the Royal Society of London A: Mathematical, Physical and Engineering Sciences, Vol. 260 (1110), pp. 221-240.

[63] Brennen, C. E., 2013, Cavitation and bubble dynamics, Cambridge University Press, UK.

[64] Rus, T., Dular, M., Širok, B., Hočevar, M. and Kern, I., 2007, An investigation of the relationship between acoustic emission, vibration, noise, and cavitation structures on a Kaplan turbine, Journal of Fluids Engineering, Vol. 129 (9), pp. 1112-1122.

[65] Liu, H., Wang, Y., Yuan, S., Tan, M. and Wang, K., 2010, Effects of blade number on characteristics of centrifugal pumps, Chinese Journal of Mechanical Engineering, Vol. 23(6), pp.742-747.

[66] Medvitz, R.B., Kunz, R.F., Boger, D.A., Lindau, J.W., Yocum, A.M. and Pauley, L.L., 2002, Performance analysis of cavitating flow in centrifugal pumps using multiphase CFD, Journal of Fluids Engineering, Vol. 124(2), pp.377-383.

[67] Markovic, S., 2006, Cavitational wear of the blades of Francis turbine, Tribology in industry, Vol. 28(3&4), pp.16-22.

[68] Escaler, X., Egusquiza, E., Farhat, M., Avellan, F. and Coussirat, M., 2006, Detection of cavitation in hydraulic turbines, Mechanical systems and signal processing, Vol. 20(4), pp.983-1007.

[69] Gülich, J. F., 2008, Centrifugal Pumps, Springer-Verlag Berlin Heidelberg, New York, US. DOI: 10.1007/978-3-642-12824-0.

[70] Zhi-yong D., 2006, "Cavitation Control by Aeration and Its Compressible characteristics", Journal of Hydrodynamics, Ser.B, 18(4), pp.499-504

[71] Tomov P., Khelladi S., Ravelet F., Sarraf C., Bakir F., and Vertenoeuil P., 2016, "Experimental Study of Aerated Cavitation in a Horizontal Venturi Nozzle", Experimental Thermal and Fluid Science, 70, pp.85-95.

[72] Rivetti A., Angulo M., Lucino C., and Liscia S., 2015, "Pressurized Air Injection in an Axial Hydro-Turbine Model for The Mitigation of Tip Leakage Cavitation", 9th International Symposium on Cavitation (CAV2015), Journal of Physics: Conference Series 656.

[73] Elgammal T, Amano RS, 2018, "Effectiveness of Central Swirlers in the Thermal Uniformity of Jet-in-Crossflow Mixing" ASME. J. Energy Resour. Technol., 140(10): pp. 101202-101202-11, doi:10.1115/1.4040075.

[74] Nicoud, F., and Ducros, F., 1999, "Subgrid-Scale Stress Modelling Based on the Square of the Velocity Gradient Tensor," Flow, Turbulence and Combustion, 62, pp. 183-200.

[75] McKay, M.D., Beckman, R.J. and Conover, W.J., 2000. A comparison of three methods for selecting values of input variables in the analysis of output from a computer code. *Technometrics*, *42*(1), pp.55-61.

[76] Bruns, A., 1998. A local search heuristic for the two-stage capacitated facility location problem. In *Advances in distribution logistics* (pp. 143-164). Springer Berlin Heidelberg.

[77] Lasdon, L.S., Fox, R.L. and Ratner, M.W., 1974. Nonlinear optimization using the generalized reduced gradient method. *Revue française d'automatique, d'informatique et de recherche opérationnelle. Recherche opérationnelle*, *8*(3), pp.73-103.

[78] Floudas, C.A., 2013. *Deterministic global optimization: theory, methods and applications* (Vol. 37). Springer Science & Business Media.

[79] Rigoni, E. and Poles, S., 2005. NBI and MOGA-II, two complementary algorithms for multi-objective optimizations. In *Dagstuhl Seminar Proceedings*. Schloss Dagstuhl-Leibniz-Zentrum für Informatik.

[80] Gleisberg, T., Höche, S., Krauss, F., Schälicke, A., Schumann, S. and Winter, J.C., 2004. SHERPA 1. α, a proof-of-concept version. *Journal of High Energy Physics*, *2004*(02), p.056.

[81] Chase, N., Redemacher, M., Goodman, E., Averill, R. and Sidhu, R., 2010. A benchmark study of optimization search algorithms. *MI, USA: Red Cedar Technology*.

[82] ElGammal, T., Yen, Y. H., Amano, R. S., Millevolte, J., Muller, R. J., and Lequesne, B., 2016, Numerical Investigations on Intake Tube Design of Micro Kaplan Hydro-Turbine System, Proceedings of the ASME 2016 Fluids Engineering Division Summer Meeting (FEDSM2016), July 10-14, 2016, Washington, DC, USA.

[83] Yen, Y. H., ElGammal, T., Amano, R. S., Millevolte, J., Muller, R. J., and Lequesne, B., 2016, Numerical Optimization of Micro Kaplan Hydro Turbine System, Proceedings of the

ASME 2016 Fluids Engineering Division Summer Meeting (FEDSM2016), July 10-14, 2016, Washington, DC, USA.

[84] Noh, W.F. and Woodward, P., 1976, "SLIC (Simple Line Interface Calculation)", Proceedings of the Fifth International Conference on Numerical Methods in Fluid Dynamics, Twente University, Enschede, NL, pp. 330-340. Springer Berlin Heidelberg.

[85] Hirt, C.W. and Nichols, B.D., 1981, "Volume of Fluid (VOF) Method for the Dynamics of Free Boundaries", Journal of computational physics, 39(1), pp.201-225.

[86] Leonard, A., 1975, "Energy Cascade in Large-Eddy Simulations of Turbulent Fluid Flows.", Advances in geophysics 18 (1975): 237-248.

[87] Schmitt, F.G., 2007, "About Boussinesq's Turbulent Viscosity Hypothesis: Historical Remarks and a Direct Evaluation of its Validity", Comptes Rendus Mécanique, 335(9-10), pp.617-627.

[88] Ducros, F., Nicoud, F. and Poinsot, T., 1998, "Wall-Adapting Local Eddy-Viscosity Models for Simulations in Complex Geometries", Numerical Methods for Fluid Dynamics VI, pp.293-299.

[89] Brooks, F.J., 2000, "GE gas turbine performance characteristics," GE Power Systems, Schenectady, NY.

[90] Petchers, N., 2003, Combined heating, cooling & power handbook: technologies & applications: an integrated approach to energy resource optimization, The Fairmont Press, Inc.

APPENDIX I: UNCERTAINTY ANALYSIS

- **Minimum Number of Experiments:** $(M + 1)(M + 2)/2 = (5)(6)/2 = 15$

- **Maximum Number of Experiments:** $(M + 1)(M + 2) = (5)(6) = 30$

- **24 Combinations by Uniform Latin Hypercube Table:**

	T_{ex}	T_{in}	V_{ex}	V_{in}
Calculation 0	Reading# 2	2	1	1
Calculation 1	1	2	3	1
Calculation 2	3	3	2	2
Calculation 3	3	2	3	3
Calculation 4	3	1	2	3
Calculation 5	1	1	1	2
Calculation 6	2	2	3	1
Calculation 7	1	3	2	3
Calculation 8	3	3	1	1
Calculation 9	1	1	1	3
Calculation 10	2	1	1	1
Calculation 11	1	2	2	1
Calculation 12	1	2	1	2
Calculation 13	1	1	2	1
Calculation 14	2	3	3	3
Calculation 15	2	3	1	2
Calculation 16	3	3	2	1
Calculation 17	1	3	3	3
Calculation 18	3	2	2	3
Calculation 19	2	2	3	1
Calculation 20	3	3	1	2
Calculation 21	2	1	3	2
Calculation 22	1	3	1	2
Calculation 23	3	1	3	2

- **Average Points Calculations:** $\sum_{i=1}^{N_{calculations}} \dfrac{f_i^*|_{point}}{N_{calculations}}$

- **Average f^* for the 7 points of Staggered Hole (SH) case:**

Point	0 (center)	1	2	3	4	5	6 (surface)
Avg. f^*	0.684477	0.663657	0.48553635	0.122354	-0.18762	-0.48372	-0.48372

- **Sample Standard Deviation:** $\sqrt{\dfrac{\sum_{i=1}^{N_{calculations}}(f_i^*-f_{avg}^*)^2\big|_{point}}{N_{calculations}-1}}$

- **Sample Standard Deviation of f^* for the 7 points of Staggered Hole (SH) case:**

Point	0 (center)	1	2	3	4	5	6 (surface)
STD	0.108356	0.104314	0.090923449	0.06969	0.0495	0.034449	0.034449

- **Average Sample Standard Deviation for the whole f^* line:**

$$\sum_{i=1}^{N_{points}}\frac{STD_i}{N_{points}} = 0.07$$

APPENDIX II: IMAGE PROCESSING CODES

High-Speed Images Analysis

```
tic %starts timer
dbstop if error % stops script and shows line with error if error is found in script
clr % clears workspace for fresh start
pixscale = 1.1245 / 165.6; %this is hard coded, also a close aproximation, will need to be
adjusted each time the camera was moved
    % finds area of cavitiation in pixels (unit of measurement)
    % path = addpath( genpath( 'C:\Users\ccasper\Desktop\Image Processing' ) ); % defines path
and adds all folders to search path
    % comparison_image = imread( 'C001H001S0001_1000001.jpg' );
    % process_comparison = imadjust( adapthisteq( comparison_image ) );
    % crop_comparison = imcrop( process_comparison , [ 480 260 520 480 ] );
    Images = dir( 'C:\Users\ccasper\Desktop\Image
Processing\Cavitation\Cavitation_8_14_2018\R2_2000rpm\C001H001S0001_test\*.jpg' );
    % ^^ this line defines a structer array for all .jpg files in the directory ^^
    Cavitation_percent = zeros( length( Images ) , 1 );
    %    for i = 1 : 1 length( Images ) %use this to look at an
    %    individual image
    for i = 1 : length( Images ) %use parfor for speed
        image_name( 1 : ( length( Images ) ) , : ) = transpose( { Images( : ).name } );% grabs image
name from structure array
        timestamp( 1 : ( length( Images ) ) , : ) = transpose( { Images( : ).date } );% grabs date from
structure array(for listing in logical order if needed)
        analyse_image = imread( Images( i ).name ); % image to be analysed
        image_filename = ( Images( i ).name ); % pulls image filename from structure array
        fprintf( 'Working on %s image...\n' , image_filename ); % this shows where we are in the
script when script is running
        adapt_image = adapthisteq( analyse_image ); % uses historgram adaption to adjust contrast
        adjust_image = imadjust( adapt_image ); % adjusts lower contrast by -1% and upper
contrast by +1%
        crop_image = imcrop( adjust_image,[ 275 370 415 440 ] ); % defines region of
image(possible object recognition to define crop region)
        binary_image = imbinarize( crop_image , 'adaptive' ,'ForegroundPolarity' , 'dark' ,
'sensitivity' , 0.9 ); % converts to binary, older matlab versions(2015) use the function im2bw and
dont have 'adaptive'
        Cavitation_percent ( i ) = ( (bwarea( binary_image ) ) ./ ( 441 * 416 ) ) * 100; % percent
area of cavitiation in pixels
    end

    Cavitation_percent_mean = mean( mean( Cavitation_percent ) );
```

```
    toc

    %% this section is for exporting results to excel

    %
    % Cavitation = num2cell(Cavitation);
    % fprintf('Do you wish to export image processing results to excel? \n');
    % answer = input('yes/no?: \n' , 's');
    % if strcmpi( answer, 'no' )
    %     fprintf(' Image processing for this directory is complete. \n' )
    % elseif strcmpi( answer, 'yes')
    %     excel_filename = 'Cavitation_8_14_2018_R2_2000rpm_test_1.xlsx';
    %     col_header = { 'image_filename' , 'area of cavitation(in.)' ,'timestamp'};
    %     xlswrite( excel_filename , col_header , 1 , 'A1' );
    %     xlswrite( excel_filename , image_name, 1 , 'A2' );
    %     xlswrite( excel_filename , Cavitation , 1 , 'B2' );
    %     xlswrite( excel_filename , timestamp , 1 , 'C2' );
    %     fprintf(' Results have been exported to an excel spreadsheet. \n');
    % else
    %     fprintf('invalide answer, run section again and type out exactly as shown yes or no \n');
    % end
    % toc
```

CFD Scenes Analysis

```
clr
dbstop if error
% input folder path below
images                              =                         dir('C:\Users\ccasper\Desktop\Image
Processing\CFD_images\with_cavitation\Same_location');
base_image = imread( 'R1_CR_n12.5@180000_Blade VVF_No CAV_BBG.png' );
crop_base_image = imcrop( base_image , [ 715 , 11 , 719 , 537 ] );
base_gray_image = rgb2gray( crop_base_image );
base_binary_image = imbinarize( base_gray_image );
denominator = sum( sum( base_binary_image) );
cavitation = zeros( 1 , 11 );
for i = 3 : length( images )
   analyse_image = imread( images( i ).name );
   image_name( 1 : ( length( images ) ) , : ) = transpose( { images( : ).name } );
   crop_image = imcrop( analyse_image , [ 715 , 11 , 719 , 537 ] );
   subtracted_image = analyse_image - base_image;
   gray_image = rgb2gray( subtracted_image );
   binary_image = imbinarize( gray_image );
```

172

```
    numerator = sum( sum( binary_image ) );
    cavitation( i ) = (numerator/denominator) * 100;
end
cavitation = transpose( cavitation );
cavitation = num2cell( cavitation);
results = [ image_name , cavitation ];
disp( results );
```

TAREK ELGAMMAL CURRICULUM VITAE

Work Experience

Design Optimization Engineer [2018-Present]
Bradley Corporation, Plant 1, Menomonee Falls, WI

- Investigating the design and materials of the immersion-type heating elements for low and high flow rater water heating systems.
- Design simple 1-D codes of flow and heat analysis for Bradley's tankless water heaters
- Understanding, analyzing, and simulating the water heaters based on the Uniform Energy Factor (UEF) standardized by the Department of Energy (DOE)
- Establishing CAE software criteria based on the company's projects requirements
- Surveying the market for identifying the features and offers of different computational software packages. Trial the capabilities of the software packages.

Research Assistant [2016-2018]
CFD Methodology Engineer at Harley-Davidson Product Development Center, Wauwatosa, WI

- Construct Mesh Morphing/ CAD Parametrization models on CFD simulations of OE parts.
- Architect automated topological optimization processes integrating multiple CAE software (Mesh/CAD control, CFD, and DOE/ Optimization/ Statistical Analysis Tool).
- By applying Analysis-Led-Design on multiple powertrain and aerodynamics models, managed to introduce considerable improvements in the engine and bike performances. Best Pareto designs were proposed for experimental testing and manufacturing when approved.
- Simulated a phase-change phenomenon inside the water cooling system and do thermal and hydrodynamic investigations to predict boiling-prone locations. Made optimization plans for better cooling flow distribution and reshape some passages. Selected optimum designs for the cooling circuits of no or minimum vapor generation.
- Liaison with software technical supports to have their aid and give our feedback for fulfilling the company's needs.
- Create tutorials and train other engineers to use new the tools/ software.

Research Graduate Student [2015-Present]
Prof. Ryo Amano's Combustion and Hydro-turbine Labs, Mechanical Engineering Department, CEAS, UWM.

- Working on thermal mixing and micro axial hydro-turbines projects (CFD and experiments) in the University Services and Research Building (USRB) and the Water Technology Accelerator (WaTA), Global Water Center.

- Participated and led 3 turbine projects involving earlier CFD prediction of the performance of 12-inch vertical turbine system, 3-inch horizontal turbine system, and 3-in turbine cavitation. Supervised experimental team and shared in recording the measurements at different stages.
- Optimized the geometrical aspects of some components in turbine system (e.g. Intake tube aspect ratio and the effect of bellmouth profile shape on turbine performance).
- Simulated phase-change (cavitation) initiation and propagation at different operation conditions. Build and optimized aeration ports into the system to suppress cavitation by tracking vapor content and turbine performance.
- Experimental measurements and data analysis for (Water aeration characteristics, Hydro-turbines performance, and gaseous thermal mixing) projects. Equipment used are pressure sensors and velocity meters, thermocouples, DAQ, tachometer, rotary torque sensors, magnetic flow meters, and high-speed camera with analysis software.
- Prepared project reports and (co)authored publications for DOE/NSF/ASME/AIAA.
- Communication representative for directing STAR-CCM+ research and academic licenses and updating the software in the mechanical engineering department. Responsible for distributing the research licenses running on the High-Performance Computing (HPC) clusters.
- Aided colleagues at different CFD projects: Optimizing slot dimensions in a novel airfoil design, aeration effectiveness on hydrofoil cavitation, HVAC in metro station.
- Holding training sessions for the new STAR-CCM+ users, and preparing tutoring materials.

Teaching and Research Assistant [2015-2016]
ME323 (Fluid Mechanics Lab) course/ Hydro and Gas Turbine Flow and Thermal Analyses, Mechanical Engineering Department, CEAS, UWM.
- ME 323 Fluid Mechanics Lab instructor, and researcher in the axial hydro-turbines with Cadens LLC.
- The work comprised teaching theoretical lectures about aerodynamics, pumps, Bernoulli's equation, discharge coefficient, CFD, and flow visualization using PIV.
- The job involved instructing students to handle experimental setups and generate a proper experiment with accurate data. At the end, grading the weekly technical documents (reports, letters, and memos) submitted by each group, and evaluating their presentations.

Teaching and Research Assistant [2010-2014]
Mechanical Engineering Department, Faculty of Engineering, Cairo University
Credit Hours System, Faculty of Engineering, Cairo University
- Numerical Methods in Thermo-Fluid Engineering Systems, Heat and Mass Transfer, Heat Transfer Systems Experimental Laboratories, Fine Measurements Laboratories.
- English Language, Mechanical Systems for Civil Engineering, Marketing, Economics, Communication and Presentation Skills, Life Long Skills.
- M.Sc. research

Education

Ph.D. Program- Mechanical Engineering [May 2019]
College of Engineering and Applied Sciences (CEAS), UW-Milwaukee (GPA: 4/4)
<u>Dissertation:</u> The Design and Optimization of Jet-in-Crossflow (JICF) for Engineering Applications: Thermal Uniformity in Gas Turbine and Cavitation Treatment in Hydro Turbines
<u>Ph.D. courses:</u> Advanced Engineering Mathematics I and II - Fundamentals of Fluid Mechanics - Advanced Fluid Mechanics - Heat and Mass Convection - Advanced Transport Processes

M.Sc. – Mechanical Engineering [2013]
Faculty of Engineering, Cairo University, Egypt (GPA: 3.83/4, 3rd place in 70-students class)
<u>Thesis:</u> Numerical Simulation for Thermal Flow Cases using Smoothing Particle Hydrodynamics Method. (*Distinction)*
<u>Pre-Master Courses:</u> Numerical methods - Fine Measurements - Technical writing - Thermal convection - Advanced fluid mechanics – Turbulent flow

B.Sc. (Honors) – Mechanical Engineering [2010]
Faculty of Engineering, Cairo University, Egypt
<u>Evaluation:</u> Distinction with honors (86.05%), 3rd place in 250-students class
<u>Thesis:</u> Solar Hydrogen Fuel Cell Water Heater Educational Stand

Projects

1) Solar Hydrogen Fuel Cell Water Heater Educational Stand, Cairo University, Egypt. *2009-2010 (ASHRAE, Students Activities Committee approved and funded)*
2) Testing an Educational Air Handling Unit and Writing Instructional Manual for Undergraduate Laboratory. Egypt. *2014*
3) Numerical and Experimental Design of Hydro Turbine System. UWM. *2015-2016 (DOE funded)*
4) CFD analysis of Cavitation Treatment over Hydrofoil Surface. UWM. *2016*
5) Numerical and Experimental Investigation of Cavitation Treatment in Kaplan Hydro-Turbine. UWM. *2016-2017 (NSF I/U CRC)*
6) Numerical Exploration of Cavitation Treatment Methodology in Kaplan Hydro-Turbine. *2017-Present*

Trainings and Internships

1) Maintenance Intern in Sugar and Integral Industries company, Giza, Egypt. *2007*
2) Production & Maintenance Intern in Flora paper mills company, Giza, Egypt. *2008*
3) Production & Maintenance in Petrobel for petroleum company, Mansoura, Egypt. *2008*
4) Surface well testing Intern in Schlumberger Egypt/ El-Katamia site, Giza, Egypt. *2009*

Awards

- Schlumberger Award for Academic Excellence, *2009*
- Best student in Mechanical Power department, CUFE, *2009 & 2010*
- ASHRAE funded senior graduation project, CUFE, *2009- 2010*
- Teaching Assistantship and M.Sc. Degree tuition remission, CUFE, *2010*
- University of Cincinnati Ph.D. degree offer, *Fall 2013 (Declined)*
- University of Birmingham Ph.D. offer, *Fall 2014 (Declined)*
- University of Wisconsin-Milwaukee Ph.D. offer, *Fall 2014*
- University of Wisconsin-Milwaukee Dean's Fellowship, *2014- 2018*
- 2nd Place of UW-Milwaukee CEAS Poster Competition, *Spring 2019*

Languages

Arabic: Native Language

English: Very good (TOEFL: 90), work communication language for 4 years

Computer skills

Coding	**MatLab (Self-learning and work levels)**
	1) ***Modelling the performance of integrated renewable energies systems***: Photovoltaic, electrolyzer, and fuel cell
	2) ***Constructing SPH simulation codes:*** Heat conduction, air compression stroke in a cylinder, and wave propagation in air chamber.
CAD	**AutoCAD**, **PTC Creo, SolidWorks (Self-learning Level)**
	1) Designing hydro-turbine rotor
	2) 3D sketching of annular mixing chamber
Simulation	**STAR CCM+ (Work Level)**
	1) R&D (CAD manipulation and surface repair, Rotational Domains, Thermal analysis, VOF Multiphase, Phase-Change, LES Unsteady Turbulence, Mesh Deformation Tool, and Optimate+)
	2) Undergrad, grad students, and engineers-level instructor/ guide
Optimization	**Sculptor (Work Level)**
	1) Designing groups for geometry (CAD or Mesh) morphing
	2) Design of Experiments and Optimization based on the limits of the mesh morphing control groups
	ModeFrontier (Work Level)
	1) Designing a full optimization workflow coupled with Sculptor and STARCCM+ for mesh morphing engine intake parts and mixing chamber components

Publications

177

Organizations

- **American Institute of Aeronautics and Astronautics (AIAA)**
  UWM Student Chapter (Secretary), June 2015- June 2017
- **American Institute of Aeronautics and Astronautics (AIAA) member**
- **American Society of Mechanical Engineers (ASME) member**